

DEPARTAMENTO DE ASTROFÍSICA
Universidad de La Laguna

STUDY OF ACTIVE GALACTIC NUCLEI IN THE OTELO SURVEY

Marina Ramón Pérez

Memoria presentada para optar al grado de
Doctora por la Universidad de La Laguna

Directores:

Dr. Jordi Cepa
Dr. Ángel Bongiovanni
Dra. Ana María Pérez García



INSTITUTO DE ASTROFÍSICA DE CANARIAS
Junio de 2017

Este documento incorpora firma electrónica, y es copia auténtica de un documento electrónico archivado por la ULL según la Ley 39/2015.
Su autenticidad puede ser contrastada en la siguiente dirección <https://sede.ull.es/validacion/>

Identificador del documento:	969870	Código de verificación:	8KFVZkZp
Firmado por:	MARINA RAMÓN PÉREZ UNIVERSIDAD DE LA LAGUNA	Fecha:	28/06/2017 21:15:24
	ANGEL MANUEL BONGIOVANNI PEREZ UNIVERSIDAD DE LA LAGUNA		29/06/2017 09:30:15
	JORGE CEPA NOGUE UNIVERSIDAD DE LA LAGUNA		29/06/2017 09:33:05
	ANA MARIA PEREZ GARCIA UNIVERSIDAD DE LA LAGUNA		29/06/2017 11:12:35
	ERNESTO PEREDA DE PABLO UNIVERSIDAD DE LA LAGUNA		04/07/2017 18:28:07

Examination date: September 2017
Thesis supervisors: Dr. Jordi Cepa, Dr. Ángel Bongiovanni and Dra. Ana María Pérez García

© Marina Ramón Pérez 2017

Este documento incorpora firma electrónica, y es copia auténtica de un documento electrónico archivado por la ULL según la Ley 39/2015.
Su autenticidad puede ser contrastada en la siguiente dirección <https://sede.ull.es/validacion/>

Identificador del documento:	969870	Código de verificación:	8KFVZkZp
Firmado por:	MARINA RAMÓN PÉREZ UNIVERSIDAD DE LA LAGUNA	Fecha:	28/06/2017 21:15:24
	ANGEL MANUEL BONGIOVANNI PEREZ UNIVERSIDAD DE LA LAGUNA		29/06/2017 09:30:15
	JORGE CEPA NOGUE UNIVERSIDAD DE LA LAGUNA		29/06/2017 09:33:05
	ANA MARIA PEREZ GARCIA UNIVERSIDAD DE LA LAGUNA		29/06/2017 11:12:35
	ERNESTO PEREDA DE PABLO UNIVERSIDAD DE LA LAGUNA		04/07/2017 18:28:07

*A Canarias,
por sus cielos, por su gente
y por cambiarme la vida*

Este documento incorpora firma electrónica, y es copia auténtica de un documento electrónico archivado por la ULL según la Ley 39/2015.
Su autenticidad puede ser contrastada en la siguiente dirección <https://sede.ull.es/validacion/>

Identificador del documento:	969870	Código de verificación:	8KFVZkZp
Firmado por:	MARINA RAMÓN PÉREZ UNIVERSIDAD DE LA LAGUNA	Fecha:	28/06/2017 21:15:24
	ANGEL MANUEL BONGIOVANNI PEREZ UNIVERSIDAD DE LA LAGUNA		29/06/2017 09:30:15
	JORGE CEPA NOGUE UNIVERSIDAD DE LA LAGUNA		29/06/2017 09:33:05
	ANA MARIA PEREZ GARCIA UNIVERSIDAD DE LA LAGUNA		29/06/2017 11:12:35
	ERNESTO PEREDA DE PABLO UNIVERSIDAD DE LA LAGUNA		04/07/2017 18:28:07

Este documento incorpora firma electrónica, y es copia auténtica de un documento electrónico archivado por la ULL según la Ley 39/2015.
Su autenticidad puede ser contrastada en la siguiente dirección <https://sede.ull.es/validacion/>

Identificador del documento: 969870

Código de verificación: 8KFVZkZp

Fecha: 28/06/2017 21:15:24

Firmado por: MARINA RAMÓN PÉREZ
UNIVERSIDAD DE LA LAGUNA

29/06/2017 09:30:15

ANGEL MANUEL BONGIOVANNI PEREZ
UNIVERSIDAD DE LA LAGUNA

29/06/2017 09:33:05

JORGE CEPA NOGUE
UNIVERSIDAD DE LA LAGUNA

29/06/2017 11:12:35

ANA MARIA PEREZ GARCIA
UNIVERSIDAD DE LA LAGUNA

04/07/2017 18:28:07

ERNESTO PEREDA DE PABLO
UNIVERSIDAD DE LA LAGUNA

RESUMEN

Los cartografiados celestes han sido, históricamente, el principal método de obtención de datos astronómicos para el estudio del Universo. Esta tesis se centra en uno de ellos, OTELO, un cartografiado en líneas de emisión que utiliza los filtros sintonizables del instrumento OSIRIS del Gran Telescopio CANARIAS, actualmente el mayor telescopio óptico reflector completamente orientable del mundo. El uso combinado de los filtros sintonizables, que permiten obtener espectroscopía de baja resolución en dos dimensiones de todas las fuentes del campo, y de un telescopio de gran diámetro, capaz de alcanzar magnitudes límite extremadamente profundas, es ideal para la búsqueda de objetos emisores débiles.

En particular, nos hemos centrado en el estudio de los núcleos activos de galaxias (AGN, por sus siglas en inglés), uno de los objetos más brillantes y fascinantes del Universo. Las galaxias que albergan un AGN muestran una intensa emisión en su núcleo, fruto de la acreción de material por parte de un agujero negro supermasivo ubicado en su centro, según el modelo actualmente aceptado. Su estudio puede darnos información valiosa acerca de la formación y evolución de las galaxias en el Universo.

Durante esta tesis, hemos llevado a cabo la reducción y la calibración de los datos de OTELO desde cero, un proceso que ha requerido múltiples iteraciones y el diseño de procedimientos específicos. A continuación se ha obtenido un catálogo profundo multi-rango de todas las fuentes del campo. El siguiente paso ha sido la selección de los objetos emisores usando, por un lado, la información contenida en el catálogo y, por otro, los pseudo-espectros previamente construidos para cada fuente, que constituyen una herramienta única fruto del uso de filtros sintonizables. Nos hemos centrado, específicamente, en la población de emisores H α a $z \sim 0.40$, una de las líneas de emisión más intensas del espectro óptico de las galaxias, directamente relacionada con su formación estelar y con la actividad nuclear cuando ésta está presente. A continuación, hemos seleccionado los AGN del campo utilizando cuatro métodos distintos, cada uno de ellos centrado en un rangopectral diferente. Finalmente hemos analizado la muestra de AGN, en un estudio que incluye su demografía y morfología, la búsqueda de galaxias infrarrojas luminosas y ultra-luminosas (LIRGs/ULIRGs), la obtención de la función de luminosidad (LF) de H α a $z \sim 0.40$ y un análisis del entorno a ese desplazamiento al rojo.

El principal producto de esta tesis es el catálogo de objetos emisores de OTELO, un catálogo profundo y multi-rango que será la base de futuros trabajos. Además, hemos obtenido muestras fiables de emisores H α y de AGN en el campo de OTELO. El análisis de la población de AGN nos ha permitido confirmar resultados previos, como el predominio de galaxias de tipo tardío, una mayor incidencia de AGN entre los ULIRGs que entre los LIRGs o la efectividad de los rayos-X a la hora de seleccionar los AGN, entre otras muchas cosas. La función de luminosidad H α obtenida a $z \sim 0.40$ nos ha permitido, además, extender el límite de anteriores LFs, llegando a luminosidades casi 1 dex más débiles que el resto de los trabajos publicados hasta la fecha. Conociendo los AGN a $z \sim 0.40$, hemos podido estimar también la tasa de formación estelar de las galaxias con formación estelar a ese desplazamiento al rojo, así como la contribución de los AGN a la luminosidad total.

Este documento incorpora firma electrónica, y es copia auténtica de un documento electrónico archivado por la ULL según la Ley 39/2015.
Su autenticidad puede ser contrastada en la siguiente dirección <https://sede.ull.es/validacion/>

Identificador del documento:	969870	Código de verificación:	8KFVZkZp
Firmado por:	MARINA RAMÓN PÉREZ UNIVERSIDAD DE LA LAGUNA	Fecha:	28/06/2017 21:15:24
	ANGEL MANUEL BONGIOVANNI PEREZ UNIVERSIDAD DE LA LAGUNA		29/06/2017 09:30:15
	JORGE CEPA NOGUE UNIVERSIDAD DE LA LAGUNA		29/06/2017 09:33:05
	ANA MARIA PEREZ GARCIA UNIVERSIDAD DE LA LAGUNA		29/06/2017 11:12:35
	ERNESTO PEREDA DE PABLO UNIVERSIDAD DE LA LAGUNA		04/07/2017 18:28:07

Este documento incorpora firma electrónica, y es copia auténtica de un documento electrónico archivado por la ULL según la Ley 39/2015.
Su autenticidad puede ser contrastada en la siguiente dirección <https://sede.ull.es/validacion/>

Identificador del documento: 969870

Código de verificación: 8KFVZkZp

Fecha: 28/06/2017 21:15:24

Firmado por: MARINA RAMÓN PÉREZ
UNIVERSIDAD DE LA LAGUNA

29/06/2017 09:30:15

ANGEL MANUEL BONGIOVANNI PEREZ
UNIVERSIDAD DE LA LAGUNA

29/06/2017 09:33:05

JORGE CEPA NOGUE
UNIVERSIDAD DE LA LAGUNA

29/06/2017 11:12:35

ANA MARIA PEREZ GARCIA
UNIVERSIDAD DE LA LAGUNA

04/07/2017 18:28:07

ERNESTO PEREDA DE PABLO
UNIVERSIDAD DE LA LAGUNA

SUMMARY

Surveys have historically been the main tool to gather astronomical information about the Universe. This thesis focuses on one of them, the OTELO survey, an emission-line survey carried out with the tunable filters of the OSIRIS instrument at the Gran Telescopio CANARIAS, currently the largest fully steerable optical reflecting telescope in the world. The combined use of tunable filters, that allowed us obtaining 2D low-resolution spectroscopy of all the sources in the field, and a large diameter telescope, which reaches very deep limiting fluxes, is ideal for the search of faint emitters.

In particular, we have concentrated in the study of active galactic nuclei (AGN), one of the brightest and most intriguing objects in the Universe. Galaxies hosting an AGN show strong nuclear emission due to the accretion of material by the central supermassive black hole, according to the currently accepted paradigm. Their study provides invaluable information about the formation and evolution of galaxies in the Universe.

During this thesis, we have performed the reduction and calibration of OTELO data from scratch, a process that has required multiple iterations and the design of specific procedures. A deep multiwavelength catalogue of sources in the field has been obtained. The next step has been the selection of emission-line objects using the information gathered in the multiwavelength catalogue as well as the pseudo-spectra built for every source in the field, an unique tool only available when working with tunable filters. We have specifically focused on the H α population at $z \sim 0.40$, one of the most intense emission-lines in the optical spectrum of galaxies which can give valuable information about the star-formation and nuclear activity when present. After that, the selection of AGN has been performed with the use of four different methods, each targeting a different spectral range. Finally, we have analysed the AGN sample, in a study that included demographics, morphology, the search for luminous and ultra-luminous infrared galaxies (LIRGs/ULIRGs), the obtention of the H α luminosity function at $z \sim 0.40$ and an analysis of the environment at this redshift.

The main product of this thesis is OTELO's deep, multiwavelength catalogue of emission-line objects, which will be the basis for future works. In addition, we have obtained reliable samples of H α emitters and of AGN in the field. The analysis performed over the AGN population has allowed us to confirm previous results, such as the prevalence of late-type galaxies, the higher incidence of AGN in ULIRGs than in LIRGs or the effectiveness of the X-rays selection method for AGN, among many others. In addition, the H α luminosity function (LF) obtained at $z \sim 0.40$ has allowed us to extend the faint-end of previous LFs, reaching luminosities almost 1 dex fainter than those of previously published works. By characterizing the AGN sources at $z \sim 0.40$, we have also been able to estimate the star-formation rate of star-forming galaxies at this redshift, as well as the contribution of AGN to the total luminosity.

Este documento incorpora firma electrónica, y es copia auténtica de un documento electrónico archivado por la ULL según la Ley 39/2015.
Su autenticidad puede ser contrastada en la siguiente dirección <https://sede.ull.es/validacion/>

Identificador del documento:	969870	Código de verificación:	8KFVZkZp
Firmado por:	MARINA RAMÓN PÉREZ UNIVERSIDAD DE LA LAGUNA	Fecha:	28/06/2017 21:15:24
	ANGEL MANUEL BONGIOVANNI PEREZ UNIVERSIDAD DE LA LAGUNA		29/06/2017 09:30:15
	JORGE CEPA NOGUE UNIVERSIDAD DE LA LAGUNA		29/06/2017 09:33:05
	ANA MARIA PEREZ GARCIA UNIVERSIDAD DE LA LAGUNA		29/06/2017 11:12:35
	ERNESTO PEREDA DE PABLO UNIVERSIDAD DE LA LAGUNA		04/07/2017 18:28:07

Este documento incorpora firma electrónica, y es copia auténtica de un documento electrónico archivado por la ULL según la Ley 39/2015.
Su autenticidad puede ser contrastada en la siguiente dirección <https://sede.ull.es/validacion/>

Identificador del documento: 969870

Código de verificación: 8KFVZkZp

Fecha: 28/06/2017 21:15:24

Firmado por: MARINA RAMÓN PÉREZ
UNIVERSIDAD DE LA LAGUNA

29/06/2017 09:30:15

ANGEL MANUEL BONGIOVANNI PEREZ
UNIVERSIDAD DE LA LAGUNA

29/06/2017 09:33:05

JORGE CEPA NOGUE
UNIVERSIDAD DE LA LAGUNA

29/06/2017 11:12:35

ANA MARIA PEREZ GARCIA
UNIVERSIDAD DE LA LAGUNA

04/07/2017 18:28:07

ERNESTO PEREDA DE PABLO
UNIVERSIDAD DE LA LAGUNA

ACKNOWLEDGEMENTS

This work was supported by the Spanish Ministerio de Economía y Competitividad (MINECO) under the grant AYA2011-29517-C03-01.

This thesis is based on observations made with the Gran Telescopio CANARIAS (GTC), installed in the Spanish Observatorio del Roque de los Muchachos of the Instituto de Astrofísica de Canarias, in the island of La Palma.

This study made use of data from AEGIS, a multiwavelength sky survey conducted with the Chandra, GALEX, Hubble, Keck, CFHT, MMT, Subaru, Palomar, Spitzer, VLA, and other telescopes and supported in part by the NSF, NASA, and the STFC.

This thesis has used data from the public data release of the PACS Evolutionary Probe PEP (Lutz et al. 2011).

This research made use of photometric redshifts produced jointly by Terapix and VVDS teams.

This research has made use of data from the HerMES project. HerMES is a Herschel Key Programme utilising Guaranteed Time from the SPIRE instrument team, ESAC scientists and a mission scientist. The HerMES data was accessed through the Herschel Database in Marseille (HeDaM) operated by CeSAM and hosted by the Laboratoire d’Astrophysique de Marseille.

This research made use of the software IRAF (Image Reduction and Analysis Facility). IRAF is distributed by the National Optical Astronomy Observatory, which is operated by the Association of Universities for Research in Astronomy (AURA) under cooperative agreement with the National Science Foundation.

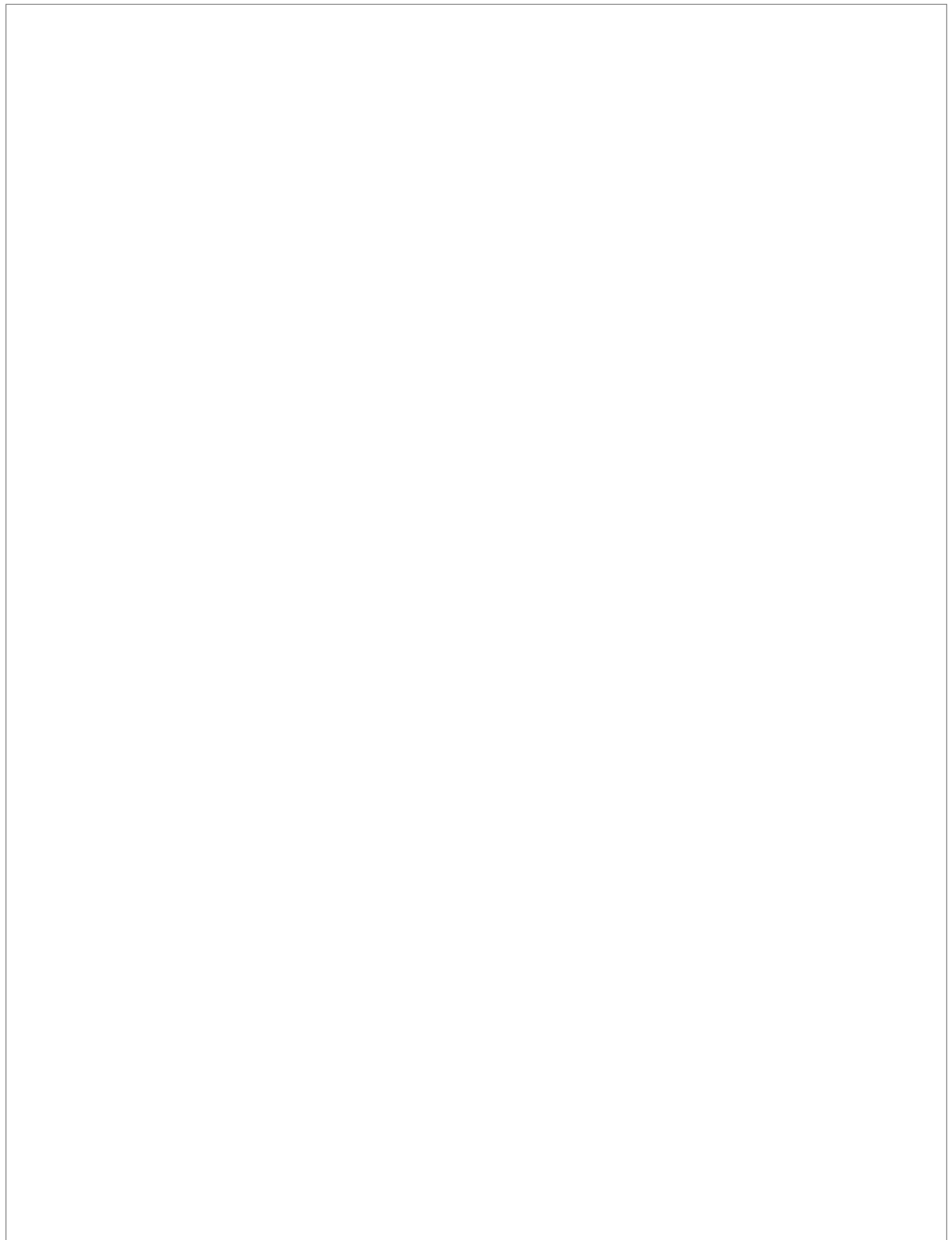
This work made use of SExtractor, a software for source extraction (Bertin & Arnouts 1996).

This research made use of TOPCAT, an interactive graphical viewer and editor for tabular data (Taylor 2005).

This research used LePhare code, developed by Arnouts & Ilbert.

Este documento incorpora firma electrónica, y es copia auténtica de un documento electrónico archivado por la ULL según la Ley 39/2015.
Su autenticidad puede ser contrastada en la siguiente dirección <https://sede.ull.es/validacion/>

Identificador del documento:	969870	Código de verificación:	8KFVZkZp
Firmado por:	MARINA RAMÓN PÉREZ UNIVERSIDAD DE LA LAGUNA	Fecha:	28/06/2017 21:15:24
	ANGEL MANUEL BONGIOVANNI PEREZ UNIVERSIDAD DE LA LAGUNA		29/06/2017 09:30:15
	JORGE CEPA NOGUE UNIVERSIDAD DE LA LAGUNA		29/06/2017 09:33:05
	ANA MARIA PEREZ GARCIA UNIVERSIDAD DE LA LAGUNA		29/06/2017 11:12:35
	ERNESTO PEREDA DE PABLO UNIVERSIDAD DE LA LAGUNA		04/07/2017 18:28:07



Este documento incorpora firma electrónica, y es copia auténtica de un documento electrónico archivado por la ULL según la Ley 39/2015. <i>Su autenticidad puede ser contrastada en la siguiente dirección https://sede.ull.es/validacion/</i>		
Identificador del documento:	969870	Código de verificación:
Firmado por:	MARINA RAMÓN PÉREZ UNIVERSIDAD DE LA LAGUNA	Fecha: 28/06/2017 21:15:24
	ANGEL MANUEL BONGIOVANNI PEREZ UNIVERSIDAD DE LA LAGUNA	29/06/2017 09:30:15
	JORGE CEPA NOGUE UNIVERSIDAD DE LA LAGUNA	29/06/2017 09:33:05
	ANA MARIA PEREZ GARCIA UNIVERSIDAD DE LA LAGUNA	29/06/2017 11:12:35
	ERNESTO PEREDA DE PABLO UNIVERSIDAD DE LA LAGUNA	04/07/2017 18:28:07

AGRADECIMIENTOS

*Gracias a la vida,
que me ha dado tanto...*

Estos años de tesis y de vida me han hecho crecer, dudar, cambiar y ser más fuerte. Y, como casi todo, no ha sido un camino recorrido en solitario. Aquí van, pues, estos agradecimientos a esas personas que han colaborado, en cualquier medida, a que esto saliera adelante.

En primer lugar quiero agradecer a mi director de tesis, Jordi Cepa, por haberme dado la oportunidad de empezar este proyecto y por sus comentarios y correcciones, tan rápidas como necesarias. En segundo lugar, a mis co-directores Ángel y Ana, que han hecho que esto llegara a buen puerto. Ángel, eres un ejemplo de pasión, dedicación y sacrificio. Gracias por las horas que has invertido en mí, por la paciencia, la ayuda y las conversaciones. Ana, gracias por tu optimismo y pragmatismo, por tu ayuda a pesar de la distancia y por creer en mí. Sin duda, esta tesis es tan vuestra como mía.

Quiero agradecer también al resto de integrantes del equipo OTELO que, en mayor o menor medida, han aportado su granito de arena a esta tesis. A Ricardo por algún que otro *Skype*, por sus sugerencias y sus explicaciones. A Miguel S. por su interés y preocupación por que todo saliera bien. A Miguel C. por su humor y su ayuda. A Iván por sus consejos científicos y sus comentarios, siempre acertados. A Jakub por acompañarme en las reuniones y por el tiempo que ha empleado en los diferentes análisis. A Irene por su simpatía, por estar siempre dispuesta a ayudar y por los ánimos. A todos, en general, gracias por el inmenso apoyo que me habéis brindado.

En esta última etapa de la tesis, si no la más difícil sí la más estresante, quiero agradecer especialmente a Cristina por leerse y corregir mi tesis a pesar de sus múltiples obligaciones. Gracias por tu tiempo y tus comentarios, que han mejorado sustancialmente este escrito, y también por ser un ejemplo de mujer comprometida dentro de este pequeño mundo que es la Astrofísica.

Durante la tesis he tenido la oportunidad de pasar algún tiempo lejos de Canarias, en otros centros de investigación, y no quería dejar de dar las gracias a todas las personas que han hecho que mis estancias fueran provechosas y que me han acogido con los brazos abiertos. Gracias a toda la gente del IFCA, en Santander, por los cafés y las risas, y en especial a Ignacio por ser tan cercano y amable conmigo. Gracias a la gente de ESAC, en Madrid, por hacerme sentir como en casa y en particular a Bea, Irene, Mario, Paco, Jesús y Benja por la simpatía y el buen rollo.

Ahora que se acerca el final y echo la vista atrás, estoy más convencida que nunca de que lo mejor de una tesis no es la tesis en sí, sino la gente que conoces por el camino. Quiero agradecer a todas esas personas que han coincidido en tiempo y espacio conmigo, y que han hecho que mi vida fuera mucho mejor. A Davi, Mavi y Xisco por compartir conmigo los inicios en la Astrofísica y las noches en el Blues. A Jasmin, por ser la

Este documento incorpora firma electrónica, y es copia auténtica de un documento electrónico archivado por la ULL según la Ley 39/2015.
Su autenticidad puede ser contrastada en la siguiente dirección <https://sede.ull.es/validacion/>

Identificador del documento:	969870	Código de verificación:	8KFVZkZp
Firmado por:	MARINA RAMÓN PÉREZ UNIVERSIDAD DE LA LAGUNA	Fecha:	28/06/2017 21:15:24
	ANGEL MANUEL BONGIOVANNI PEREZ UNIVERSIDAD DE LA LAGUNA		29/06/2017 09:30:15
	JORGE CEPA NOGUE UNIVERSIDAD DE LA LAGUNA		29/06/2017 09:33:05
	ANA MARIA PEREZ GARCIA UNIVERSIDAD DE LA LAGUNA		29/06/2017 11:12:35
	ERNESTO PEREDA DE PABLO UNIVERSIDAD DE LA LAGUNA		04/07/2017 18:28:07

mejor compañera de piso, por su eterna sonrisa y su amistad. A Alberto, Andrés, Javi, Luis, Parda, Rosa y Víctor, por las comidas multitudinarias en el IAC, por las risas, las barbacoas, los días de playa o de paseo y todo lo compartido. A Bea, además, por sus consejos de hermana mayor, su apoyo y cada conversación. A Alba, Andrea y Sara M. por todo lo anterior y por ser la Resistencia en estos últimos tiempos. A Laura por Principio Cero. A Sara B. por su amistad y por las cañas. A María por ser un pilar fundamental en mi vida, por los sueños y las horas compartidas, por que nos sigan confundiendo toda la vida.

Quiero agradecer también a un grupo que, sin duda, marcó estos años y con los que compartí, quizás, los momentos más felices de este tiempo. Al IAC Climbing Group, gracias por todo. A Mela por su simpatía y locura, por llegar siempre tarde y por los gritos de ánimo desde abajo. A Nacho por ser el mejor *coach*, por sus charlas, sus consejos y las canciones en su coche. A Irantzu por ser de las personas más generosas que conozco, por estar siempre ahí y porque sé que me llevo una amiga para toda la vida. A todos, gracias por los días maravillosos en Arico, en Fasnia, en el roco o donde fuera, por la ensaladilla donde Antonio y por la superación de nuestros miedos.

Por supuesto, si tuviera que limitar mis agradecimientos a solo dos personas, estos irían para mis padres que son responsables, por razones obvias, de que haya llegado hasta aquí. Gracias, ante todo, por el cariño y el amor inmenso que me habéis dado siempre. Mamá, gracias por la comprensión, la preocupación y las llamadas de teléfono. Papá, gracias por tu confianza en mí y por todo lo que me has enseñado. A ambos, gracias por ser el nido al que poder volver siempre. Aprovecho para extender este agradecimiento al resto de mi familia y en especial a mis hermanos, Diego y Anabel, a mis queridos abuelos y a mi tía. Gracias por estar siempre ahí.

Por último, quiero agradecer desde el fondo de mi corazón a la persona que más ha sufrido conmigo estos años y que con mayor paciencia ha sabido soportar mis momentos de duda. Iker, gracias por apoyarme siempre, tanto con palabras como con actos, por estar a mi lado aunque estuvieras lejos y por creer en mí más que yo misma. Porque si algo he de agradecer a esta tesis es el haberte conocido. Zu zara nire poz guztien iturria.

Marina Ramón Pérez
La Laguna, Junio 2017.

Este documento incorpora firma electrónica, y es copia auténtica de un documento electrónico archivado por la ULL según la Ley 39/2015.
Su autenticidad puede ser contrastada en la siguiente dirección <https://sede.ull.es/validacion/>

Identificador del documento:	Código de verificación:	Fecha:
969870	8KFVZkZp	28/06/2017 21:15:24
MARINA RAMÓN PÉREZ UNIVERSIDAD DE LA LAGUNA		29/06/2017 09:30:15
ANGEL MANUEL BONGIOVANNI PEREZ UNIVERSIDAD DE LA LAGUNA		29/06/2017 09:33:05
JORGE CEPA NOGUE UNIVERSIDAD DE LA LAGUNA		29/06/2017 11:12:35
ANA MARIA PEREZ GARCIA UNIVERSIDAD DE LA LAGUNA		04/07/2017 18:28:07
ERNESTO PEREDA DE PABLO UNIVERSIDAD DE LA LAGUNA		

CONTENTS

List of figures	xv
List of tables	xix
List of acronyms	xxi
1 Introduction	1
1.1 A world of surveys	1
1.2 The emission line Universe	2
1.2.1 Active Galactic Nuclei: an overview	4
1.2.2 Emission-line surveys	9
1.3 The OSIRIS Tunable Emission Line Object survey	10
1.4 Motivation of this thesis	14
2 Observations with Tunable Filters	15
2.1 Characteristics of Tunable Filters	15
2.2 OSIRIS's Tunable Filters	18
2.2.1 Characteristics of OSIRIS TF data	19
2.2.2 Application to OTELO survey	21
3 Data reduction and calibrations	23
3.1 Data reduction	23
3.1.1 First steps	23
3.1.2 Flat-field correction and bad-pixel fixing	25
3.1.3 Sky rings removal	25
3.1.4 Defringing	29
3.2 Astrometry	29
3.3 Construction of OTELO's catalogue	30
3.3.1 OTELO's deep image	31
3.3.2 Extraction and measurement of the sources	32
3.3.3 Determining the optical center	34
3.3.4 Flux and wavelength calibrations	36
3.3.5 Composition of pseudo-spectra	40

Este documento incorpora firma electrónica, y es copia auténtica de un documento electrónico archivado por la ULL según la Ley 39/2015.
Su autenticidad puede ser contrastada en la siguiente dirección <https://sede.ull.es/validacion/>

Identificador del documento: 969870	Código de verificación: 8KFVZkZp
Firmado por: MARINA RAMÓN PÉREZ UNIVERSIDAD DE LA LAGUNA	Fecha: 28/06/2017 21:15:24
ANGEL MANUEL BONGIOVANNI PEREZ UNIVERSIDAD DE LA LAGUNA	29/06/2017 09:30:15
JORGE CEPA NOGUE UNIVERSIDAD DE LA LAGUNA	29/06/2017 09:33:05
ANA MARIA PEREZ GARCIA UNIVERSIDAD DE LA LAGUNA	29/06/2017 11:12:35
ERNESTO PEREDA DE PABLO UNIVERSIDAD DE LA LAGUNA	04/07/2017 18:28:07

4 OTELO's multiwavelength catalogue	43
4.1 Nuclear catalogue	44
4.2 Auxiliary data	47
4.2.1 Photometric catalogues	48
4.2.2 Redshift catalogues	51
4.3 Cross-matching of catalogues	54
4.4 OTELO's final multiwavelength catalogue: a summary	59
5 Selection and identification of Hα emitters	63
5.1 Selection of emitting objects	63
5.1.1 Pre-selection of candidates	63
5.1.2 Visual classification of candidates	65
5.2 Selection of H α emitters candidates	71
5.2.1 Detection limits in OTELO	71
5.2.2 Photometric redshift determination	75
5.2.3 Colour-colour diagram	79
5.2.4 Narrow-band excess	80
5.3 Identification of H α emitters	82
6 Selection of AGN	87
6.1 AGN at z~0.40	87
6.1.1 Broad-Line AGN	88
6.1.2 Measurement of H α and [NII] fluxes and EW	91
6.1.3 Discrimination between SFG and AGN	92
6.2 X-ray selection	94
6.3 Mid-infrared selection	95
7 Analysis of AGN	99
7.1 Demography	99
7.2 Morphology	105
7.3 Luminous and ultra-luminous infrared galaxies	107
7.4 Analysis of AGN at z~0.40	111
7.4.1 Environment and density	111
7.4.2 Luminosity function at z~0.40	116
8 Summary and conclusions	123
Appendix A AGN morphologies (examples)	127
Bibliography	143

Este documento incorpora firma electrónica, y es copia auténtica de un documento electrónico archivado por la ULL según la Ley 39/2015.
Su autenticidad puede ser contrastada en la siguiente dirección <https://sede.ull.es/validacion/>

Identificador del documento: 969870	Código de verificación: 8KFVZkZp
Firmado por: MARINA RAMÓN PÉREZ UNIVERSIDAD DE LA LAGUNA	Fecha: 28/06/2017 21:15:24
ANGEL MANUEL BONGIOVANNI PEREZ UNIVERSIDAD DE LA LAGUNA	29/06/2017 09:30:15
JORGE CEPA NOGUE UNIVERSIDAD DE LA LAGUNA	29/06/2017 09:33:05
ANA MARIA PEREZ GARCIA UNIVERSIDAD DE LA LAGUNA	29/06/2017 11:12:35
ERNESTO PEREDA DE PABLO UNIVERSIDAD DE LA LAGUNA	04/07/2017 18:28:07

LIST OF FIGURES

1.1	BPT diagram	3
1.2	Examples of galaxies hosting an AGN	4
1.3	Unified model scheme for AGN	6
1.4	Typical SEDs of different classes of AGN	7
1.5	Gran Telescopio CANARIAS (GTC)	11
1.6	Interior view of the Gran Telescopio CANARIAS	11
1.7	Extended Groth Strip (HST)	12
1.8	La Palma night-sky spectrum	12
2.1	Scheme of a Fabry-Perot interferometer	16
2.2	Traditional Fabry-Perot interferometer compared to a tunable filter	16
2.3	Transmission profile of a tunable filter	17
2.4	OSIRIS instrument	18
2.5	OSIRIS's red tunable filter	19
2.6	Example of OTELO's raw image	20
3.1	OTELO's image before and after the removal of cosmic rays and ratio of both	24
3.2	Close-up of an OTELO's image before and after the sky rings subtraction process and some of its intermediate steps	26
3.3	An example of the different sky rings subtraction tests described in the text	27
3.4	Comparison of the flux recovery after the sky subtraction step using different techniques.	28
3.5	Example of fringe pattern in one of OTELO's images	29
3.6	OTELO's deep image.	32
3.7	Determination of the optical center coordinates	35
3.8	Estimated efficiencies of the different system's componentes.	36
3.9	Unvignetted $\sim 7.5 \times 7.4$ OTELO's field and calibration stars in each detector	37
3.10	Spectra of the calibration stars present in OTELO's field of view	38
3.11	Total system efficiency	40
4.1	Simulated images with different PSF for the study of the photometric parameters	45
4.2	Difference between the measured magnitude obtained by SExtractor and the true magnitude from the simulated catalogue	46
4.3	Photometric errors obtained from measurements on the artificial z-band image	47

Este documento incorpora firma electrónica, y es copia auténtica de un documento electrónico archivado por la ULL según la Ley 39/2015.
Su autenticidad puede ser contrastada en la siguiente dirección <https://sede.ull.es/validacion/>

Identificador del documento: 969870	Código de verificación: 8KFVZkZp
Firmado por: MARINA RAMÓN PÉREZ UNIVERSIDAD DE LA LAGUNA	Fecha: 28/06/2017 21:15:24
ANGEL MANUEL BONGIOVANNI PEREZ UNIVERSIDAD DE LA LAGUNA	29/06/2017 09:30:15
JORGE CEPA NOGUE UNIVERSIDAD DE LA LAGUNA	29/06/2017 09:33:05
ANA MARIA PEREZ GARCIA UNIVERSIDAD DE LA LAGUNA	29/06/2017 11:12:35
ERNESTO PEREDA DE PABLO UNIVERSIDAD DE LA LAGUNA	04/07/2017 18:28:07

4.4	Measured “colours” (flux differences) obtained from paired combinations of the artificial images with different mean FWHM	47
4.5	Distribution of AB magnitudes in the complementary catalogues.	48
4.6	X-Rays sources in OTELO’s field of view.	49
4.7	IRAC sources in OTELO’s field of view.	50
4.8	Errors of IRAC sources in OTELO’s field of view.	51
4.9	Spatial distribution of the sources in the auxiliary catalogues	52
4.10	Bands included in the final OTELO’s multiwavelength catalogue	53
4.11	Distribution of $q(m)$ and $n(m)$ for each photometric auxiliary catalogue	55
4.12	Individual reliabilities of each counterpart, R_C , as a function of the likelihood ratio, LR	57
4.13	Distribution of individual reliabilities, R_C , in each one of the photometric auxiliary catalogues	58
4.14	Distribution of OTELO’s sources with integrated magnitude over 26.5	59
4.15	Distribution of the integrated magnitudes of OTELO’s sources as measured in its deep image .	60
5.1	Convolution of a SDSS spectrum with OTELO’s TF response and conditions for the pre-selection of an ELC by the automatic algorithm	64
5.2	SDSS emission spectrum convolved to OTELO’s TFs spectral response	65
5.3	Examples of objects classified as uncertain	66
5.4	Example of an object with absorption features	67
5.5	Examples of discarded objects	67
5.6	Examples of objects classified as emitters	68
5.7	Emitting object from category a.1)	69
5.8	Emitting object from category a.2)	70
5.9	Mean value of detection in simulation given the FWHM and the amplitude of the H α gaussian	72
5.10	Mean value of detection in simulation given the FWHM and the continuum of the H α gaussian	73
5.11	Mean value of detection in simulation given the amplitude and the continuum of the H α gaussian	73
5.12	Minimum detected EW as a function of the pseudo-spectrum continuum	74
5.13	Percentage of detected objects in the simulation depending on the equivalent width of the H α gaussian line	75
5.14	Templates used to build LePhare’s galaxies library	76
5.15	Examples of SED fitting performed by LePhare.	77
5.16	Distribution of photometric redshifts	78
5.17	Photometric redshifts versus spectroscopic redshifts from DEEP2	78
5.18	Colour-colour diagram of AEGIS and zCOSMOS spectroscopic sources.	79
5.19	Narrow-band excess as a function of narrow-band magnitude for OTELO sources.	80
5.20	First section of the analysis questionnaire about the pseudo-spectrum of the object	82
5.21	Second section of the analysis questionnaire about the appearance of the object in OTELO’s deep image and in the images of the complementary data	83
5.22	Third section of the analysis questionnaire about the photo-z analysis of the object	84
6.1	Spectra of real BLAGN and their simulated pseudo-spectra	88
6.2	Simulated pseudo-spectra of H α +[NII] lines with different widths	89
6.3	Simulated pseudo-spectra of H α +[NII] lines not centered in OTELO wavelength window	89
6.4	Objects from OTELO survey showing H α +[NII] emission and classified as BLAGN	90

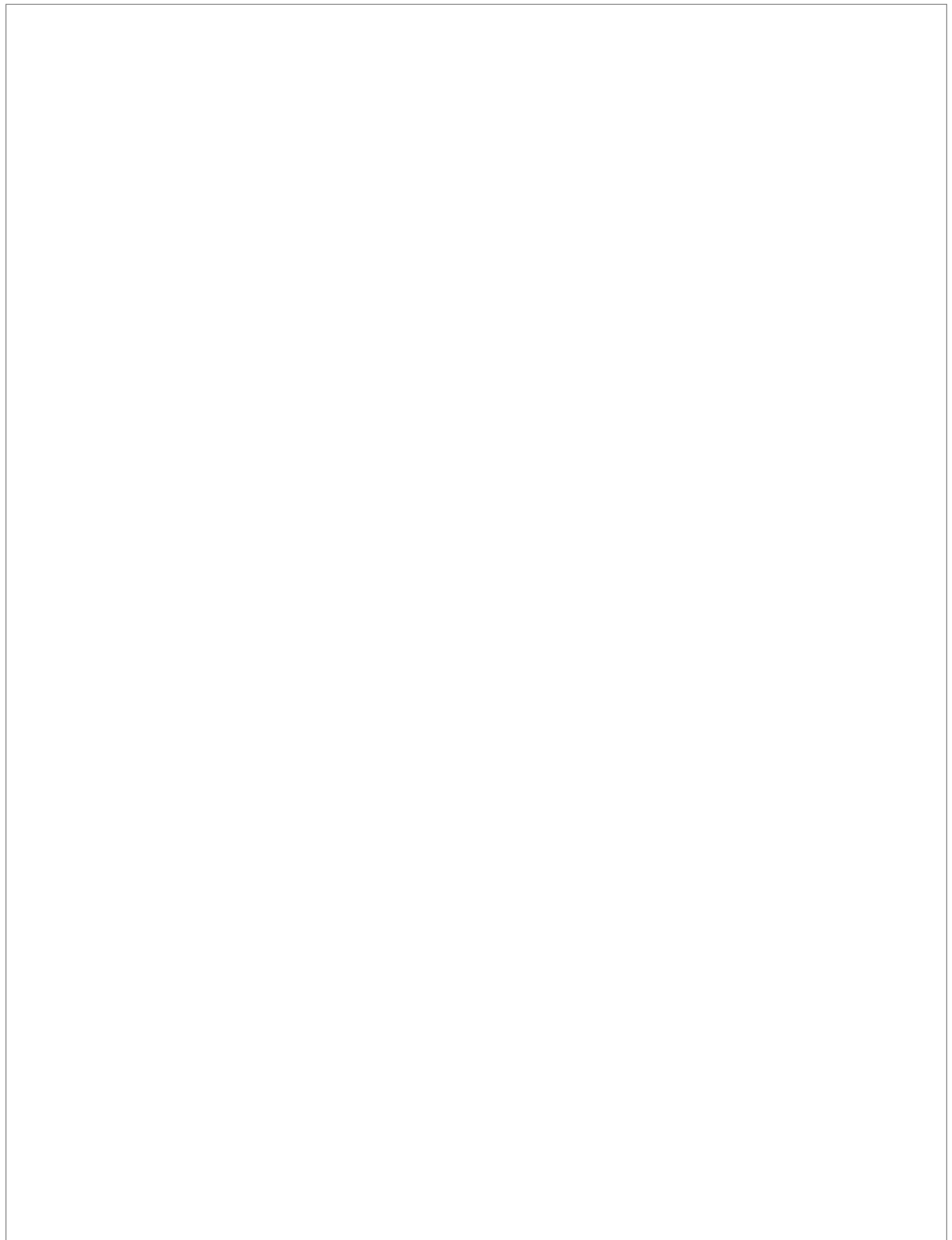
Este documento incorpora firma electrónica, y es copia auténtica de un documento electrónico archivado por la ULL según la Ley 39/2015.
Su autenticidad puede ser contrastada en la siguiente dirección <https://sede.ull.es/validacion/>

Identificador del documento:	Código de verificación:
969870	8KFVZkZp
Firmado por: MARINA RAMÓN PÉREZ UNIVERSIDAD DE LA LAGUNA	Fecha: 28/06/2017 21:15:24
ANGEL MANUEL BONGIOVANNI PEREZ UNIVERSIDAD DE LA LAGUNA	29/06/2017 09:30:15
JORGE CEPA NOGUE UNIVERSIDAD DE LA LAGUNA	29/06/2017 09:33:05
ANA MARIA PEREZ GARCIA UNIVERSIDAD DE LA LAGUNA	29/06/2017 11:12:35
ERNESTO PEREDA DE PABLO UNIVERSIDAD DE LA LAGUNA	04/07/2017 18:28:07

6.5	Histogram of H α fluxes	92
6.6	EW $\alpha\alpha_2$ diagnostic diagram to distinguish star-forming galaxies from AGN	93
6.7	X-ray-to-optical flux ratio as a function of the optical band	94
6.8	Revised IRAC criteria from Donley et al. (2012) to separate AGN from star-forming galaxies	96
6.9	IRAC+MIPS infrared criteria by Messias et al. (2012) to select AGN	97
7.1	Distribution of redshifts for all the objects in OTELO's catalogue, ELC and AGN	100
7.2	Magnitude distribution in the r band	100
7.3	X-ray-to-optical flux ratio as a function of the hardness ratio	102
7.4	Histogram of H α fluxes for the H α emitters and the AGN at $z \sim 0.40$	104
7.5	Distribution of Sersic indices	106
7.6	Comparison of methods to calculate the infrared luminosity.	108
7.7	Distribution of infrared luminosities	109
7.8	Infrared luminosity in OTELO as a function of redshift	109
7.9	Distribution of redshifts for LIRGs and ULIRGs	110
7.10	Distribution of sources at $z \sim 0.40$ in OTELO	111
7.11	Distribution of the surface density parameter (Σ_5) I	112
7.12	Distributions of D_5 for the total sample of OTELO's objects, the AGN and the control sample (non-AGN)	113
7.13	Distribution of the surface density parameter (Σ_5) II	114
7.14	Distributions of D_5 for the sample of H α emitters, passive galaxies, AGN and star-forming galaxies	114
7.15	$J(D_5)$ function II	115
7.16	Mean detection probability as a function of H α line flux	116
7.17	H α luminosity function at $z \sim 0.40$	118
7.18	Difference between the OTELO H α LF of the total sample of emitters at $z \sim 0.40$ and that of the star-forming galaxies only	121
A.1	Morphology of the object #1873	128
A.2	Morphology of the object #8762	129
A.3	Morphology of the object #2146	130
A.4	Morphology of the object #3854	131
A.5	Morphology of the object #6395	132
A.6	Morphology of the object #5662	133
A.7	Morphology of the object #3216	134
A.8	Morphology of the object #6173	135
A.9	Morphology of the object #5495	136
A.10	Morphology of the object #8459	137
A.11	Morphology of the object #8351	138
A.12	Morphology of the object #11168	139
A.13	Morphology of the object #7800	140
A.14	Morphology of the object #10965	141
A.15	Morphology of the object #7772	142

Este documento incorpora firma electrónica, y es copia auténtica de un documento electrónico archivado por la ULL según la Ley 39/2015.
Su autenticidad puede ser contrastada en la siguiente dirección <https://sede.ull.es/validacion/>

Identificador del documento:	Código de verificación:
969870	8KFVZkZp
Firmado por: MARINA RAMÓN PÉREZ UNIVERSIDAD DE LA LAGUNA	Fecha: 28/06/2017 21:15:24
ANGEL MANUEL BONGIOVANNI PÉREZ UNIVERSIDAD DE LA LAGUNA	29/06/2017 09:30:15
JORGE CEPA NOGUE UNIVERSIDAD DE LA LAGUNA	29/06/2017 09:33:05
ANA MARIA PÉREZ GARCIA UNIVERSIDAD DE LA LAGUNA	29/06/2017 11:12:35
ERNESTO PEREDA DE PABLO UNIVERSIDAD DE LA LAGUNA	04/07/2017 18:28:07



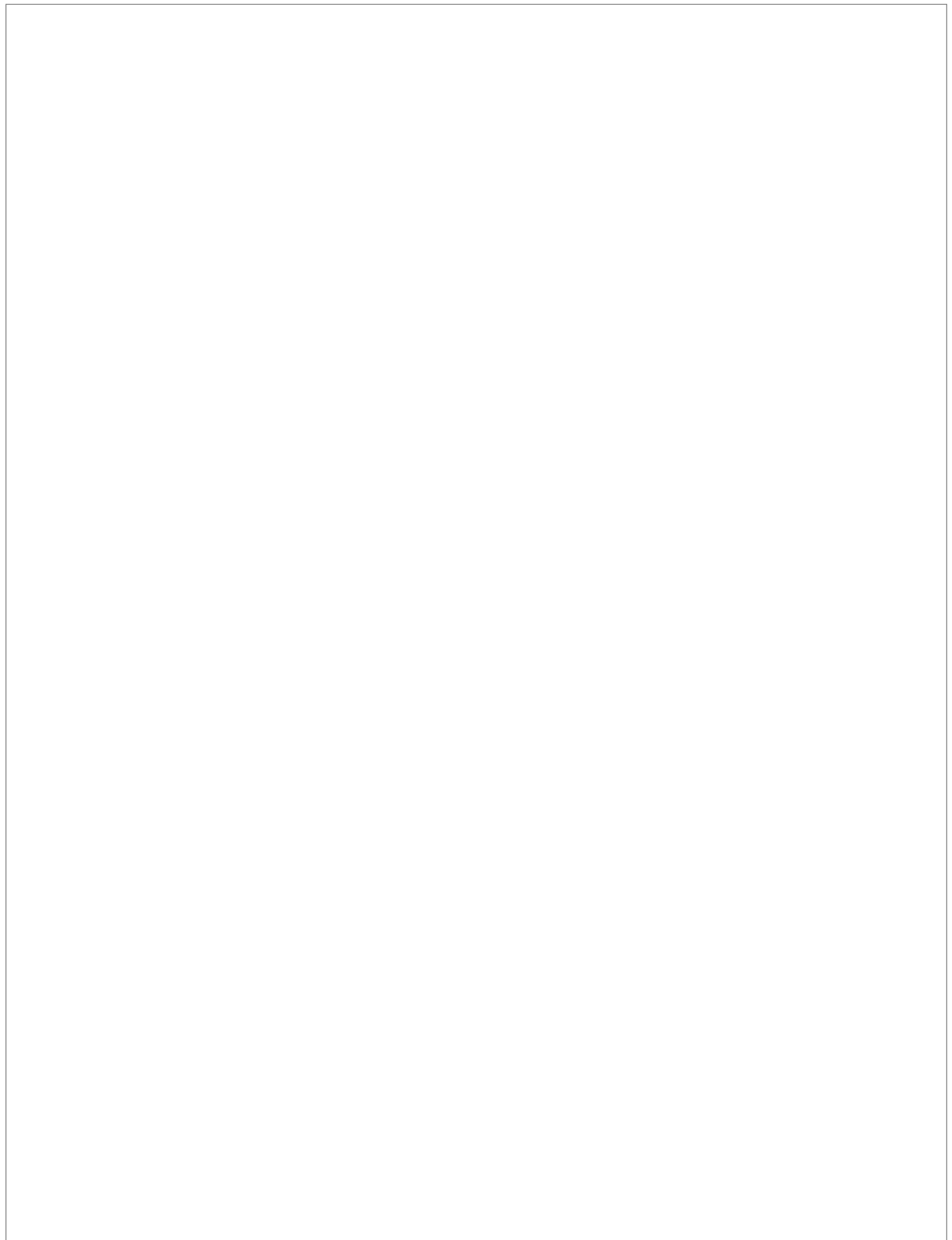
Este documento incorpora firma electrónica, y es copia auténtica de un documento electrónico archivado por la ULL según la Ley 39/2015. <i>Su autenticidad puede ser contrastada en la siguiente dirección https://sede.ull.es/validacion/</i>		
Identificador del documento:	969870	Código de verificación: 8KFVZkZp
Firmado por:	MARINA RAMÓN PÉREZ UNIVERSIDAD DE LA LAGUNA	Fecha: 28/06/2017 21:15:24
	ANGEL MANUEL BONGIOVANNI PEREZ UNIVERSIDAD DE LA LAGUNA	29/06/2017 09:30:15
	JORGE CEPA NOGUE UNIVERSIDAD DE LA LAGUNA	29/06/2017 09:33:05
	ANA MARIA PEREZ GARCIA UNIVERSIDAD DE LA LAGUNA	29/06/2017 11:12:35
	ERNESTO PEREDA DE PABLO UNIVERSIDAD DE LA LAGUNA	04/07/2017 18:28:07

LIST OF TABLES

1.1	Mean redshift of relevant emission lines in OTELO survey	13
1.2	Description of OTELO's observations	13
1.3	Main features of the OTELO survey	13
3.1	Statistics of the flux recovery after the sky subtraction step using different techniques	28
3.2	Main configuration parameters of the SWarp software	31
3.3	Main configuration parameters of the SExtractor software	33
3.4	Optical center coordinates with respect to CCD1	35
4.1	Properties of the images used to build OTELO's nuclear catalogue	44
4.2	Auxiliary catalogues used for the construction of OTELO's multiwavelength catalogue	48
4.3	Results of the cross-correlation of catalogues	56
4.4	OTELO's catalogue (Part I)	61
4.5	OTELO's catalogue (Part II)	62
5.1	Selection of H α candidates sample	81
6.1	Summary of AGN selection	97
7.1	Classification of AGN according to the way they have been selected	101
7.2	OTELO sources at $z \sim 0.40$ and fraction of emitters and AGN	103
7.3	Morphological classification of OTELO's AGN	105
7.4	Number of LIRGs and ULIRGs found in OTELO	110
7.5	Schechter parameters of the H α luminosity functions at $z \sim 0.4$	119
7.6	Star formation rate density at $z \sim 0.40$	120

Este documento incorpora firma electrónica, y es copia auténtica de un documento electrónico archivado por la ULL según la Ley 39/2015.
Su autenticidad puede ser contrastada en la siguiente dirección <https://sede.ull.es/validacion/>

Identificador del documento:	969870	Código de verificación:	8KFVZkZp
Firmado por:	MARINA RAMÓN PÉREZ UNIVERSIDAD DE LA LAGUNA	Fecha:	28/06/2017 21:15:24
	ANGEL MANUEL BONGIOVANNI PEREZ UNIVERSIDAD DE LA LAGUNA		29/06/2017 09:30:15
	JORGE CEPA NOGUE UNIVERSIDAD DE LA LAGUNA		29/06/2017 09:33:05
	ANA MARIA PEREZ GARCIA UNIVERSIDAD DE LA LAGUNA		29/06/2017 11:12:35
	ERNESTO PEREDA DE PABLO UNIVERSIDAD DE LA LAGUNA		04/07/2017 18:28:07



Este documento incorpora firma electrónica, y es copia auténtica de un documento electrónico archivado por la ULL según la Ley 39/2015. <i>Su autenticidad puede ser contrastada en la siguiente dirección https://sede.ull.es/validacion/</i>		
Identificador del documento:	969870	Código de verificación:
Firmado por:	MARINA RAMÓN PÉREZ UNIVERSIDAD DE LA LAGUNA	Fecha: 28/06/2017 21:15:24
	ANGEL MANUEL BONGIOVANNI PEREZ UNIVERSIDAD DE LA LAGUNA	29/06/2017 09:30:15
	JORGE CEPA NOGUE UNIVERSIDAD DE LA LAGUNA	29/06/2017 09:33:05
	ANA MARIA PEREZ GARCIA UNIVERSIDAD DE LA LAGUNA	29/06/2017 11:12:35
	ERNESTO PEREDA DE PABLO UNIVERSIDAD DE LA LAGUNA	04/07/2017 18:28:07

LIST OF ACRONYMS

ADU Analog-to-Digital Unit
AEGIS All-wavelength Extended Groth strip International Survey
AGN Active Galactic Nuclei
BLAGN Broad-Line AGN
CCD Charge-Coupled Device
CFHTLS Canada-France-Hawaii Telescope Legacy Survey
EGS Extended Groth Strip
ELC Emission Line Candidate
EW Equivalent Width
FIR Far-InfraRed
FWHM Full Width at Half Maximum
GALEX GALaxy Evolution EXplorer
GTC Gran Telescopio de Canarias
HerMES Herschel Multi-Tiered Extragalactic Survey
IMF Initial Mass Function
IR InfraRed
IRAC InfraRed Array Camera
IRAF Image Reduction and Analysis Facility
GTC Gran Telescopio de Canarias
LF Luminosity Function
LINER Low-Ionization Nuclear Emission-line Region
LIRG Luminous InfraRed Galaxy

Este documento incorpora firma electrónica, y es copia auténtica de un documento electrónico archivado por la ULL según la Ley 39/2015.
Su autenticidad puede ser contrastada en la siguiente dirección <https://sede.ull.es/validacion/>

Identificador del documento:	969870	Código de verificación:	8KFVZkZp
Firmado por:	MARINA RAMÓN PÉREZ UNIVERSIDAD DE LA LAGUNA	Fecha:	28/06/2017 21:15:24
	ANGEL MANUEL BONGIOVANNI PEREZ UNIVERSIDAD DE LA LAGUNA		29/06/2017 09:30:15
	JORGE CEPA NOGUE UNIVERSIDAD DE LA LAGUNA		29/06/2017 09:33:05
	ANA MARIA PEREZ GARCIA UNIVERSIDAD DE LA LAGUNA		29/06/2017 11:12:35
	ERNESTO PEREDA DE PABLO UNIVERSIDAD DE LA LAGUNA		04/07/2017 18:28:07

- MIPS** Multiband Imaging Photometer
- MIR** Mid-InfraRed
- NLAGN** Narrow-Line AGN
- OS** Order-Sorter
- OSIRIS** Optical System for Imaging and low-Intermediate-Resolution Integrated Spectroscopy
- ORM** Observatorio del Roque de los Muchachos
- OTELO** Osiris Tunable Emission Line Object survey
- PACS** Photoconductor Array Camera and Spectrometer
- PEP** PACS Evolutionary Probe
- PS** Pseudo-Spectrum
- PSF** Point Spread Function
- QSO** Quasi-Stellar Source
- SED** Spectral Energy Distribution
- SFG** Star-Forming Galaxies
- SFR** Star Formation Rate
- SMBH** Super Massive Black Hole
- SPIRE** Spectral and Photometric Imaging Receiver
- TF** Tunable Filter
- ULIRG** Ultra Luminous InfraRed Galaxy
- UV** Ultra Violet

Este documento incorpora firma electrónica, y es copia auténtica de un documento electrónico archivado por la ULL según la Ley 39/2015.
Su autenticidad puede ser contrastada en la siguiente dirección <https://sede.ull.es/validacion/>

Identificador del documento:	969870	Código de verificación:	8KFVZkZp
Firmado por:	MARINA RAMÓN PÉREZ UNIVERSIDAD DE LA LAGUNA	Fecha:	28/06/2017 21:15:24
	ANGEL MANUEL BONGIOVANNI PEREZ UNIVERSIDAD DE LA LAGUNA		29/06/2017 09:30:15
	JORGE CEPA NOGUE UNIVERSIDAD DE LA LAGUNA		29/06/2017 09:33:05
	ANA MARIA PEREZ GARCIA UNIVERSIDAD DE LA LAGUNA		29/06/2017 11:12:35
	ERNESTO PEREDA DE PABLO UNIVERSIDAD DE LA LAGUNA		04/07/2017 18:28:07

1

INTRODUCTION

In this introduction, we briefly review the history of astronomical surveys of galaxies and their different properties. Then, the emission-line Universe is described, pointing out the importance of such spectral features. Active galactic nuclei (AGN), as a particular case of emitting objects and the principal topic of this thesis, are introduced. We describe their main characteristics and the open issues on the field. The different techniques to study emission-line objects are then compared, as well as some of the current surveys on the topic. Finally, the OTELO survey is described and the objectives of this thesis are summarised.

1.1 A world of surveys

Since the first human looked up at the sky and wondered about the vast, daunting Universe, much effort has been made in order to solve its mysteries. A major technological milestone was the invention of the telescope, in the XVII century, that allowed us to redefine our place in the Universe. Soon after, the systematic observation of the sky with this instrument began and the first general astronomical catalogues were published. The *Catalogue des Nébuleuses et des Amas d'Étoiles* by Charles Messier (1771), or the *New General Catalogue*, compiled by John Dreyer a century later on the basis of the work made by the Herschel family, are some examples.

At the end of the XIX century, the advent of photography and large field cameras represented a revolution for astronomical surveys. From then on, the coverage of extensive areas of the sky was possible, facilitating the compilation of data. The Harvard College Observatory, for instance, gathered photographic plates of the sky, known as the *Harvard Plate Collection*, during almost a century, starting in ~1880. Catalogues with thousands of entries started being published, such as the Henry Draper Catalogue in the 1920s, with 225000 stars, or the Shapley-Ames Catalogue in the 1930s, containing 1249 galaxies. The Monte Palomar Observatory from Caltech and its Schmidt telescopes also contributed greatly to the mapping of the sky. Two thirds of it, up to $m_{lim} \sim 21$ mag, were covered with the *Palomar Observatory Sky Survey* (POSS-I, 1949-1958), which was followed by the POSS-II almost 4 decades later.

Surveys in other wavelength ranges than the optical started to blossom in parallel. Radio astronomy developed after World War II and the first efficient infrared detectors enabled the observations in this range soon after. High energy astrophysics, such as ultraviolet (UV), X-rays and γ -rays, appeared when the observation

Este documento incorpora firma electrónica, y es copia auténtica de un documento electrónico archivado por la ULL según la Ley 39/2015.
Su autenticidad puede ser contrastada en la siguiente dirección <https://sede.ull.es/validacion/>

Identificador del documento:	969870	Código de verificación:	8KFVZkZp
Firmado por:	MARINA RAMÓN PÉREZ UNIVERSIDAD DE LA LAGUNA	Fecha:	28/06/2017 21:15:24
	ANGEL MANUEL BONGIOVANNI PEREZ UNIVERSIDAD DE LA LAGUNA		29/06/2017 09:30:15
	JORGE CEPA NOGUE UNIVERSIDAD DE LA LAGUNA		29/06/2017 09:33:05
	ANA MARIA PEREZ GARCIA UNIVERSIDAD DE LA LAGUNA		29/06/2017 11:12:35
	ERNESTO PEREDA DE PABLO UNIVERSIDAD DE LA LAGUNA		04/07/2017 18:28:07

of the sky from outer space became possible, following the space race. And, more recently, the detection of gravitational waves by the LIGO team has opened a whole new window, offering unprecedented possibilities in the observation of the Universe (Abbott et al. 2016).

At the turn of the XX century, another revolution arose with the development of computing facilities and digital detectors. This brought a major increase in the number of astrophysical surveys and in the acquisition of data. Surveys such as the *Two Micron All-Sky Survey* (2MASS) or the *Sloan Digital Sky Survey* (SDSS), among others, provided (and still do) an incredible amount of data to the community, enriching our field of research and allowing the study of the large scale structure of the Universe for the first time. Due to the ever-increasing number of data collected in recent years, the development of efficient tools to manage it has become crucial. As an example, data science and machine learning seem more and more imperative for the future of Astrophysics.

Nowadays, there is a large number of surveys being carried out, with the most diverse properties. They can be ground or space-based, photometric or spectroscopic, deep (over a small field) or shallow (over a larger one), general or optimized for a particular science case, multiwavelength or not, etc. In the extragalactic domain, spectroscopic surveys¹ such as zCOSMOS (Lilly et al. 2007) or GAMA (Baldry et al. 2010) focus mainly on obtaining accurate redshifts of the targets, previously selected from broad-band imaging surveys. Despite the fact that spectroscopy delivers high quality spectra of the sources, from which different parameters can be extracted (abundances, star-formation rates, metallicities, etc), the invested time, both in the acquisition of the data and in its reduction and calibration, is very high, slowing down the scientific exploitation. On the other hand, extragalactic imaging surveys are an efficient way of collecting data from a large number of sources simultaneously and with much less effort, although with less detail. Broad-band imaging represents a good technique to study bright continuum objects, while medium-band imaging surveys are more detailed. Some recent examples of extragalactic imaging surveys in medium bands are SHARDS (Pérez-González & Cava 2013), ALHAMBRA (Moles et al. 2008) or J-PAS (Benítez et al. 2014). Narrow-band surveys, on the other hand, permit the detection of emitting objects with a faint continuum. They will be described in Section 1.2.2. For a deeper historical review on astrophysical surveys, the reader is referred to Djorgovski et al. (2013).

The question that naturally arises after reading the previous is the following: with the amount of astrophysical data already compiled, do we really need another survey? In the next sections we will try to justify this.

1.2 The emission line Universe

Emission lines are present in the Universe in a wide range of astronomical objects, from planetary nebulae to starburst galaxies or AGN. The detection of sources with strong emission lines in their spectrum is especially key for the study of the most distant and faint objects in the Universe. It allows for their discovery even if the continuum flux is very weak, thus uncovering a great number of unique and fascinating objects and related phenomena (Cepa 2009).

Important parameters can be derived from the analysis of emission lines, such as chemical abundances, electronic density, temperature or the star-formation rate. Some of the most relevant optical emission-lines in the study of galaxies, because of their intensity and the information they provide, are Ly α (1215 Å), [OII] (3726,3729 Å), H β (4861 Å), [OIII] (4363, 5007 Å), H α (6563 Å) or [NII] (6584 Å). The star-formation rate, for instance, can be derived from the H α and H β luminosities, and their ratio gives information about the intrinsic extinction. On the other hand, the ratios [OIII] λ (4363, 5007 Å) and [SII] λ (6716, 6731) are related

¹See <http://www.astro.ljmu.ac.uk/ikb/research/galaxy-redshift-surveys.html> for a detailed list of galaxy redshift surveys.

Este documento incorpora firma electrónica, y es copia auténtica de un documento electrónico archivado por la ULL según la Ley 39/2015. Su autenticidad puede ser contrastada en la siguiente dirección https://sede.ull.es/validacion/		
Identificador del documento:	Código de verificación:	
Firmado por: MARINA RAMÓN PÉREZ UNIVERSIDAD DE LA LAGUNA	969870	8KFVZkZp
		Fecha: 28/06/2017 21:15:24
ANGEL MANUEL BONGIOVANNI PEREZ UNIVERSIDAD DE LA LAGUNA		29/06/2017 09:30:15
JORGE CEPA NOGUE UNIVERSIDAD DE LA LAGUNA		29/06/2017 09:33:05
ANA MARIA PEREZ GARCIA UNIVERSIDAD DE LA LAGUNA		29/06/2017 11:12:35
ERNESTO PEREDA DE PABLO UNIVERSIDAD DE LA LAGUNA		04/07/2017 18:28:07

with the temperature and the density of the gas, respectively. The study of emission-lines also enables the classification of different types of objects, for example using the BPT diagram shown in Fig. 1.1 (Baldwin et al. 1981).

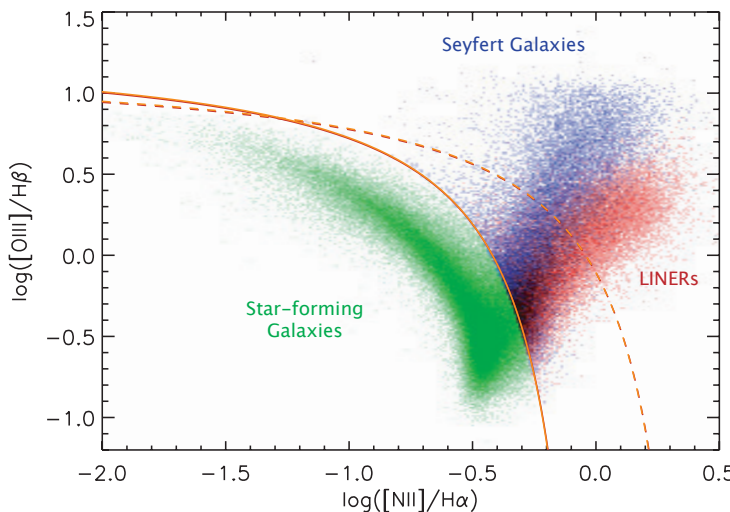


Figure 1.1: Baldwin, Phillips & Terlevich diagram (1981), better known as BPT diagram. The figure shows emission-line galaxies from the Sloan Digital Sky Survey. The line ratios permit to discriminate between star-forming galaxies and Seyferts/LINERs. Credit: see http://www.eso.org/rforsbury/research/AGN2-07/AGN2-07_Messenger_v5.1.html.

Emission-lines are also key for the construction of the luminosity function (LF), which gives the number of galaxies per luminosity interval (see Johnston 2011 for a review on the topic). The luminosity function, Φ (erg/s/Mpc³), is an essential empirical tool to evaluate the distribution and large-scale structures of galaxies in the Universe. By tracing a specific emission-line across different redshifts, galaxy evolution can also be studied. In the case of the H α emission line, the luminosity function allows us to estimate the star-formation rate over different cosmological times, giving invaluable information about the way our Universe has evolved.

Given its importance, the luminosity function is usually one of the first things to be derived in any survey. However, this is not always a simple task, as corrections from incompleteness and extinction must be made. The LF can be calculated in any wavelength range, at any redshift, and for different kinds of objects (quiescent or star-forming galaxies, AGN...). Some of the most recent examples in the literature are the luminosity functions of Ly α emitters at $z = 7.7$ or $z = 2.23$ (Tilvi et al. 2010 and Sobral et al. 2017), galaxies in the submillimeter range ($250\mu\text{m}$, Eales et al. 2010), in the B-band (López-Sanjuan et al. 2017), in the 1.4 GHz or CO radio bands (Pracy et al. 2016 and Decarli et al. 2016) or the UV and mid-infrared (MIR) luminosity functions for quasars (Manti et al. 2017 and Singal et al. 2016). As for the H α LF, Sobral et al. (2013) have studied its evolution through different cosmic times. However, at $z \sim 0.40$, a great discrepancy exists between their LF and that of other works (Drake et al. 2013, Ly et al. 2007), specially at low luminosities. As a consequence, obtaining deep H α data to extend the faint end of the LF would be of great importance in order to constrain the star-formation rate at that redshift and to determine the number of expected galaxies at low-luminosities.

Este documento incorpora firma electrónica, y es copia auténtica de un documento electrónico archivado por la ULL según la Ley 39/2015. Su autenticidad puede ser contrastada en la siguiente dirección https://sede.ull.es/validacion/		
Identificador del documento:	969870	Código de verificación: 8KFVZkZp
Firmado por:	MARINA RAMÓN PÉREZ UNIVERSIDAD DE LA LAGUNA	Fecha: 28/06/2017 21:15:24
	ANGEL MANUEL BONGIOVANNI PEREZ UNIVERSIDAD DE LA LAGUNA	29/06/2017 09:30:15
	JORGE CEPA NOGUE UNIVERSIDAD DE LA LAGUNA	29/06/2017 09:33:05
	ANA MARIA PEREZ GARCIA UNIVERSIDAD DE LA LAGUNA	29/06/2017 11:12:35
	ERNESTO PEREDA DE PABLO UNIVERSIDAD DE LA LAGUNA	04/07/2017 18:28:07

In what follows, an overview of active galactic nuclei, the main topic of this work, is presented and some of the techniques and surveys targeting emission-line objects are described.

1.2.1 Active Galactic Nuclei: an overview

Active galactic nuclei are one of the most intriguing and widely studied phenomena in the Universe. Galaxies hosting an AGN show an intense activity in a small, concentrated nuclear region, which makes them much brighter than inactive galaxies of the same Hubble type. Unlike star-forming galaxies, the intense activity of an AGN has a non-stellar origin, although both types of objects share the presence of strong emission lines in their spectra. The enormous luminosity of AGN makes them easily recognizable at great cosmological distances, therefore their study gives us clues about the formation and evolution of galaxies in the Universe (Blandford et al. 1990).



Figure 1.2: Examples of galaxies hosting an AGN. Upper left: radio galaxy Hercules A at $z = 0.156$, showing spectacular jets of material coming from the inner core of the galaxy. Upper right: SDSS 1510+07 at $z = 0.0458$, showing extended emission-line structures. Lower left: NGC 1275, showing filaments of cool gas surrounding the galaxy. Lower right: spiral galaxy M106, a Seyfert galaxy with strong X-ray emission. Credit: HUBBLE SITE gallery.

The origin of such a strong activity is believed to be caused by the presence, in the inner core of the galaxy, of a supermassive black hole (SMBH) which is absorbing material from a surrounding accretion disk. This infalling material produces radiation which is re-emitted across the entire spectrum (Osterbrock & Ferland 2006). The huge amount of energy produced by an AGN generally peaks in the UV and is also very powerful in the X-rays and the infrared (IR).

Since the discovery of strong emission lines in the spectrum of NGC 1068 by Edward A. Fath at the beginning of the 20th century, through the works of Seyfert in the 1940s and the explosion of radio astronomy

Este documento incorpora firma electrónica, y es copia auténtica de un documento electrónico archivado por la ULL según la Ley 39/2015.
Su autenticidad puede ser contrastada en la siguiente dirección <https://sede.ull.es/validacion/>

Identificador del documento:	969870	Código de verificación:	8KFVZkZp
Firmado por:	MARINA RAMÓN PÉREZ UNIVERSIDAD DE LA LAGUNA	Fecha:	28/06/2017 21:15:24
	ANGEL MANUEL BONGIOVANNI PÉREZ UNIVERSIDAD DE LA LAGUNA		29/06/2017 09:30:15
	JORGE CEPA NOGUE UNIVERSIDAD DE LA LAGUNA		29/06/2017 09:33:05
	ANA MARÍA PÉREZ GARCIA UNIVERSIDAD DE LA LAGUNA		29/06/2017 11:12:35
	ERNESTO PEREDA DE PABLO UNIVERSIDAD DE LA LAGUNA		04/07/2017 18:28:07

after World War II, to the posterior and modern multiwavelength studies of AGN, these objects have been found in a great variety of galaxy shapes, sizes and types, and our knowledge about their inner mechanisms has increased enormously (Shields 1999). Some of the different categories of AGN that were originally proposed, sometimes non-excluding, are briefly described hereunder:

- **Type 1 and type 2:** This classification is based on the width of the permitted emission lines, such as H α , H β , C IV λ 1549 or Mg II λ 2798. Type 1 are those AGN showing both broad (> 1000 km/s) and narrow ($\sim 300 - 1000$ km/s) permitted lines, while type 2 AGN exhibit narrow emission lines only.
- **Radio-loud and radio-quiet:** On the basis of their radio emission, AGN can be classified into radio-loud or radio-quiet sources. The former usually show intense relativistic jets, such as those shown in the upper left panel of Fig. 1.2, that can reach up to Megaparsec scales. The radio-loudness is described in terms of the eponymous parameter, $R \equiv L_{\nu_{radio}}/L_{\nu_{optical}}$.
- **Seyfert:** Seyfert galaxies have a very bright nucleus and are usually nearby spiral galaxies. Their spectra show intense emission lines as well as stellar absorption ones, and can also be classified into type 1 or 2.
- **QSO:** QSO or quasars are the most distant and luminous type of AGN. Their nuclei can outshine the host galaxy more than a hundred times, enabling their detection even at very high redshifts. Their point-like appearance is at the origin of their designation as *quasi-stellar sources*.
- **LINERs:** LINERs (*Low-Ionization Nuclear Emission-line Region*) are a type of low luminosity AGN showing low ionisation emission lines and strong absorption lines. Their low ionisation emission lines, for instance λ 6300 or [N II] λ 6548,6583, are very strong. Most of the AGN at low redshift are hosted by LINERs.
- **Blazars:** Although AGN tend to be variable, Blazars are the most variable type of AGN, with days or even hours variation scales. They are usually strong radio and γ -emission sources and present a high polarization degree.

Other astrophysical objects closely related to AGN are luminous (LIRGs) and ultra-luminous infrared galaxies (ULIRGs). These galaxies emit strongly in the IR range ($> 10^{11}$ and $10^{12} L_{\odot}$, respectively) and are among the brightest objects in the Universe. Moreover, they are believed to represent a link between AGN and starburst galaxies (Sanders & Mirabel 1996) and are usually associated with late stages in merger systems (Lonsdale et al. 2006). Also, the number of these objects increases dramatically with redshift and so does their fraction of AGN, although this may be a selection effect as faint systems are not visible at high redshift. In any case, the study of LIRGs and ULIRGs is essential in order to disentangle some issues connected to AGN and galaxy evolution.

Despite the great diversity of AGN, they all share a common structure with different components (see Fig. 1.3), although not all of them are necessarily present in every AGN. We briefly describe these components below:

- **The central engine:** The responsible for the huge emission of an AGN is a super-massive black hole (SMBH), located at the center of the galaxy, which is accreting the surrounding material. The infall of this material into the black hole results in the conversion of its gravitational potential energy into kinetic and thermal energy, producing the strong radiative emission in the entire wavelength spectrum that is characteristic of an AGN. Typical masses of SMBHs in AGN are $\sim 10^6 - 10^9 M_{\odot}$.

Este documento incorpora firma electrónica, y es copia auténtica de un documento electrónico archivado por la ULL según la Ley 39/2015. Su autenticidad puede ser contrastada en la siguiente dirección https://sede.ull.es/validacion/		
Identificador del documento:	Código de verificación:	
Firmado por: MARINA RAMÓN PÉREZ UNIVERSIDAD DE LA LAGUNA	969870	Código de verificación: 8KFVZkZp Fecha: 28/06/2017 21:15:24
ANGEL MANUEL BONGIOVANNI PÉREZ UNIVERSIDAD DE LA LAGUNA		29/06/2017 09:30:15
JORGE CEPA NOGUE UNIVERSIDAD DE LA LAGUNA		29/06/2017 09:33:05
ANA MARIA PÉREZ GARCIA UNIVERSIDAD DE LA LAGUNA		29/06/2017 11:12:35
ERNESTO PEREDA DE PABLO UNIVERSIDAD DE LA LAGUNA		04/07/2017 18:28:07

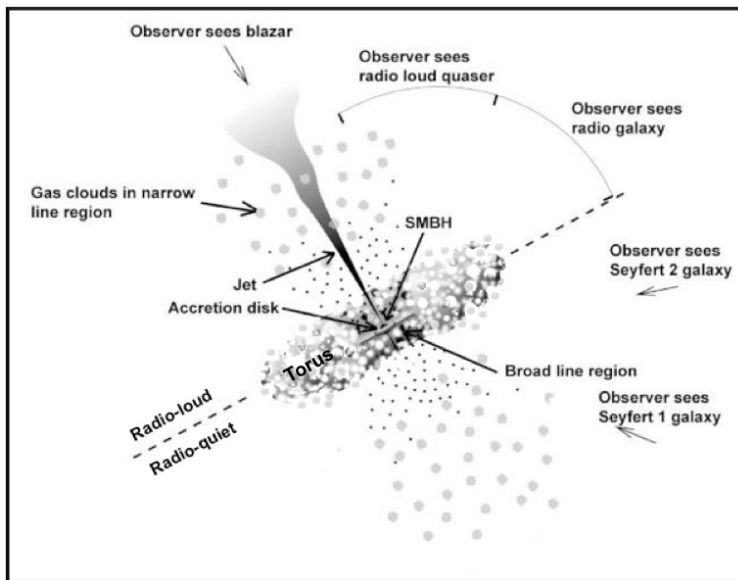


Figure 1.3: Unified model scheme for AGN (Antonucci 1993). Credit: Modification of the image from the Fermi Gamma Ray Space Telescope website.

- **The accretion disk:** The optically thick accretion disk immediately surrounding the SMBH (at sub-parsec scales) is the structure that enables the accretion, moving the material inwards. The huge energy produced in the accretion heats the disk as a gradient, reaching extremely high temperatures, up to $\sim 10^5$ K. The thermal radiation of the disk is responsible for part of the optical, UV and X-rays continuum emission of the AGN, peaking in the UV. In addition, it is believed that a corona of electrons produces the hard X-rays continuum (0.2-10 keV) as a consequence of non-thermal processes, such as inverse Compton scattering.
- **The broad-line region (BLR):** It is located close to the central engine (up to 1 pc away) and is the place where AGN's broad permitted lines arise. The BLR is composed of clouds of gas with significant turbulent motions due to the proximity to the SMBH. This causes the broadening of lines, which can go from ~ 1000 km/s up to ~ 10000 km/s. These broad-lines are characteristic of type 1 AGNs.
- **The torus:** At larger scales than the accretion disk, the SMBH is surrounded by a torus-shaped structure composed of cold gas and dust. This torus, which can measure from ~ 0.1 to 10 pc in Seyfert galaxies, obscures the central region when the AGN is observed edge-on. The radiation from the nucleus is reprocessed by the dust torus and re-emitted at infrared wavelengths. The modelling of the torus emission is then key to characterize it. We now know that it is a clumpy rather than smooth structure (Ramos Almeida et al. 2011, Hönig & Kishimoto 2010).
- **The narrow-line region (NLR):** It is located further away from the central engine than the BLR, extending to hundreds or even thousands of parsecs distances. The density of the gas in this region is low, with values of $\sim 10^3 - 10^6$ cm $^{-3}$. Due to the smaller velocity of its gas particles, lines emerging from

Este documento incorpora firma electrónica, y es copia auténtica de un documento electrónico archivado por la ULL según la Ley 39/2015.
Su autenticidad puede ser contrastada en la siguiente dirección <https://sede.ull.es/validacion/>

Identificador del documento:	969870	Código de verificación:	8KFVZkZp
Firmado por:	MARINA RAMÓN PÉREZ UNIVERSIDAD DE LA LAGUNA	Fecha:	28/06/2017 21:15:24
	ANGEL MANUEL BONGIOVANNI PEREZ UNIVERSIDAD DE LA LAGUNA		29/06/2017 09:30:15
	JORGE CEPA NOGUE UNIVERSIDAD DE LA LAGUNA		29/06/2017 09:33:05
	ANA MARIA PEREZ GARCIA UNIVERSIDAD DE LA LAGUNA		29/06/2017 11:12:35
	ERNESTO PEREDA DE PABLO UNIVERSIDAD DE LA LAGUNA		04/07/2017 18:28:07

this region have typical widths of a few hundreds of km/s only. These lines are seen both in type 1 and 2 AGN, as the torus does not obscure this zone.

- **The relativistic jet:** Most radio-loud AGN possess a relativistic jet coming out of the central region and extending up to hundred kiloparsec distances in opposite directions. The emission of these jets is mainly due to the synchrotron radiation of very energetic, accelerated particles. The jets are highly collimated and polarized, and are believed to be related to the magnetic fields present in the central region of AGN. See Marscher (2006) for a review on AGN relativistic jets.

It is now known that the different spectral properties of type 1 and type 2 AGN may be mainly attributed to the viewing angle of the source, something that was first proposed by Antonucci (1993). According to this unified model, type 1 AGN are objects viewed face-on, whose central engine is directly visible, while type 2 are sources viewed edge-on, with the torus hiding the BLR. Blazars, on the other hand, are seen along the line of sight of the relativistic jet. The understanding of AGN diversity also includes other relevant factors besides the viewing angle, such as the power of the central engine or the accretion rate and efficiency of the SMBH. We refer the reader to Netzer (2015) for a detailed review on this topic.

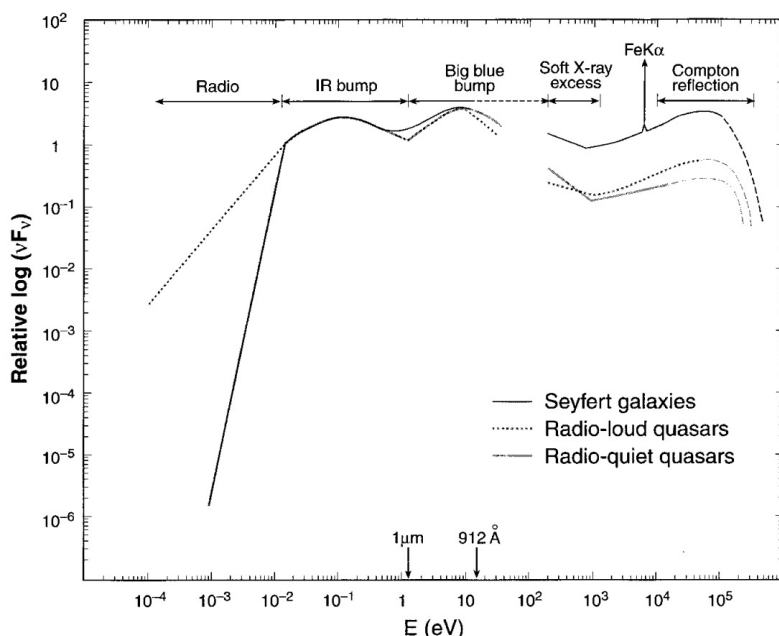


Figure 1.4: Typical SEDs of different classes of AGN. Some of their most characteristic spectral features, such as the IR bump or the big blue bump, are shown. Credit: Koratkar & Blaes (1999).

As a consequence of the different physical processes taking place in an AGN, their spectra have certain characteristics that make them unique (see Fig. 1.4). The spectral energy distribution (SED) of an AGN usually shows a peak at $\sim 60\mu\text{m}$, which is called the IR bump ($\sim 100 - 1\mu\text{m}$). The IR emission of an AGN is mainly due to thermal processes (re-emission of optical, UV and X-rays radiation from the central engine by the heated

Este documento incorpora firma electrónica, y es copia auténtica de un documento electrónico archivado por la ULL según la Ley 39/2015.
Su autenticidad puede ser contrastada en la siguiente dirección <https://sede.ull.es/validacion/>

Identificador del documento:	969870	Código de verificación:	8KFVZkZp
Firmado por:	MARINA RAMÓN PÉREZ UNIVERSIDAD DE LA LAGUNA	Fecha:	28/06/2017 21:15:24
	ANGEL MANUEL BONGIOVANNI PEREZ UNIVERSIDAD DE LA LAGUNA		29/06/2017 09:30:15
	JORGE CEPA NOGUE UNIVERSIDAD DE LA LAGUNA		29/06/2017 09:33:05
	ANA MARIA PEREZ GARCIA UNIVERSIDAD DE LA LAGUNA		29/06/2017 11:12:35
	ERNESTO PEREDA DE PABLO UNIVERSIDAD DE LA LAGUNA		04/07/2017 18:28:07

dusty surrounding torus) but can also be a consequence of non-thermal ones. In the optical and IR range, the SED of an AGN generally exhibits a power-law form such as:

$$L_\nu \propto \nu^{-\alpha}, \quad (1.1)$$

where $\alpha \sim 1 - 2$ is the spectral index, which depends on the considered spectral interval (Netzer 2013).

At optical and UV bands, the thermal emission from the accretion disk is responsible for a strong and broad feature called the big blue bump, one of the most noticeable signatures of an AGN. This feature starts at $\sim 1\mu\text{m}$ and peaks at $\sim 1000\text{\AA}$, sometimes reaching the soft X-rays region of the spectrum. In the optical, a great number of intense emission lines are usually superimposed to this continuum, such as H α , H β , H γ , [NII] (6548, 6584), Li λ 6507, [OI] (6300, 6363), [OIII] (4959, 5007) or He II λ 4686.

In the X-ray domain, the AGN spectrum is also governed by a power-law. The strong X-ray emission of AGN is produced by inverse Compton scattering of the UV and optical photons in the central region close to the SMBH. Some AGN also exhibit a soft X-rays excess below 2 keV, possibly originating in the corona surrounding the accretion disk. In the hard X-ray band, the strong Fe K α emission line at 6.5 keV and a Compton reflection bump above 10 keV are sometimes found, superimposed to the continuum power-law.

AGN can be selected in a variety of ways, based on their different spectral properties. One of the best ways is to perform spectroscopy in the optical or infrared range so as to determine if the underlying ionising continuum is of stellar type or rather follows a power-law such as Eq. 1.1. The intensity of optical emission lines can also be analysed, as proposed by Baldwin et al. (1981) and later by Veilleux & Osterbrock (1987). However, when spectroscopy is not available, other selection techniques must be used. As will be seen in Chapter 6, some of these alternative methods imply looking at the galaxy MIR colours (Lacy et al. 2004, Stern et al. 2005, Donley et al. 2012), while others focus on the X-rays emission (Mushotzky 2004). In many cases, as in the present work, the separation of the AGN from its host galaxy is not possible and so the analysed flux is the combination of both. Either way, a selection of AGN based only in a single method introduces a strong bias and always leaves some objects behind. This is why a multiwavelength selection of AGN, as that performed in this work, is preferred.

Some fundamental questions in the AGN field involve the triggering and evolution of AGN and their connection to the rest of galaxies in the environment. Recent evidence suggests that galaxies hosting an AGN may represent an intermediate transition population from blue, disk-dominated galaxies to red, bulge-dominated ones. In this scenario, mergers between gas-rich disk galaxies would lead to the powering of the AGN and the formation of bulges. AGN triggering can also be associated to secular processes, such as bars or instabilities, or even a combination of both in some cases (Hopkins et al. 2008).

Regarding the environmental dependency, Miller et al. (2003) observed a constant fraction of AGN with projected galaxy density in the local Universe, while the fraction of star-forming galaxies decreased with density and the opposite happened to passive galaxies (with no emission lines). Other authors found no statistical difference between the environments of AGN and those of passive galaxies (see, for instance, Virani et al. 2000 or Waskett et al. 2005). More recently, however, Manzer & De Robertis (2014) found a significantly higher fraction of AGNs in groups compared to isolated galaxies at low redshift. They also found that star-forming galaxies prefer isolated environments, which is connected to the availability of cool gas in those regions. The study of AGN environments is certainly crucial in order to understand how the activity of AGN is powered (is it by mergers or interactions with other galaxies?) or how an AGN evolves.

Este documento incorpora firma electrónica, y es copia auténtica de un documento electrónico archivado por la ULL según la Ley 39/2015.
Su autenticidad puede ser contrastada en la siguiente dirección <https://sede.ull.es/validacion/>

Identificador del documento: 969870	Código de verificación: 8KFVZkZp
Firmado por: MARINA RAMÓN PÉREZ UNIVERSIDAD DE LA LAGUNA	Fecha: 28/06/2017 21:15:24
ANGEL MANUEL BONGIOVANNI PÉREZ UNIVERSIDAD DE LA LAGUNA	29/06/2017 09:30:15
JORGE CEPA NOGUE UNIVERSIDAD DE LA LAGUNA	29/06/2017 09:33:05
ANA MARIA PÉREZ GARCIA UNIVERSIDAD DE LA LAGUNA	29/06/2017 11:12:35
ERNESTO PEREDA DE PABLO UNIVERSIDAD DE LA LAGUNA	04/07/2017 18:28:07

Although much knowledge about the AGN phenomenon has been gathered over the years, a lot of questions on the topic still remain open (Beckmann & Shrader 2012). Some of them involve the accretion mechanisms of the SMBH (the nature vs nurture dilemma, see Micic 2013), the physics of jets or the properties of the obscuring torus in the unified model. Moreover, if we broaden our perspective, AGN are not only exotic and interesting astrophysical objects. They can tell us a lot about the formation of galaxies in the early Universe and their posterior evolution. Has every galaxy been through an AGN phase during its life? In which cosmological epoch did the AGN phenomenon begin? What is the role of AGN feeding and feedback in galaxy evolution? Is the large-scale environment of AGN different than that of the rest of galaxies? What types of galaxies are more likely to host an AGN? The answers to these questions will undoubtedly contribute to a better understanding of our Universe.

1.2.2 Emission-line surveys

In the last years, a great amount of work has been devoted to the development and improvement of instruments and techniques for the detection of emission-line objects, specifically. The two main methods are narrow-band or Tunable Filters (TF) imaging and spectroscopy. The former offers certain advantages over the latter, such as a greater ease in the acquisition and reduction of the data, and a much deeper exploration of the sky. It also enables the simultaneous observation of a large number of objects and the creation of celestial maps with the spatial distribution of the emitting sources. Furthermore, the sky contamination is reduced when using narrow-band imaging, as only a small wavelength range can pass through the filter. However, this is also the main drawback of imaging versus spectroscopy, since it does not allow us to obtain the full spectrum of the source. This handicap can still be overcome with the use of TFs, which provide a set of quasi-monochromatic images of the field in a large wavelength range with which low-resolution spectroscopy can be made.

Another advantage of TFs is that they enable the observation of flux-limited samples of objects confined to a small redshift window. For a given small redshift range, all the objects with certain magnitude and equivalent width requirements are detected. If we target a specific emission line, the selected sample can give straightforward information about related parameters such as star-formation rate (in the case of H α), temperature or density, for instance.

Some examples of very recent emission-line surveys targeting, among other lines, H α are the High-redshift(Z) Emission Line Survey (HIZELS²) or the SSP-HSC emission-line galaxies survey³. The former is an ambitious attempt to select samples of H α emitters at different redshifts so as to estimate the cosmological evolution of their luminosity function. It covers ~ 2 deg 2 and uses the Wide Field Camera (WFCAM) of the 3.8m United Kingdom Infrared Telescope (UKIRT), the Suprime-Cam of the 8.2m Subaru telescope and the High Acuity Wide field K-band Imager (HAWK-I) of the 8.2m Very Large Telescope (VLT). The filters employed are medium and narrow-band, such as the NB921 filter with $\lambda_c \sim 9183\text{\AA}$ and FWHM $\sim 135\text{\AA}$ to target the H α emission at $z \sim 0.40$. The second survey, which also targets the [OIII] and [OII] emission at different redshifts, uses the Hyper Suprime-Cam on the Subaru telescope as well to cover 17 deg 2 of the sky. The filter used to select H α emitters is the same as in the previous case, with a limiting magnitude of 25.6 mag at 5 σ .

These surveys represent a colossal and fruitful attempt to study the emission-line Universe. They cover wide areas of the sky, dodging in this way the cosmic variance, and enabling the obtention of large samples of line-emitters. However, the selection of emitters is done by looking for a colour excess in the narrow-band, a

²See Geach et al. (2008) and Sobral et al. (2013).

³Subaru Strategic Program (SSP) with Hyper Suprime-Cam (HSC). See Hayashi et al. (2017).

Este documento incorpora firma electrónica, y es copia auténtica de un documento electrónico archivado por la ULL según la Ley 39/2015. Su autenticidad puede ser contrastada en la siguiente dirección https://sede.ull.es/validacion/		
Identificador del documento:	969870	Código de verificación: 8KFVZkZp
Firmado por:	MARINA RAMÓN PÉREZ UNIVERSIDAD DE LA LAGUNA	Fecha: 28/06/2017 21:15:24
	ANGEL MANUEL BONGIOVANNI PEREZ UNIVERSIDAD DE LA LAGUNA	29/06/2017 09:30:15
	JORGE CEPA NOGUE UNIVERSIDAD DE LA LAGUNA	29/06/2017 09:33:05
	ANA MARIA PEREZ GARCIA UNIVERSIDAD DE LA LAGUNA	29/06/2017 11:12:35
	ERNESTO PEREDA DE PABLO UNIVERSIDAD DE LA LAGUNA	04/07/2017 18:28:07

technique that can introduce contaminants. The number of AGN, on the other hand, is difficult to estimate and often relies on previous assumptions. Also, these surveys are useful to sample the brightest objects but fail in detecting the faintest ones, due to their limited depth. The use of TFs avoids the first problem, as line-emitters are detected based on the presence of an emission line in a low-resolution spectrum (or “pseudo-spectrum”, as will be seen later). In addition, the FWHM of TFs, much narrower than those of narrow-bands, permits the detection of objects with smaller equivalent widths. Finally, the use of TFs in a larger diameter telescope can decrease the limiting fluxes reached in a survey, allowing the detection of fainter objects. The search for emission-line objects using TFs on the largest telescope in the world is the aim of the OTELO survey, the core of this thesis, which is described in the next section.

1.3 The OSIRIS Tunable Emission Line Object survey

The OSIRIS Tunable Emission Line Object project (OTELO, Cepa et al. 2003) is an ambitious emission-line survey which makes use of the red TF of the OSIRIS instrument (Cepa et al. 2003), installed in the 10.4 m Gran Telescopio CANARIAS (Alvarez et al. 1998), currently the largest fully steerable optical reflecting telescope in the world (see Figures 1.5 and 1.6). The combined use of TFs and a large diameter telescope is ideal for the search of faint emission-line objects. As will be seen in detail in Chapter 2, TFs allow us obtaining narrow-band image in the entire wavelength range of OSIRIS, which covers the optical part of the spectrum (365 - 1000 nm). This added to the large field of view of OSIRIS ($8.6 \times 8.6 \text{ arcmin}^2$) makes it possible to obtain low-resolution spectroscopy of a considerable number of sources simultaneously. The large collecting capacity of a 10 m telescope also implies a much deeper observation of the sky, which is of great value when trying to detect emitting objects, specially at high redshift. OTELO intends to detect all the emitting objects in its field up to $z \sim 6.55$, which will allow us to study in great detail a variety of astrophysical objects, such as AGN (Sánchez-Portal et al. 2005), QSO (González-Serrano et al. 2005), Ly α emitters (González-Serrano et al. 2005) or star-forming galaxies, among others, and to deduce essential parameters such as metallicities, luminosity functions, chemical abundances, star-formation rates, etc. With these features, OTELO aims to become the deepest and largest emission-line survey to date, gathering data that will contribute in a significant way to the field of Extragalactic Astrophysics.

OTELO’s field corresponds to an OSIRIS pointing to the Extended Groth Strip (EGS), a $70 \times 10 \text{ arcmin}^2$ region of the sky located close to the Ursa Major constellation, which is at about 10 hours 40 minutes right ascension and 56° north declination (see Fig. 1.7). The EGS contains more than 50000 galaxies and has been widely studied, in particular by the All-wavelength Extended Groth Strip International Survey⁴ (Davis et al. 2007). AEGIS data are of great interest to OTELO, as it will be seen in Chapter 4.

The OTELO survey was conceived as a blind, magnitude-limited spectral tomography. The survey covered $\sim 55 \text{ arcmin}^2$ in one pointing, given the large effective field of view of OSIRIS (see Chapter 3). The wavelengths of observation were chosen to make them coincide with a window in the infrared airglow emission of the sky, where telluric emission lines are weaker and thus the atmospheric contamination is lower (see Fig. 1.8). The spectral range (9070 – 9280 Å) was sampled every 6 Å with a full-width at half maximum (FWHM) of about 12 Å, with the aim of deblending the H α and [NII] $\lambda 6784$ emission lines (Lara-López et al. 2011). This procedure, called tomography, enables 2D low resolution spectroscopy of all the sources in the field simultaneously. More details about the use of TFs and the tomography technique are given in Chapter 2.

⁴AEGIS, see <http://aegis.ucolick.org/astronomers.html>.

Este documento incorpora firma electrónica, y es copia auténtica de un documento electrónico archivado por la ULL según la Ley 39/2015. Su autenticidad puede ser contrastada en la siguiente dirección https://sede.ull.es/validacion/		
Identificador del documento:	Código de verificación:	
Firmado por: MARINA RAMÓN PÉREZ UNIVERSIDAD DE LA LAGUNA	969870	Código de verificación: 8KFVZkZp Fecha: 28/06/2017 21:15:24
ANGEL MANUEL BONGIOVANNI PÉREZ UNIVERSIDAD DE LA LAGUNA		29/06/2017 09:30:15
JORGE CEPA NOGUE UNIVERSIDAD DE LA LAGUNA		29/06/2017 09:33:05
ANA MARÍA PÉREZ GARCIA UNIVERSIDAD DE LA LAGUNA		29/06/2017 11:12:35
ERNESTO PEREDA DE PABLO UNIVERSIDAD DE LA LAGUNA		04/07/2017 18:28:07



Figure 1.5: Gran Telescopio CANARIAS (GTC) located at El Roque de los Muchachos Observatory (ORM), La Palma, Canary Islands (Spain).

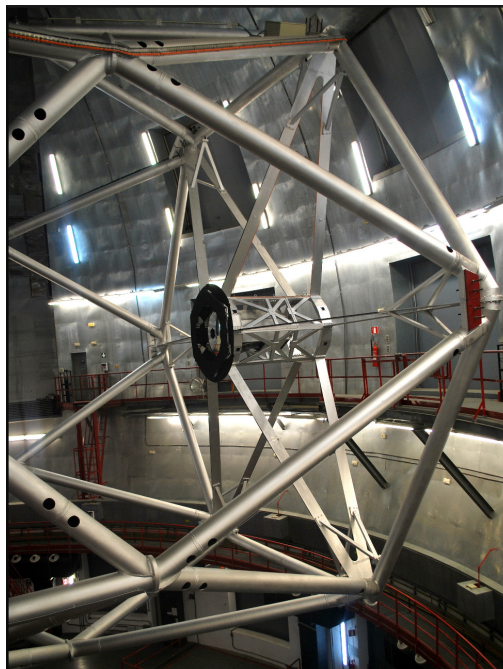


Figure 1.6: Interior view of the Gran Telescopio CANARIAS located at the ORM, La Palma, Canary Islands (Spain), showing the secondary mirror.

Este documento incorpora firma electrónica, y es copia auténtica de un documento electrónico archivado por la ULL según la Ley 39/2015.
Su autenticidad puede ser contrastada en la siguiente dirección <https://sede.ull.es/validacion/>

Identificador del documento: 969870

Código de verificación: 8KFVZkZp

Fecha: 28/06/2017 21:15:24

Firmado por: MARINA RAMÓN PÉREZ
UNIVERSIDAD DE LA LAGUNA

29/06/2017 09:30:15

ANGEL MANUEL BONGIOVANNI PEREZ
UNIVERSIDAD DE LA LAGUNA

29/06/2017 09:33:05

JORGE CEPA NOGUE
UNIVERSIDAD DE LA LAGUNA

29/06/2017 11:12:35

ANA MARIA PEREZ GARCIA
UNIVERSIDAD DE LA LAGUNA

04/07/2017 18:28:07

ERNESTO PEREDA DE PABLO
UNIVERSIDAD DE LA LAGUNA

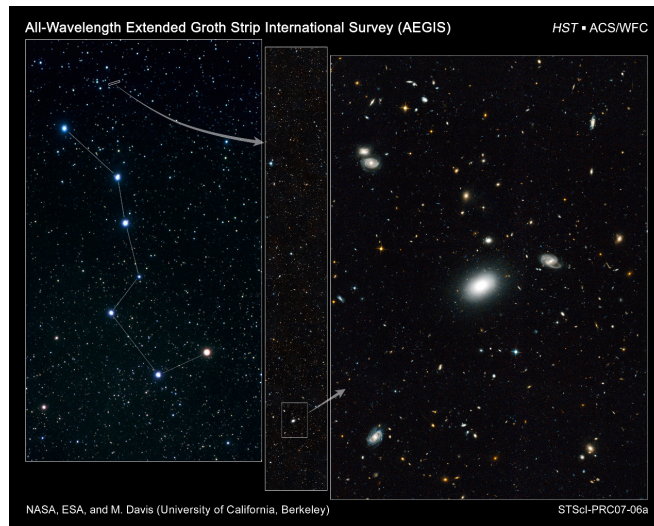


Figure 1.7: Size of the Extended Groth Strip. AEGIS's target field, compared to the Big Dipper of the Ursa Major constellation. Image from the Hubble Space Telescope. Credit: NASA, ESA, M. Davis (University of California, Berkeley), S. Faber (University of California, Santa Cruz), and A. Koekemoer (STScI).

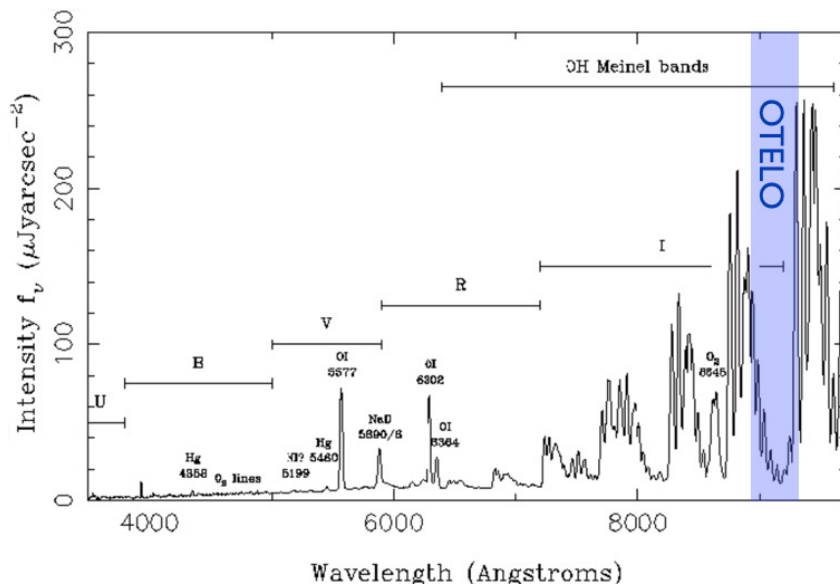


Figure 1.8: Typical La Palma night-sky spectrum in the optical and near infrared. The Meinel bands of OH in the infrared spectrum of the airglow are visible. OTELO's spectral range, shown in blue, coincides with a window in the airglow emission. Image taken from the ORM observing conditions website and modified by the author.

Este documento incorpora firma electrónica, y es copia auténtica de un documento electrónico archivado por la ULL según la Ley 39/2015. <i>Su autenticidad puede ser contrastada en la siguiente dirección https://sede.ull.es/validacion/</i>		
Identificador del documento:	969870	Código de verificación: 8KFVZkZp
Firmado por:	MARINA RAMÓN PÉREZ UNIVERSIDAD DE LA LAGUNA	Fecha: 28/06/2017 21:15:24
	ANGEL MANUEL BONGIOVANNI PEREZ UNIVERSIDAD DE LA LAGUNA	29/06/2017 09:30:15
	JORGE CEPA NOGUE UNIVERSIDAD DE LA LAGUNA	29/06/2017 09:33:05
	ANA MARIA PEREZ GARCIA UNIVERSIDAD DE LA LAGUNA	29/06/2017 11:12:35
	ERNESTO PEREDA DE PABLO UNIVERSIDAD DE LA LAGUNA	04/07/2017 18:28:07

The spectral tomography carried out in OTELO permits the study of different emission lines in well defined redshift windows. The H α +[NII] lines, for instance, are observed at $z \sim 0.40$, while the Ly α emitters fall at $z \sim 6.55$. Other relevant emission lines and the mean redshift at which they are observed in the OTELO survey are described in Table 1.1.

Table 1.1: Relevant emission lines, their wavelengths at rest-frame and the mean redshift at which they are seen in OTELO survey, considering 9175Å as the central wavelength of OTELO's spectral window.

Emission line	λ_0	$< z >$
H α	6563 Å	0.40
[OIII]	5007 Å	0.83
H β	4861 Å	0.89
[OII]	3726 Å	1.46
Ly α	1215 Å	6.55

The OTELO observations were undertaken during the period between April 2010 and June 2014, devoting more than 100 hours of GTC's guaranteed time to them. They were distributed in 108 observing blocks (OB), the images in each OB corresponding to the same night. In total, 256 raw images were obtained with a mean seeing of 0.825 ± 0.078 arcsec. A summary of OTELO observations is shown in Table 1.2, while the main characteristics of OTELO survey are displayed in Table 1.3.

Table 1.2: Description of OTELO's observations.

Year	Observing Blocks	λ_0 (Å)	$< \text{Seeing} >$
2010	1 – 18	9280 – 9250	0.83 ± 0.06
2011	19 – 39	9244 – 9208	0.83 ± 0.08
2013	40 – 66	9202 – 9154	0.82 ± 0.09
2014	67 – 108	9148 – 9070	0.82 ± 0.07

Table 1.3: Main features of the OTELO survey.

Parameter	Value
Centre coordinates	$\alpha=14h\ 17m\ 20s$, $\delta=+52^\circ\ 27'\ 05''$
Spatial coverage	~ 55 arcmin 2
Wavelength coverage	9070 – 9280 Å
FWHM	12 Å
Sampling interval	6 Å
Wavelength accuracy	± 1 Å
Photometric accuracy	± 0.05 mag

Este documento incorpora firma electrónica, y es copia auténtica de un documento electrónico archivado por la ULL según la Ley 39/2015.
Su autenticidad puede ser contrastada en la siguiente dirección <https://sede.ull.es/validacion/>

Identificador del documento: 969870	Código de verificación: 8KFVZkZp
Firmado por: MARINA RAMÓN PÉREZ UNIVERSIDAD DE LA LAGUNA	Fecha: 28/06/2017 21:15:24
ANGEL MANUEL BONGIOVANNI PÉREZ UNIVERSIDAD DE LA LAGUNA	29/06/2017 09:30:15
JORGE CEPA NOGUE UNIVERSIDAD DE LA LAGUNA	29/06/2017 09:33:05
ANA MARIA PÉREZ GARCIA UNIVERSIDAD DE LA LAGUNA	29/06/2017 11:12:35
ERNESTO PEREDA DE PABLO UNIVERSIDAD DE LA LAGUNA	04/07/2017 18:28:07

1.4 Motivation of this thesis

In this introduction, I have made a quick review of the different types of surveys that have historically been conducted in an attempt to better understand our Universe. Among them, the use of TFs in large telescopes, a more recent development, stands out as an efficient way of obtaining low-resolution spectroscopy of a large number of sources simultaneously and also of exploring the sky at deeper magnitudes. This technique is particularly useful for the detection of emitting objects even at high redshifts. The importance of emission lines is justified by the great number of different astrophysical sources that exhibits them. An example are AGN, one of the most energetic and intriguing objects in the Universe. Their study is crucial to learn about galaxy formation and evolution, and the different mechanisms implied. In this context, the OTELO project is an emission-line based survey using the TFs of OSIRIS on the GTC which aims to contribute to answering those essential questions, among others.

In this thesis, we aim to take advantage of OTELO's capabilities to study the AGN population in the field. In particular, we aim to perform an analysis of the properties of these objects, including their demography and morphology. Focusing on the population of H α emitters at $z \sim 0.40$, an attempt will be made at studying the environments of AGN and non-AGN at that redshift. Another objective of this work is to obtain the H α LF in order to extend its faint end and thus constrain the star formation rate and the number of galaxies at low-luminosities. The AGN contribution to this LF will also be estimated.

To accomplish this, a number of steps must be followed, that constitute goals in themselves. The most important one is the obtention of OTELO's deep and multiwavelength catalogue of emitting objects in the field. This will represent a fundamental tool not only for this work, but also for future studies. To summarise, the goals of this thesis are the following:

- to obtain a deep multiwavelength catalogue of all the emission-line objects in OTELO's field,
- to prove OTELO's potential in the selection of emitting objects, specially at $z \sim 0.40$,
- to select a sample of AGN in the field,
- to perform an analysis of the properties of these objects,
- to study the large-scale environments of AGN and non-AGN at $z \sim 0.40$,
- to obtain a luminosity function of H α at $z \sim 0.40$ and
- to estimate the AGN contribution to the total luminosity at that redshift.

To do so, we first describe the TFs of the OSIRIS instrument and the reduction and calibration processes of OTELO's data (Chapters 2 and 3). We then construct a multiwavelength catalogue of all the sources in the field (Chapter 4). After that, we describe the methods of detection of the emitting sources, focusing on the selection of H α emitters (Chapter 5). We then search for AGN in the field using different methods that target different wavelength ranges (Chapter 6) and we analyse the AGN population (Chapter 7). Finally, the conclusions of this work are described in Chapter 8.

Este documento incorpora firma electrónica, y es copia auténtica de un documento electrónico archivado por la ULL según la Ley 39/2015.
Su autenticidad puede ser contrastada en la siguiente dirección <https://sede.ull.es/validacion/>

Identificador del documento:	Código de verificación:
969870	8KFVZkZp
Firmado por: MARINA RAMÓN PÉREZ UNIVERSIDAD DE LA LAGUNA	Fecha: 28/06/2017 21:15:24
ANGEL MANUEL BONGIOVANNI PÉREZ UNIVERSIDAD DE LA LAGUNA	29/06/2017 09:30:15
JORGE CEPA NOGUE UNIVERSIDAD DE LA LAGUNA	29/06/2017 09:33:05
ANA MARIA PÉREZ GARCIA UNIVERSIDAD DE LA LAGUNA	29/06/2017 11:12:35
ERNESTO PEREDA DE PABLO UNIVERSIDAD DE LA LAGUNA	04/07/2017 18:28:07

2

OBSERVATIONS WITH TUNABLE FILTERS

The basic characteristics of interferometry and tunable filters are introduced in this Chapter. The OSIRIS instrument of the GTC is described, as well as the properties of OTELO survey and its data.

It was at the end of the 19th century that Alfred Perot and Charles Fabry explored the interference phenomena of light and came across a new and powerful form of interferometer using two parallel silvered plates (Perot & Fabry 1899; Fabry & Perot 1901). Soon after, the so-called Fabry-Perot interferometer was used for astronomical purposes for the first time, to study nebulae bright lines (Fabry & Buisson 1911).

In 1981, Atherton & Reay built a low-resolution Fabry-Perot interferometer with a much smaller gap between its plates and the possibility of varying the distance between them, giving birth to what we call today a tunable filter. These extremely useful devices have since then been successfully implemented and used in Astrophysics. One of the first TFs, no longer in use, was the Taurus Tunable Filter (TTF, see Bland-Hawthorn & Jones 1998) of the 3.9-meter Anglo-Australian telescope, located in Siding Spring Observatory, Australia. Another example is the Maryland-Magellan Tunable Filter (MMTF, see Veilleux et al. 2010) of the 6.5-meter Magellan-Baade telescope in Las Campanas Observatory, Chile.

Tunable filters enable consecutive narrow-band imaging in a wide wavelength range and with a chosen bandwidth. When combined with an instrument with an extended field of view, they provide low-resolution spectroscopy of a large number of sources simultaneously. This makes them a very powerful and worthwhile device for various astrophysical goals.

2.1 Characteristics of Tunable Filters

A TF is a low-resolution Fabry-Perot interferometer composed of two highly reflective parallel plates. The light entering the interferometer suffers multiple reflections between the plates which cause destructive and constructive interferences (see Fig. 2.1). In a conventional Fabry-Perot interferometer, the resulting central interference region, the Jacquinot spot, is a narrow ring on the sky. However, with their much smaller plate spacing, TFs produce a wide circular region of interference covering a greater region of the sky (see Fig. 2.2).

Este documento incorpora firma electrónica, y es copia auténtica de un documento electrónico archivado por la ULL según la Ley 39/2015.
Su autenticidad puede ser contrastada en la siguiente dirección <https://sede.ull.es/validacion/>

Identificador del documento:	969870	Código de verificación:	8KFVZkZp
Firmado por:	MARINA RAMÓN PÉREZ UNIVERSIDAD DE LA LAGUNA	Fecha:	28/06/2017 21:15:24
	ANGEL MANUEL BONGIOVANNI PEREZ UNIVERSIDAD DE LA LAGUNA		29/06/2017 09:30:15
	JORGE CEPA NOGUE UNIVERSIDAD DE LA LAGUNA		29/06/2017 09:33:05
	ANA MARIA PEREZ GARCIA UNIVERSIDAD DE LA LAGUNA		29/06/2017 11:12:35
	ERNESTO PEREDA DE PABLO UNIVERSIDAD DE LA LAGUNA		04/07/2017 18:28:07

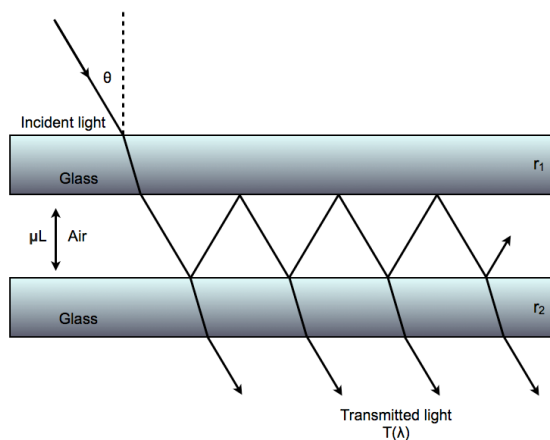


Figure 2.1: In a Fabry-Perot interferometer, light suffers multiple reflections in the cavity between the plates. θ is the angle of incidence of light, r_1 and r_2 the coating reflectivities of the plates, μ the refractive index of the cavity's medium (usually air with $\mu = 1.00$) and L the spacing between the plates. The transmission profile of the light, $T(\lambda)$, is an Airy function. Image inspired by Jones 2001.

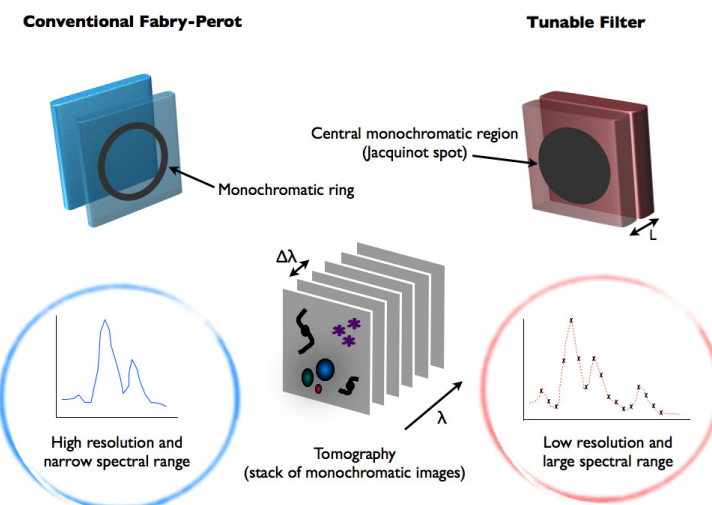


Figure 2.2: Traditional Fabry-Perot interferometer (left) compared to a tunable filter (right). The smaller gap between the plates of the latter provides a larger region of interference (the Jacquinot spot), low-resolution spectroscopy and a larger wavelength range. In the middle of the figure, the tomography technique is represented, consisting in taking a set of images of the same pointing at different consecutive wavelengths separated by $\Delta\lambda$. Image inspired by Jones et al. 2001 and Pintos-Castro 2014.

Este documento incorpora firma electrónica, y es copia auténtica de un documento electrónico archivado por la ULL según la Ley 39/2015.
Su autenticidad puede ser contrastada en la siguiente dirección <https://sede.ull.es/validacion/>

Identificador del documento: 969870

Código de verificación: 8KFVZkZp

Firmado por: MARINA RAMÓN PÉREZ
UNIVERSIDAD DE LA LAGUNA

Fecha: 28/06/2017 21:15:24

ANGEL MANUEL BONGIOVANNI PEREZ
UNIVERSIDAD DE LA LAGUNA

29/06/2017 09:30:15

JORGE CEPA NOGUE
UNIVERSIDAD DE LA LAGUNA

29/06/2017 09:33:05

ANA MARIA PEREZ GARCIA
UNIVERSIDAD DE LA LAGUNA

29/06/2017 11:12:35

ERNESTO PEREDA DE PABLO
UNIVERSIDAD DE LA LAGUNA

04/07/2017 18:28:07

The transmission profile of a TF is an Airy function which depends on the angle of incidence of light (θ), the coating reflectivities of the plates (r_1 and r_2), the refractive index of the cavity's medium (usually air with $\mu = 1.00$) and the spacing between the plates (L):

$$T(\lambda) = \left[1 + \frac{4\sqrt{r_1 r_2}}{(1 - \sqrt{r_1 r_2})^2} \sin^2 \left(\frac{2\pi\mu L}{\lambda} \cos \theta \right) \right]^{-1} \quad (2.1)$$

$T(\lambda)$ shows periodic and narrow high transmission intervals which correspond to resonances in the system's cavity (see Figure 2.3). These maxima occur for specific orders of interference m :

$$m\lambda = 2\mu L \cos \theta \quad (2.2)$$

In order to select one of these bands and block the rest of them it is necessary to use Order-Sorter (OS) filters. The transmission profile of a TF, the Airy function, can be expressed in terms of the central wavelength of the transmission maximum (λ_c) and the full width at half maximum ($\delta\lambda$) with a power series approximation:

$$T(\lambda) \sim \left[1 + 4 \left(\frac{\lambda - \lambda_c}{\delta\lambda} \right)^2 \right]^{-1} \quad (2.3)$$

The most interesting and useful feature of a TF is that it allows to choose these two fundamental parameters (λ_c and $\delta\lambda$) by varying with high precision the distance L between the plates. Assuming that the coating

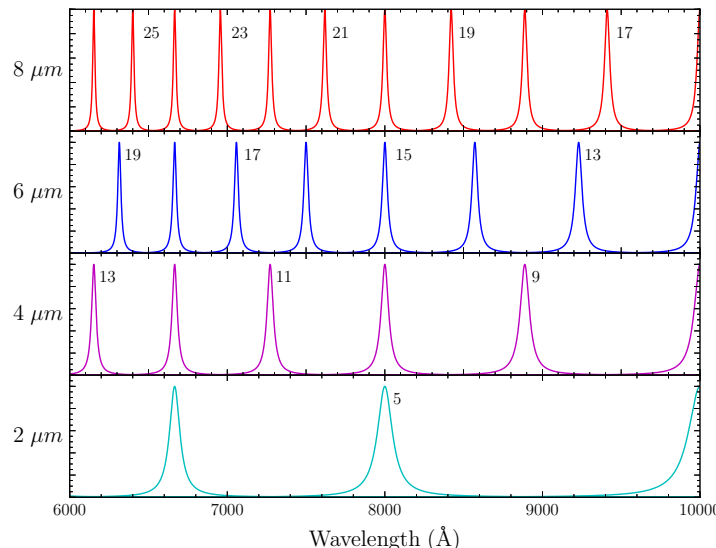


Figure 2.3: Transmission profile of a tunable filter as a function of L , the separation between the plates (left). Odd interference orders m are indicated. As can be deduced from equations 2.4 and 2.5, for a given central wavelength, a greater distance between the plates results in a greater interference order m with a smaller width and closer orders. Image inspired by Jones 2001.

reflectivities of the plates are identical ($r_1 = r_2 = R$), λ_c and $\delta\lambda$ can be expressed in terms of L and the rest of the non-variable parameters from equations 2.1, 2.2 and 2.3:

$$\lambda_c = \frac{2\mu L \cos \theta}{m} \quad (2.4)$$

$$\delta\lambda = \frac{\lambda(1-R)}{m\pi R^{1/2}}, \quad (2.5)$$

2.2 OSIRIS's Tunable Filters

OSIRIS (Optical System for Imaging and low Resolution Integrated Spectroscopy, Cepa et al. 2003) is an imager and spectrograph of low and intermediate resolution covering the optical wavelength range (365 - 1050 nm). It is one of the main instruments of the Gran Telescopio CANARIAS (GTC), located at the Observatorio del Roque de los Muchachos, La Palma (see Figure 2.4). With a primary mirror of 10.4 meters, the GTC is currently the largest fully steerable optical reflecting telescope in the world. OSIRIS's characteristics make it suitable for obtaining both imaging and long-slit and multi-object spectroscopy. Its wide unvignetted field of view of 7.8 x 7.8 arcmin (divided in 2 CCDs), combined with its high efficiency and the large collecting area of the GTC, makes it the perfect instrument for deep surveys. However, the main characteristic of OSIRIS that distinguishes it from other instruments in large telescopes (8-10 m) is the availability of tunable filters.

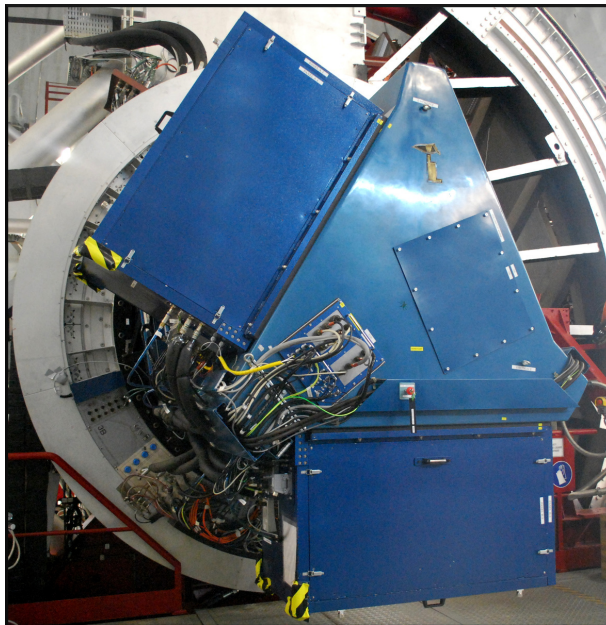


Figure 2.4: OSIRIS instrument (Optical System for Imaging and low Resolution Integrated Spectroscopy, Cepa et al. 2003) at the Gran Telescopio CANARIAS (Observatorio del Roque de los Muchachos, La Palma).

Este documento incorpora firma electrónica, y es copia auténtica de un documento electrónico archivado por la ULL según la Ley 39/2015.
Su autenticidad puede ser contrastada en la siguiente dirección <https://sede.ull.es/validacion/>

Identificador del documento:	969870	Código de verificación:	8KFVZkZp
Firmado por:	MARINA RAMÓN PÉREZ UNIVERSIDAD DE LA LAGUNA	Fecha:	28/06/2017 21:15:24
	ANGEL MANUEL BONGIOVANNI PEREZ UNIVERSIDAD DE LA LAGUNA		29/06/2017 09:30:15
	JORGE CEPA NOGUE UNIVERSIDAD DE LA LAGUNA		29/06/2017 09:33:05
	ANA MARIA PEREZ GARCIA UNIVERSIDAD DE LA LAGUNA		29/06/2017 11:12:35
	ERNESTO PEREDA DE PABLO UNIVERSIDAD DE LA LAGUNA		04/07/2017 18:28:07

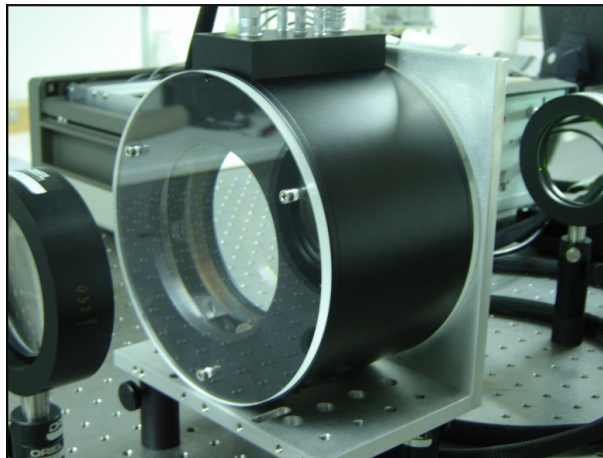


Figure 2.5: OSIRIS's red tunable filter. Image taken from OSIRIS's user manual.

OSIRIS possesses two different TFs, one operating in the blue wavelength range (450-671 nm) and another one in the red (651-934.5 nm; see Figure 2.5). The separation as well as the parallelism of the plates of OSIRIS's TFs are controlled with high precision and velocity by means of piezoelectric devices between them. These TFs enable narrow-band imaging across almost all the spectral range covered by OSIRIS. The fact that the central wavelength and width of the transmission band can be selected implies that a large number of narrow filters, that would otherwise be used, are no longer needed.

2.2.1 Characteristics of OSIRIS TF data

The astronomical images resulting from observations with TFs have certain characteristics that distinguish them from standard images. As can be deduced from equation 2.2, the angle of incidence of light in the TF, θ , determines the effective wavelength of the observation. The **optical center** corresponds to the location in the CCD for which the incident rays hit the TF at $\theta = 0$. These rays have the exact same wavelength at which the TF was tuned. The rest of the rays, that penetrate with slightly different angles, have smaller (bluer) wavelengths and reach more external zones of the detector. As a consequence, the resulting image is not strictly monochromatic, but rather shows a wavelength shift towards the blue as we go to outer regions in the field of view. This shift implies that quasi-monochromatic emission lines of the sky appear as concentric rings in the images (see Figure 2.6). The removal of these rings, a crucial step in the reduction of the data, is described in Chapter 3.

The incident angle, θ , and the radial distance to the optical center, r , are theoretically related by means of the ratio between the telescope (GTC) and the instrument (OSIRIS) collimator mirror focal lengths. For OSIRIS' red TF, the observed empirical dependency of wavelength on r is given by the following expression (González et al. 2014):

$$\lambda = \lambda_0 - 5.04r^2 + a_3(\lambda)r^3 , \quad (2.6)$$

Este documento incorpora firma electrónica, y es copia auténtica de un documento electrónico archivado por la ULL según la Ley 39/2015.
Su autenticidad puede ser contrastada en la siguiente dirección <https://sede.ull.es/validacion/>

Firmado por:	Identificador del documento:	Código de verificación:	Fecha:
MARINA RAMÓN PÉREZ UNIVERSIDAD DE LA LAGUNA	969870	8KFVZkZp	28/06/2017 21:15:24
ANGEL MANUEL BONGIOVANNI PEREZ UNIVERSIDAD DE LA LAGUNA			29/06/2017 09:30:15
JORGE CEPA NOGUE UNIVERSIDAD DE LA LAGUNA			29/06/2017 09:33:05
ANA MARIA PEREZ GARCIA UNIVERSIDAD DE LA LAGUNA			29/06/2017 11:12:35
ERNESTO PEREDA DE PABLO UNIVERSIDAD DE LA LAGUNA			04/07/2017 18:28:07

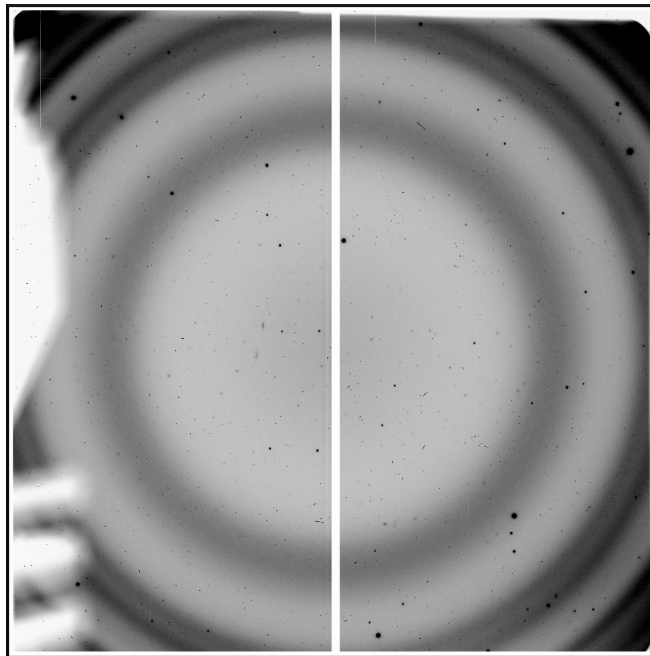


Figure 2.6: OTELO's raw image corresponding to a central wavelength of 9148Å. The colours have been inverted for a better display. The white zones in the left edge of the image are due to the concealment caused by elements of the system such as the filter wheel or the folder mirror. Sky emission lines can be seen as concentric rings in the image. The center of those rings is the so-called *optical center*, the location in the CCD for which incident rays hit the TF at $\theta = 0$.

where λ_0 is the wavelength to which the TF is tuned (Å), r is expressed in arcmin and $a_3(\lambda)$ is a third-order term given by:

$$a_3(\lambda) = 6.0396 - 1.5698 \times 10^{-3}\lambda + 1.0024 \times 10^{-7}\lambda^2 \quad (2.7)$$

This empirical parametrisation obeys to the fact that, in general, the performance of a Fabry-Perot interferometer is highly dependent on the properties of the cavity coatings. As demonstrated in González et al. (2014), a chromatic dispersion caused by the multilayered thick coatings of OSIRIS's red TF gives rise to a phase effect which significantly departs from the theoretical expression.

The use of Order-Sorter filters to select the wavelength band corresponding to a single interference order m is mandatory when observing with TFs. OSIRIS has 22 of such filters for its red TF¹. For each observation, the most appropriate OS filter has to be chosen. The use of OS filters determines the effective field of view of the images, as their function is only guaranteed in a circle of 4 arcmin diameter around the optical center. At larger distances, the fluxes of the objects may be contaminated with other non-desired interference orders. This must be taken into account when trimming the images in the reduction process (see section 3.1.1).

Another characteristic of the images from TFs is the emergence of spurious objects (or *ghosts*) as a consequence of the multiple reflections of light from the brightest objects in the field. These ghosts appear in

¹See OSIRIS's user manual for more details.

Identificador del documento: 969870	Código de verificación: 8KFVZkZp
Firmado por: MARINA RAMÓN PÉREZ UNIVERSIDAD DE LA LAGUNA	Fecha: 28/06/2017 21:15:24
ANGEL MANUEL BONGIOVANNI PEREZ UNIVERSIDAD DE LA LAGUNA	29/06/2017 09:30:15
JORGE CEPA NOGUE UNIVERSIDAD DE LA LAGUNA	29/06/2017 09:33:05
ANA MARIA PEREZ GARCIA UNIVERSIDAD DE LA LAGUNA	29/06/2017 11:12:35
ERNESTO PEREDA DE PABLO UNIVERSIDAD DE LA LAGUNA	04/07/2017 18:28:07

the image at symmetrical positions from the object that causes them with respect to the optical center². The positions of these ghosts with respect to the real sources shift from one dithered image to another. Therefore, the combination of images with different dithering allow their identification and removal. Using a dithering pattern is also required for the removal of the fringing pattern, which is described in section 3.1.4.

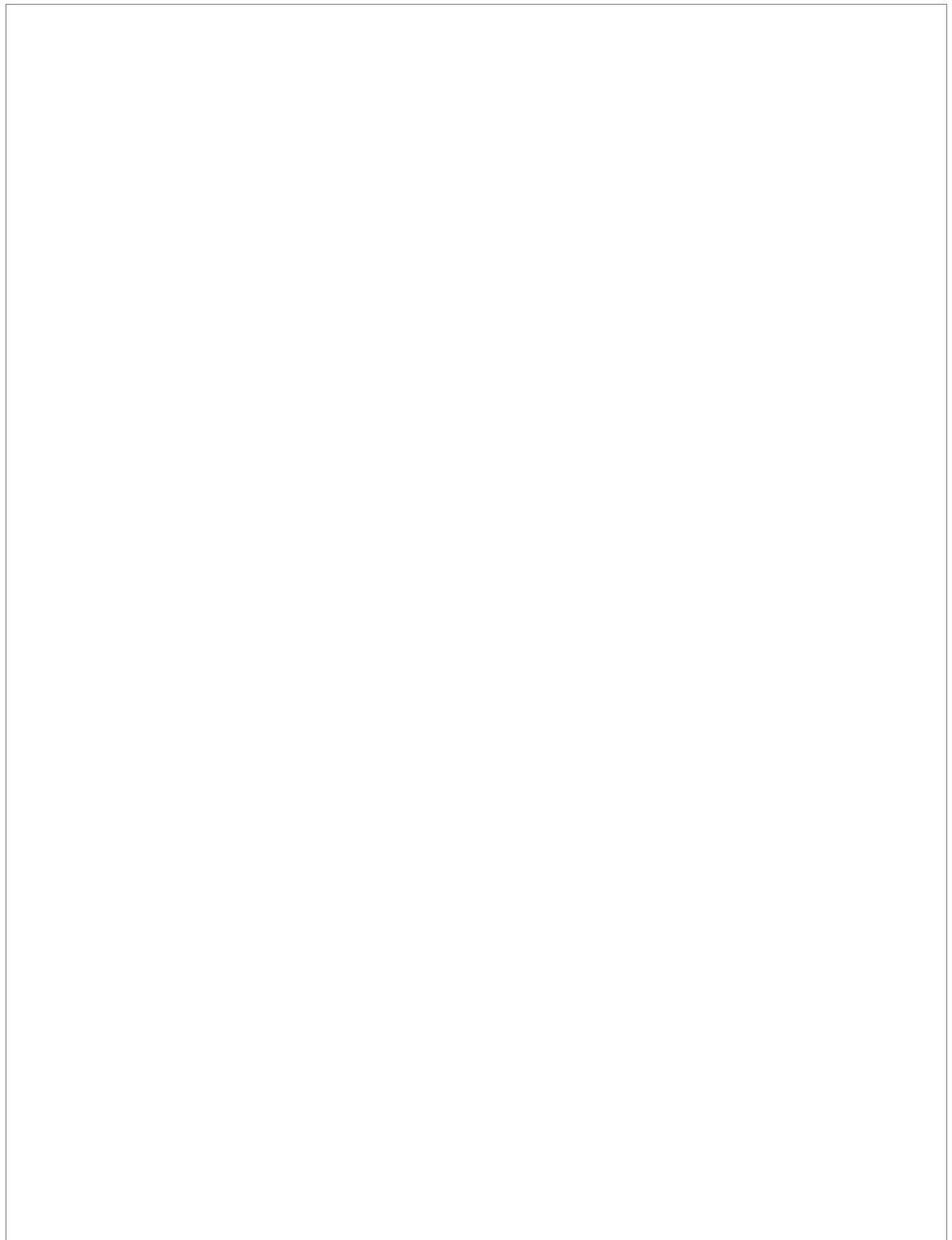
2.2.2 Application to OTELO survey

For the OTELO survey, we used the red TF of OSIRIS to observe in the infrared domain, in the range 9280-9070 Å. This spectral range, which is a gap between strong sky emission lines, was scanned using the ‘tomography’ technique, which consists in collecting a set of images of the same pointing at different consecutive wavelengths (see Figure 2.2). The spectral separation between the images was 6Å and the mean FWHM was set at \sim 12Å. These values were chosen to obtain a resolution good enough to deblend the [NII] line ($\lambda = 6583\text{Å}$) from H α ($\lambda = 6563\text{Å}$), in order to estimate metallicities and separate different types of AGN (Lara-López et al. 2011).

For each central wavelength, 3 Observing Blocks (OB) were acquired, each one containing 2 images. Therefore, 6 images (or ‘slices’), such as the one shown in Fig. 2.6, were taken for a given value of L , the separation of the plates. The images had an exposure time of 1100 seconds each and followed a dithering pattern in order to make certain steps of the reduction easier (see Chapter 3). Those slices with the same observation wavelength constitute a ‘scan’. In total, OTELO’s tomography was composed of 36 scans and 216 slices of the full field (i.e. 432 images of individual CCDs). By doing aperture photometry in the images, a ‘pseudo-spectrum’ (from now on, ‘PS’) can be obtained for every source in the field. In a PS, each point represents the integrated flux of the object in one scan. See Fig. 5.7 for an example of an OTELO’s object PS and Section 3.3.5 for a description on how they were obtained.

²See Appendix B in Jones et al. 2002 for a description of ghost families in observations with TFs.

Este documento incorpora firma electrónica, y es copia auténtica de un documento electrónico archivado por la ULL según la Ley 39/2015. Su autenticidad puede ser contrastada en la siguiente dirección https://sede.ull.es/validacion/		
Identificador del documento:	969870	Código de verificación: 8KFVZkZp
Firmado por:	MARINA RAMÓN PÉREZ UNIVERSIDAD DE LA LAGUNA	Fecha: 28/06/2017 21:15:24
	ANGEL MANUEL BONGIOVANNI PEREZ UNIVERSIDAD DE LA LAGUNA	29/06/2017 09:30:15
	JORGE CEPA NOGUE UNIVERSIDAD DE LA LAGUNA	29/06/2017 09:33:05
	ANA MARIA PEREZ GARCIA UNIVERSIDAD DE LA LAGUNA	29/06/2017 11:12:35
	ERNESTO PEREDA DE PABLO UNIVERSIDAD DE LA LAGUNA	04/07/2017 18:28:07



Este documento incorpora firma electrónica, y es copia auténtica de un documento electrónico archivado por la ULL según la Ley 39/2015. <i>Su autenticidad puede ser contrastada en la siguiente dirección https://sede.ull.es/validacion/</i>		
Identificador del documento:	969870	Código de verificación:
Firmado por:	MARINA RAMÓN PÉREZ UNIVERSIDAD DE LA LAGUNA	Fecha: 28/06/2017 21:15:24
	ANGEL MANUEL BONGIOVANNI PEREZ UNIVERSIDAD DE LA LAGUNA	29/06/2017 09:30:15
	JORGE CEPA NOGUE UNIVERSIDAD DE LA LAGUNA	29/06/2017 09:33:05
	ANA MARIA PEREZ GARCIA UNIVERSIDAD DE LA LAGUNA	29/06/2017 11:12:35
	ERNESTO PEREDA DE PABLO UNIVERSIDAD DE LA LAGUNA	04/07/2017 18:28:07

3

DATA REDUCTION AND CALIBRATIONS

The reduction of the data from OTELO survey is explained in this Chapter. This process involves a bias correction, the removal of cosmic rays, the trimming and alignment of the images, a flat-field correction, the removal of sky rings and the defringing procedure. The astrometry, as well as the flux and wavelength calibrations, are also described. Finally, the construction of OTELO's catalogue, which includes the extraction of the sources' photometry and the composition of their pseudo-spectra is explained.

As explained in Chapter 2, images from tunable filters have certain characteristics that require special treatment when it comes to their reduction and calibration. In the case of OTELO's data, the OSIRIS Offline Pipeline Software (OOPS¹) was not used since it does not include one of the most important steps of the data reduction, the removal of cosmic rays. Instead, all the steps in the reduction of the data were completed using standard IRAF² (Image Reduction and Analysis Facility) routines, along with the IRAF package TFRed³. TFRed was originally designed by H. Jones for the reduction of extragalactic fields images from TFs, and was later modified by A. Bongiovanni in order to adapt it to OSIRIS images. The reduction of OTELO data implied numerous iterations and the development of new IRAF and IDL⁴ routines by the work team to tackle some of the issues that arised in the process, in particular the sky rings subtraction (see section 3.1.3).

3.1 Data reduction

3.1.1 First steps

The first steps in the reduction of OTELO's data included a bias correction, the removal of cosmic rays and the trimming of the images. The bias correction is required in order to remove the zero-level of counts that each of the pixels of the CCDs have. These counts are introduced to ensure the generation of electric current when the images are taken, and must be subtracted individually. To achieve this correction, 'zero-exposure'

¹Available for download at the GTC OSIRIS' blog.

²IRAF is distributed by the National Optical Astronomy Observatory, which is operated by the Association of Universities for Research in Astronomy (AURA) under a cooperative agreement with the National Science Foundation.

³See Jones et al. (2001).

⁴Interactive Data Language.

Este documento incorpora firma electrónica, y es copia auténtica de un documento electrónico archivado por la ULL según la Ley 39/2015.
Su autenticidad puede ser contrastada en la siguiente dirección <https://sede.ull.es/validacion/>

Identificador del documento:	969870	Código de verificación:	8KFVZkZp
Firmado por:	MARINA RAMÓN PÉREZ UNIVERSIDAD DE LA LAGUNA	Fecha:	28/06/2017 21:15:24
	ANGEL MANUEL BONGIOVANNI PEREZ UNIVERSIDAD DE LA LAGUNA		29/06/2017 09:30:15
	JORGE CEPA NOGUE UNIVERSIDAD DE LA LAGUNA		29/06/2017 09:33:05
	ANA MARIA PEREZ GARCIA UNIVERSIDAD DE LA LAGUNA		29/06/2017 11:12:35
	ERNESTO PEREDA DE PABLO UNIVERSIDAD DE LA LAGUNA		04/07/2017 18:28:07

images are taken when no light reaches the detector. Additionally, a few initial columns with the values of a bias along the readout direction are added to each science image by the detector controller electronics. This is called the *overscan* region. As long as the bias images do not show any spatial structure, it is preferable to subtract the overscan to each image since this correction adds less noise. Moreover, the overscan value is acquired at the same time as the scientific image; therefore, possible variations of the bias level during the night (due to fluctuations in temperature, for instance) can be taken into account. In our case, we tried a combined approach so as to consider both the spatial variations across the CCD and the intrinsic variations during the night. We first subtracted a 9-order Legendre polynomial fit of the overscan using IRAF's task `ccdproc`. Then, we mean-combined ~ 10 bias images without overscan and subtracted the result to the science images using `imarith` task.

The next step in the reduction of the data was the elimination of cosmic rays. Cosmic rays are highly-charged particles, such as protons, electrons or atomic nuclei, that bombard the Earth from outer space. They cause the appearance of random traces over the astronomical images which need to be removed. In order to do so, the Laplacian Cosmic Ray Identification algorithm by van Dokkum (2001) was used. This IRAF-based task employs a Laplacian algorithm to identify and remove the cosmic rays over individual astronomical images, without the need of using several exposures combined. This is especially useful in our case, since the combination of the images with different dithering in a scan occurs only at the end of the reduction process given the wavelength dependence across the field of view described in Chapter 2. The algorithm identifies cosmic-rays of different shapes and sizes based on the sharpness of their edges, and is particularly helpful in distinguishing them from poorly sampled point sources. After trying different numbers of iterations of the Laplacian algorithm, an optimal number of 4 was finally chosen in order to remove the majority of the cosmic rays traces while minimising the invested time. An example of an image before and after this reduction step, as well as an image of the cosmic-rays that have been removed with the algorithm, can be seen in Figure 3.1.

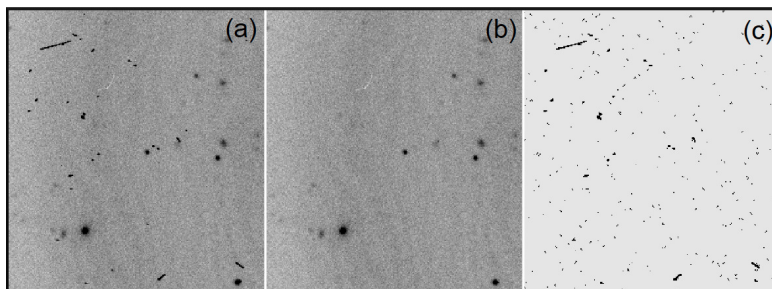


Figure 3.1: Example of an image before (a) and after (b) the removal of cosmic rays (central wavelength: 9280Å, CCD1). The ratio of both images, showing all the cosmic-rays that have been removed, is displayed in frame (c). Four iterations of the Laplacian algorithm by van Dokkum (2001) were required.

The images were then trimmed in order to eliminate the vignetted zones around the borders, specially in the left edge of CCD1, and to make sure that no contamination with other interference orders was introduced. The trimming section was [300:1046, 200:1970] for CCD1 and [26:1006, 200:1970] for CCD2, resulting in 747×1771 and 981×1771 pixels images, respectively. The resulting unvignetted field of $\sim 7.5 \times 7.4$ arcmin can be seen in Fig. 3.9.

Este documento incorpora firma electrónica, y es copia auténtica de un documento electrónico archivado por la ULL según la Ley 39/2015.
Su autenticidad puede ser contrastada en la siguiente dirección <https://sede.ull.es/validacion/>

Identificador del documento: 969870	Código de verificación: 8KFVZkZp
Firmado por: MARINA RAMÓN PÉREZ UNIVERSIDAD DE LA LAGUNA	Fecha: 28/06/2017 21:15:24
ANGEL MANUEL BONGIOVANNI PEREZ UNIVERSIDAD DE LA LAGUNA	29/06/2017 09:30:15
JORGE CEPA NOGUE UNIVERSIDAD DE LA LAGUNA	29/06/2017 09:33:05
ANA MARIA PEREZ GARCIA UNIVERSIDAD DE LA LAGUNA	29/06/2017 11:12:35
ERNESTO PEREDA DE PABLO UNIVERSIDAD DE LA LAGUNA	04/07/2017 18:28:07

3.1.2 Flat-field correction and bad-pixel fixing

A flat-field correction is required in every astronomical image in order to consider the different response of each CCD pixel to light, which can be due to intrinsic variations in sensitivity or to external factors. To do so, science images are divided by normalised flat images which account for the pixels response under an homogeneous illumination. Those flat images are usually obtained by pointing the telescope towards an uniformly illuminated field, such as the background sky or the telescope dome itself. In this work, we built for each image a super-flat which took into account both the high-frequency (small scale) fluctuations and the low-frequency (large-scale) ones.

In conventional TF data reduction, flat-fielding is not a straightforward step because sensitivity variations across the field depend radially on wavelength for a given tuning and, in the particular case of this survey, a non-negligible fringing component is present in all frames. Hence, for each mosaic component, observing epoch and TF tuning we combined different bias-reduced, defringed and bad-pixel fixed TF dome flats. These were then corrected by illumination in order to remove the low-frequency variations using a mode-scaled OS sky (twilight) flat. In this way, we obtained the high-frequency flats which account for the pixel-to-pixel fluctuations in each image.

On the other hand, low-frequency fluctuations maps were acquired from a median combination of the airglow emission in the 6 science images corresponding to a scan, which were obtained from a 2σ object masking above the median background level. Such fluctuations were measured in concentric radii each 50 pixel around the optical center. These values were normalised and then used to generate a low-order surface, which constitutes an analogous of a large-scale night sky flat. This large-scale map and the previous small one were combined in a super-flat used for reducing individual mosaic components. The mean background homogeneity of science frames after applying this procedure was better than 3.4%.

Bad pixel masks for each observing epoch were then obtained using a set of reduced OS night sky flats, following the methodology by ESO⁵. A number of flats with low counts (~ 6000 - 12000) were median combined, and the same was done for high counts flats (~ 33000). The normalised ratio of such low to high intensity level flats was used as a bad-pixel mask. Using IRAF's `ccdmask` task, we identified those pixels for which this ratio was greater than 15%. Bad pixels in the images were finally corrected using the IRAF `fixpix` task, which makes an interpolation of neighboring pixels.

3.1.3 Sky rings removal

As explained in Chapter 2, the field observed by a TF is not strictly monochromatic but rather shows a radial gradient in wavelength due to the differences in the incident angle of light. For this reason, the further an object falls from the optical center, the bluest its observed wavelength. As a consequence, airglow emission illuminating the exit pupil of the telescope is seen in the images as bright concentric rings around the projection of the TF's optical axis. These are specially intense in the near infrared, as can be seen in the first image of Figure 3.3. Although OTELO survey sampled a spectral region between Meinel bands, airglow OH emission bands, even with minor strengths, severely affect the observations with large exposure times. Unlike the previous step (flat-field correction), sky rings represent an additive contribution to the images, since emission lines from the atmosphere appear superimposed to the observed field. Therefore, their removal is crucial in order to ensure the photometric integrity of all sources, specially the faintest ones.

The Nod & Shuffle technique (Glazebrook & Bland-Hawthorn 2001), which consists in nodding the telescope during the observation between targets and sky, was discarded from the very beginning, as it would

⁵See <https://www.eso.org/sci/facilities/lasilla/instruments/efosc/inst/BADPIXMASK.html>.

Este documento incorpora firma electrónica, y es copia auténtica de un documento electrónico archivado por la ULL según la Ley 39/2015. Su autenticidad puede ser contrastada en la siguiente dirección https://sede.ull.es/validacion/		
Identificador del documento:	Código de verificación:	
Firmado por: MARINA RAMÓN PÉREZ UNIVERSIDAD DE LA LAGUNA	969870	Código de verificación: 8KFVZkZp Fecha: 28/06/2017 21:15:24
ANGEL MANUEL BONGIOVANNI PÉREZ UNIVERSIDAD DE LA LAGUNA		29/06/2017 09:30:15
JORGE CEPA NOGUE UNIVERSIDAD DE LA LAGUNA		29/06/2017 09:33:05
ANA MARIA PÉREZ GARCIA UNIVERSIDAD DE LA LAGUNA		29/06/2017 11:12:35
ERNESTO PEREDA DE PABLO UNIVERSIDAD DE LA LAGUNA		04/07/2017 18:28:07

translate in a reduction of the field of view and in an increase of the observation time. For that reason, the sky rings problem was tackled during the reduction process, following different approaches. The first one was to use the IRAF task `tringSub`, designed by Jones et al. (2001) as part of its TFRed package. It consists in subtracting an optionally smoothed background map from the science image, which is previously created by median filtering regularly shifted (only a few pixels) copies of the individual image to be reduced. This technique leaves little or no night-sky residual, according to the authors, and is specially effective when the objects of interest are much smaller than the ring structure, as in the case of OTELO survey.

The second approach follows the philosophy of the Maryland-Magellan TF Data Reduction Pipeline developed by Veilleux et al. (2010). They first perform a filtering of sources and cosmic rays, and then model the sky background by obtaining an azimuthally averaged sky spectrum which is swept around the known position of the optical axis. A similar methodology is followed by Weinzirl et al. (2015), who describe a technique based on an image transformation to polar coordinates with the purpose of subtracting the airglow emission, this time as straight patterns, and then applying an inverse transformation to restore the image's geometry. Although both techniques are qualitatively similar, we have not tested the performance of the latter in order to avoid flux conservation issues in the projection/reprojection processes.

For OTELO's images, we tried to combine the advantages of the cited algorithms by performing the sky spectrum subtraction on each individual image with an automatic, two-step approach. We first use the `tringSub` task described above to obtain a background model resulting from a median filtering of 8 offsetted (~ 10 pixels) copies of the input image (see panel (b) in Fig. 3.2). This model is subtracted to the science image in order to get a first cleaned image, useful only for source mapping. Then, we use the IRAF `objmask` task to create an object mask for each individual image by flagging positive features 2σ above the residual background. This initial guess of a background-subtracted image is also used to create a fringing model. The original image is then defringed and their sources are replaced by neighbouring background values using the object mask previously created (see panel (c) in Fig. 3.2). As can be seen in the black circles in panels (b) and (c) of Fig. 3.2, both the sky model made with `tringSub` and the one obtained after the object's masking show residuals in the zones where sources have been masked. That is why a few more steps, using a specifically designed program that we call `ringsub`, are necessary in order to obtain a realistic sky model.

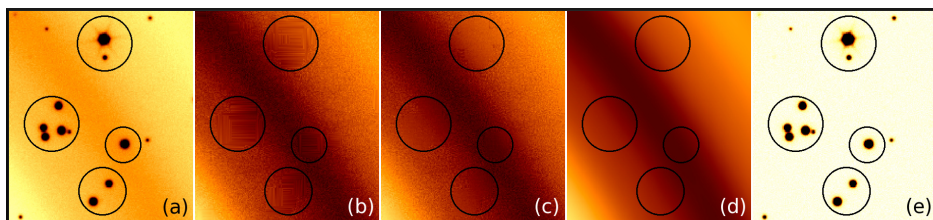


Figure 3.2: Close-up of an OTELO's image before (a) and after (e) the sky rings subtraction process and some of its intermediate steps. A sky ring crosses the image from the upper left corner to the lower right one. From left to right: (a) original image at 9130Å from CCD2 with 500 fake stars added, zoomed in into the upper right corner, (b) first sky model as obtained with `tringSub`, used to create an object mask for the original image, (c) sky model obtained from masking the objects of the science image, (d) final sky model obtained with our program `ringsub` and (e) final image after the sky subtraction. The black circles indicate regions with sources in the original image. Note how in panels (b) and (c) a residual appears in those regions, as a result of the interpolation made to mask the objects. However, our sky model in panel (d) reproduces correctly the sky background while avoiding this problem.

After that, a series of replicas of the resulting (c) image are created by rotating it around the optical centre at optimised angles. Such angles result from an equilibrium between maximum pixel sampling and the

maintenance of the sky ring ellipticity (<0.3% in our case⁶) below a pixel in the radial direction. A median combination of these replicas before trimming to the original image size results in a sky background base image with no interpolation residuals, as those have been blurred with the combination of the rotated images. The final background model is obtained by fitting a high-order Legendre polynomial to this base image, yielding an smoothed and realistic model of the original image sky (see panel (d) in Fig. 3.2). The fitting parameters are chosen for each image depending on the number of rings. The procedure ends when this final mathematical sky model is subtracted to the original science image (see the result in panel (e) of Fig. 3.2).

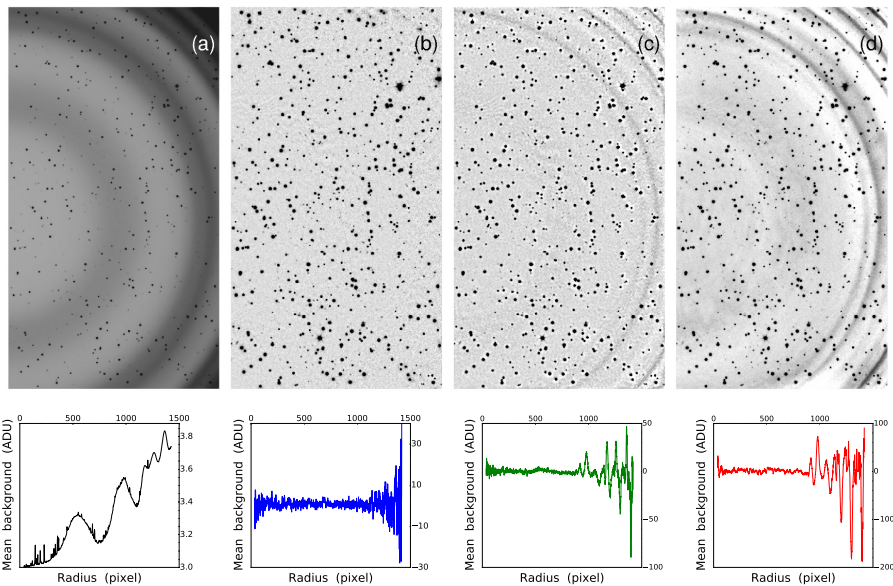


Figure 3.3: An example of the different sky rings subtraction tests described in the text. Panel (a) shows one selected raw image of CCD2 corresponding to a central wavelength of 9130Å, with 500 artificial stars added. Rings patterns produced by airglow bands are evident. Panels (b), (c) and (d) show sky-subtracted and defringed images by using, respectively, our `ringsub` algorithm, the `tringSub` one, and the azimuthally averaged approach. Below each panel the mean radial spectrum (1 pixel sampling) of the image background or residual is shown.

The whole procedure, named `ringsub`, was written in a single parametric IRAF script with null user interaction⁷. We tested `ringsub` and compared its performance with the `tringSub` and the azimuthally averaged algorithms. We selected science frames with large sky background fluctuations (around $\lambda_0 = 9140\text{\AA}$) and used the IRAF `starlist` task to create catalogues of 500 artificial stars uniformly distributed in position and brightness, according to the instrumental flux range of the tested images. These stars were added on the images using the IRAF `mkobject` task and their fluxes were recovered using the software SExtractor (Bertin & Arnouts 1996) in standard mode after subtracting the sky background. Figure 3.3 shows an example of an OTELO image (CCD2) before sky subtraction and with the fake stars already added. Additional panels show the result of sky subtraction and the mean background level in each case. The use of `ringsub` produces the

⁶J. Cepa 2017, private communication.

⁷It is available by request to the authors.

smallest background residuals. Moreover, when we compare the reference-to-measured mock star flux ratio for each sky subtraction approach, we see that the algorithm adopted in this work yields the nearest results to the unity with the smallest standard deviation (see Table 3.1 and Fig. 3.4).

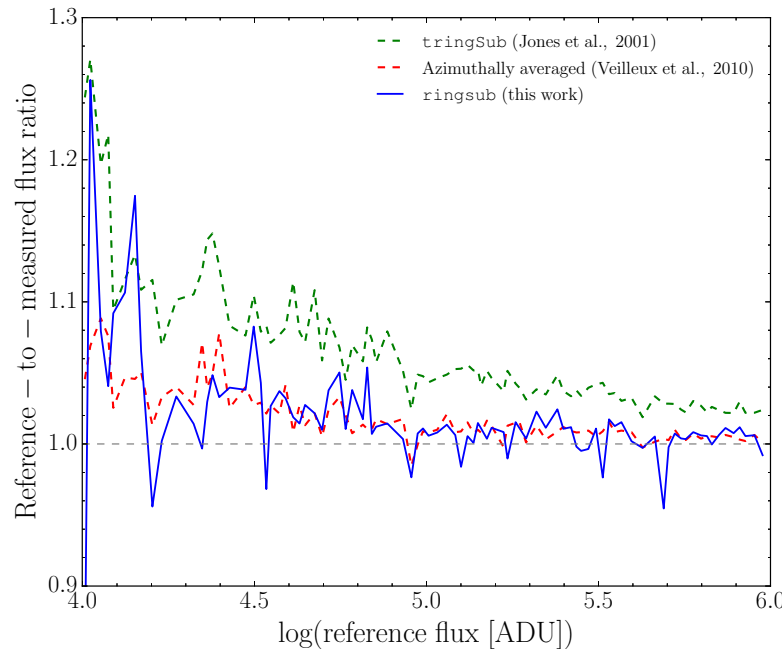


Figure 3.4: Comparison of the flux recovery (reference-to-measured flux ratio of 500 artificial stars added to a raw image) after the sky subtraction step using different techniques: the `ringsub` procedure adopted in this work (thick blue line), the `tringSub` task (dashed green line), and the azimuthally averaged spectrum approach (dashed red line). The former and the latter show a similar flux recovery behaviour, whereas the `tringSub` approach leads to a flux overestimation of $\sim 5\%$ (see Table 3.1 for statistics).

Table 3.1: Statistics of the flux recovery (reference-to-measured flux ratio of 500 artificial stars added to a raw image) after the sky subtraction step using different techniques (see Fig. 3.4 for a visual representation). The algorithm adopted in this work, `ringsub`, yields a mean ratio similar to the azimuthally averaged algorithm but with smaller standard deviations.

Algorithm	Mean ratio	σ of ratio	minimum ratio	maximum ratio
Azimuthally averaged	1.0177	0.0434	0.8350	1.2562
<code>tringSub</code>	1.0657	0.04807	1.0188	1.2707
<code>ringsub</code> (this work)	1.0182	0.0192	0.9847	1.0884

Este documento incorpora firma electrónica, y es copia auténtica de un documento electrónico archivado por la ULL según la Ley 39/2015.
Su autenticidad puede ser contrastada en la siguiente dirección <https://sede.ull.es/validacion/>

Identificador del documento: 969870 Código de verificación: 8KFVZkZp

Firmado por: MARINA RAMÓN PÉREZ UNIVERSIDAD DE LA LAGUNA	Fecha: 28/06/2017 21:15:24
ANGEL MANUEL BONGIOVANNI PEREZ UNIVERSIDAD DE LA LAGUNA	29/06/2017 09:30:15
JORGE CEPA NOGUE UNIVERSIDAD DE LA LAGUNA	29/06/2017 09:33:05
ANA MARIA PEREZ GARCIA UNIVERSIDAD DE LA LAGUNA	29/06/2017 11:12:35
ERNESTO PEREDA DE PABLO UNIVERSIDAD DE LA LAGUNA	04/07/2017 18:28:07

3.1.4 Defringing

The last step in the reduction process was the defringing. As can be seen in Figure 3.5, a fringe pattern is visible on OTELO's images and needs to be removed. This phenomenon appears as a consequence of the multiple reflections of light between the parallel plates which form the CCD surfaces. The resulting phase differences cause wave interferences (both constructive and destructive) generating a fringing pattern. As the detector is not perfectly flat, this pattern can be highly irregular. The fringing phenomenon appears when the entering light is nearly monochromatic and is more relevant as the wavelength approaches the CCD thickness. For these reasons, this effect is significant whenever the field is illuminated with intense, quasi-monochromatic emission lines such as the sky lines. Otherwise, constructive and destructive interferences tend to mutually cancel. This phenomenon is particularly relevant in the red, and it does not depend on the type of filter used (narrow or broad).

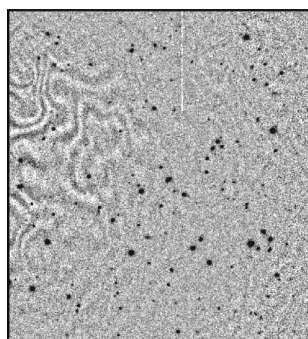


Figure 3.5: Example of fringe pattern in one of OTELO's images. The image has been zoomed and smoothed with a gaussian-kernel and the colours have been inverted for a better visualisation of the fringing.

Just like sky rings, the contribution of interference fringes is additive and must be subtracted using a master fringe template which reflects the fringe pattern in each science image. This master fringe template was obtained by carefully median-combining object-masked images from the same OB having different dithering. The resulting image is a statistically zero counts level model which represents the fringe pattern. The defringing was performed by subtracting to each science image its corresponding master fringe template, using the IRAF `rmfringe` task in two iterations.

3.2 Astrometry

Astrometry calibration is the process by which precise astronomical coordinates are assigned to each point of an image, and represents a fundamental step of the reduction process. A precise astrometry is essential not only to reference targets under a celestial coordinate system which will later enable the cross-matching of different catalogues, but also to place all the individual science images in a common spatial frame that will allow a proper mosaic assembly and coaddition with small internal errors (accuracies of a few tenths of pixel, in the case of OTELO). Moreover, the wavelength calibration, detailed in section 3.3.4, is highly dependent on the accuracy of the astrometry, as it is based on the calculus of radial distances to the optical center. None of OTELO's images from the 2010 and 2011 campaigns had WCS headers and for the rest of them they were only approximate, hence it was necessary to obtain astrometric solutions for each individual image.

Este documento incorpora firma electrónica, y es copia auténtica de un documento electrónico archivado por la ULL según la Ley 39/2015. <i>Su autenticidad puede ser contrastada en la siguiente dirección https://sede.ull.es/validacion/</i>		
Identificador del documento:	969870	Código de verificación: 8KFVZkZp
Firmado por:	MARINA RAMÓN PÉREZ UNIVERSIDAD DE LA LAGUNA	Fecha: 28/06/2017 21:15:24
	ANGEL MANUEL BONGIOVANNI PEREZ UNIVERSIDAD DE LA LAGUNA	29/06/2017 09:30:15
	JORGE CEPA NOGUE UNIVERSIDAD DE LA LAGUNA	29/06/2017 09:33:05
	ANA MARIA PEREZ GARCIA UNIVERSIDAD DE LA LAGUNA	29/06/2017 11:12:35
	ERNESTO PEREDA DE PABLO UNIVERSIDAD DE LA LAGUNA	04/07/2017 18:28:07

Astrometry is usually carried out in various steps. First, objects are detected in the images to calibrate using an automatic task or software, such as `daofind` or `starfind` from IRAF, or SExtractor. Then, a catalogue of reference from the same field and with good accuracy is cross-matched with the detected sources, using the IRAF `ccxymatch` task. Based on those matchings, a last task is used, `ccmap`, in order to find the astrometric solution that will provide celestial coordinates to the whole image. Finally, the assembly and composition of mosaics is performed.

In our case, we used a reference catalogue based on the Canada-France-Hawaii Telescope Legacy Survey (CFHTLS) Deep Field 3. We searched for the deep fields with 25% best seeing images (D3-25) having z -band data and whose internal root mean square (RMS) of astrometric errors were 0.075 and 0.074 arcsec in equatorial coordinates (α, δ). As for their external errors, the D3-25 catalogue had an accuracy of 0.23 arcsec in each coordinate when compared to the 2MASS⁸ astrometric positions. Based on that, we designed a custom catalogue by selecting all non-saturated, point-like sources (`CLASS_STAR > 0.94`) up to magnitude AB = 23 (that is, around the provided limiting magnitude of point-like sources with a $\text{SNR} \gtrsim 10$ in science exposures). This reference catalogue was composed of 892 entries with a resulting maximal RMS internal error in position of 0.03 arcsec.

A list of sources from each individual OTEL0's mosaic component was then obtained using SExtractor, after trying different source extraction softwares such as the IRAF tasks `daofind` and `starfind`. Although both `daofind` and SExtractor yield satisfactory results regarding the object's centroids determination (see Annunziatella et al. 2013), we chose the latter for consistency with the rest of our work (specially section 3.3). The reference catalogue was then cross-matched to this list of sources by using the `ccxymatch` task. An equal number of astrometric solutions was obtained with the use of the `ccmap` task by adopting a fourth-order polynomial geometry and the non-standard TNX⁹ WCS, which has proven to be the optimal projection for astrometric reduction of OSIRIS instrument images¹⁰. The internal mean accuracy of the individual WCS solutions obtained (RMS residuals) was of 0.043 ± 0.007 arcsec in the space of standard coordinates (ξ, η). Taking into account in quadrature the upper error limit of the reference catalogue, internal deviations of WCS are below 0.068 arcsec in both coordinates. This translates to ~ 0.27 pixels in plate scale. Therefore, image registration and coaddition are self-consistent within this sub-pixel regime.

Individual components of each mosaic were then warped (distorted) and referenced to each other using the IRAF `mscimage` task, according to the corresponding higher order polynomial coefficients of the astrometric solution and conserving the integrated flux per unit area. We also created weight maps of the images, expressed in units of relative inverse variance per pixel. These weight maps influence the determination of flux errors and prevent false-positive detections. Moreover, 20 out of the 216 individual images of OTEL0 were affected by satellite trails, which were represented by zero weight traces in those maps. Finally, based on the linear part of the WCS, each mosaic and its corresponding weight map was assembled with sub-pixel accuracy using the SWarp application (Bertin et al. 2002).

3.3 Construction of OTEL0's catalogue

Once the images are reduced and astrometrically calibrated, the construction of OTEL0's catalogue is the next step. This implies the obtention of a deep image in the first place, for the sources to be detected with an

⁸The Two Micron All Sky Survey (Skrutskie et al. 1995).

⁹See <http://iraf.noao.edu/projects/ccdmosaic/ttx.html> for more details.

¹⁰OSIRIS's team provided the astrometric solution to GRANTECAN in the framework of the instrument's scientific commissioning.

Este documento incorpora firma electrónica, y es copia auténtica de un documento electrónico archivado por la ULL según la Ley 39/2015. Su autenticidad puede ser contrastada en la siguiente dirección https://sede.ull.es/validacion/		
Identificador del documento:	Código de verificación:	
Firmado por: MARINA RAMÓN PÉREZ UNIVERSIDAD DE LA LAGUNA	969870	Código de verificación: 8KFVZkZp Fecha: 28/06/2017 21:15:24
ANGEL MANUEL BONGIOVANNI PÉREZ UNIVERSIDAD DE LA LAGUNA		29/06/2017 09:30:15
JORGE CEPA NOGUE UNIVERSIDAD DE LA LAGUNA		29/06/2017 09:33:05
ANA MARIA PÉREZ GARCIA UNIVERSIDAD DE LA LAGUNA		29/06/2017 11:12:35
ERNESTO PEREDA DE PABLO UNIVERSIDAD DE LA LAGUNA		04/07/2017 18:28:07

optimised signal-to-noise ratio. Then, the extraction of sources and the measurement of their fluxes, properly calibrated, is performed. Finally, a pseudo-spectrum is composed for each source in the field.

3.3.1 OTELO's deep image

The use of a deep image, resulting from the coaddition of all the science images in the tomography, is crucial because it allows to integrate in a single image all the fluxes of the different slices, thus reaching the maximum possible depth. This image will serve as a detection image, allowing the discovery of faint continuum sources that would otherwise be missed in the individual images¹¹.

The coaddition of images can be done in several ways, using, for instance, Lucky Imaging, Fourier-based methods or pixelwise statistics (see Homrighausen et al. 2011 for a recent review of these techniques). In our case, we discarded the image convolution to the worst seeing prior to coaddition, as it alters the information contained in the image, resulting in a PSF degradation of almost the whole input image set, the amplification of the background noise in high frequencies and the creation of correlated artifacts. Instead, we proceeded as follows. We first combined the most dithered apart images in a scan¹² (up to 5 out of 6) with the best mean FWHM, to ensure the rejection of diametric ghosts. In this way, nearly 83% of all the science frames were coadded in their corresponding slices. The remaining ones did not contribute to OTELO's deep image, but were naturally taken into account in the flux measurements described in section 3.3.2. The combination was done using the clipped-mean algorithm described in Gruen et al. (2014) and implemented in the SWarp software (Bertin et al. 2002), specifically designed to reject artifacts present in individual images contributing to a stack. The PSF differences of the selected images in each slice stacking were below the requirements established by the authors ($\sim 10\%$). The main configuration parameters adopted to run SWarp are shown in Table 3.2. We compared the results obtained with this procedure with the ones using the median combination of individual frames. Although the flux recovery was similar in both cases, the median combination approach was not so efficient in discarding diametric ghosts of extended bright sources as the clipped-mean one, due to the discrete number of individual frames available for each slice.

Table 3.2: Main configuration parameters of the SWarp software, used to obtain the 36 slices contributing to OTELO's deep image.

Parameter	Value
WEIGHT_TYPE	MAP_WEIGHT
COMBINE_TYPE	CLIPPED
RESAMPLE	Y
RESAMPLE_TYPE	LANCZOS3
SUBTRACT_BACK	N

The resulting 36 stacks were finally averaged using SWarp again in order to obtain OTELO's deep image, which is shown in Fig. 3.6. All the coaddition products included their corresponding weight maps. In particular, we used the local variance in the weight map of OTELO's deep image to define the highest sensitivity survey

¹¹Unfortunately, it also means that sources whose continuum is not detected but the emission line is, may be overlooked. These kind of sources will be detected in future works using other techniques.

¹²Although images with different dithering have slightly different central observation wavelengths, this is not relevant when building OTELO's deep image, as the aim here is to obtain the maximum possible depth for the subsequent detection of sources.

Identificador del documento: 969870	Código de verificación: 8KFVZkZp
Firmado por: MARINA RAMÓN PÉREZ UNIVERSIDAD DE LA LAGUNA	Fecha: 28/06/2017 21:15:24
ANGEL MANUEL BONGIOVANNI PÉREZ UNIVERSIDAD DE LA LAGUNA	29/06/2017 09:30:15
JORGE CEPA NOGUE UNIVERSIDAD DE LA LAGUNA	29/06/2017 09:33:05
ANA MARIA PÉREZ GARCIA UNIVERSIDAD DE LA LAGUNA	29/06/2017 11:12:35
ERNESTO PEREDA DE PABLO UNIVERSIDAD DE LA LAGUNA	04/07/2017 18:28:07

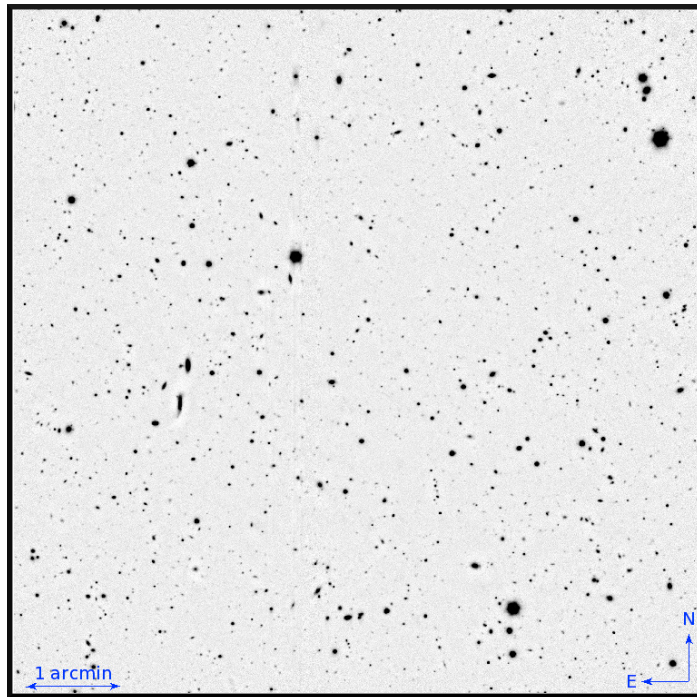


Figure 3.6: OTELO's deep image, obtained by combining the most dithered apart images in a scan and then averaging the 36 resulting stacks. The effective field of view is $\sim 7.5 \times 7.4 \text{ arcmin}^2$.

area (i.e. the region of $\sim 7.5 \times 7.4 \text{ arcmin}^2$, or $1754 \times 1734 \text{ pixel}^2$, represented in Figures 3.6 and 3.9). After this, and as a requirement for the following source extraction procedure, all the science frames were trimmed to the same size of OTELO's deep image.

3.3.2 Extraction and measurement of the sources

The extraction of sources was performed as follows: first, sources were detected on OTELO's deep image and then their fluxes were measured over the 36 individual science frames. All of this was done using the software SExtractor in dual mode, which is an easy and efficient detection tool, specially when it comes to faint, extended sources (see Masias et al. 2012 for a recent review of source detection techniques). The threshold level and final detection (segmentation) map of OTELO's deep image were then translated to each science frame to be analysed. We chose the most appropriate configuration parameters for SExtractor, considering the peculiarities of the survey. These are shown in Table 3.3 and justified in the next paragraphs.

Following the astrometry analysis (see section 3.2) and the quality control of OTELO's deep image, the plate scale (PIXEL_SCALE) was fixed to 0.254 arcsec/pixel and the mean FWHM (SEEING_FWHM) to 0.8 arcsec.

The adopted detection and analysis thresholds can be defined as a multiple of the local background variance (σ). High values of those parameters imply missing the faintest sources, while low ones will pollute the final catalogue by increasing the probability of false-positive detections, despite the previous steps taken to avoid

Este documento incorpora firma electrónica, y es copia auténtica de un documento electrónico archivado por la ULL según la Ley 39/2015.
Su autenticidad puede ser contrastada en la siguiente dirección <https://sede.ull.es/validacion/>

Identificador del documento:	969870	Código de verificación:	8KFVZkZp
Firmado por:	MARINA RAMÓN PÉREZ UNIVERSIDAD DE LA LAGUNA	Fecha:	28/06/2017 21:15:24
	ANGEL MANUEL BONGIOVANNI PEREZ UNIVERSIDAD DE LA LAGUNA		29/06/2017 09:30:15
	JORGE CEPA NOGUE UNIVERSIDAD DE LA LAGUNA		29/06/2017 09:33:05
	ANA MARIA PEREZ GARCIA UNIVERSIDAD DE LA LAGUNA		29/06/2017 11:12:35
	ERNESTO PEREDA DE PABLO UNIVERSIDAD DE LA LAGUNA		04/07/2017 18:28:07

Table 3.3: Main configuration parameters of the SExtractor software, used in dual mode for the instrumental flux measurements of sources using OTELO's deep image as the detection image.

Parameter	Value
DETECT_MINAREA	4 pixels
THRESH_TYPE	RELATIVE
DETECT_THRESH (=ANALYSIS_THRESH)	0.73σ
FILTER_NAME	tophat_3.0_3x3.conv
DEBLEND_NTHRESH	64 branches
DEBLEND_MINCONT	0.001 fraction
CLEAN	Y
CLEAN_PARAM	1.0
WEIGHT_TYPE	MAP_WEIGHT
PIXEL_SCALE	0.254 arcsec/pixel
MAG_ZEROPOINT	30.504
BACK_TYPE	LOCAL
BACK_SIZE	64×64 pixels
BACK_FILTERSIZE	8 pixels
SEEING_FWHM	0.80 arcsec

this problem, such as the use of bad-pixel masks, the adoption of the clipped-mean algorithm for slice stacking or the construction of weight maps (see sections 3.1.2, 3.3.1 and 3.2, respectively). It is possible to obtain a quick estimation of false source count statistics using SExtractor with the default parameters on OTELO's deep image and its inverted image ($\text{OTELO}_{\text{deep}} \times -1$). However, in our case, the likelihood of a source will be later quantified on the basis of the analysis of its pseudo-spectrum and its cross-correlation to other ancillary data (see Chapters 4 and 5). Also, the faintest sources without counterparts can be analyzed further on. Thus, we lowered the detection threshold to the statistical level required to recover sources whose pseudo-spectra contain at least 2 consecutive slices with integrated flux 3σ above the continuum of the pseudo-spectrum (see Chapter 5 for a more detailed explanation on the selection of emitting sources).

With this hypothesis in mind, we performed the following analysis in order to obtain the detection/analysis threshold value. We selected three sky regions of 30×30 pixels in OTELO's deep image and trimmed them from the 36 slices used to create OTELO's deep image, thus resulting in 3×36 stamps. Then, for each set of stamps, we added artificial point-like sources (as described in section 3.1.3) with $\text{SNR} \simeq 3$ on selected pairs of stamps, leaving the remaining stamps of each collection intact. The flux of each artificial source was carefully scaled to 3σ above the selected slice cutout background level. This procedure was repeated six times for each collection. After this, the 36 cutouts of each collection and execution were averaged in the same way as OTELO's deep image (see section 3.3.1). We then used SExtractor over those averaged images with a detection/analysis threshold varying in successive steps of 0.1σ (σ being the standard deviation of the background in the averaged image) until the fluxes of the artificial sources were recovered. By linearly fitting the input SNR against the recovering thresholds, we finally obtained the detection/analysis threshold that exactly satisfies our initial hypothesis. The values found after this procedure are in agreement with the detection (= analysis) threshold adopted by Jones et al. (2002) and Galametz et al. (2013) for faint source extraction.

Este documento incorpora firma electrónica, y es copia auténtica de un documento electrónico archivado por la ULL según la Ley 39/2015.
Su autenticidad puede ser contrastada en la siguiente dirección <https://sede.ull.es/validacion/>

Identificador del documento: 969870	Código de verificación: 8KFVZkZp
Firmado por: MARINA RAMÓN PÉREZ UNIVERSIDAD DE LA LAGUNA	Fecha: 28/06/2017 21:15:24
ANGEL MANUEL BONGIOVANNI PÉREZ UNIVERSIDAD DE LA LAGUNA	29/06/2017 09:30:15
JORGE CEPA NOGUE UNIVERSIDAD DE LA LAGUNA	29/06/2017 09:33:05
ANA MARIA PEREZ GARCIA UNIVERSIDAD DE LA LAGUNA	29/06/2017 11:12:35
ERNESTO PEREDA DE PABLO UNIVERSIDAD DE LA LAGUNA	04/07/2017 18:28:07

From this procedure, we also bounded the minimum area above the threshold that a true detection should have. The SExtractor manual suggests setting the DETECT_MINAREA parameter to 1-5 pixels. Consistently, we fixed it to 4 pixels, which is equivalent to a circular area with radius $\sim 0.5 \times \text{SEEING_FWHM}$.

As for the deblending of sources, SExtractor splits hierarchically an object in smaller (child) ones depending on the count peaks and neighbouring fluctuations found on a raw detection. The deblending threshold (DEBLEND_NTHRESH) can be set as powers of 2 (the default value being 32) and establishes the allowed number of levels in this object's hierarchy. In addition, DEBLEND_MINCONT, the contrast parameter, defines the minimum flux ratio between peaks in order to consider them as different objects¹³. We finally adopted the deblending parameters used by Annunziatella et al. (2013) from their analysis of source extraction software after performing some tests on our data and verifying that the number of real detections was maximised in this way. We proceeded in the same way with the background estimation parameters (i.e. mesh gridding map and background smoothing factor), except that we leaned towards a local (rather than global) estimation of the background around a given detection, in order to take into account the small sky noise fluctuations on our images as a function of the radius to the optical centre. Image filtering was done by means of a “top-hat” function, which is optimised to detect extended, low surface brightness objects.

The instrumental fluxes measured on OTELLO’s deep image were directly converted to AB magnitudes. Using the effective gain and exposure time, as well as the estimation of the zero-point magnitude corresponding to the synthetic spectral response of OTELLO’s deep image, we obtained a MAG_ZEROPOINT of 30.504 mag.

Once the configuration parameters of SExtractor were obtained, the detection of sources and the measurement of their fluxes were performed. Instrumental Kron (AUTO), isophotal (ISO) and aperture (with APER: 2 and 3 arcsec in diameter) fluxes and their corresponding errors were measured in each of the 216 individual frames, apart from the source geometry (including the isophotal area, A_{ISO}) and the extraction flags. Flux measurement uncertainties were determined by means of the following expression:

$$\Delta F_{ADU} = \sqrt{A_{ISO, APER} \sigma^2 + F_{ADU}/g_{eff}} \quad (3.1)$$

where $A_{ISO, APER}$ are the isophotal or aperture areas, respectively, in pixels, σ is the source local background RMS, and g_{eff} is the effective gain in e⁻/ADU, depending on the measured image (OTELLO’s deep or individual frame). The fluxes and errors obtained in this way were converted to physical units by means of the subsequent flux calibration. Also, an effective wavelength of observation was assigned to each measured flux before generating the pseudo-spectra. Both the wavelength and flux calibrations are described in the next sections.

3.3.3 Determining the optical center

With the aim of calibrating the images in flux and wavelength (subsection 3.3.4), the coordinates of the optical center in each of the mosaics need to be known. OTELLO’s images can be divided in two different epochs for this purpose: OBs 1-21 (epoch 1) and OBs 22-108 (epoch 2). The reason is that OSIRIS’s camera and detectors were disassembled in order to fix the cryostat between OTELLO’s 21th and 22th observing block, which affected the optical center’s aforesaid location. Nevertheless, the estimation of the optical center coordinates was performed for each year of observation so as to check the consistency.

In order to do so, we made use of the spurious *ghosts* described in Chapter 2 that appear on the images as a consequence of the multiple reflections of light coming from the brightest objects in the field. By identifying

¹³See the SExtractor manual for more details.

Este documento incorpora firma electrónica, y es copia auténtica de un documento electrónico archivado por la ULL según la Ley 39/2015. Su autenticidad puede ser contrastada en la siguiente dirección https://sede.ull.es/validacion/		
Identificador del documento:	Código de verificación:	
Firmado por: MARINA RAMÓN PÉREZ UNIVERSIDAD DE LA LAGUNA	969870	Fecha: 28/06/2017 21:15:24
ANGEL MANUEL BONGIOVANNI PEREZ UNIVERSIDAD DE LA LAGUNA		29/06/2017 09:30:15
JORGE CEPA NOGUE UNIVERSIDAD DE LA LAGUNA		29/06/2017 09:33:05
ANA MARIA PÉREZ GARCIA UNIVERSIDAD DE LA LAGUNA		29/06/2017 11:12:35
ERNESTO PEREDA DE PABLO UNIVERSIDAD DE LA LAGUNA		04/07/2017 18:28:07

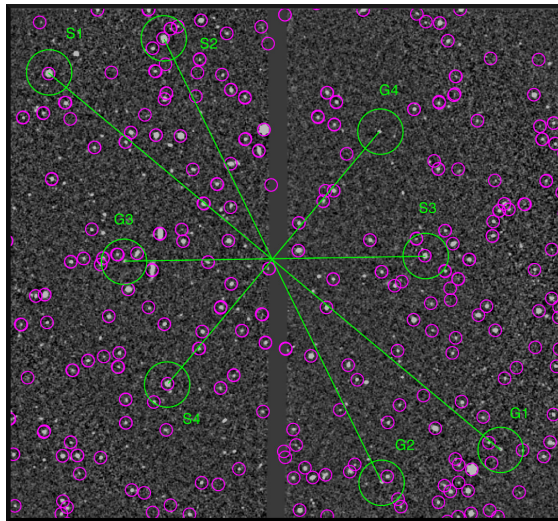


Figure 3.7: Example of OTELO's mosaic showing four bright sources ($S_1, S_2\dots$) and their corresponding ghosts ($G_1, G_2\dots$). Sources from the Sloan Digital Sky Survey (SDSS) catalogue are shown in magenta (see <http://classic.sdss.org/dr7/>). Ghosts (with an intensity of a small percentage that of the original source, see Jones et al. 2002) are seen in OTELO's image but do not correspond to any source in the SDSS catalogue. The union point of the four green lines (source-ghost) corresponds to the location of the optical center.

several bright sources and their corresponding ghosts, one can easily trace the location of the optical center as the union point of the different *source-ghost* lines, as Fig. 3.7 demonstrates. The optical center coordinates were derived from the calculation of the different straight lines equations with an error less than 0.1 pixel. Table 3.4 shows the optical center coordinates for each one of the epochs and for both the original and the trimmed images, with respect to CCD1.

Table 3.4: Optical center coordinates with an error < 0.10 pixel with respect to CCD1, for epoch 1 (OBs 1-21) and epoch 2 (OBs 22-108), and for both the original 2×2 binning images and the trimmed images.

	Original images	Trimmed images
Epoch 1	(1050.66, 979.56)	(751.65, 780.56)
Epoch 2	(1048.61, 979.71)	(749.61, 780.71)

The IRAF task `wcstran` was then used to convert those coordinates to equatorial ones using the astrometrical information of the image saved on its header. Finally, the trimmed mosaics were aligned using the deep image as a reference and the IRAF task `wregister`.

Este documento incorpora firma electrónica, y es copia auténtica de un documento electrónico archivado por la ULL según la Ley 39/2015. Su autenticidad puede ser contrastada en la siguiente dirección https://sede.ull.es/validacion/		
Identificador del documento: 969870		Código de verificación: 8KFVZkZp
Firmado por: MARINA RAMÓN PÉREZ UNIVERSIDAD DE LA LAGUNA	Fecha: 28/06/2017 21:15:24	
ANGEL MANUEL BONGIOVANNI PEREZ UNIVERSIDAD DE LA LAGUNA	29/06/2017 09:30:15	
JORGE CEPA NOGUE UNIVERSIDAD DE LA LAGUNA	29/06/2017 09:33:05	
ANA MARIA PEREZ GARCIA UNIVERSIDAD DE LA LAGUNA	29/06/2017 11:12:35	
ERNESTO PEREDA DE PABLO UNIVERSIDAD DE LA LAGUNA	04/07/2017 18:28:07	

3.3.4 Flux and wavelength calibrations

Flux calibration is necessary in order to convert the fluxes extracted by SExtractor from ADU (Analog to Digital Unit) to physical units (erg/s/cm^2). For each observation, the total efficiency of the system (telescope, optics and detector), that is, the ratio between the measured flux, F_m , and the real flux, F_r , of an object, must be known. Figure 3.8 shows the estimated individual efficiencies of the different components of the GTC+OSIRIS+TF system (mirrors, camera, detectors, filters...), calculated from first principles by J.I. González-Serrano (private communication). According to this, the total system efficiency should be around $\sim 20\%$. To calculate its empirical value, two calibration stars (EGS125 and EGS129), each in one of the detectors, were studied and calibrated with OSIRIS long-slit spectroscopy as a first step.

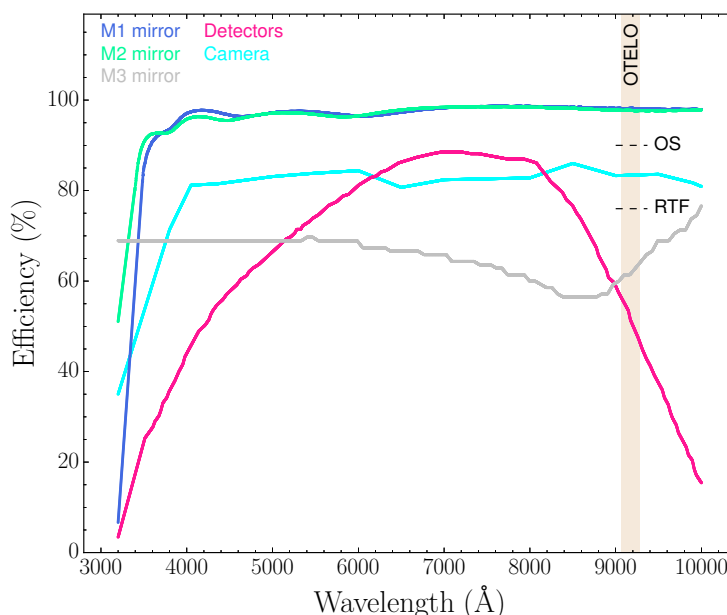


Figure 3.8: Estimated efficiencies of the different system's components (J.I. González-Serrano, private communication). Blue line: M1 mirror, green line: M2 mirror, gray line: M3 mirror (Nasmyth), pink line: detectors (CCDs), cyan line: camera. The pale shaded region represents OTELO's spectral range. The two black dashed horizontal lines represent the efficiencies of the red TF and the order-sorter filter 911/42 (OS), respectively. The total system efficiency can be estimated from the product of all these components, yielding a value close to $\sim 20\%$.

Calibration of EGS125 and EGS129. In order to perform the flux calibration of OTELO's sources, two F8 sub-dwarf stars in the field, one in each CCD, were chosen as calibrators (see Fig. 3.9). They themselves were previously calibrated with the help of a spectrophotometric standard, HD126511, chosen from the STIS Next Generation Spectral Library¹⁴, with spectral type G5 and a V magnitude of 8.359. About ~ 1 hour of

¹⁴See <https://archive.stsci.edu/prepds/stisngsl/>.

Este documento incorpora firma electrónica, y es copia auténtica de un documento electrónico archivado por la ULL según la Ley 39/2015. Su autenticidad puede ser contrastada en la siguiente dirección https://sede.ull.es/validacion/		
Identificador del documento:	969870	Código de verificación: 8KFVZkZp
Firmado por:	MARINA RAMÓN PÉREZ UNIVERSIDAD DE LA LAGUNA	Fecha: 28/06/2017 21:15:24
	ANGEL MANUEL BONGIOVANNI PEREZ UNIVERSIDAD DE LA LAGUNA	29/06/2017 09:30:15
	JORGE CEPA NOGUE UNIVERSIDAD DE LA LAGUNA	29/06/2017 09:33:05
	ANA MARIA PEREZ GARCIA UNIVERSIDAD DE LA LAGUNA	29/06/2017 11:12:35
	ERNESTO PEREDA DE PABLO UNIVERSIDAD DE LA LAGUNA	04/07/2017 18:28:07

observation time under photometric conditions was devoted to obtain low-resolution spectra of those three stars by OTELO's team. The observations were carried out using the OSIRIS long-slit mode with a red grism at resolution ~ 500 . A slit of 1.5 arcsec was used in order to achieve the maximum flux accuracy, given the mean seeing of 0.80 arcsec. According to the AB magnitudes of the targets in the r band, the total integration time was generous enough to reach a SNR $\simeq 10$ between 5500 and 9500 Å.

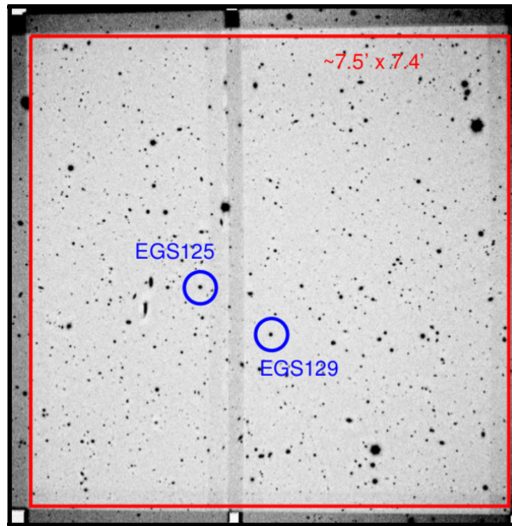


Figure 3.9: Unvignetted $\sim 7.5' \times 7.4'$ OTELO's field (red square) and calibration stars (blue circles) in each detector (EGS125 for CCD1 and EGS129 for CCD2).

The spectra of EGS125 and EGS129 were reduced in the usual way using IRAF's noao spectral reduction packages. The reduction steps were the following:

- **Bias:** bias frames were combined and subtracted from the science spectra using the `imcombine` and `ccdproc` tasks.
- **Flat-field:** high-count flat-field images were combined and the resulting image was corrected by the fitting of a continuum lamp spectrum (with `flatcombine` and `response`). The sky spectrum included in the science images was averaged and a sky flat was interactively fitted by a spline function using the task `illumination`.
- **Wavelength calibration:** wavelength calibration was carried out using the task `transform`. To this aim, spectral lines from Ne and HgAr lamps exposures obtained with the same rotator angle as the science exposures were interactively identified and analysed using the tasks `identify` and `fitcoords`.
- **Sky subtraction:** the sky background from the individual 2D spectra was subtracted using the IRAF task `background`.
- **Flux calibration:** the individual 2D spectra were combined and collapsed in the spatial direction. A dereddened sensitivity curve for flux calibration was obtained from the spectrophotometric standard star spectrum, and the instrumental fluxes of OTELO's calibration stars were converted to physical units.

Este documento incorpora firma electrónica, y es copia auténtica de un documento electrónico archivado por la ULL según la Ley 39/2015.
Su autenticidad puede ser contrastada en la siguiente dirección <https://sede.ull.es/validacion/>

Identificador del documento: 969870	Código de verificación: 8KFVZkZp
Firmado por: MARINA RAMÓN PÉREZ UNIVERSIDAD DE LA LAGUNA	Fecha: 28/06/2017 21:15:24
ANGEL MANUEL BONGIOVANNI PEREZ UNIVERSIDAD DE LA LAGUNA	29/06/2017 09:30:15
JORGE CEPA NOGUE UNIVERSIDAD DE LA LAGUNA	29/06/2017 09:33:05
ANA MARIA PEREZ GARCIA UNIVERSIDAD DE LA LAGUNA	29/06/2017 11:12:35
ERNESTO PEREDA DE PABLO UNIVERSIDAD DE LA LAGUNA	04/07/2017 18:28:07

Figure 3.10 shows the reduced spectra of the calibrations stars resulting from this procedure. The mean flux error of the spectra was better than 6%.

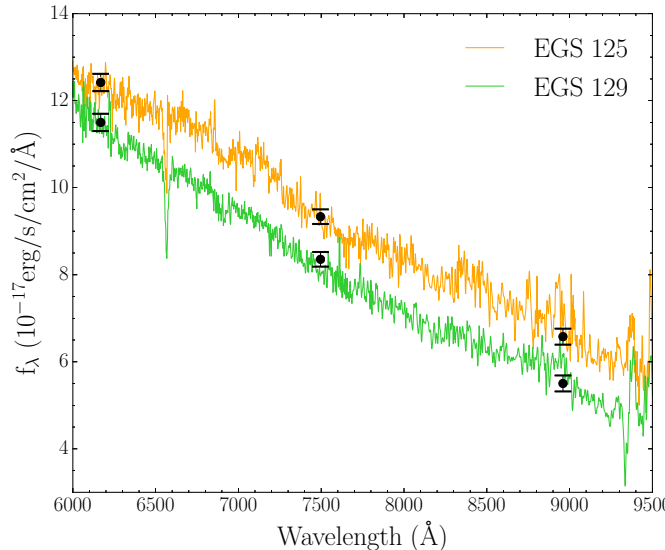


Figure 3.10: Spectra of the calibration stars present in OTELO's field of view, as indicated in Figure 3.9. Black dots correspond to their fluxes in r , i , and z bands from SDSS-DR12. These spectra were used to estimate the total efficiency of the system and its deviations depending on the particular conditions of each individual observation.

Calibration of OTELO's sources. Once the calibration stars, EGS125 and EGS129, were properly calibrated, wavelength and flux calibrations of the rest of the sources in OTELO's field of view was performed. Given the wavelength dependency across the field of view, the different airmasses and atmospheric conditions during the night, and that the detector system is a mosaic, the calibration depends on the wavelength (λ_{ob}) at which the source is observed, the science frame (i) and the detector of the OSIRIS mosaic (CCD1 or CCD2). For that reason, isophotal fluxes $F_m(\lambda_{ob}, i, CCD)$ were measured in each individual image.

First of all, wavelength calibration was performed using the relation between λ and the radial distance, r , given by equations 2.6 and 2.7. Knowing the coordinates of the optical center (see subsection 3.3.3) and of the calibration stars in each frame, as well as the central wavelength (λ_0) at which the TF was tuned in each observation, the effective wavelength of observation of the calibration stars (λ_{ob}) as a function of the radial distance to the optical center in arcmin is determined. This wavelength calibration is also performed for the rest of the sources in OTELO's catalogue.

Once the wavelength calibration of EGS125 and EGS129 was done, their extracted fluxes were converted from ADU to physical units by means of the following relation:

$$F_m(\lambda_{ob}, i) = \frac{gK(\lambda_{ob}, i)E_\gamma(\lambda_{ob})}{tA_{tel}} F_{ADU}(\lambda_{ob}, i) \quad (3.2)$$

Este documento incorpora firma electrónica, y es copia auténtica de un documento electrónico archivado por la ULL según la Ley 39/2015.
Su autenticidad puede ser contrastada en la siguiente dirección <https://sede.ull.es/validacion/>

Identificador del documento: 969870	Código de verificación: 8KFVZkZp
Firmado por: MARINA RAMÓN PÉREZ UNIVERSIDAD DE LA LAGUNA	Fecha: 28/06/2017 21:15:24
ANGEL MANUEL BONGIOVANNI PEREZ UNIVERSIDAD DE LA LAGUNA	29/06/2017 09:30:15
JORGE CEPA NOGUE UNIVERSIDAD DE LA LAGUNA	29/06/2017 09:33:05
ANA MARIA PEREZ GARCIA UNIVERSIDAD DE LA LAGUNA	29/06/2017 11:12:35
ERNESTO PEREDA DE PABLO UNIVERSIDAD DE LA LAGUNA	04/07/2017 18:28:07

where g is the CCD gain (0.95 electrons/ADU), $E_\gamma(\lambda_{ob}) = hc/\lambda$ is the energy of a photon (in erg), t is the exposure time (in seconds), A_{tel} is the effective collecting area of the telescope (in cm²) and $K(\lambda_{ob}, i)$ is the correction for atmospheric extinction, given by:

$$K(\lambda_{ob}, i) = 10^{k(\lambda_{ob})\langle \chi \rangle} \quad (3.3)$$

which depends on the extinction coefficient, $k(\lambda_{ob})$, and the mean airmass of the observation, $\langle \chi \rangle$. In our case, we estimated $k(\lambda_{ob})$ by fitting the extinction curve of La Palma¹⁵ in the wavelength range defined in the survey. The uncertainty in the efficiency is defined by the sum in quadrature of the error in the measured and reference flux.

The real fluxes of the calibration stars (F_r) were obtained by convolving their fluxes F as measured with long-slit spectroscopy with the Airy profile approximation of Equation 2.3, by doing $\lambda_c = \lambda_{ob}$, and integrating:

$$F_r = \int_{8500}^{9500} F(\lambda) T(\lambda) d\lambda \quad (3.4)$$

The efficiency is then calculated as:

$$\epsilon = \frac{F_m}{F_r} \quad (3.5)$$

Fig. 3.11 shows the empirical efficiencies of the system for both detectors calculated in this way, as well as the expected theoretical efficiencies estimated during the scientific commissioning and by the OSIRIS SNR Calculator. Our efficiency measurements are according to the estimations obtained by Sánchez-Portal et al. (2015) for the H α imaging of a galaxy cluster at $z = 0.395$ with OSIRIS red TF in the framework of the GLACE survey, as well as with the efficiency estimations compiled by Cabrera-Lavers et al. (2014) for the same device. Moreover, our empirical values of the total efficiency are in agreement with what was expected from the sum of the individual efficiencies of the system as calculated from first principles (see Fig. 3.8). We noted a systematic differential sensitivity of a factor ~ 1.12 between both detectors in favor of CCD2. Nonetheless, the general behaviour of the efficiencies are compatible with a second order polynomial, which was used to perform the calibration at the observed wavelength of each source and TF tuning as $\epsilon(\lambda, CCD)$. Sensitivity differences between detectors, as well as small fluctuations of the total efficiency around polynomial fits were taken into account in the flux estimations.

Once the system's efficiency is known for each observation and detector, the final step is to use it in order to convert the instrumental flux of each source s , measured on a given CCD, to physical flux density in CGS units (erg/s/cm²/Å) by means of the following expression:

$$f(\lambda_{ob}, CCD)_s = \frac{F_m}{\delta \lambda_e \epsilon} = \frac{g K(\lambda_{ob}) E_\gamma(\lambda_{ob})}{t A_{tel} \delta \lambda_e \epsilon(\lambda_{ob}, CCD)} F_{ADU}(\lambda_{ob}, s) \quad (3.6)$$

where $\epsilon(\lambda_{ob}, CCD)$ is the total efficiency calculated from fitting at λ_{ob} , $\delta \lambda_e$ is the effective passband width in Å ($\equiv \frac{\pi}{2} \delta \lambda_{FWHM}$, see Jones 2001), and the remaining terms are as in Eq. 3.2. The estimation of the flux errors takes into account the efficiency error, depending on the detector and the source flux measurement uncertainty (see subsection 3.3.2).

¹⁵See http://www.ing.iac.es/Astronomy/observing/manuals/ps/tech_notes/tn031.pdf for more details.

Este documento incorpora firma electrónica, y es copia auténtica de un documento electrónico archivado por la ULL según la Ley 39/2015. Su autenticidad puede ser contrastada en la siguiente dirección https://sede.ull.es/validacion/		
Identificador del documento:	Código de verificación:	
Firmado por: MARINA RAMÓN PÉREZ UNIVERSIDAD DE LA LAGUNA		Fecha: 28/06/2017 21:15:24
ANGEL MANUEL BONGIOVANNI PÉREZ UNIVERSIDAD DE LA LAGUNA		29/06/2017 09:30:15
JORGE CEPA NOGUE UNIVERSIDAD DE LA LAGUNA		29/06/2017 09:33:05
ANA MARIA PÉREZ GARCIA UNIVERSIDAD DE LA LAGUNA		29/06/2017 11:12:35
ERNESTO PEREDA DE PABLO UNIVERSIDAD DE LA LAGUNA		04/07/2017 18:28:07

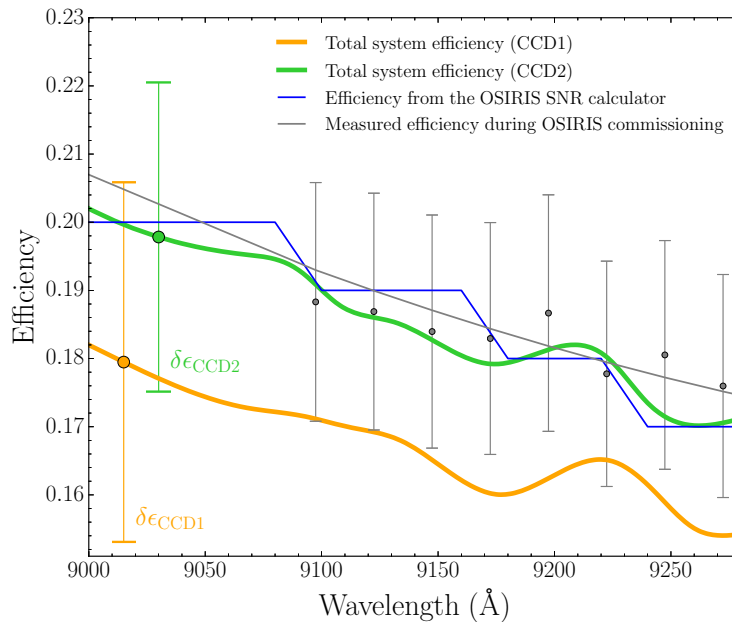


Figure 3.11: Total efficiency of the GTC+OSIRIS+TF system for CCD1 (orange curve) and CCD2 (green curve), based on the OTELO survey calibration stars, averaged for each slice and spline fitted. The gray dots represent the efficiency obtained by Cabrera-Lavers et al. (2014) during OSIRIS commissioning, and the gray line is a polynomial fit to those values. The blue stepped line represents the efficiency as tabulated by the OSIRIS SNR Calculator. The empirical values of the total efficiency range between ~ 16 and 21% , in agreement with what was expected from Fig. 3.8.

3.3.5 Composition of pseudo-spectra

Once the sources are detected in OTELO’s deep image and their photometry performed on each of the 216 individual slices of the tomography (see section 3.3.2), the fluxes are properly transformed from ADU to physical units following the calibrations described in section 3.3.4.

By combining the flux measurements of an object in each scan, its spectral energy distribution (SED), convolved to OSIRIS red TF response, can be assembled. This produces a sort of low-resolution spectrum for each object in the field, which is called a ‘pseudo-spectrum’. In a pseudo-spectrum, each point represents the integrated flux of the object in one scan. Unlike a spectrum, a pseudo-spectrum is not continuous and should be deconvolved before its analysis. Some examples of real PS obtained in OTELO survey can be seen in Figures 5.3, 5.4 and 5.5.

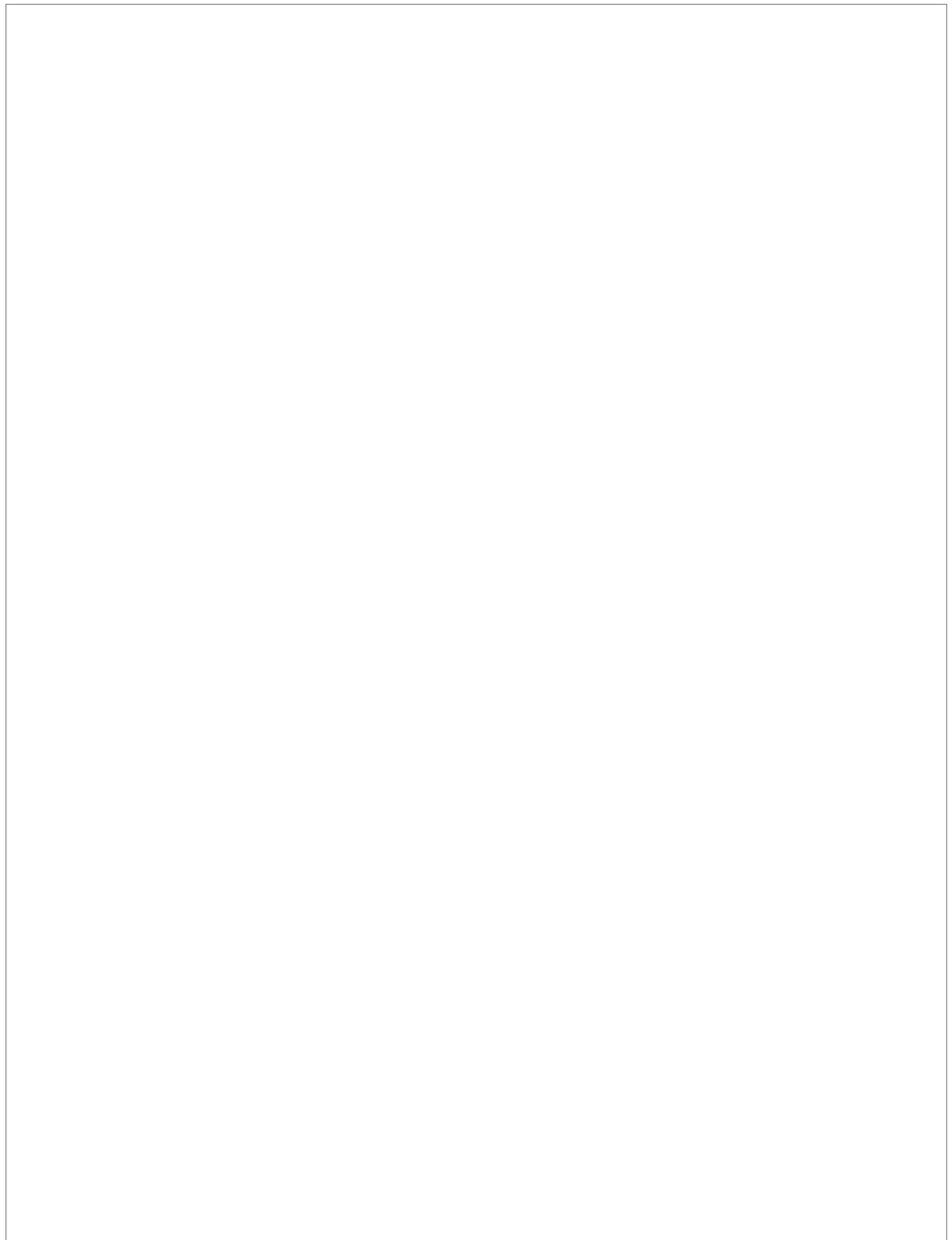
The procedure to construct the pseudo-spectra is the following. For a given object we have 216 flux measurements $F_i(\lambda_{obs})$, where $i = 0, 1, \dots, 216$ indicates the science frame and λ_{obs} their corresponding effective wavelength. We used the isophotal flux as the best approximation to the corrected aperture flux in crowded fields. It was the photometric parameter with the smallest deviations ($\sim 4\%$) when comparing the pseudo-spectra of the calibration stars of OTELO with the TF convolution of their spectra (shown in Fig. 3.10).

Este documento incorpora firma electrónica, y es copia auténtica de un documento electrónico archivado por la ULL según la Ley 39/2015. Su autenticidad puede ser contrastada en la siguiente dirección https://sede.ull.es/validacion/		
Identificador del documento:	969870	Código de verificación: 8KFVZkZp
Firmado por:	MARINA RAMÓN PÉREZ UNIVERSIDAD DE LA LAGUNA	Fecha: 28/06/2017 21:15:24
	ANGEL MANUEL BONGIOVANNI PEREZ UNIVERSIDAD DE LA LAGUNA	29/06/2017 09:30:15
	JORGE CEPA NOGUE UNIVERSIDAD DE LA LAGUNA	29/06/2017 09:33:05
	ANA MARIA PEREZ GARCIA UNIVERSIDAD DE LA LAGUNA	29/06/2017 11:12:35
	ERNESTO PEREDA DE PABLO UNIVERSIDAD DE LA LAGUNA	04/07/2017 18:28:07

In order to construct the pseudo-spectrum of an object, its measured fluxes must be grouped and combined in wavelength windows representing OTELO scan steps. Considering the dithering pattern, as well as the wavelength change towards the blue with the distance to the optical center (Eq. 2.6), the effective wavelength of observation of a source (λ_{ob}) not only varies within a given slice in a scan, but this variation is amplified almost quadratically as the mean radial distance of the source to the optical centre increases. Thus, for an object falling close to the optical center, the fluxes can be grouped in the wavelength windows described in section 2.2.2: 9280 – 9070Å, each 6Å. However, as the source lies further away from the optical center, such a combination could mean that fluxes from different, adjacent slices are mixed. To tackle this problem, we sorted in wavelength the 216 $F_i(\lambda_{ob})$ fluxes and effective wavelengths of a given source. We then used an algorithm that searches the optimal wavelength windows to group the data such that, in every window, the maximum wavelength difference among the set of fluxes is smaller than the scan step, $\delta\lambda_{FWHM}/2$. The algorithm also finds the optimal equal-spaced wavelength sequence for each source. Each element of this sequence will be a wavelength label of the resulting pseudo-spectrum. In each group, the n -fluxes associated to each wavelength are combined using a weighted mean scheme, using the inverse square of the flux error as a weighting factor. Finally, the resulting pseudo-spectrum is rescaled to flux density units (erg/s/cm²/Å).

Este documento incorpora firma electrónica, y es copia auténtica de un documento electrónico archivado por la ULL según la Ley 39/2015.
Su autenticidad puede ser contrastada en la siguiente dirección <https://sede.ull.es/validacion/>

Identificador del documento:	969870	Código de verificación:	8KFVZkZp
Firmado por:	MARINA RAMÓN PÉREZ UNIVERSIDAD DE LA LAGUNA	Fecha:	28/06/2017 21:15:24
	ANGEL MANUEL BONGIOVANNI PEREZ UNIVERSIDAD DE LA LAGUNA		29/06/2017 09:30:15
	JORGE CEPA NOGUE UNIVERSIDAD DE LA LAGUNA		29/06/2017 09:33:05
	ANA MARIA PEREZ GARCIA UNIVERSIDAD DE LA LAGUNA		29/06/2017 11:12:35
	ERNESTO PEREDA DE PABLO UNIVERSIDAD DE LA LAGUNA		04/07/2017 18:28:07



Este documento incorpora firma electrónica, y es copia auténtica de un documento electrónico archivado por la ULL según la Ley 39/2015. <i>Su autenticidad puede ser contrastada en la siguiente dirección https://sede.ull.es/validacion/</i>		
Identificador del documento:	969870	Código de verificación:
Firmado por:	MARINA RAMÓN PÉREZ UNIVERSIDAD DE LA LAGUNA	Fecha: 28/06/2017 21:15:24
	ANGEL MANUEL BONGIOVANNI PEREZ UNIVERSIDAD DE LA LAGUNA	29/06/2017 09:30:15
	JORGE CEPA NOGUE UNIVERSIDAD DE LA LAGUNA	29/06/2017 09:33:05
	ANA MARIA PEREZ GARCIA UNIVERSIDAD DE LA LAGUNA	29/06/2017 11:12:35
	ERNESTO PEREDA DE PABLO UNIVERSIDAD DE LA LAGUNA	04/07/2017 18:28:07

4

OTELO'S MULTIWAVELENGTH CATALOGUE

The auxiliary data used to complement OTELO's catalogue are described in this Chapter, as well as the approach followed to obtain reliable photometric measurements in different bands and the methodology adopted to match distinct catalogues. Data from the X-rays to the far infrared (FIR), mainly from the AEGIS survey, are employed to build a multiwavelength catalogue, which is later used to derive photometric redshifts and other parameters of the objects in the field. Two redshift catalogues are also used to include this information in the final catalogue of OTELO. This catalogue and its properties are described at the end of the Chapter.

Obtaining a consistent multiwavelength catalogue of OTELO is one of the main goals of the survey, as it allows to condense all the available astronomical information of the field, easing the following scientific exploitation. Moreover, a multiwavelength approach is essential to derive certain parameters of the objects detected in OTELO's images, such as their photometric redshifts.

The Extended Groth Strip, which is displayed in Figure 1.7, was chosen because it is one of the most widely studied regions in the sky. As its name suggests, the All-wavelength Extended Groth strip International Survey (AEGIS, Davis et al. 2007) has observed this particular region of the sky from X-Rays to radio waves, supplying an immense amount of data to the astronomical community. When building OTELO's multiwavelength catalogue, we took advantage of this valuable information. First, we used images from the CFHTLS, HST-ACS and WIRDS surveys in order to obtain direct photometry of our objects in their optical and NIR bands and construct OTELO's initial catalogue (called the "nuclear catalogue"; see section 4.1). This required a detailed study so as to choose the best photometric parameter for the measurement of fluxes in the images. Then, we cross-matched complementary public catalogues to our own with the purpose of extending the spectral range (section 4.2). Such a cross-matching of different catalogues in different wavelengths is not a simple task, and also involved a precise analysis in order to take into account the variations of the source's positions due to their diverse astrometrical errors in each catalogue, as well as their magnitudes in the different bands.

Este documento incorpora firma electrónica, y es copia auténtica de un documento electrónico archivado por la ULL según la Ley 39/2015.
Su autenticidad puede ser contrastada en la siguiente dirección <https://sede.ull.es/validacion/>

Identificador del documento:	969870	Código de verificación:	8KFVZkZp
Firmado por:	MARINA RAMÓN PÉREZ UNIVERSIDAD DE LA LAGUNA	Fecha:	28/06/2017 21:15:24
	ANGEL MANUEL BONGIOVANNI PEREZ UNIVERSIDAD DE LA LAGUNA		29/06/2017 09:30:15
	JORGE CEPA NOGUE UNIVERSIDAD DE LA LAGUNA		29/06/2017 09:33:05
	ANA MARIA PEREZ GARCIA UNIVERSIDAD DE LA LAGUNA		29/06/2017 11:12:35
	ERNESTO PEREDA DE PABLO UNIVERSIDAD DE LA LAGUNA		04/07/2017 18:28:07

4.1 Nuclear catalogue

In order to construct OTELO's nuclear catalogue, we used optical data from the Canada-France-Hawaii Telescope Legacy Survey¹ (T0007 release) and the Hubble Space Telescope Advanced Camera for Surveys², as well as data in the NIR from the WIRcam Deep Survey³ (T0002 release).

The CFHTLS Deep-3 field, which covers a 1×1 deg² region in the sky with 0.186 arcsec/pixel, also includes OTELO's field. The data is composed of 24 u, g, r, i and z stacks reaching an AB limiting magnitude from 25 to 26 with a completeness of 80% in extended sources. On the other hand, the ACS images of the EGS field were obtained as part of the GO Program 10134 (Davis et al. 2007) and include the F606W and F814W bands. This data was reduced, mosaiced and pixel-resampled from 0.03 to 0.1 arcsec/pixel by A. Koekemoer⁴. As for the WIRDS images, they cover a subregion of the CFHTLS deep fields and include the J, H and Ks bands. This survey reaches an AB limiting magnitude from 24 to 25 for point sources with a 50% of completeness, making it one of the deepest homogenous surveys in the NIR to date (Bielby et al. 2012).

In the first place, the mentioned images and their corresponding weight maps were trimmed to OTELO's deep image field of view with an excess of 1 arcmin in each dimension. Then, a pixel homogeneisation to our image, conserving the integrated flux per unit area, was carried out using the SWarp software. We also unified the WCS calibration of each image using the reference catalogue and procedures described in section 3.2. Finally, the spatial registration and trimming of the images was made using IRAF's task `wregister`. After that, we obtained a mean value of the Point Spread Function (PSF) for each image, by performing a fit using the PSFEx application (Bertin 2011). The PSF of the images ranged between ~ 0.8 and 1 arcsec. This variation could be a critical issue when a robust photometry across the different bands is required. Table 4.1 summarises the main properties of the images used for the construction of OTELO's nuclear catalogue.

Table 4.1: Properties of the images used to build OTELO's nuclear catalogue. The first column indicates the image survey. The second column indicates the image filter. The following columns show the different properties of the corresponding filter. (*): The limiting magnitude is defined as 5 times the median of the background noise measured on the image. (**): The HST-ACS images have been convolved to the PSF of OTELO's deep image.

Survey	Filter	λ_{eff} (Å)	FWHM (Å)	Limiting magnitude* (AB)	Photometric zero-point (AB)	PSF FWHM (arcsec)
OTELO	synthesis of the TF responses	9175.0	228.9	27.8	30.504	0.87
CFHTLS	u	3881.6	574.8	30.2	30.000	1.00
CFHTLS	g	4767.0	1322.4	30.6	30.000	0.91
CFHTLS	r	6191.7	1099.1	30.3	30.000	0.86
CFHTLS	i	7467.4	1316.1	29.9	30.000	0.82
CFHTLS	z	8824.0	998.4	28.9	30.000	0.77
HST-ACS**	F606W	5810.1	1776.5	29.2	26.486	0.87
HST-ACS**	F814W	7985.4	1876.7	28.6	25.937	0.90
WIRDS	J	12481.5	1547.9	27.4	30.000	0.86
WIRDS	H	16158.2	2885.7	26.8	30.000	0.79
WIRDS	Ks	21337.8	3208.6	26.8	30.000	0.81

¹CFHTLS.

²HST-ACS.

³WIRDS.

⁴ See http://aegis.ucolick.org/mosaic_page.htm.

Este documento incorpora firma electrónica, y es copia auténtica de un documento electrónico archivado por la ULL según la Ley 39/2015. Su autenticidad puede ser contrastada en la siguiente dirección https://sede.ull.es/validacion/		
Identificador del documento: 969870		Código de verificación: 8KFVZkZp
Firmado por: MARINA RAMÓN PÉREZ UNIVERSIDAD DE LA LAGUNA	Fecha: 28/06/2017 21:15:24	
ANGEL MANUEL BONGIOVANNI PÉREZ UNIVERSIDAD DE LA LAGUNA	29/06/2017 09:30:15	
JORGE CEPA NOGUE UNIVERSIDAD DE LA LAGUNA	29/06/2017 09:33:05	
ANA MARIA PÉREZ GARCIA UNIVERSIDAD DE LA LAGUNA	29/06/2017 11:12:35	
ERNESTO PEREDA DE PABLO UNIVERSIDAD DE LA LAGUNA	04/07/2017 18:28:07	

Different software utilities have been developed in the past years in order to obtain reliable and homogeneous photometry from multi-wavelength ground- and space-based surveys having different bandwidths and PSFs. Most of these tools are based on real or model source profiles, including PSF models. For optical and NIR data, some of the most used ones are ColorPRO (Coe et al. 2006), PyGFit (Mancone et al. 2013) or T-PHOT (Merlin et al. 2016). In our case, we explored different approaches to obtain reliable fluxes and “colours” (flux differences) from the image set contributing to OTELO’s nuclear catalogue in a quick and accurate way. We decided to employ OTELO’s deep image as the origin of the source detection (as we did for the extraction of our sources, see section 3.3.2) and to use a single photometric parameter for the measurement of fluxes.

Inspired by the results of the analysis of the SExtractor PSF-model photometry described by Annunziatella et al. (2013), along with the simulations framework of Chang et al. (2015) to model data from the Dark Energy Survey, we carried out our own tests in order to determine if the DETMODEL parameter from SExtractor fulfills our requirements within a reasonable error, compared to others. For that, we built an artificial source catalogue in the z-band (hereafter, z_{true}) using the Stuff application (Bertin 2009), which simulated the corresponding real data of the nuclear catalogue. That included identical pixel and image sizes, background noise level, effective gain and photometric zero-point. This catalogue was then used as input of the SkyMaker software (Bertin 2009), in order to create 3 images which only differ in their PSF FWHM: 0.7, 0.9 and 1.1 arcsec. These values cover the mean FWHM range of the real images (see Table 4.1). Figure 4.1 shows a cutout of each of these artificial images. We then obtained the PSF model of each artificial z-band image with PSFEx, and recovered the source fluxes with SExtractor in dual mode (as in section 3.3.2), using the intermediate image (with the PSF FWHM closest to that of OTELO’s deep image) as the detection image.

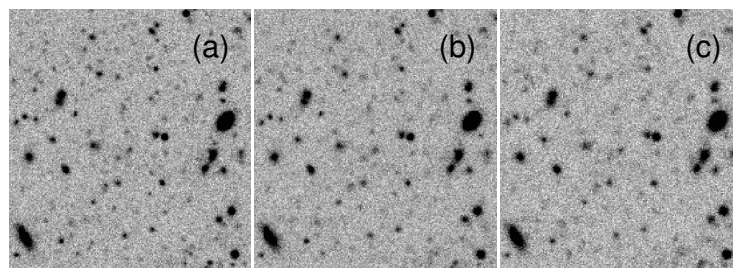


Figure 4.1: Artificial images ($10 \times 10 \text{ arcmin}^2$ cutout) obtained with SkyMaker from a simulated z-band catalogue created with the Stuff application. Images differ only in the FWHM of their PSF: (a) 0.7, (b) 0.9 and (c) 1.1 arcsec. These images were used to study the behaviour of SExtractor in recovering fluxes and “colours” (flux differences), so as to obtain photometric parameters (including PSF-model photometry) under similar conditions as those of the images used to construct OTELO’s nuclear catalogue. See the text for more details.

Three different photometric parameters from SExtractor were tested on the three artificial images with different PSF FWHM: AUTO (Kron photometry, usually the primary choice for total flux measurement), ISOCOR (isophotal photometry) and DETMODEL (which first performs a model fitting on the detection image, and then fits this model to each measurement image separately). These parameters were selected from a larger set and were the ones presenting the best performances. We discarded detections with FLAGS different from 0 so as to only compare reliable measurements. The catalogues obtained in each case were cross-matched with the original one containing the z_{true} photometry.

Figure 4.2 shows the differences in magnitude found between z_{true} and the measured photometry in each case. According to the moving median (pink lines) plotted in each case, and independently from the mean

Este documento incorpora firma electrónica, y es copia auténtica de un documento electrónico archivado por la ULL según la Ley 39/2015. Su autenticidad puede ser contrastada en la siguiente dirección https://sede.ull.es/validacion/		
Identificador del documento: 969870	Código de verificación: 8KFVZkZp	Fecha: 28/06/2017 21:15:24
Firmado por: MARINA RAMÓN PÉREZ UNIVERSIDAD DE LA LAGUNA		29/06/2017 09:30:15
ANGEL MANUEL BONGIOVANNI PÉREZ UNIVERSIDAD DE LA LAGUNA		29/06/2017 09:33:05
JORGE CEPA NOGUE UNIVERSIDAD DE LA LAGUNA		29/06/2017 11:12:35
ANA MARIA PÉREZ GARCIA UNIVERSIDAD DE LA LAGUNA		04/07/2017 18:28:07
ERNESTO PEREDA DE PABLO UNIVERSIDAD DE LA LAGUNA		

FWHM, the DETMODEL parameter seems to be the best choice for the recovery of the total flux. Photometric errors obtained from measurements on the detection image (the one with mean FWHM = 0.9 arcsec) are represented in Figure 4.3. The DETMODEL and ISOCOR parameters give a favourable balance against AUTO photometry distribution. Similar errors distributions were found on the images with mean FWHM of 0.7 and 1.1 arcsec.

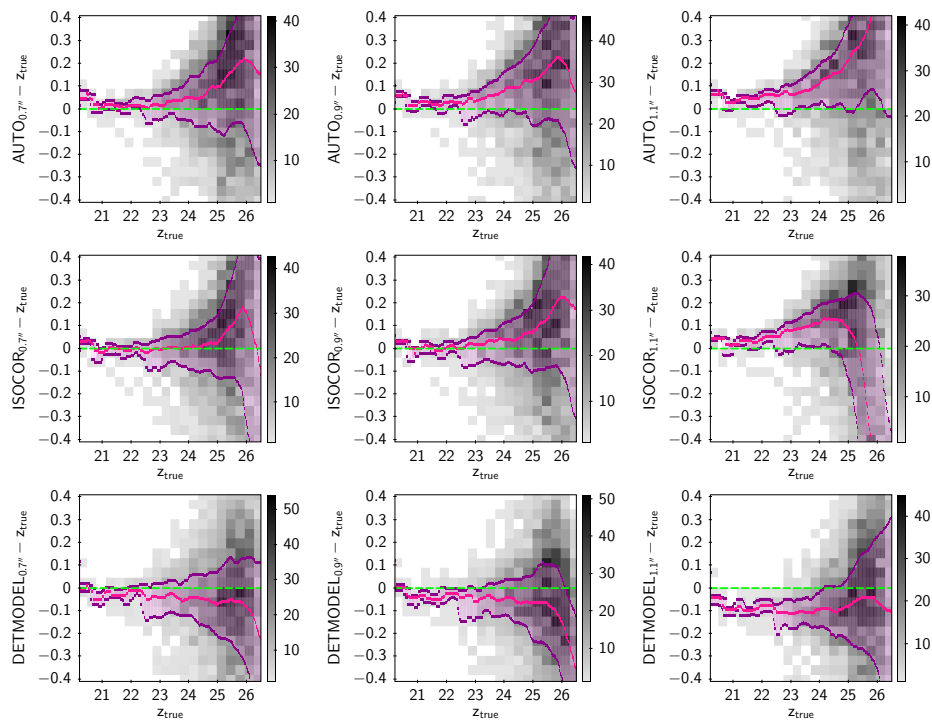


Figure 4.2: Difference between the measured magnitude as obtained by SExtractor and the true magnitude from the simulated catalogue. Each column shows the result of the test in one of the 3 z-band artificial images which only differ in their PSF FWHM (0.7, 0.9 and 1.1 arcsec, from left to right). Each row shows the result of the test using one of the 3 different photometric parameters from SExtractor (AUTO, ISOCOR and DETMODEL, from top to bottom). The gray pixels represent the density of sources in the z-band simulated catalogue. The green line represents the 0 value (no deviation in magnitude). Pink lines show the moving median of the deviation. Purple lines represent the 0.25 and 0.57 quartiles.

Regarding colours (or flux differences), we compared the fluxes measured in image pairs with different mean FWHM. In this case, we tested the following photometric parameters: APER (3 arcsec aperture photometry), ISOCOR and DETMODEL. As in the case of the Kron magnitude for total flux measurement, apertures are the conventional choice to build colours, although Benítez et al. (2004) claimed that isophotal magnitudes provide the best estimate of a galaxy’s “true” colours under the same FWHM. In our tests, as can be seen in Figure 4.4, the behaviour of DETMODEL colours was slightly better than that of the APER ones, and the ISOCOR colours were even closer to zero differences for bright sources but failed for faint sources. In any case, the deviation of the colours measured by DETMODEL was within a reasonable margin.

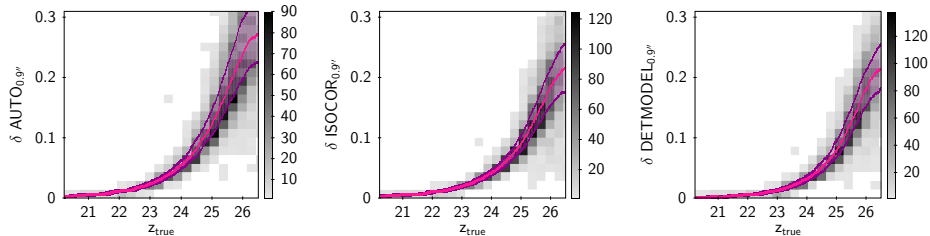


Figure 4.3: Photometric errors obtained from measurements on the artificial z-band image having a mean FWHM of 0.9 arcsec. The 3 photometric parameters that were used for the tests are the same as in Figure 4.2 (AUTO, ISOCOR and DETMODEL, from left to right). The gray pixels represent the density of sources in the z-band simulated catalogue. Pink lines represent the moving median. Purple lines represent the 0.25 and 0.57 quartiles. Similar error distributions were found on the images with different mean FWHM (0.7 and 1.1 arcsec).

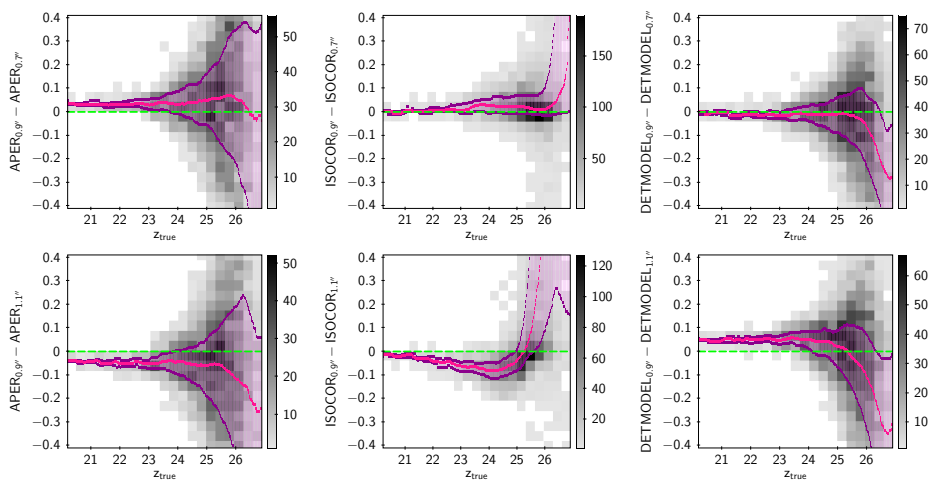


Figure 4.4: Measured “colours” (flux differences) obtained from paired combinations of the artificial images with different FWHM. Each column shows a different photometric parameter used (APER, ISOCOR and DETMODEL, from left to right). The gray pixels represent the density of sources in the z-band simulated catalogue. The green line represents the 0 value (no colour). Pink lines show the moving median of the deviation. Purple lines represent the 0.25 and 0.57 quartiles.

In the light of the results of our tests in magnitude and colour recovery, and in order to select a single photometric parameter which works correctly in the case of OTELO, we finally decided to chose the DETMODEL parameter from SExtractor. We performed the flux measurements on the 10 different auxiliary images, thus obtaining photometry of OTELO’s sources in 10 new bands that were included in our catalogue: u, g, r, i, z, F606W (renamed as HST-V), F814W (renamed as HST-I), J, H and Ks.

4.2 Auxiliary data

Once OTELO’s nuclear catalogue was obtained, it was cross-matched with public catalogues in order to build the final multiwavelength catalogue. The public data which were used for this purpose completed the

Este documento incorpora firma electrónica, y es copia auténtica de un documento electrónico archivado por la ULL según la Ley 39/2015. Su autenticidad puede ser contrastada en la siguiente dirección https://sede.ull.es/validacion/		
Identificador del documento:	969870	Código de verificación: 8KFVZkZp
Firmado por:	MARINA RAMÓN PÉREZ UNIVERSIDAD DE LA LAGUNA	Fecha: 28/06/2017 21:15:24
	ANGEL MANUEL BONGIOVANNI PEREZ UNIVERSIDAD DE LA LAGUNA	29/06/2017 09:30:15
	JORGE CEPA NOGUE UNIVERSIDAD DE LA LAGUNA	29/06/2017 09:33:05
	ANA MARIA PEREZ GARCIA UNIVERSIDAD DE LA LAGUNA	29/06/2017 11:12:35
	ERNESTO PEREDA DE PABLO UNIVERSIDAD DE LA LAGUNA	04/07/2017 18:28:07

information in the infrared as well as in the most energetic part of the electromagnetic spectrum (X-Rays and UV). In addition, two redshift catalogues were employed in order to increase our knowledge of OTELO's sources. A summary of all the auxiliary data is shown in Table 4.2. The distribution of AB magnitudes of each catalogue is shown in Figure 4.5.

Table 4.2: Auxiliary catalogues used for the construction of OTELO's multiwavelength catalogue.

	Catalogue	Bands	Astrometrical Errors	Reference
X-Rays	Chandra	0.5–7 keV	0.7"	Pović et al. (2009)
Ultraviolet	Galex	NUV, FUV	0.6"	Morrissey et al. (2007)
Mid-infrared	Spitzer (IRAC)	3.6, 4.5, 5.8, & 8 μ m	0.37"	Barro et al. (2011)
Far-infrared (I)	Spitzer (MIPS) & Herschel (PACS)	24, 100 & 160 μ m	1.0"	Lutz et al. (2011)
Far-infrared (II)	Herschel (SPIRE)	250, 300 & 500 μ m	0.5"	Roseboom et al. (2010)
Photo-z	CFHTLS T0004 Deep3		0.26"	Coupon et al. (2009)
Spec-z	DEEP2 Galaxy Redshift Survey		0.50"	Newman et al. (2013)

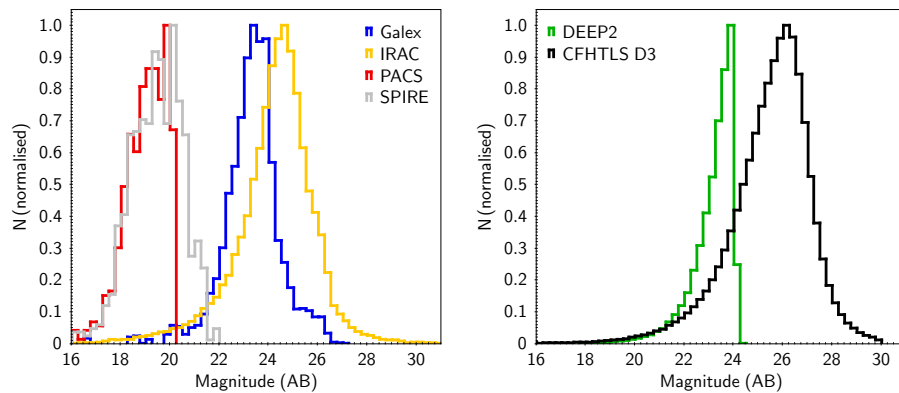


Figure 4.5: Distribution of AB magnitudes in the complementary catalogues (left: photometric catalogues, right: redshift catalogues). Blue line: NUV magnitude from the GALEX catalogue (Morrissey et al. 2007), yellow line: r magnitude from the IRAC catalogue of Barro et al. (2011), red line: 24 μ m MIPS magnitude from the PACS catalogue (Lutz et al. 2011), gray line: 24 μ m MIPS magnitude from the SPIRE catalogue (Roseboom et al. 2010), green line: r band from the spectroscopic DEEP2 Galaxy Redshift Survey catalogue (Coil et al. 2004), black line: i' magnitude from the CFHTLS T0004 D3 photo-z catalogue (Coupon et al. 2009).

4.2.1 Photometric catalogues

Five different photometric catalogues were used to complement in X-Rays, UV and IR the nuclear catalogue of OTELO, which initially only comprised optical information.

In X-rays, the catalogue from Pović et al. (2009) was employed. This catalogue was obtained by OTELO's team in order to have a morphological classification of the X-Rays emitters in the field. It is based on public data from the Chandra Data Archive⁵ in 5 bands: full (0.5–7 keV), soft (0.5–2 keV), hard (2–7 keV), hard2 (2–4.5 keV), and vhard (4–7 keV). The catalogue contains 639 sources, of which 74 fall in OTELO's field

⁵See <http://asc.harvard.edu/cda/>.

Este documento incorpora firma electrónica, y es copia auténtica de un documento electrónico archivado por la ULL según la Ley 39/2015. Su autenticidad puede ser contrastada en la siguiente dirección https://sede.ull.es/validacion/		
Identificador del documento: 969870		Código de verificación: 8KFVZkZp
Firmado por: MARINA RAMÓN PÉREZ UNIVERSIDAD DE LA LAGUNA	Fecha: 28/06/2017 21:15:24	
ANGEL MANUEL BONGIOVANNI PEREZ UNIVERSIDAD DE LA LAGUNA	29/06/2017 09:30:15	
JORGE CEPA NOGUE UNIVERSIDAD DE LA LAGUNA	29/06/2017 09:33:05	
ANA MARIA PEREZ GARCIA UNIVERSIDAD DE LA LAGUNA	29/06/2017 11:12:35	
ERNESTO PEREDA DE PABLO UNIVERSIDAD DE LA LAGUNA	04/07/2017 18:28:07	

of view. Their astrometrical error is $0.7''$. Another catalogue in X-Rays, the AEGIS-X catalogue (Laird et al. 2009), was also used to increase the number of X-Rays emitters. This catalogue is also composed of data from the Chandra observatory and comprises 1325 sources in the Extended Groth Strip, 50 of them in our field. The fluxes are measured in 4 bands: full (0.5–7 keV), soft (0.5–2 keV), hard (2–7 keV) and ultrahard (5–7 keV). As can be seen in Figure 4.6, most of the sources from the AEGIS-X catalogue coincide with the sources from Pović et al. (2009). Both X-Rays catalogues were first cross-matched to each other with search radii up to 2.5 arcsec (corresponding to 2.5 times the quadratic sum of their positional errors) using TOPCAT⁶, in order to ensure the matching of coinciding sources. In this range, 42 sources had a match, of which more than 90% were closer than $0.5''$ from their counterpart and could thus be taken as secure matches, considering that both catalogues cover the same spectral range and have similar astrometrical errors. Based on that, a new X-Ray catalogue was constructed, including those 42 sources plus the remaining 32 sources from Pović et al. (2009) and the 8 sources from Laird et al. (2009). In the case of the 42 coinciding sources, Pović et al.'s coordinates were kept, as well as the largest astrometrical error of both catalogues.

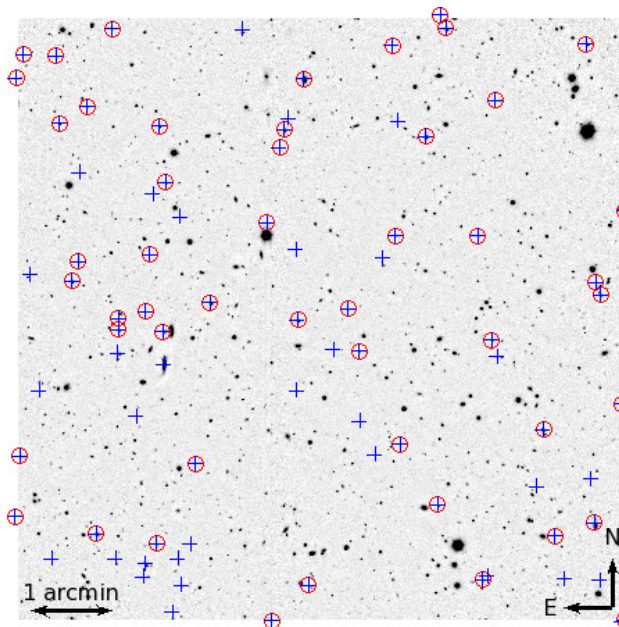


Figure 4.6: Spatial distribution of X-Rays sources in OTELO's field of view. The blue crosses correspond to the sources in the catalogue of Pović et al. (2009), while the red open circles indicate the ones from Laird et al. (2009).

In the UV, we employed data from the Galaxy Evolution Explorer orbiting telescope (GALEX, Martin et al. 2005), collected as part of the AEGIS survey. We used a version of the UV catalogue with deblended sources⁷ in order to avoid problems of multiple matches between its sources and ours. This catalogue comprises 5185

⁶Tool for Operations on Catalogues And Tables (see Taylor 2005).

⁷The deblending was performed using the CFHTLS catalogue. This catalogue has not been published but can be downloaded from <http://www.galex.caltech.edu/researcher/techdoc-ch5a.html>.

Este documento incorpora firma electrónica, y es copia auténtica de un documento electrónico archivado por la ULL según la Ley 39/2015. Su autenticidad puede ser contrastada en la siguiente dirección https://sede.ull.es/validacion/		
Identificador del documento: 969870	Código de verificación: 8KFVZkZp	
Firmado por: MARINA RAMÓN PÉREZ UNIVERSIDAD DE LA LAGUNA		Fecha: 28/06/2017 21:15:24
ANGEL MANUEL BONGIOVANNI PEREZ UNIVERSIDAD DE LA LAGUNA		29/06/2017 09:30:15
JORGE CEPA NOGUE UNIVERSIDAD DE LA LAGUNA		29/06/2017 09:33:05
ANA MARIA PEREZ GARCIA UNIVERSIDAD DE LA LAGUNA		29/06/2017 11:12:35
ERNESTO PEREDA DE PABLO UNIVERSIDAD DE LA LAGUNA		04/07/2017 18:28:07

objects only in our field. An astrometrical error of $0.59''$ was adopted both in NUV and FUV bands, in order to take into account the maximum astrometrical error as described by Morrissey et al. (2007).

In the infrared, we used data from the Herschel Space Observatory and from the Spitzer Space Telescope (hereafter Herschel and Spitzer; see Pilbratt et al. 2010 and Werner et al. 2004, respectively). We employed the first full public data release from the PACS⁸ Evolutionary Probe (PEP) survey of Herschel, which includes data in the Extended Groth Strip (Lutz et al. 2011). This catalogue uses the $24\ \mu\text{m}$ MIPS⁹ band of Spitzer as a prior to select the 100 and $160\ \mu\text{m}$ PACS bands. 553 objects from this catalogue fall within OTELO's field of view. According to Lutz et al. (2011), the astrometry precision of the catalogue is below one arcsecond, hence we adopted a maximum positional error of $1.0''$ for those sources.

We also took advantage of the third data release of the Herschel Multi-Tiered Extragalactic Survey (HerMES, Oliver et al. 2012), which makes use of the SPIRE¹⁰ instrument on board the Herschel Space Observatory. This catalogue employs the $24\ \mu\text{m}$ MIPS band as a prior to select the 250 , 350 and $500\ \mu\text{m}$ bands. It contains 822 sources in OTELO's field with an astrometrical precision of $0.5''$ (Roseboom et al. 2010).

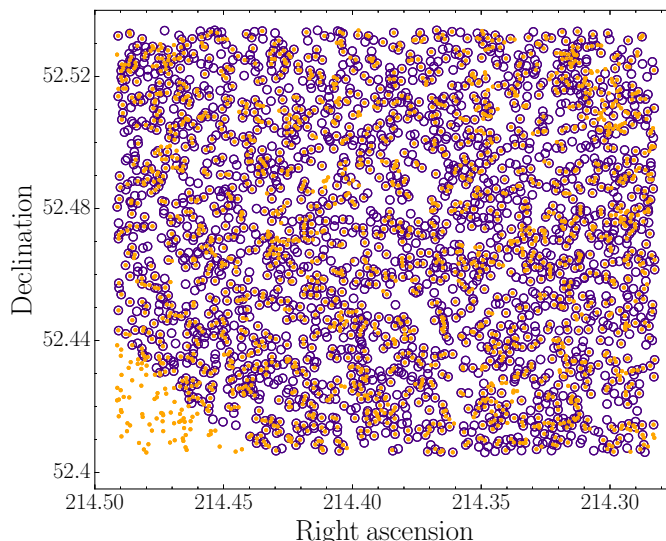


Figure 4.7: Spatial distribution of IRAC sources in OTELO's field of view. The orange dots correspond to the sources in the catalogue of Barro et al. (2011), while the purple open circles indicate the ones from Barmby et al.'s catalogue (2008). Note how the lower left corner of the field is not covered by the latter.

As for Spitzer, we initially employed the IRAC¹¹ $3.6\ \mu\text{m}$ -selected catalogue of the Extended Groth Strip from Barmby et al. 2008, which contains the 4 IRAC bands (3.6 , 4.5 , 5.8 and $8\ \mu\text{m}$) and 2374 objects in our field with a precision in astrometry of $0.37''$. However, this catalogue does not comprise the lower left corner of our field and has extremely large errors in magnitude for the faintest sources, as can be seen in figures 4.7 and

⁸Photoconductor Array Camera and Spectrometer (Poglitsch et al. 2010).

⁹Multiband Imaging Photometer (Rieke et al. 2004).

¹⁰Spectral and Photometric Imaging Receiver (Griffin et al. 2008).

¹¹InfraRed Array Camera (Fazio et al. 2004).

Este documento incorpora firma electrónica, y es copia auténtica de un documento electrónico archivado por la ULL según la Ley 39/2015. Su autenticidad puede ser contrastada en la siguiente dirección https://sede.ull.es/validacion/		
Identificador del documento:	969870	Código de verificación: 8KFVZkZp
Firmado por:	MARINA RAMÓN PÉREZ UNIVERSIDAD DE LA LAGUNA	Fecha: 28/06/2017 21:15:24
	ANGEL MANUEL BONGIOVANNI PEREZ UNIVERSIDAD DE LA LAGUNA	29/06/2017 09:30:15
	JORGE CEPA NOGUE UNIVERSIDAD DE LA LAGUNA	29/06/2017 09:33:05
	ANA MARIA PEREZ GARCIA UNIVERSIDAD DE LA LAGUNA	29/06/2017 11:12:35
	ERNESTO PEREDA DE PABLO UNIVERSIDAD DE LA LAGUNA	04/07/2017 18:28:07

4.8. We therefore added the catalogue made by Barro et al. in 2011, that comprises 2317 sources in our field selected over the $3.6\mu\text{m}$ and $4.5\mu\text{m}$ IRAC images and measured with aperture photometry. We cross-matched these two catalogues with our own independently, and when both had a match we favored Barro et al. (2011) photometry.

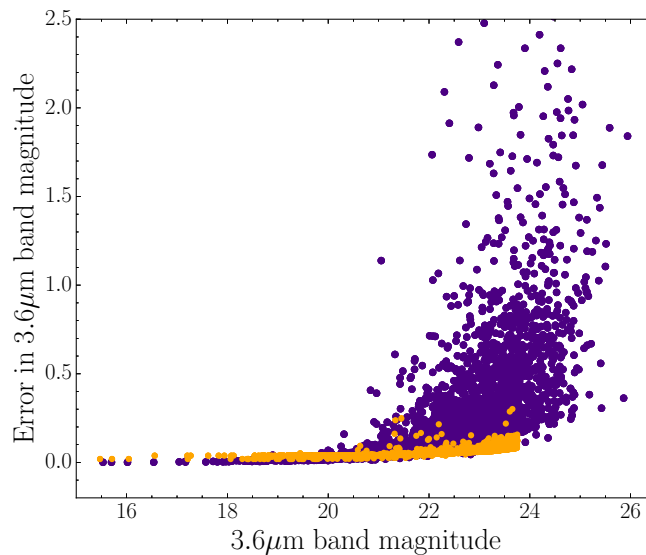


Figure 4.8: Errors in the IRAC $3.6\mu\text{m}$ band magnitude, from Barmby et al. 2008 (purple) and from Barro et al. 2011 (orange). Although the latter does not comprise sources over 24 magnitudes, its errors are smaller and thus preferable.

4.2.2 Redshift catalogues

In order to facilitate the subsequent identification and analysis of the sources found in OTELO's field of view, two public redshift catalogues were employed to add this information to the final multiwavelength catalogue. The photometric and spectroscopic redshifts gathered in these catalogues, when paired to OTELO's sources, allowed for the verification of our own derived redshifts.

The first redshift catalogue was the CFHTLS T0004 Deep3 photo-z catalogue (Coupon et al. 2009), distributed by the TERAPIX¹² centre. It contains more than 500,000 sources with photometric redshifts in an area of 0.83 deg^2 . In OTELO's field of view, this catalogue includes 7725 sources. The mean RMS external error in astrometry with respect to the reference catalogue, 2MASS, is $0.24'' \pm 0.02''$ in both directions as indicated in the TERAPIX webpage. We hence considered a maximum positional error of $0.26''$ for all the sources.

The second catalogue was the 4th data release of the DEEP2 Galaxy Redshift Survey (Newman et al. 2013), which targeted over 50,000 galaxies using the Deep Extragalactic Imaging Multi-Object Spectrograph

¹²Traitement Élémentaire, Réduction et Analyse des PIXels.

(DEIMOS¹³) on the Keck II telescope of the Mauna Kea observatory (Hawaii). Those targets were selected from a broad-band photometric catalogue obtained with the Canada-France-Hawaii Telescope and had absolute errors of 0.5'', as defined by the USNO-A2.0 catalogue used for the astrometry (Coil et al. 2004). It contains 517 sources with spectroscopic redshift in OTELO's field.

The spatial distribution of sources in the UV and IR catalogues, as well as in the redshift ones can be seen in Fig. 4.9. In Fig. 4.10, all the bands included in OTELO's final multiwavelength catalogue are shown.

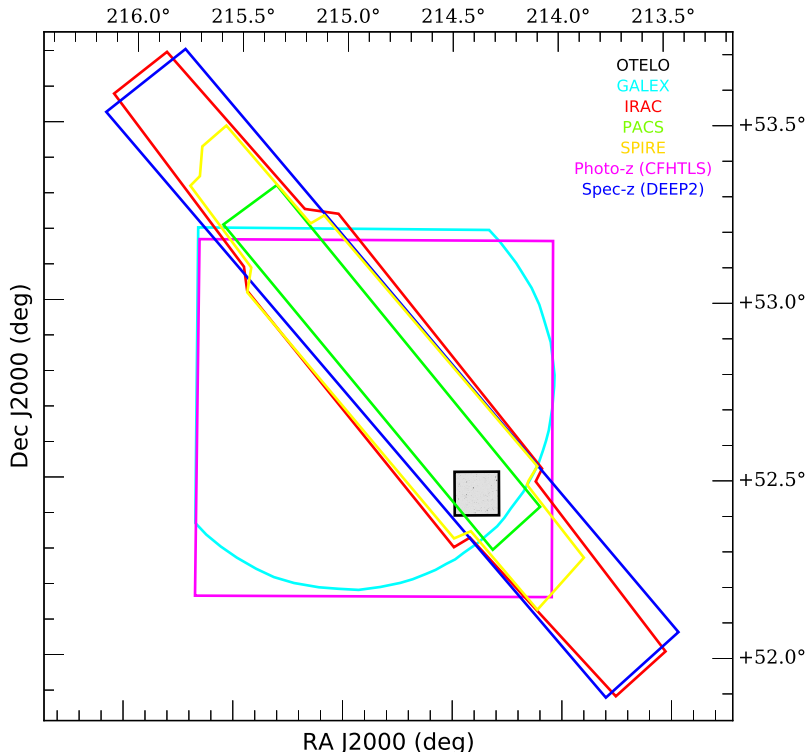


Figure 4.9: Spatial distribution of the sources in the UV, IR and redshift catalogues used to build OTELO's multiwavelength catalogue. In black: OTELO, cyan: GALEX, red: IRAC, green: PACS, yellow: SPIRE, magenta: photo-z (CFHTLS), blue: spec-z (DEEP2).

¹³See Phillips et al. (2002).

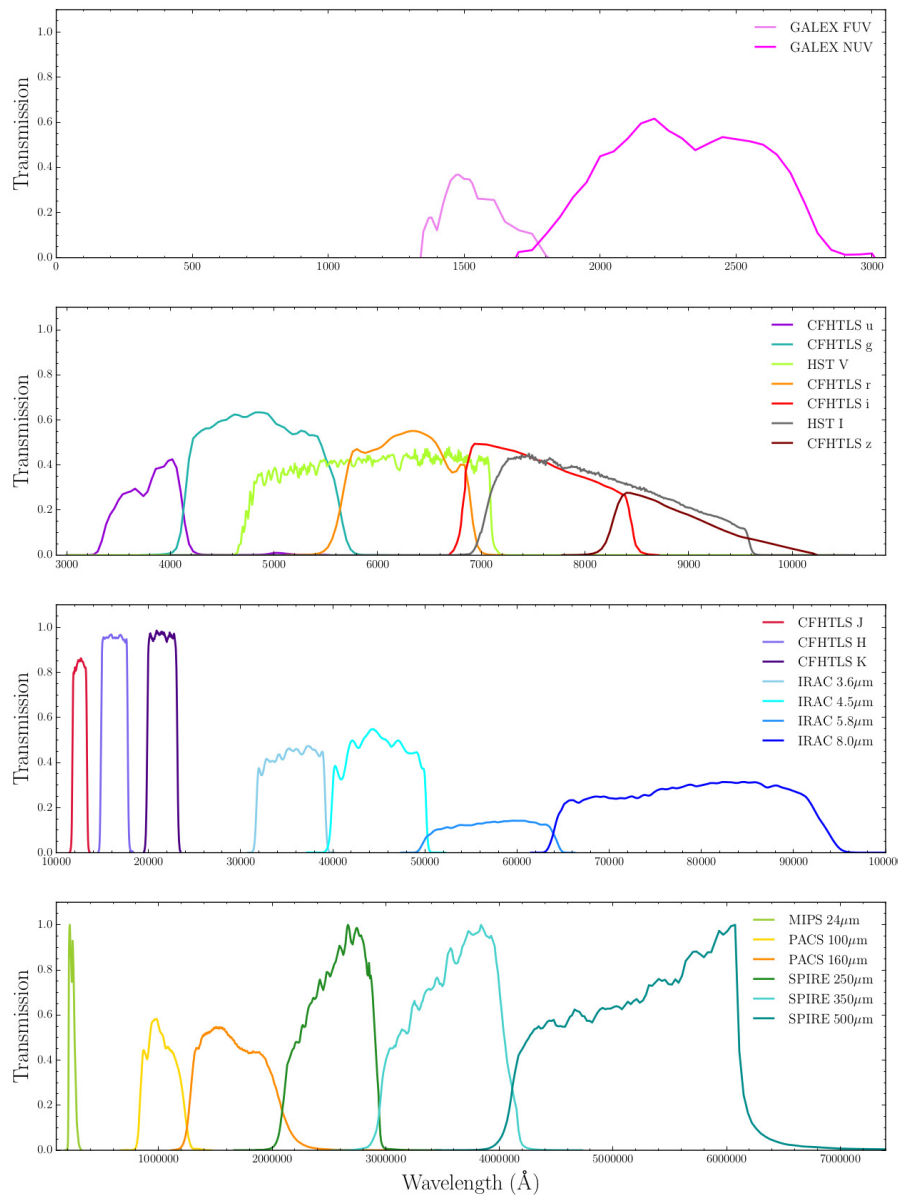


Figure 4.10: Bands included in the final OTELO's multiwavelength catalogue. From top to bottom: ultraviolet (GALEX), optical (CFHTLS and HST), mid-infrared (WIRDS and IRAC) and far-infrared (MIPS, PACS and SPIRE).

Este documento incorpora firma electrónica, y es copia auténtica de un documento electrónico archivado por la ULL según la Ley 39/2015. <i>Su autenticidad puede ser contrastada en la siguiente dirección https://sede.ull.es/validacion/</i>		
Identificador del documento:	969870	Código de verificación: 8KFVZkZp
Firmado por:	MARINA RAMÓN PÉREZ UNIVERSIDAD DE LA LAGUNA	Fecha: 28/06/2017 21:15:24
	ANGEL MANUEL BONGIOVANNI PEREZ UNIVERSIDAD DE LA LAGUNA	29/06/2017 09:30:15
	JORGE CEPA NOGUE UNIVERSIDAD DE LA LAGUNA	29/06/2017 09:33:05
	ANA MARIA PEREZ GARCIA UNIVERSIDAD DE LA LAGUNA	29/06/2017 11:12:35
	ERNESTO PEREDA DE PABLO UNIVERSIDAD DE LA LAGUNA	04/07/2017 18:28:07

4.3 Cross-matching of catalogues

Due to the variations in position, magnitude and point spread function (PSF) of the same source in different catalogues, their cross-correlation is not a straightforward task which could be easily done using a matching criterion based on the proximity of sources (as with TOPCAT). Instead, it requires a more accurate statistical analysis to determine which of the objects found at a certain radius from the original source is the correct match.

To correlate the X-Rays, UV, IR and redshift catalogues with OTELO's, we used the methodology first developed by de Ruiter et al. (1977), and then improved by Sutherland & Saunders (1992), which defines a likelihood-ratio (*LR*) to distinguish between true counterparts and false identifications. This approach has been successfully used to match sources with intrinsic uncertainties due to their different PSF, such as radio and X-Ray sources to optical or IR ones (e.g. Ciliegi et al. 2003; Luo et al. 2010; Pineau et al. 2011). Given a source detected at any other band than the optical, de Ruiter et al. (1977) described the *LR* as the ratio between the probability of finding its true optical counterpart at a certain distance, and the probability of finding a background source at that distance instead. For that, they assumed that background sources follow a Poisson distribution and took only into account the radial distance of the optical sources to the non-optical ones and the positional errors of both.

Sutherland & Saunders (1992) later introduced the magnitude information to improve the *LR* technique. They calculated not only the probability that the true counterpart laid at a given distance from the non-optical source, but also that its magnitude laid in a certain interval. In this work we have followed that approach and used the procedure developed by Pérez-Martínez, R.M. (2016), where he defines the *LR* as:

$$LR = \frac{q(m)f(r)}{n(m,r)}, \quad (4.1)$$

$q(m)$ being the magnitude distribution of the true counterparts, $f(r)$ the probability distribution function of a true counterpart being at a distance r from the object and $n(m,r)$ the surface density of background objects with the same magnitude m as the candidate.

The probability distribution $f(r)$ is a two dimensional gaussian which only depends on the positional errors of the sources and the separation between them:

$$f(r) = \frac{1}{2\pi\sigma^2} \exp\left(\frac{-r^2}{2\sigma}\right) \quad (4.2)$$

The standard deviation is $\sigma = \sqrt{\sigma_{opt} + \sigma_X}$, where σ_{opt} and σ_X are the positional errors of the optical and non-optical sources respectively, which depend, in turn, on their errors in RA and Dec.

The surface density of background objects with magnitude m , $n(m)$, is estimated for each object to be matched. It is calculated as the ratio between a certain number of sources of the same magnitude as the candidate and the area occupied by them. For this purpose and to avoid selecting true counterparts, only the 5th, 6th, 7th, 8th, 9th and 10th closest sources with magnitude m are chosen.

The magnitude distribution of the true counterparts, $q(m)$, is calculated by means of a recursive algorithm which initially selects all the sources lying within 0.5'' from the source to match. This radius is sufficiently small so that the number of background sources inside is minimum, but at the same time ensures that most of the real counterparts are contained. In other words, we assume that the sources selected in this way are good counterparts with little contamination in order to calculate the magnitude distribution of the true sources. The final distribution of $q(m)$ and $n(m)$ for each catalogue can be seen in Fig. 4.11.

Este documento incorpora firma electrónica, y es copia auténtica de un documento electrónico archivado por la ULL según la Ley 39/2015.
Su autenticidad puede ser contrastada en la siguiente dirección <https://sede.ull.es/validacion/>

Identificador del documento: 969870	Código de verificación: 8KFVZkZp
Firmado por: MARINA RAMÓN PÉREZ UNIVERSIDAD DE LA LAGUNA	Fecha: 28/06/2017 21:15:24
ANGEL MANUEL BONGIOVANNI PEREZ UNIVERSIDAD DE LA LAGUNA	29/06/2017 09:30:15
JORGE CEPA NOGUE UNIVERSIDAD DE LA LAGUNA	29/06/2017 09:33:05
ANA MARIA PEREZ GARCIA UNIVERSIDAD DE LA LAGUNA	29/06/2017 11:12:35
ERNESTO PEREDA DE PABLO UNIVERSIDAD DE LA LAGUNA	04/07/2017 18:28:07

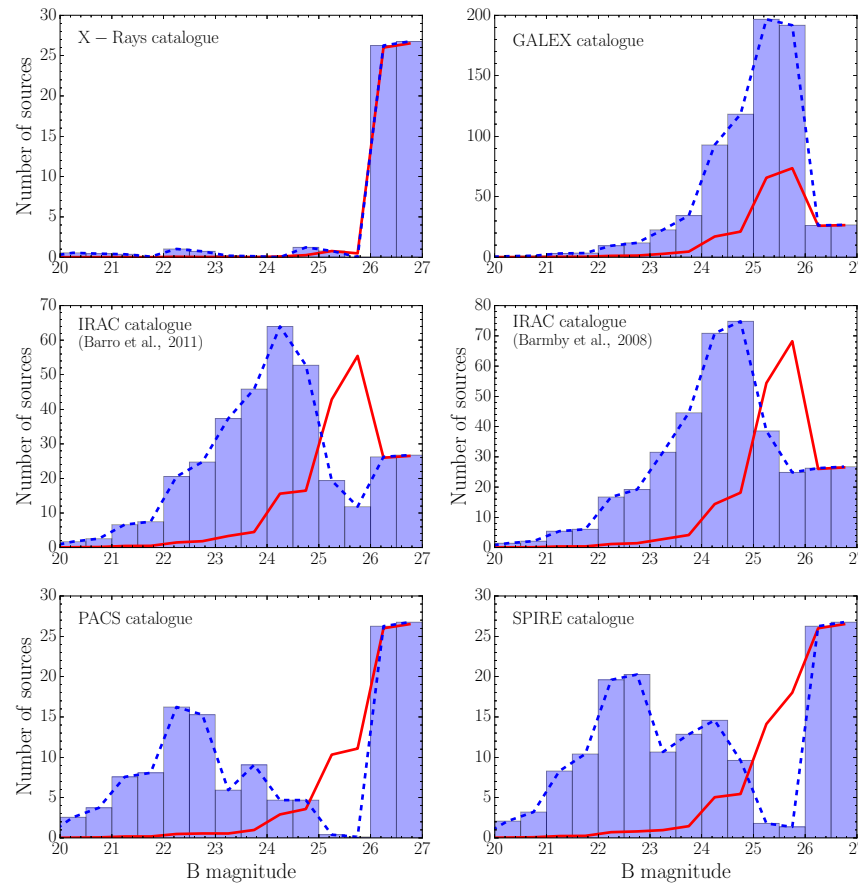


Figure 4.11: Distribution of $q(m)$ and $n(m)$ for each photometric auxiliary catalogue. The blue histogram represents the magnitude distribution of true counterparts, $q(m)$, while the blue dashed line is $q(m)$ smoothed with a boxcar average. The solid red line represents the magnitude distribution of the surface density of background objects, $n(m)$. Note how $n(m)$ peaks at fainter magnitudes than $q(m)$ in the case of the IR catalogues.

For each catalogue to match, the procedure obtains a threshold value of the likelihood-ratio (LR_{th}) above which the counterparts are reliable. Only counterparts whose LR is above LR_{th} are retained. This value is obtained by iteration, taking into account the expected magnitude distribution of the candidates, in order to maximize the sum of two parameters. The first one is the reliability R of the catalogues cross-correlation, which

Este documento incorpora firma electrónica, y es copia auténtica de un documento electrónico archivado por la ULL según la Ley 39/2015.
Su autenticidad puede ser contrastada en la siguiente dirección <https://sede.ull.es/validacion/>

Identificador del documento: 969870

Código de verificación: 8KFVZkZp

Fecha: 28/06/2017 21:15:24

Firmado por: MARINA RAMÓN PÉREZ
UNIVERSIDAD DE LA LAGUNA

29/06/2017 09:30:15

ANGEL MANUEL BONGIOVANNI PEREZ
UNIVERSIDAD DE LA LAGUNA

29/06/2017 09:33:05

JORGE CEPA NOGUE
UNIVERSIDAD DE LA LAGUNA

29/06/2017 11:12:35

ANA MARIA PÉREZ GARCIA
UNIVERSIDAD DE LA LAGUNA

04/07/2017 18:28:07

ERNESTO PEREDA DE PABLO
UNIVERSIDAD DE LA LAGUNA

is the average of the individual reliabilities R_C of each counterpart. R_C indicates the probability of a given source being the true counterpart of the source to match:

$$R_C = \frac{LR}{\sum LR + (1 - Q)}, \quad (4.3)$$

where the sum is over all the candidates found for a given source, and Q is the fraction of the true counterparts we are able to detect ($Q = \int_{-\infty}^{m_{lim}} q(m) dm$). The other parameter to maximize is the catalogue completeness, C , defined as the ratio of the sum of the reliabilities of all the sources over the total number of objects in the non optical catalogue. It gives an idea of the number of sources for which a match has been found over the total number of sources in the auxiliary catalogue:

$$C = \frac{\sum R_C}{N} \quad (4.4)$$

Fig. 4.12 shows the individual reliabilities of each counterpart, R_C , as a function of the likelihood ratio, LR . It can be seen that R_C increases rapidly with LR and reaches a constant high value for each one of the different catalogues.

Depending on the density of objects on the auxiliary catalogue, a first radial search in 2, 3 or 5 arcsec was performed. From all the sources found at that distance, only the ones with a good LR were retained after computing it for all of them with the methodology explained above. In this way, we were able to eliminate the uncertainty when multiple candidates were found. A summary of the likelihood-ratio matching parameters and results obtained after applying this procedure is shown in Table 4.3. In the particular case of the IRAC mid-infrared matches, we obtained very similar values of R and C when crossing Barmby et al. and Barro et al. catalogues with our own independently. In total, 2530 IRAC matches were found to OTELO's sources, of which 1521 belonged to both catalogues, 607 were unique to the former and 402 were unique to the latter. As we favoured Barro et al.'s photometry, the table shows the LR_{th} , R and C values of its matching. However, $N_{matches}$ shows the total number of IRAC sources that were matched using both catalogues (1521), while N_X represents the total number of unique IRAC sources considering that sources within 1 arcsec of radial distance in the two IRAC catalogues were the same.

Table 4.3: Results of the cross-correlation of catalogues. LR_{th} : value of LR used as threshold, R : reliability of the matching, C : completeness, N_X : number of sources in the non-optical catalogue and $N_{matches}$: number of reliable matches found. See text for details, specially for the mid-infrared (IRAC) case (*).

Catalogue	LR_{th}	R	C	N_X	$N_{matches}$
X-Rays	0.069	0.810	0.553	82	56
Ultraviolet	0.105	0.907	0.753	5185	4223
Mid-infrared*	0.047	0.959	0.818	3033	2530
Far-infrared (MIPS & PACS)	0.007	0.782	0.702	553	476
Far-infrared (SPIRE)	0.023	0.962	0.876	822	749
Photo-z	0.281	0.901	0.568	7725	4860
Spec-z	0.542	0.992	0.886	517	461

Finally, Fig. 4.13 shows the distribution of R_C in each auxiliary catalogue. In all of them, most of the sources have high values of R_C , proving that the overall catalogue cross-matching was well performed. The X-rays and PACS catalogue show more spread out values, meaning that their reliability is lower than that of the rest of the catalogues (but still, very high as can be seen in Table 4.3).

Este documento incorpora firma electrónica, y es copia auténtica de un documento electrónico archivado por la ULL según la Ley 39/2015. Su autenticidad puede ser contrastada en la siguiente dirección https://sede.ull.es/validacion/		
Identificador del documento: 969870		Código de verificación: 8KFVZkZp
Firmado por: MARINA RAMÓN PÉREZ UNIVERSIDAD DE LA LAGUNA	Fecha: 28/06/2017 21:15:24	
ANGEL MANUEL BONGIOVANNI PEREZ UNIVERSIDAD DE LA LAGUNA	29/06/2017 09:30:15	
JORGE CEPA NOGUE UNIVERSIDAD DE LA LAGUNA	29/06/2017 09:33:05	
ANA MARIA PEREZ GARCIA UNIVERSIDAD DE LA LAGUNA	29/06/2017 11:12:35	
ERNESTO PEREDA DE PABLO UNIVERSIDAD DE LA LAGUNA	04/07/2017 18:28:07	

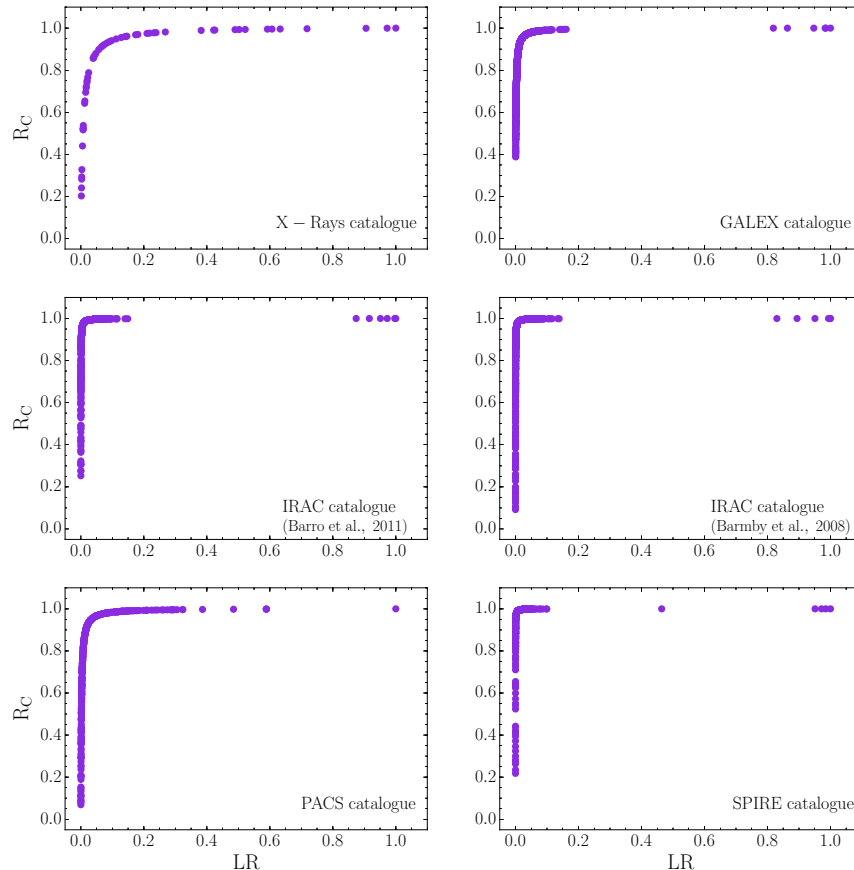


Figure 4.12: Individual reliabilities of each counterpart, R_C , as a function of the likelihood ratio, LR (normalised), for each one of the photometric auxiliary catalogues. Note how R_C increases with LR , rapidly reaching a constant high value.

Este documento incorpora firma electrónica, y es copia auténtica de un documento electrónico archivado por la ULL según la Ley 39/2015.
Su autenticidad puede ser contrastada en la siguiente dirección <https://sede.ull.es/validacion/>

Identificador del documento: 969870

Código de verificación: 8KFVZkZp

Firmado por: MARINA RAMÓN PÉREZ
UNIVERSIDAD DE LA LAGUNA

Fecha: 28/06/2017 21:15:24

ANGEL MANUEL BONGIOVANNI PEREZ
UNIVERSIDAD DE LA LAGUNA

29/06/2017 09:30:15

JORGE CEPA NOGUE
UNIVERSIDAD DE LA LAGUNA

29/06/2017 09:33:05

ANA MARIA PEREZ GARCIA
UNIVERSIDAD DE LA LAGUNA

29/06/2017 11:12:35

ERNESTO PEREDA DE PABLO
UNIVERSIDAD DE LA LAGUNA

04/07/2017 18:28:07

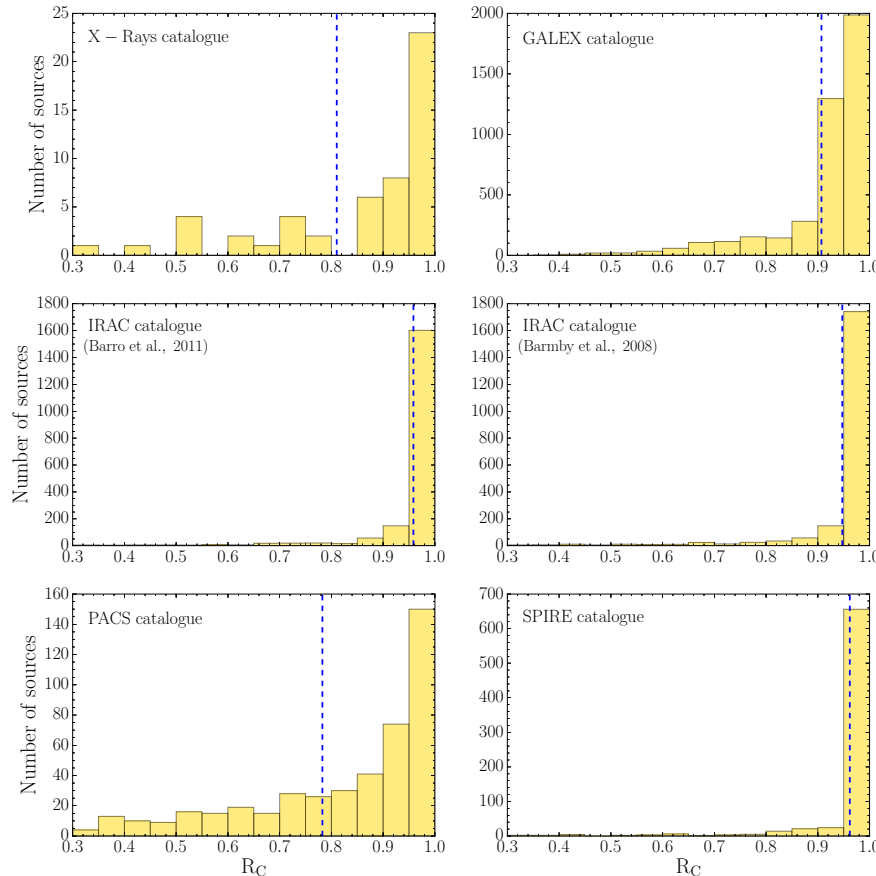


Figure 4.13: Distribution of individual reliabilities, R_C , in each one of the photometric auxiliary catalogues. The blue dashed lines represent the value of R as in Table 4.3. In all the cases, most of the sources have high values of R_C , proving that the overall catalogue cross-matching was well performed.

Este documento incorpora firma electrónica, y es copia auténtica de un documento electrónico archivado por la ULL según la Ley 39/2015.
Su autenticidad puede ser contrastada en la siguiente dirección <https://sede.ull.es/validacion/>

Identificador del documento: 969870

Código de verificación: 8KFVZkZp

Firmado por: MARINA RAMÓN PÉREZ
UNIVERSIDAD DE LA LAGUNA

Fecha: 28/06/2017 21:15:24

ANGEL MANUEL BONGIOVANNI PEREZ
UNIVERSIDAD DE LA LAGUNA

29/06/2017 09:30:15

JORGE CEPA NOGUE
UNIVERSIDAD DE LA LAGUNA

29/06/2017 09:33:05

ANA MARIA PEREZ GARCIA
UNIVERSIDAD DE LA LAGUNA

29/06/2017 11:12:35

ERNESTO PEREDA DE PABLO
UNIVERSIDAD DE LA LAGUNA

04/07/2017 18:28:07

4.4 OTELO's final multiwavelength catalogue: a summary

The final catalogue of OTELO comprises 11237 sources detected over its deep image up to 0.73σ (see Fig. 4.14). This is the raw catalogue as extracted by SExtractor (see section 3.3.2), without discarding possible spurious objects. The limiting flux of the catalogue, integrated over all the slices of the tomography, is 6.8×10^{-18} erg/s/cm² at 3σ , which corresponds to a limiting AB magnitude of 26.50. The completeness flux, the flux up to which a complete sample of the objects in the field is obtained, is given by the peak of the distribution of fluxes and corresponds to 1.08×10^{-17} erg/s/cm², i.e., an AB magnitude of 26. This includes 8055 sources. The distribution of AB magnitudes can be seen in the histogram plotted in Fig. 4.15. Both the limiting and the completeness magnitudes are also shown.

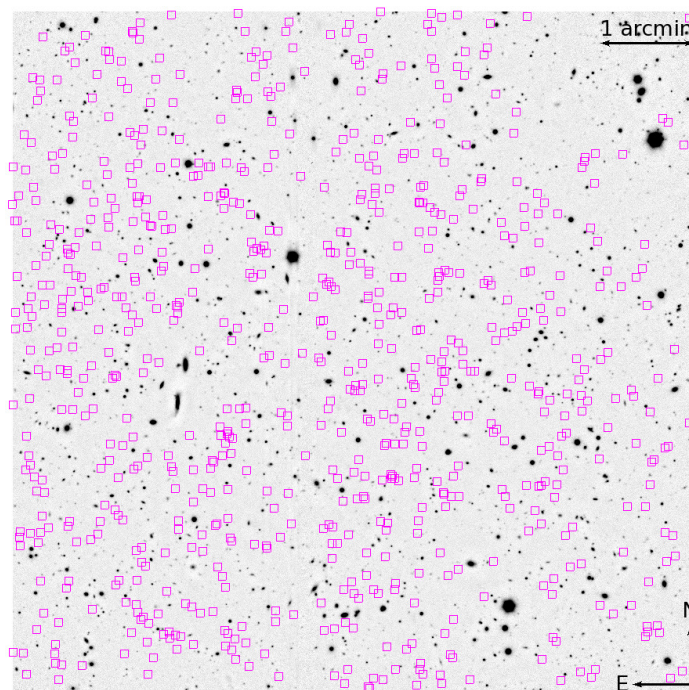


Figure 4.14: Distribution of OTELO's sources with integrated magnitude over 26.5.

OTELO's deep data have been supplemented with detailed photometry measurements of the 11237 detected sources over CFHTLS, HST and WIRDS images, obtaining 10 additional bands: u, g, r, i, z (CFHTLS), V, I (HST) and J, H, K_s (WIRDS). More than 95% of OTELO's sources have complementary photometry in these bands.

Furthermore, this nuclear catalogue has been cross-matched to 8 ancillary public catalogues, which comprise data from X-Rays to FIR from the Space Observatories Chandra, Galex, Spitzer and Herschel, as well as both photometric and spectroscopic redshift catalogues from the CFHTLS Deep3 and DEEP2 surveys. An extract from the final catalogue is shown in Tables 4.4 and 4.5.

Este documento incorpora firma electrónica, y es copia auténtica de un documento electrónico archivado por la ULL según la Ley 39/2015.
Su autenticidad puede ser contrastada en la siguiente dirección <https://sede.ull.es/validacion/>

Identificador del documento:	969870	Código de verificación:	8KFVZkZp
Firmado por:	MARINA RAMÓN PÉREZ UNIVERSIDAD DE LA LAGUNA	Fecha:	28/06/2017 21:15:24
	ANGEL MANUEL BONGIOVANNI PEREZ UNIVERSIDAD DE LA LAGUNA		29/06/2017 09:30:15
	JORGE CEPA NOGUE UNIVERSIDAD DE LA LAGUNA		29/06/2017 09:33:05
	ANA MARIA PEREZ GARCIA UNIVERSIDAD DE LA LAGUNA		29/06/2017 11:12:35
	ERNESTO PEREDA DE PABLO UNIVERSIDAD DE LA LAGUNA		04/07/2017 18:28:07

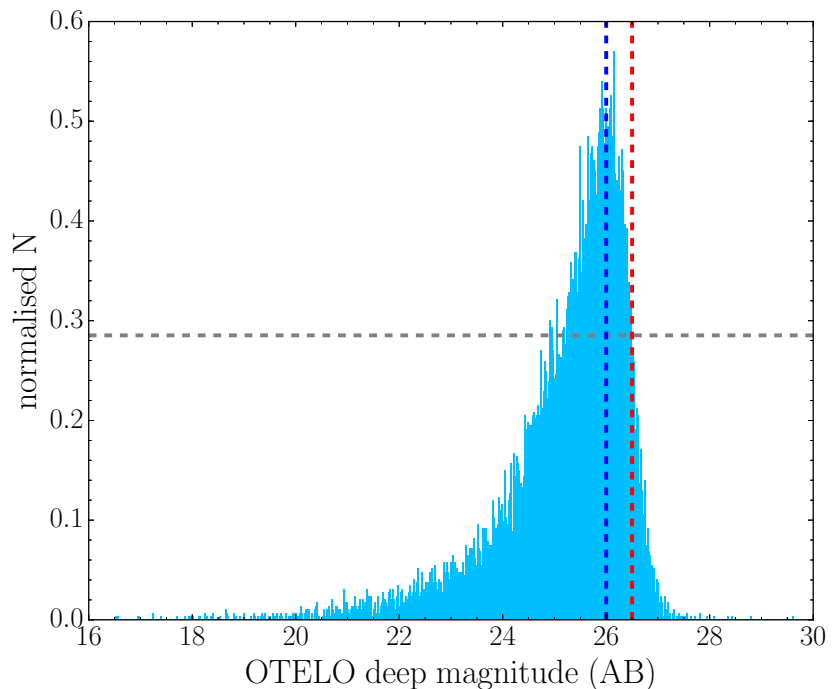


Figure 4.15: Distribution of the integrated magnitudes of OTELO's sources as measured in its deep image. The limiting AB magnitude at 3σ and 50% completeness is ~ 26.5 (red line), while the 100% completeness AB magnitude is ~ 26 (blue line). The grey dashed line represents the half maximum value of the distribution.

Este documento incorpora firma electrónica, y es copia auténtica de un documento electrónico archivado por la ULL según la Ley 39/2015.
Su autenticidad puede ser contrastada en la siguiente dirección <https://sede.ull.es/validacion/>

Identificador del documento: 969870

Código de verificación: 8KFVZkZp

Firmado por: MARINA RAMÓN PÉREZ
UNIVERSIDAD DE LA LAGUNA

Fecha: 28/06/2017 21:15:24

ANGEL MANUEL BONGIOVANNI PEREZ
UNIVERSIDAD DE LA LAGUNA

29/06/2017 09:30:15

JORGE CEPA NOGUE
UNIVERSIDAD DE LA LAGUNA

29/06/2017 09:33:05

ANA MARIA PEREZ GARCIA
UNIVERSIDAD DE LA LAGUNA

29/06/2017 11:12:35

ERNESTO PEREDA DE PABLO
UNIVERSIDAD DE LA LAGUNA

04/07/2017 18:28:07

Table 4.4: OTELO's catalogue (Part I)

First columns of OTELO's catalogue: OTELO's id, coordinates and measurements performed with SExtractor over OTELO's deep image (see section 3.3).
 (1): OTELO's identification number, (2) and (3): logical coordinates of the object in OTELO's deep image, (4) and (5): rectangular coordinates (J2000.0) of the object in OTELO's deep image, (6): magnitude from the detection model-fitting in the deep band [AB], (7): RMS error of the detection model-fitting magnitude [AB], (8): spread parameter from model-fitting, (9): spread parameter error from model-fitting, (10): SExtractor star/galaxy classifier output and (11): extraction flags.

idobj	x	y	ra	dec	dmodelID	edmodelID	spreadmD	espreadmD	clasD	iflagD
(1)	(2)	(3)	(4)	(5)	(6)	(7)	(8)	(9)	(10)	(11)
1	814.617	106.755	214.394452	52.4162826	18.804	6.0E-4	-0.001	5.52E-6	0.986	0

X-rays and UV measurements taken from the auxiliary catalogues (see section 4.2). Columns (1)-(6) are just a sample of the X-rays bands included in OTELO's catalogue, see subsection 4.2.1 for more details.
 (1): flux in the full band (0.5-7 keV) [erg/cm²/s], (2): error in the full band [erg/cm²/s], (3): flux in the soft band (0.5-2 keV) [erg/cm²/s], (4): error in the soft band [erg/cm²/s], (5): flux in the hard band (2-7 keV) [erg/cm²/s], (6): error in the hard band [erg/cm²/s], (7): deblended FUV flux [AB], (8): deblended FUV flux error [AB], (9): deblended NUV flux [AB], (10): deblended NUV flux error [AB].

fluxFULL	efluxFULL	fluxSOFT	efluxSOFT	fluxHARD	efluxHARD	FUV_DB	FUV_DB_ERR	NUV_DB	NUV_DB_ERR
(1)	(2)	(3)	(4)	(5)	(6)	(7)	(8)	(9)	(10)
99.0	.99.0	.99.0	.99.0	.99.0	.99.0	27.071	0.782	29.697	8.018

Este documento incorpora firma electrónica, y es copia auténtica de un documento electrónico archivado por la ULL según la Ley 39/2015.
Su autenticidad puede ser contrastada en la siguiente dirección <https://sede.ull.es/validacion/>

Identificador del documento: 969870 Código de verificación: 8KFVZkZp

Firmado por: MARINA RAMÓN PÉREZ UNIVERSIDAD DE LA LAGUNA	Fecha: 28/06/2017 21:15:24
ANGEL MANUEL BONGIOVANNI PEREZ UNIVERSIDAD DE LA LAGUNA	29/06/2017 09:30:15
JORGE CEPA NOGUE UNIVERSIDAD DE LA LAGUNA	29/06/2017 09:33:05
ANA MARIA PEREZ GARCIA UNIVERSIDAD DE LA LAGUNA	29/06/2017 11:12:35
ERNESTO PEREDA DE PABLO UNIVERSIDAD DE LA LAGUNA	04/07/2017 18:28:07

Table 4.5: OTELO's catalogue (Part II)

Optical/NIR measurements performed with SExtractor over the ancillary data images (see section 4.1) and MIR measurements taken from the auxiliary catalogues (see section 4.2).
 (1): magnitude from the detection model-fitting in the X band [AB], (2): RMS error of the detection model-fitting magnitude [AB], (3): spread parameter from model-fitting, (4): spread parameter error from model-fitting, (5): SExtractor star/galaxy classifier output, (6): extraction flags, (7) magnitude in the IRAC 3.6 μm band [AB], (8): magnitude error in the IRAC 3.6 μm band [AB], (9) magnitude in the IRAC 4.5 μm band [AB], (10): magnitude error in the IRAC 4.5 μm band [AB], (11) magnitude in the IRAC 5.8 μm band [AB], (12): magnitude error in the IRAC 5.8 μm band [AB], (13) magnitude in the IRAC 8.0 μm band [AB] and (14): magnitude error in the IRAC 8.0 μm band [AB]. Columns (1)-(6) are repeated for each one of the following bands (X): u=CFHTLS u, g=CFHTLS g, r=CFHTLS r, i=CFHTLS i, z=CFHTLS z, hstV=ACS 606W, hstI=ACS 814W, j=WIRDS J, h=WIRDS H and k=s=WIRDS Ks. In this table, X = u.

dmodelX (1)	edmodelX (2)	spreadnX (3)	espreadnX (4)	clasX (5)	iflagX (6)	mag36 (7)	e_mag36 (8)	mag45 (9)	e_mag45 (10)	mag58 (11)	e_mag58 (12)	mag80 (13)	e_mag80 (14)
23.654	0.005	-8.353E-4	5.192E-5	0.972	0	19.884	0.039	20.284	0.037	20.717	0.046	21.336	0.080

FIR measurements (see section 4.2) and redshift information (see section 4.2.2) taken from the auxiliary catalogues.
 (1): magnitude in the MIPS 24 μm band [AB], (2): magnitude error in the MIPS 24 μm band [AB], (3): magnitude in the PACS 100 μm band [AB], (4): magnitude error in the PACS 100 μm band [AB], (5): magnitude in the PACS 160 μm band [AB], (6): magnitude error in the PACS 160 μm band [AB], (7): magnitude in the SPIRE 250 μm band [AB], (8): magnitude error in the SPIRE 250 μm band [AB], (9): photometric redshift from the CFHTLS T0004 Deep3 survey, (10): spectroscopic redshift from the DEEP2 Galaxy Redshift Survey and (11): object's type as classified in the DEEP2 Galaxy Redshift Survey.

MAG_24 (1)	MAGERR_24 (2)	MAG_100 (3)	MAGERR_100 (4)	MAG_160 (5)	MAGERR_160 (6)	MAG_250 (7)	MAGERR_250 (8)	photoZ (9)	specZBest (10)	specZclass (11)
99.0	-99.0	-99.0	-99.0	-99.0	-99.0	-99.0	-99.0	0	-99.0	'-99'

Este documento incorpora firma electrónica, y es copia auténtica de un documento electrónico archivado por la ULL según la Ley 39/2015.
Su autenticidad puede ser contrastada en la siguiente dirección <https://sede.ull.es/validacion/>

Identificador del documento: 969870

Código de verificación: 8KFVZkZp

Fecha: 28/06/2017 21:15:24

Firmado por: MARINA RAMÓN PÉREZ
UNIVERSIDAD DE LA LAGUNA

29/06/2017 09:30:15

ANGEL MANUEL BONGIOVANNI PEREZ
UNIVERSIDAD DE LA LAGUNA

29/06/2017 09:33:05

JORGE CEPA NOGUE
UNIVERSIDAD DE LA LAGUNA

29/06/2017 11:12:35

ANA MARIA PEREZ GARCIA
UNIVERSIDAD DE LA LAGUNA

04/07/2017 18:28:07

ERNESTO PEREDA DE PABLO
UNIVERSIDAD DE LA LAGUNA

5

SELECTION AND IDENTIFICATION OF H α EMITTERS

In this Chapter, the selection of emitting objects in OTELO's catalogue is described, as well as the identification of H α emitters. The first process requires various steps: first, the application of an automatic algorithm, then a visual inspection of the candidates and finally their classification into different categories. The methodology followed to obtain photometric redshifts is also explained, as well as the obtention of colour-colour diagrams to segregate different chemical species. Finally, the identification of H α emitters using all the information available is described.

For the purpose of this thesis, the objects showing emission lines in OTELO's catalogue, and in particular the H α emitters, had to be identified in order to study in detail the AGN population in the field. This selection and subsequent identification is thus a necessary step which must be carried out with care so as not to leave any interesting object behind.

5.1 Selection of emitting objects

The selection of the emitting objects in OTELO's field of view is made in two steps. In the first part of the process, an automatic algorithm is used in order to roughly select the possible emission-line candidates, hereafter referred to as 'ELC'. The next step is to visually inspect these candidates so as to determine whether they are true emitting objects, and to classify them into categories.

5.1.1 Pre-selection of candidates

The pre-selection of emitting candidates was performed using an automatic algorithm based on the one used by Sánchez-Portal et al. (2015). For a given pseudo-spectrum, this algorithm defines a pseudo-continuum based on a subset of sampled points which remain within 2σ around the median value of the whole pseudo-spectrum. A pseudo-continuum level f_{cont} (the median value) and noise σ_{cont} (the standard deviation) for each pseudo-spectrum are then computed. A bound value above which a flux excess could be considered as part of an emission line is defined as $f_{cont} + 2\sigma_{cont}$.

To determine if an object can be considered as an ELC by this algorithm, it has to fulfil one of the two following criteria: either two contiguous points of the pseudo-spectrum are above the upper value, or only one is above it but it has an adjacent point above $f_{cont} + \sigma_{cont}$ and another one above f_{cont} (see Figure 5.1).

Este documento incorpora firma electrónica, y es copia auténtica de un documento electrónico archivado por la ULL según la Ley 39/2015. Su autenticidad puede ser contrastada en la siguiente dirección https://sede.ull.es/validacion/		
Identificador del documento:	969870	Código de verificación: 8KFVZkZp
Firmado por:	MARINA RAMÓN PÉREZ UNIVERSIDAD DE LA LAGUNA	Fecha: 28/06/2017 21:15:24
	ANGEL MANUEL BONGIOVANNI PEREZ UNIVERSIDAD DE LA LAGUNA	29/06/2017 09:30:15
	JORGE CEPA NOGUE UNIVERSIDAD DE LA LAGUNA	29/06/2017 09:33:05
	ANA MARIA PEREZ GARCIA UNIVERSIDAD DE LA LAGUNA	29/06/2017 11:12:35
	ERNESTO PEREDA DE PABLO UNIVERSIDAD DE LA LAGUNA	04/07/2017 18:28:07

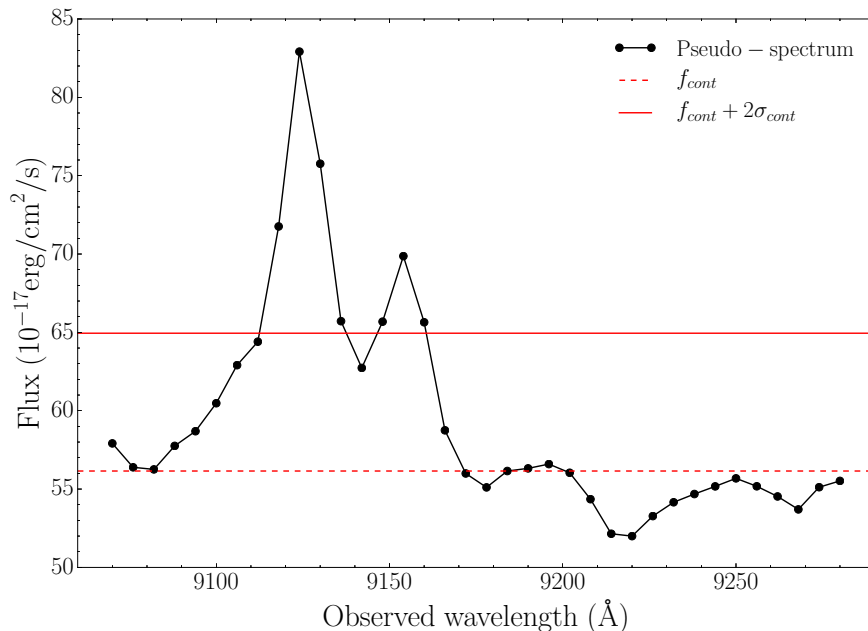


Figure 5.1: Convolution of a SDSS spectrum showing H α +[NII] emission with OSIRIS’s Tunable Filters spectral response, yielding a simulation of a pseudo-spectrum.. The red dashed line represents the pseudo-continuum, f_{cont} , defined as the median value of the pseudo-spectrum points which remain within 2σ around the median value of the whole pseudo-spectrum. The red continuous line represents $f_{cont} + 2\sigma_{cont}$, where σ_{cont} is the standard deviation of the pseudo-continuum points. The automatic algorithm used for the first pre-selection of ELC looks either for two contiguous points above the upper value, or for one above it with an adjacent point above $f_{cont} + \sigma_{cont}$ and another one above f_{cont} .

In order to determine the reliability of this automatic selection of ELC, a test was made using real spectra showing the H α emission line. 207 spectra of galaxies from the Sloan Digital Sky Survey (SDSS) with redshifts up to 0.37 and different ranges of S/N were used for this purpose. The redshift range was chosen so as to make sure that the H α line would appear in the spectral range of SDSS (4000-9000Å). The spectra were then redshifted to $z \sim 0.39$, which is the expected value at which H α would appear in OTELO’s window, and convolved to the spectral response of the tunable filters. An example of such a convolution can be seen in Figure 5.2. After being analysed by the algorithm, 194 of the 207 pseudo-spectra were classified as having an emission feature, i.e, almost 94% of the total, and only 13 were discarded (6.4%).

As seen by the test with SDSS spectra, the automatic algorithm is a good way to effectively select almost all of the possible ELC of a sample. However, it may also introduce a non-negligible number of false detections. Therefore, it is essential to verify and confirm by additional means the candidate pre-selection performed by the automatic algorithm. From the 11237 objects of OTELO’s raw catalogue, 6968 objects were pre-selected in this way as ELC (62% of the total), while 4269 were rejected (38%). The next step was to visually inspect those 6968 objects in order to classify them.

Este documento incorpora firma electrónica, y es copia auténtica de un documento electrónico archivado por la ULL según la Ley 39/2015.
Su autenticidad puede ser contrastada en la siguiente dirección <https://sede.ull.es/validacion/>

Identificador del documento:	969870	Código de verificación:	8KFVZkZp
Firmado por:	MARINA RAMÓN PÉREZ UNIVERSIDAD DE LA LAGUNA	Fecha:	28/06/2017 21:15:24
	ANGEL MANUEL BONGIOVANNI PEREZ UNIVERSIDAD DE LA LAGUNA		29/06/2017 09:30:15
	JORGE CEPA NOGUE UNIVERSIDAD DE LA LAGUNA		29/06/2017 09:33:05
	ANA MARIA PEREZ GARCIA UNIVERSIDAD DE LA LAGUNA		29/06/2017 11:12:35
	ERNESTO PEREDA DE PABLO UNIVERSIDAD DE LA LAGUNA		04/07/2017 18:28:07

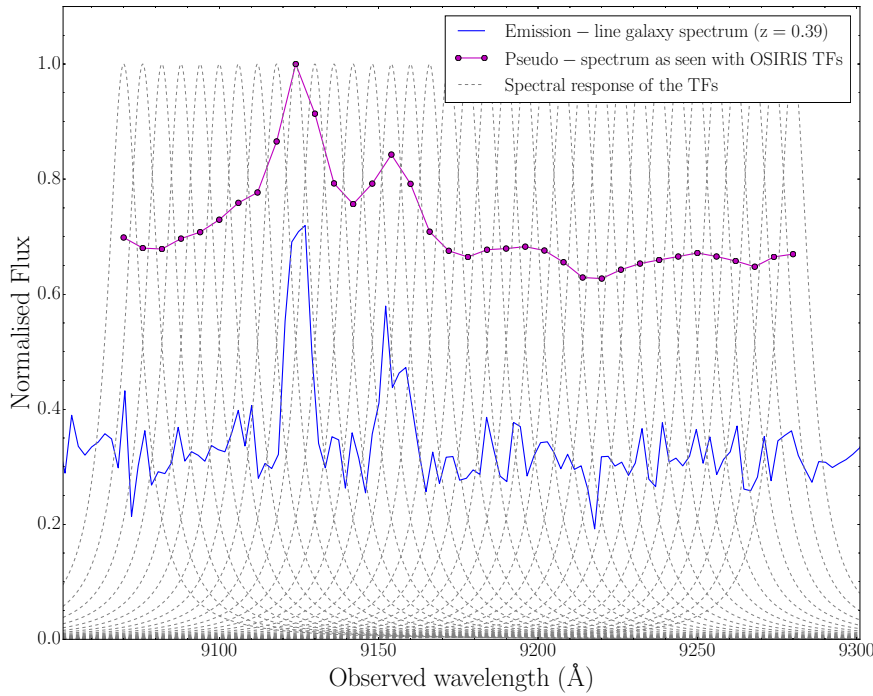


Figure 5.2: Example of a SDSS spectrum showing H α and [NII] emission lines as it would appear when convolved to OTELO’s Tunable Filters’ spectral response (same object as in Fig. 5.1). The original SDSS spectrum redshifted to $z = 0.39$ is shown in blue. In magenta, its pseudo-spectrum as it would be seen with OSIRIS’s TFs. The thin dashed grey lines represent the spectral responses of the 32 sections of OTELO’s tomography (Airy’s functions).

5.1.2 Visual classification of candidates

The visual inspection of the candidates was made by three different collaborators separately, including the PhD candidate. Not only the pseudo-spectrum was taken into account, but also the different images of the object in each one of the slices of the tomography ('thumbnails'), in order to determine the reliability of the detection and whether the object’s continuum was detected. In this way, the objects were first classified in two different categories: **a)** objects clearly showing an emission line and **b)** objects possibly showing an emission line. This second category included objects with apparent emission but with huge errors or with several unclear peaks, as those shown in Fig. 5.3. After inspection of the pseudo-spectra, a third category was added to include real objects that presented absorption features and that were erroneously selected as emitters due to their continuum: **c)** objects possibly showing an absorption line (see an example in Fig. 5.4). The objects which did not fall in any of these categories were discarded from the catalogue of ELC. In the majority of cases, despite fulfilling

one or more of the algorithm selection criteria, they corresponded to very noisy pseudo-spectra with no clear peak or an odd appearance (see some examples in Fig. 5.5).

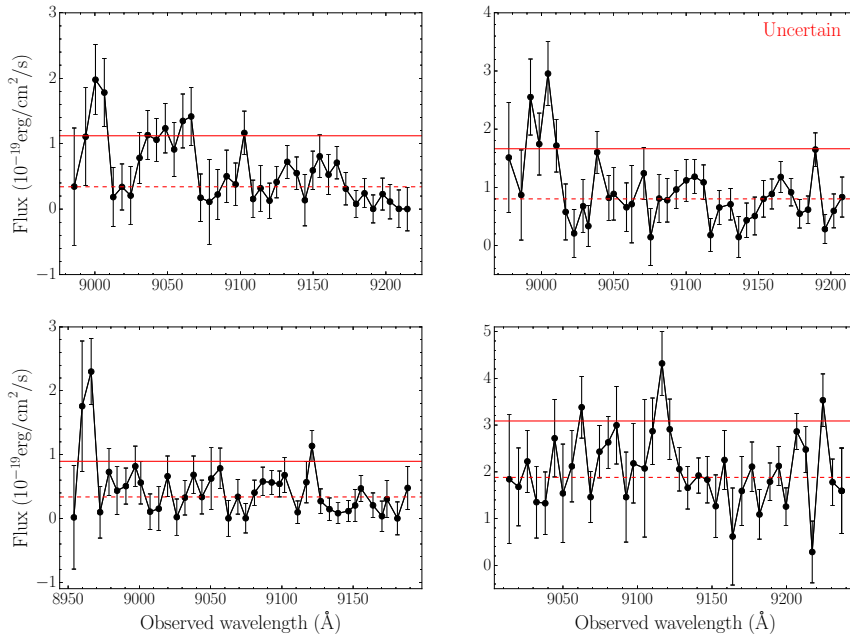


Figure 5.3: Examples of objects selected as emitting candidates by the automatic algorithm and classified as uncertain after the visual inspection (category **b**). In the majority of cases, the pseudo-spectrum shows an apparent emission but the errors are huge, or there are several unclear peaks. The red dashed line and the red continuous one are as in Fig. 5.1.

In the category of emitting objects, three sub-categories were made depending on the goodness of the detection: **a.1)** emitting objects with continuum, **a.2)** emitting objects without detected continuum, but whose emission has been detected in two contiguous slices and **a.3)** emitting objects without detected continuum, but whose emission has been detected only in one slice. Examples of objects falling in each of these sub-categories are shown in Fig. 5.6. More examples of pseudo-spectra with their corresponding ‘thumbnails’ can be found in Figs. 5.7 and 5.8.

Finally, 1030 objects were classified as emitting objects (category **a**). From them, 132 fall in the first sub-category (**a.1**), 791 in the second one (**a.2**) and 107 in the third one (**a.3**). Moreover, 64 objects were classified as potential emitting objects (category **b**) and 147 as possibly presenting an absorption line (category **c**).

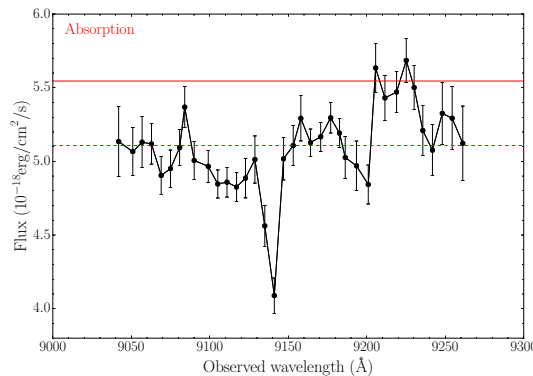


Figure 5.4: Example of an object showing absorption features, and thus classified in category c). The red dashed line and the red continuous one are as in Fig. 5.1.

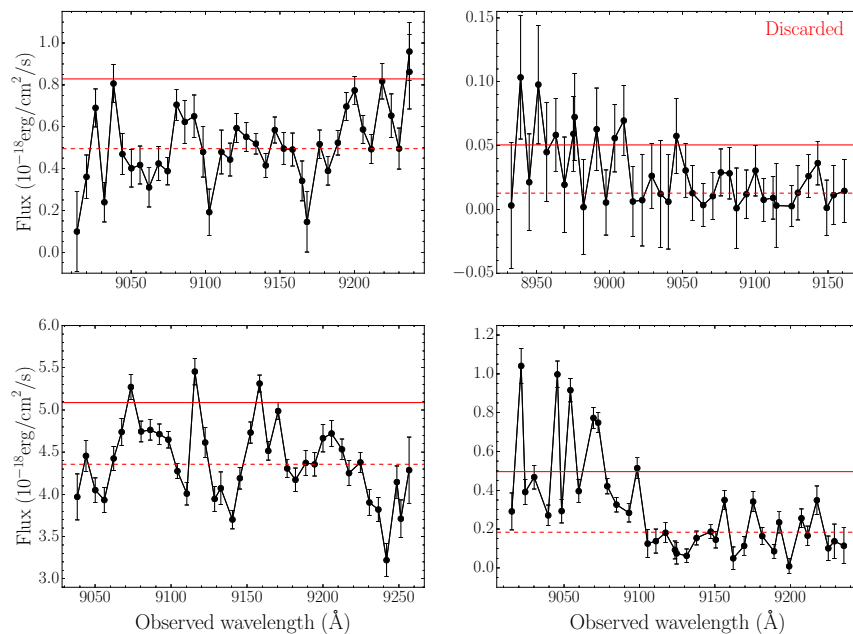


Figure 5.5: Examples of objects selected as emitting candidates by the automatic algorithm but rejected after the visual inspection. In the majority of cases, the pseudo-spectrum is noisy, does not show any clear peak or has an odd appearance, despite fulfilling one or more of the algorithm selection criteria. The red dashed line and the red continuous one are as in Fig. 5.1.

Este documento incorpora firma electrónica, y es copia auténtica de un documento electrónico archivado por la ULL según la Ley 39/2015. <i>Su autenticidad puede ser contrastada en la siguiente dirección https://sede.ull.es/validacion/</i>		
Identificador del documento:	969870	Código de verificación: 8KFVZkZp
Firmado por:	MARINA RAMÓN PÉREZ UNIVERSIDAD DE LA LAGUNA	Fecha: 28/06/2017 21:15:24
	ANGEL MANUEL BONGIOVANNI PEREZ UNIVERSIDAD DE LA LAGUNA	29/06/2017 09:30:15
	JORGE CEPA NOGUE UNIVERSIDAD DE LA LAGUNA	29/06/2017 09:33:05
	ANA MARIA PEREZ GARCIA UNIVERSIDAD DE LA LAGUNA	29/06/2017 11:12:35
	ERNESTO PEREDA DE PABLO UNIVERSIDAD DE LA LAGUNA	04/07/2017 18:28:07

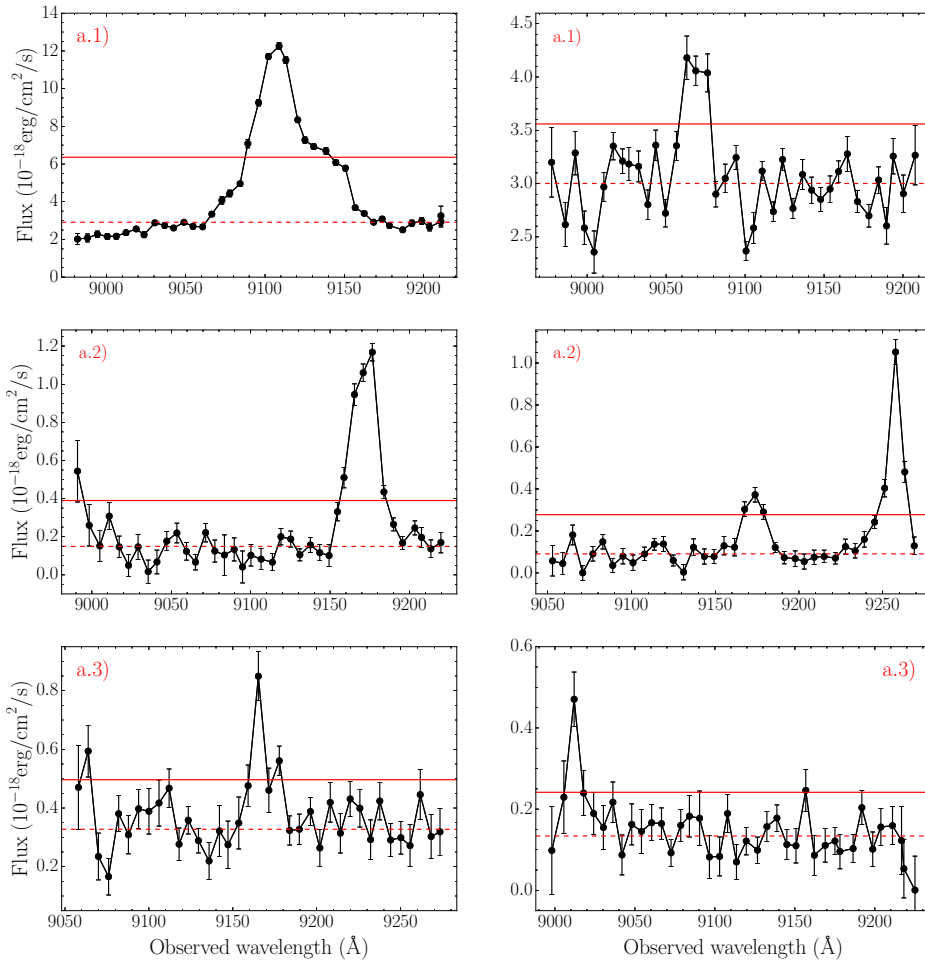


Figure 5.6: Examples of objects that were confirmed as emitters after the visual inspection. From top to bottom: **a.1**) emitting objects with continuum, **a.2**) emitting objects without detected continuum, but whose emission has been detected in two contiguous slices and **a.3**) emitting objects without detected continuum, whose emission has been detected only in one slice. The red dashed line and the red continuous one are as in Fig. 5.1.

Este documento incorpora firma electrónica, y es copia auténtica de un documento electrónico archivado por la ULL según la Ley 39/2015.
Su autenticidad puede ser contrastada en la siguiente dirección <https://sede.ull.es/validacion/>

Identificador del documento: 969870

Código de verificación: 8KFVZkZp

Fecha: 28/06/2017 21:15:24

Firmado por: MARINA RAMÓN PÉREZ
UNIVERSIDAD DE LA LAGUNA

29/06/2017 09:30:15

ANGEL MANUEL BONGIOVANNI PEREZ
UNIVERSIDAD DE LA LAGUNA

29/06/2017 09:33:05

JORGE CEPA NOGUE
UNIVERSIDAD DE LA LAGUNA

29/06/2017 11:12:35

ANA MARIA PEREZ GARCIA
UNIVERSIDAD DE LA LAGUNA

04/07/2017 18:28:07

ERNESTO PEREDA DE PABLO
UNIVERSIDAD DE LA LAGUNA

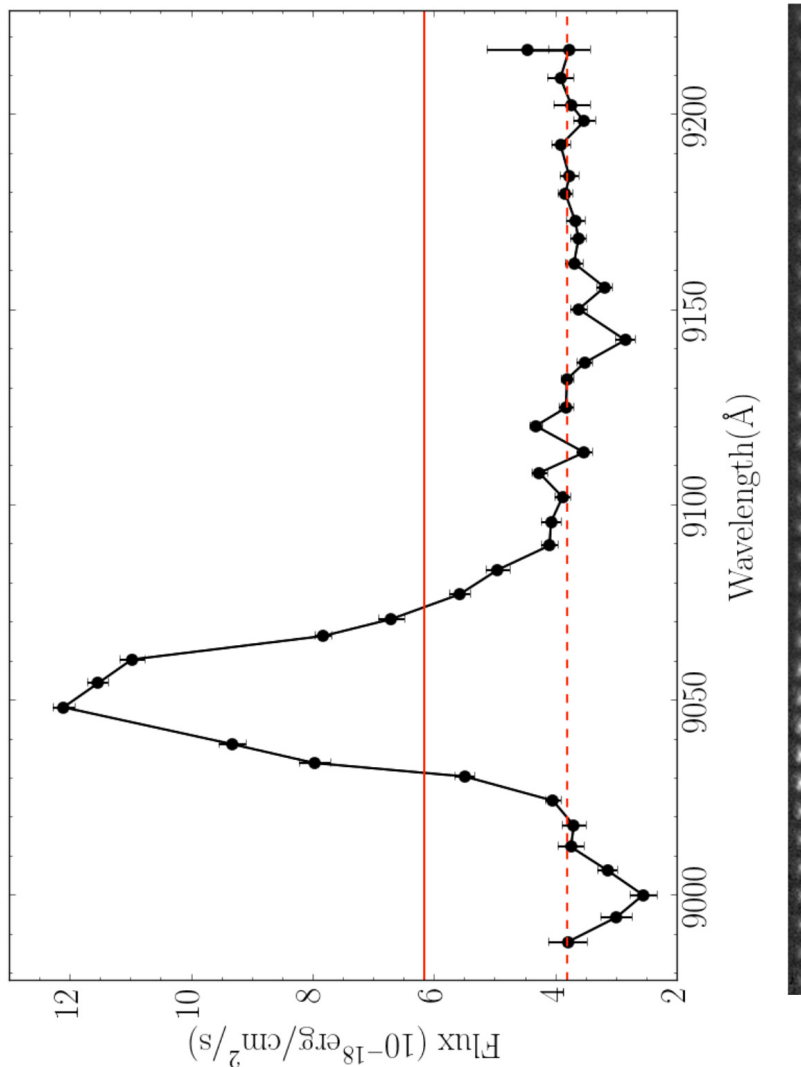


Figure 5.7: Pseudo-spectrum of an emitting object from category a.1). The strip below it corresponds to the object as seen in each one of the slices of the tomography. The red dashed line and the red continuous one are as in Fig. 5.1.

Este documento incorpora firma electrónica, y es copia auténtica de un documento electrónico archivado por la ULL según la Ley 39/2015.
Su autenticidad puede ser contrastada en la siguiente dirección <https://sede.ull.es/validacion/>

Identificador del documento: 969870

Código de verificación: 8KFVZkZp

Firmado por: MARINA RAMÓN PÉREZ
UNIVERSIDAD DE LA LAGUNA

Fecha: 28/06/2017 21:15:24

ANGEL MANUEL BONGIOVANNI PEREZ
UNIVERSIDAD DE LA LAGUNA

29/06/2017 09:30:15

JORGE CEPA NOGUE
UNIVERSIDAD DE LA LAGUNA

29/06/2017 09:33:05

ANA MARIA PEREZ GARCIA
UNIVERSIDAD DE LA LAGUNA

29/06/2017 11:12:35

ERNESTO PEREDA DE PABLO
UNIVERSIDAD DE LA LAGUNA

04/07/2017 18:28:07

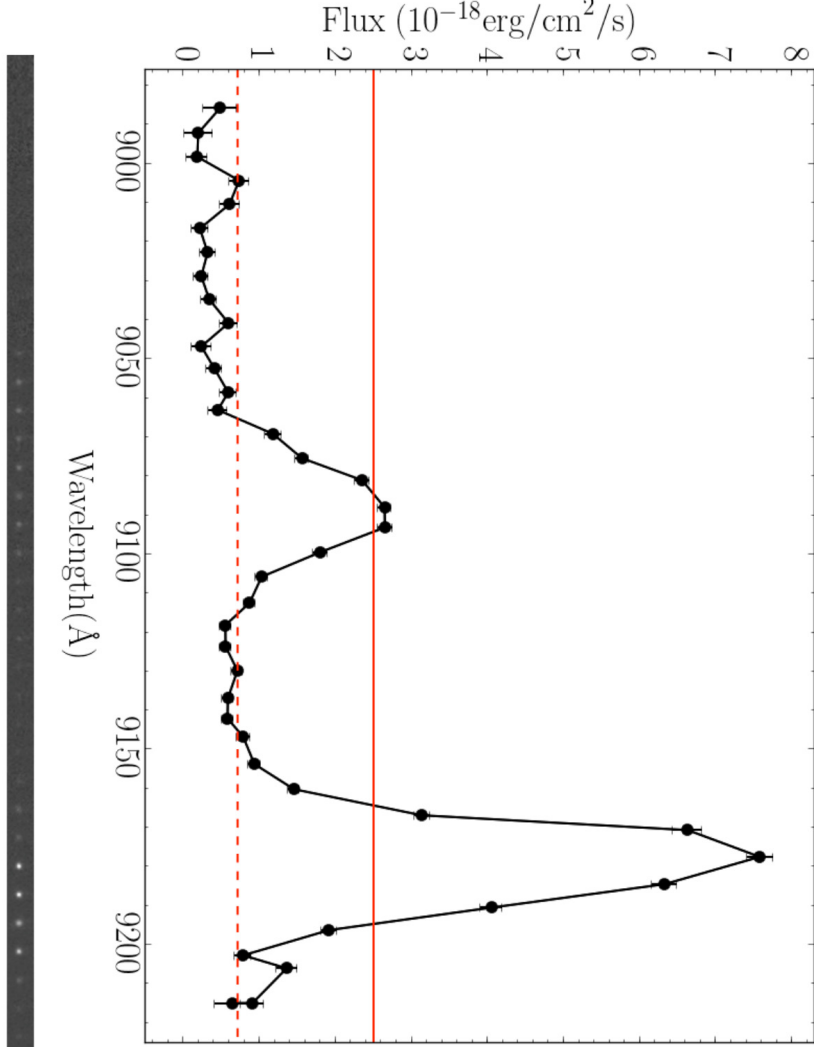


Figure 5.8: Pseudo-spectrum of an emitting object from category a.2). The strip below it corresponds to the object as seen in each one of the slices of the tomography. The red dashed line and the red continuous one are as in Fig. 5.1.

Este documento incorpora firma electrónica, y es copia auténtica de un documento electrónico archivado por la ULL según la Ley 39/2015.
Su autenticidad puede ser contrastada en la siguiente dirección <https://sede.ull.es/validacion/>

Identificador del documento: 969870

Código de verificación: 8KFVZkZp

Fecha: 28/06/2017 21:15:24

Firmado por: MARINA RAMÓN PÉREZ
UNIVERSIDAD DE LA LAGUNA

ANGEL MANUEL BONGIOVANNI PEREZ
UNIVERSIDAD DE LA LAGUNA

JORGE CEPA NOGUE
UNIVERSIDAD DE LA LAGUNA

ANA MARIA PEREZ GARCIA
UNIVERSIDAD DE LA LAGUNA

ERNESTO PEREDA DE PABLO
UNIVERSIDAD DE LA LAGUNA

29/06/2017 09:30:15

29/06/2017 09:33:05

29/06/2017 11:12:35

04/07/2017 18:28:07

5.2 Selection of H α emitters candidates

Once the emitting objects are selected, it is time to identify which chemical species are observed in each case. In this thesis, we have focused on the identification of H α emitters. First, we have conducted a simulation in order to estimate the detection limits of our survey in that case. Then, photometric redshifts have been obtained, a crucial step for which the multiwavelegh catalogue is the key tool. Other accessory methods, such as colour-colour and colour-magnitude diagrams are also used in order to refine the identification.

5.2.1 Detection limits in OTELO

In an emission-line survey which uses narrow-band filters, such as OTELO, the detection of an object depends not only on the emission line flux, but also on its strength relative to the continuum (Jones & Bland-Hawthorn 2001). This is determined by the equivalent width (EW):

$$\text{EW} = \frac{F_{\text{line}} \delta\lambda_e}{F_{\text{cont}}} , \quad (5.1)$$

where F_{line} and F_{cont} are the line and the continuum fluxes per unit wavelength, respectively, and $\delta\lambda_e$ is the effective width of the passband, i.e., the width of a rectangular bandpass with equal area to that of the real passband. The EW detection limits must be evaluated in any narrow-band survey so as to estimate what percentage of objects are missed in the detection, as well as the number of contaminants (false detections). This is crucial in order to make a correct use of a survey. In our case, the number of false detections was kept under control by doing successive analysis of the emitting objects by independent collaborators (see following subsections, and specially section 5.3). However, the number of missing objects had to be estimated.

Accordingly, the aim of the simulation we performed was to find the detection limits of OTELO survey in terms of equivalent width, so as to see what kind of objects were escaping our detection. To do so, we simulated an H α emission line in the form of a gaussian. The gaussian was centered at 6563Å and then redshifted to $z = 0.398$, where it was convolved to OTELO's spectral response. We added a random noise component with a normal distribution to the resulting pseudo-spectrum, taking into account the sky and the photonic noise summed in quadrature, as they are both independent from each other. To obtain the first noise component, we measured the standard deviation of sky counts in 14 different regions in each of the images, so as to make sure there were no significant variations of the background noise throughout the image, and took their mean value. For each slice of the tomography, composed of 6 individual images, we checked that those values were consistent and used their average value in turn. As for the photonic noise, we used the square root of the pseudo-spectrum continuum as it is drawn from a poissonian distribution.

Three independent variables of the H α gaussian were used: its full width at half maximum (FWHM), its continuum and its amplitude. We used the automatic algorithm described in section 5.1.1 in order to select the resulting pseudo-spectra as emitters. We assigned a value of '1' (or '0') whenever the detection was made (or not). We performed 500 of such independent simulations so as to have less than a 5% of uncertainty in the results.

The FWHM of the H α gaussian was varied between 1 and 100Å. The upper limit would correspond to a very broad line of \sim 3300 km/s at rest-frame and the lower limit to a narrow one (\sim 32 km/s). We assume that these values are representatives of the most likely extreme situations, e.g. broad line AGN and dwarf galaxies.

As for the continuum and amplitude values, we analysed the actual pseudo-spectra of OTELO survey (detected as emitters or not) in order to take a broad range of realistic values. The amplitude and continuum

Este documento incorpora firma electrónica, y es copia auténtica de un documento electrónico archivado por la ULL según la Ley 39/2015.
Su autenticidad puede ser contrastada en la siguiente dirección <https://sede.ull.es/validacion/>

Identificador del documento:	Código de verificación:
969870	8KFVZkZp
Firmado por: MARINA RAMÓN PÉREZ UNIVERSIDAD DE LA LAGUNA	Fecha: 28/06/2017 21:15:24
ANGEL MANUEL BONGIOVANNI PÉREZ UNIVERSIDAD DE LA LAGUNA	29/06/2017 09:30:15
JORGE CEPA NOGUE UNIVERSIDAD DE LA LAGUNA	29/06/2017 09:33:05
ANA MARIA PÉREZ GARCIA UNIVERSIDAD DE LA LAGUNA	29/06/2017 11:12:35
ERNESTO PEREDA DE PABLO UNIVERSIDAD DE LA LAGUNA	04/07/2017 18:28:07

values of a PS can be approximately translated to those of the original spectrum as $\frac{\pi}{2} \delta\lambda_{FWHM}$, where $\delta\lambda_{FWHM} \simeq 12\text{\AA}$ is the effective passband width of the TF (Jones 2001). The continuum values of OTELO's observed PS ranged between $\sim 1 \times 10^{-21}$ and $\sim 1 \times 10^{-15} \text{ erg/s/cm}^2/\text{\AA}$ and we set our simulation limits to 5×10^{-23} and $5 \times 10^{-17} \text{ erg/s/cm}^2$ for the input gaussian. On the other hand, the PS amplitudes (taken as the difference between the line's maximum and the continuum) ranged between $\sim 3 \times 10^{-20}$ and $\sim 1 \times 10^{-15} \text{ erg/s/cm}^2/\text{\AA}$ and we set our simulation limits to 1.5×10^{-21} and $5 \times 10^{-17} \text{ erg/s/cm}^2$. Thus, the faintest limits of the simulation lay comfortably beyond the upper limits of the current survey, and the conclusions can be applied to future deeper surveys.

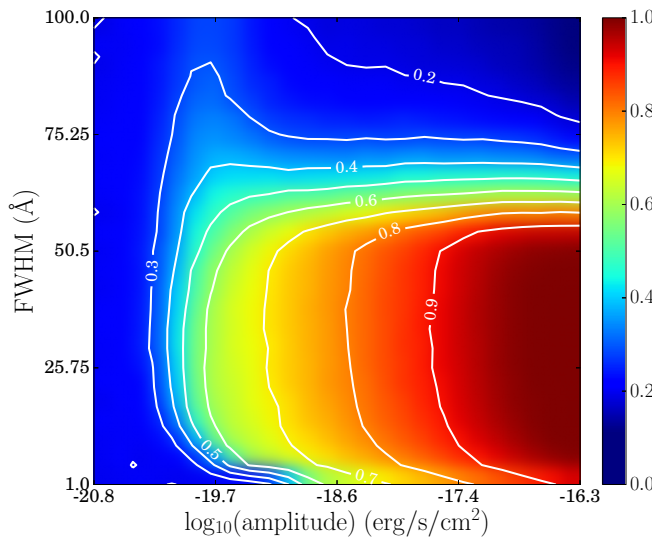


Figure 5.9: Mean value of detection in the 500 runs of the simulation (0: never detected as emitter, 1: always detected as emitter), given the FWHM and the amplitude of the H α gaussian. The continuum variable has been collapsed in the plane of the other two. White lines represent the detection probability contours.

After the 500 runs of the simulation, we obtained a 4D-data cube with every combination of FWHM, continuum, amplitude and mean level of detection (from 0 to 1). In general, the levels of detection increased with higher amplitudes and lower continuum levels, while they were confined to a certain range of FWHM, as can be seen in Fig. 5.9, 5.10 and 5.11, where, in each case, one of the three independent variables has been collapsed in the plane of the other two. According to this, for a probability threshold of $p \geq 0.50$ (i.e., considering a level of detection of at least 50% in the whole simulation) the limits of detection can be roughly set at the following parameters for the variables of the input gaussian, i.e, at rest-frame:

- FWHM $\lesssim 60\text{\AA}$
- Amplitude $\gtrsim 2 \times 10^{-20} \text{ erg/s/cm}^2$
- Continuum $\lesssim 4 \times 10^{-18} \text{ erg/s/cm}^2$

Este documento incorpora firma electrónica, y es copia auténtica de un documento electrónico archivado por la ULL según la Ley 39/2015.
Su autenticidad puede ser contrastada en la siguiente dirección <https://sede.ull.es/validacion/>

Identificador del documento:	969870	Código de verificación:	8KFVZkZp
Firmado por:	MARINA RAMÓN PÉREZ UNIVERSIDAD DE LA LAGUNA	Fecha:	28/06/2017 21:15:24
	ANGEL MANUEL BONGIOVANNI PEREZ UNIVERSIDAD DE LA LAGUNA		29/06/2017 09:30:15
	JORGE CEPA NOGUE UNIVERSIDAD DE LA LAGUNA		29/06/2017 09:33:05
	ANA MARIA PEREZ GARCIA UNIVERSIDAD DE LA LAGUNA		29/06/2017 11:12:35
	ERNESTO PEREDA DE PABLO UNIVERSIDAD DE LA LAGUNA		04/07/2017 18:28:07

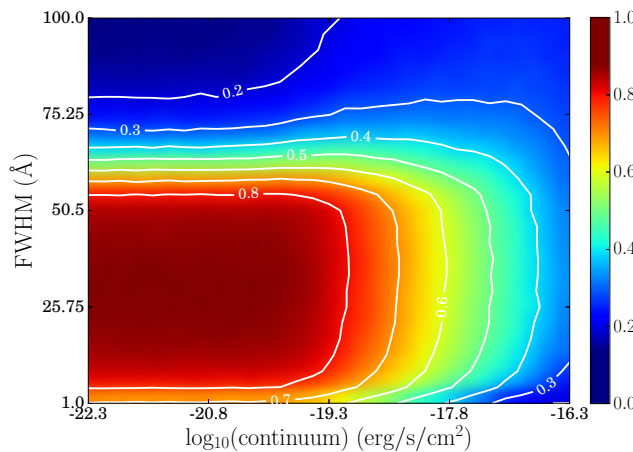


Figure 5.10: Mean value of detection in the 500 runs of the simulation (0: never detected as emitter, 1: always detected as emitter), given the FWHM and the continuum of the H α gaussian. The amplitude variable has been collapsed in the plane of the other two. White lines represent the detection probability contours.

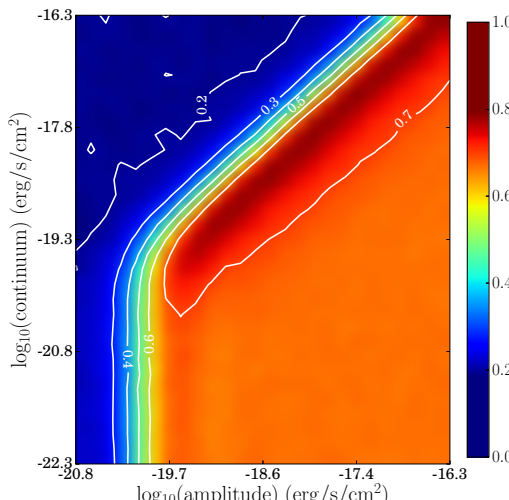


Figure 5.11: Mean value of detection in the 500 runs of the simulation (0: never detected as emitter, 1: always detected as emitter), given the continuum and the amplitude of the H α gaussian. The FWHM variable has been collapsed in the plane of the other two. White lines represent the detection probability contours.

Este documento incorpora firma electrónica, y es copia auténtica de un documento electrónico archivado por la ULL según la Ley 39/2015.
Su autenticidad puede ser contrastada en la siguiente dirección <https://sede.ull.es/validacion/>

Identificador del documento: 969870

Código de verificación: 8KFVZkZp

Firmado por: MARINA RAMÓN PÉREZ
UNIVERSIDAD DE LA LAGUNA

Fecha: 28/06/2017 21:15:24

ANGEL MANUEL BONGIOVANNI PEREZ
UNIVERSIDAD DE LA LAGUNA

29/06/2017 09:30:15

JORGE CEPA NOGUE
UNIVERSIDAD DE LA LAGUNA

29/06/2017 09:33:05

ANA MARIA PEREZ GARCIA
UNIVERSIDAD DE LA LAGUNA

29/06/2017 11:12:35

ERNESTO PEREDA DE PABLO
UNIVERSIDAD DE LA LAGUNA

04/07/2017 18:28:07

However, these are only approximate values for reference, as a true level of detection in the simulation can only be given for a combination of the three independent variables. To draw physical conclusions from the simulation, we computed for each experiment (i.e. for each combination of FWHM, continuum and amplitude values) the equivalent width (EW) of the H α line. We determined the minimum detected EW for a given probability threshold p (see Fig. 5.12). For a probability threshold of $p \geq 0.50$, for instance, the minimum detected EW is $\sim 5\text{\AA}$, while it is $\sim 10.5\text{\AA}$ for a threshold of $p \geq 0.95$. In Fig. 5.13 we have plotted the percentage of detected objects in the simulation for those values of probability threshold as a function of the equivalent width. Typical values of H α equivalent widths for different astrophysical objects, taken from the works of Gavazzi et al. (2006), Gallego et al. (1997), Stern & Laor (2012) and Gil de Paz et al. (2003), are also indicated.

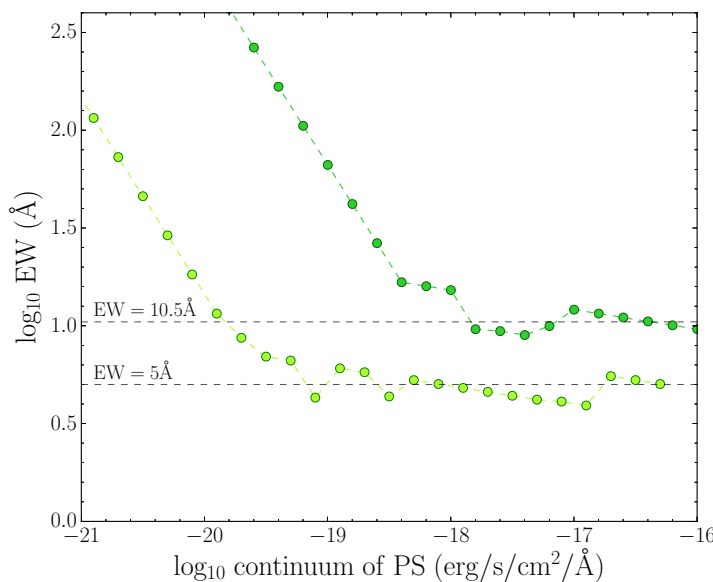


Figure 5.12: Minimum detected EW as a function of the pseudo-spectrum continuum. Dark green curve: $p \geq 0.95$ probability threshold. Light green curve: $p \geq 0.50$ probability threshold.

To summarise, the main results that can be drawn from the simulation about the detection limits of the H α line in OTELO survey are the following:

With a probability threshold of 50% ($p \geq 0.50$) we should be able to detect:

- about 1 out of 5 elliptical galaxies with $\text{EW} = 6\text{\AA}$
- more than 75% of spiral galaxies with $\text{EW} \geq 60\text{\AA}$
- between 62% and 79% of the galaxies with $100 \leq \text{EW} \leq 200\text{\AA}$
- between 55% and 60% of the galaxies with $\text{EW} \geq 200\text{\AA}$

We reach minimum EWs of:

- 5 Å with a probability of $p \geq 0.50$ for objects with a PS continuum up to $\sim 10^{-19}$ erg/s/cm 2 /Å.
- 10.5 Å with a probability of $p \geq 0.95$ for objects with a PS continuum up to $\sim 10^{-18}$ erg/s/cm 2 /Å.

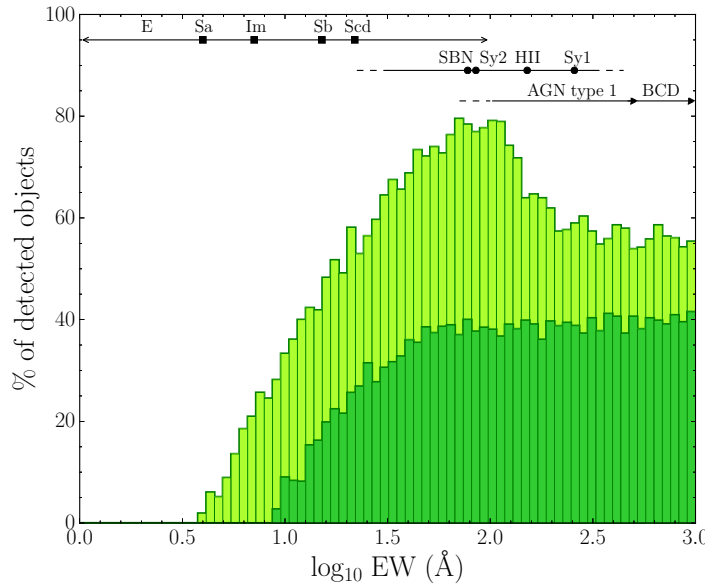


Figure 5.13: Percentage of detected objects in the simulation depending on the equivalent width of the H α gaussian line. Light green: $p \geq 0.50$ probability threshold. Dark green: $p \geq 0.95$ probability threshold. Typical values of H α equivalent widths for different astrophysical objects are also indicated. Black squares: median values of EW as in Gavazzi et al. (2006). Black circles: mean values as in Gallego et al. (1997). Black triangles: maximum values from Stern & Laor (2012) and Gil de Paz et al. (2003).

5.2.2 Photometric redshift determination

Obtaining reliable photometric redshifts of the sources in OTELO's catalogue, specially for those selected as emitters, is one of the most important steps in this work. To do it, we used the code LePhare (Arnouts et al. 1999; Ilbert et al. 2006), which has proven to perform reasonably well, specially at lower redshifts. In addition, it is the only method that includes IR templates (see Abdalla et al. 2011 and Dahmen et al. 2013 for a comparison on photo-z methods). In order to deduce the photometric redshift, LePhare uses a χ^2 approach to find the best fit between the observed SED of an object and different templates.

In our case, we used a main library for galaxies in the UV and optical range so as to obtain the photometric redshift of OTELO's sources. This library was composed of 10 SED templates: 4 representative of Hubble types (E, Sbc, Scd, Im), observed by Coleman et al. (1980), and 6 representative of starbursts, built by Kinney et al. (1996). They are shown in Fig. 5.14. We applied the extinction law of Calzetti et al. (2000), with values

Este documento incorpora firma electrónica, y es copia auténtica de un documento electrónico archivado por la ULL según la Ley 39/2015. Su autenticidad puede ser contrastada en la siguiente dirección https://sede.ull.es/validacion/		
Identificador del documento:	969870	Código de verificación: 8KFVZkZp
Firmado por:	MARINA RAMÓN PÉREZ UNIVERSIDAD DE LA LAGUNA	Fecha: 28/06/2017 21:15:24
	ANGEL MANUEL BONGIOVANNI PÉREZ UNIVERSIDAD DE LA LAGUNA	29/06/2017 09:30:15
	JORGE CEPA NOGUE UNIVERSIDAD DE LA LAGUNA	29/06/2017 09:33:05
	ANA MARÍA PÉREZ GARCIA UNIVERSIDAD DE LA LAGUNA	29/06/2017 11:12:35
	ERNESTO PEREDA DE PABLO UNIVERSIDAD DE LA LAGUNA	04/07/2017 18:28:07

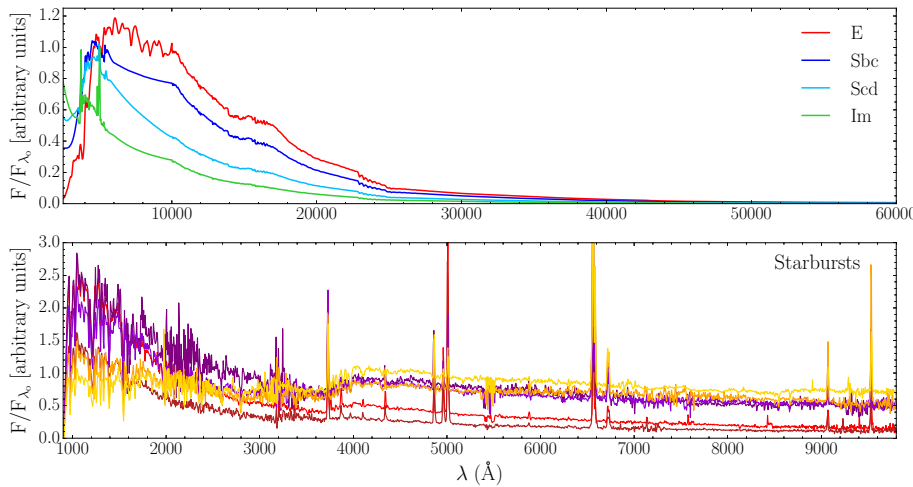


Figure 5.14: Templates used to build LePhare’s galaxies library. Upper panel: SED representatives of Hubble types (E, Sbc, Scd and Im) from Coleman et al. (1980). Lower pannel: starbursts SED from Kinney et al. (1996). All the fluxes are normalised to F_{λ_o} , where $\lambda_o = 5000\text{Å}$.

of $E(B-V)$ ranging from 0 to 1.1 in steps of 0.1, and defined a redshift interval from 0.04 to 10, in steps of 0.1. Based on the photo-z obtained with the galaxies library, a fit to the infrared part of the spectra from 5 μm was performed using the Chary & Elbaz (2001) library, which is composed of 105 IR templates with different luminosities. Infrared luminosities were then calculated by integrating the IR flux from 8 μm to 1000 μm .

In addition to this, LePhare performed two other photo-z estimations using two complementary libraries: one for QSOs and AGNs and one for stars. The QSOs and AGNs templates were taken from the SWIRE¹ library, created by Polletta et al. (2007), and included 2 Seyfert galaxies, 3 type-1 QSOs, 2 type-2 QSOs and 3 composite galaxies (starburst+AGN). As for the stars library, it consisted mainly of the 131 templates calibrated by Pickles (1998), covering all the usual stellar spectral types (O-M) and luminosity classes, plus 4 white dwarfs templates from Bohlin et al. (1995) and 26 brown dwarfs representative of stellar spectral types M, L and T from the Spex Prism² library. The photo-z values obtained with these two libraries were only used in the analysis as as supplementary information, mainly whenever the chief photo-z, given by the galaxies templates fit, was not reliable.

The procedure followed by LePhare to obtain a photometric redshift starts with the creation of the filter library, which includes all the filters described in Chapter 4 (FUV and NUV from GALEX, u, g, r, i and z from CFHT, V and I from HST, J, H and Ks from CFHT, the 4 IRAC bands, 24 μm from MIPS, 100 and 160 μm from PACS, and finally 250, 350 and 500 μm from SPIRE). In the case of the selected OTELO’s emitters, we considered the contribution of emission lines and added an extra filter to the filter library, corresponding to the spectral responses of the tunable filters and representing the spectral window of OTELO’s integrated flux. Then, given the set of filters, template magnitudes are computed at each value of redshift and extinction. Finally, a χ^2

¹Spitzer Wide-area InfraRed Extragalactic survey.

²See <http://pono.ucsd.edu/adam/brownndwarfs/spexprism/> for more details.

Este documento incorpora firma electrónica, y es copia auténtica de un documento electrónico archivado por la ULL según la Ley 39/2015. Su autenticidad puede ser contrastada en la siguiente dirección https://sede.ull.es/validacion/		
Identificador del documento: 969870	Código de verificación: 8KFVZkZp	
Firmado por: MARINA RAMÓN PÉREZ UNIVERSIDAD DE LA LAGUNA		Fecha: 28/06/2017 21:15:24
ANGEL MANUEL BONGIOVANNI PEREZ UNIVERSIDAD DE LA LAGUNA		29/06/2017 09:30:15
JORGE CEPA NOGUE UNIVERSIDAD DE LA LAGUNA		29/06/2017 09:33:05
ANA MARIA PEREZ GARCIA UNIVERSIDAD DE LA LAGUNA		29/06/2017 11:12:35
ERNESTO PEREDA DE PABLO UNIVERSIDAD DE LA LAGUNA		04/07/2017 18:28:07

fitting is performed between the observed flux of the object and each one of the templates, so as to find the best model and the corresponding redshift. Some examples of SED fitting made by LePhare are shown in Fig. 5.15.

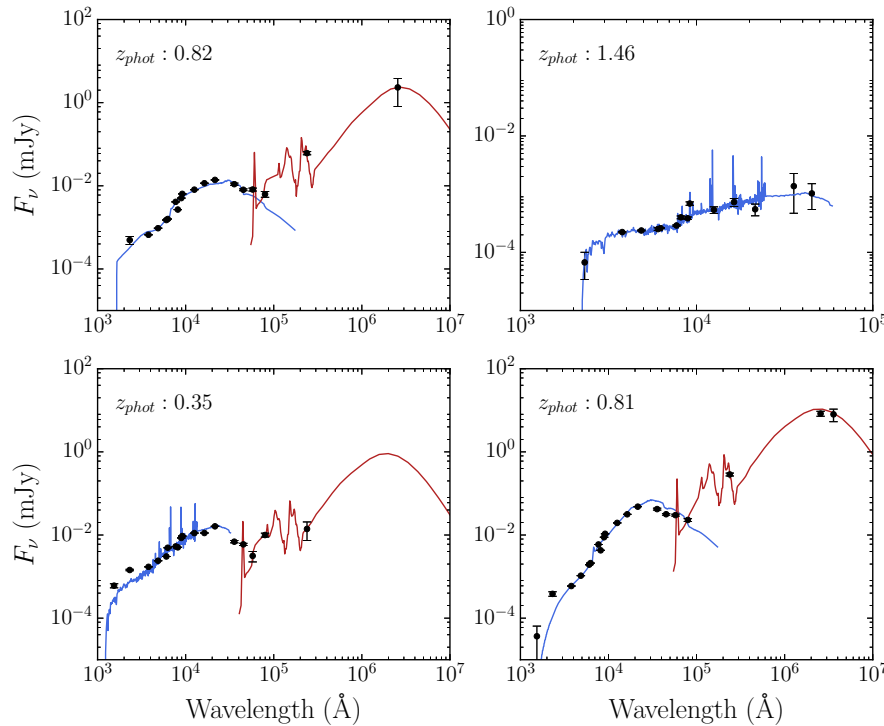


Figure 5.15: Examples of SED fitting performed by LePhare in order to obtain photometric redshifts. Black circles show the observed fluxes of the source in each of the bands, as well as its errors. The blue curves represent the templates that best fit the stellar part of the spectrum, while the red ones correspond to the best templates for the infrared part of the spectrum.

The distribution of photometric redshifts that we obtained in that way can be seen in Fig. 5.16. To calibrate the accuracy of those photo-z, we compared them to the spectroscopic redshifts up to $z=1.5$ from the DEEP2 catalogue, described in section 4.2.2. We found that the redshift accuracy is $|\Delta z/(z+1)| < 0.1$ for 79% of the emitters and 81% of the total sample of sources (see Fig. 5.17). So, for a sample with the same selection criteria as DEEP2, our photo-z are consistent.

We preselected 112 objects as H α emitting candidates having either a spectroscopic redshift in the H α +[NII] window in OTELO ($0.37 \leq z_{spec} \leq 0.42$) or a LePhare photometric redshift in a broad range around that window ($0.30 \leq z \leq 0.50$). This broad range was chosen so as to make sure not to miss any H α emitter. At this point, we did not analyse the likelihood of the redshifts, as this will be done in the following steps. Those objects, together with the ones preselected by other methods (see next subsections and table 5.1), were considered as H α candidates and later analysed in detail by a team of collaborators (see section 5.3).

Este documento incorpora firma electrónica, y es copia auténtica de un documento electrónico archivado por la ULL según la Ley 39/2015.
Su autenticidad puede ser contrastada en la siguiente dirección <https://sede.ull.es/validacion/>

Identificador del documento: 969870

Código de verificación: 8KFVZkZp

Firmado por: MARINA RAMÓN PÉREZ UNIVERSIDAD DE LA LAGUNA	Fecha: 28/06/2017 21:15:24
ANGEL MANUEL BONGIOVANNI PEREZ UNIVERSIDAD DE LA LAGUNA	29/06/2017 09:30:15
JORGE CEPA NOGUE UNIVERSIDAD DE LA LAGUNA	29/06/2017 09:33:05
ANA MARIA PEREZ GARCIA UNIVERSIDAD DE LA LAGUNA	29/06/2017 11:12:35
ERNESTO PEREDA DE PABLO UNIVERSIDAD DE LA LAGUNA	04/07/2017 18:28:07

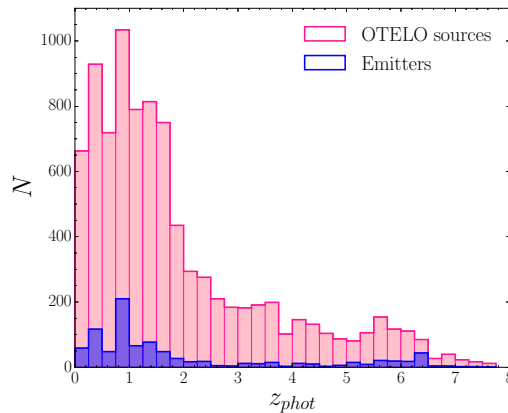


Figure 5.16: Distribution of photometric redshifts obtained with LePhare for the entire sample of OTELO sources (pink) and for the selected emitters (blue).

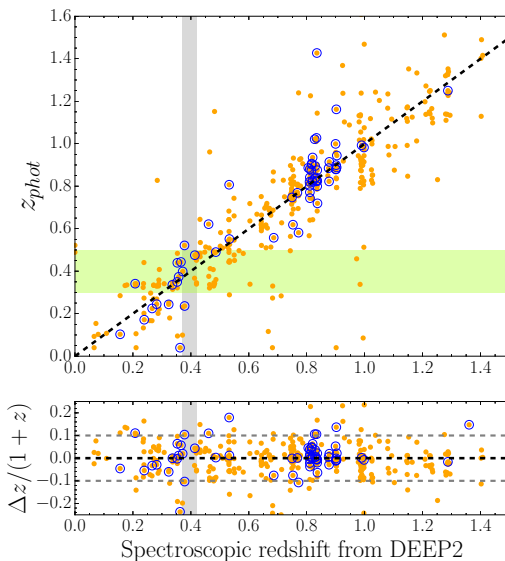


Figure 5.17: Photometric redshifts obtained for OTELO sources compared to the spectroscopic redshifts measured by DEEP2 up to $z = 1.5$. The orange dots represent all the OTELO sources, while the blue circles are the selected emitters. In the upper panel, the black dashed line represents $z_{phot} = z_{spec}$. The grey shaded area corresponds to $0.37 \leq z_{spec} \leq 0.42$ and the green one to $0.30 \leq z_{phot} \leq 0.50$. All the emitting objects falling in one of these areas were preselected as H α candidates. In the lower panel, the black and the two gray dashed lines mark, respectively, $\Delta z / (1 + z) = 0, 0.1$ and -0.1 .

5.2.3 Colour-colour diagram

The next tool we used for the identification of emitting objects was the location of OTELO's sources in a colour-colour diagram, where objects appear naturally distributed according to their redshift. We applied this technique to H α emitters as well as H β +[OIII] ones. We employed the AEGIS (Davis et al. 2007) and zCOSMOS (Lilly et al. 2007) data, with spectroscopic redshifts up to $z \sim 1.20$, to build the $(g - r)$ vs. $(r - z)$ diagram that is shown in Fig. 5.18. We performed a 2D gaussian-kernel density estimation of the distribution of points, in order to define 1σ contours around two different sets of points. One was the set containing the objects with $0.36 < z_{spec} < 0.41$, which corresponds to the redshift interval where H α +[NII] emitters would be found in OTELO survey. The corresponding 1σ contour is displayed as a grey curve in Fig. 5.18. The other contour (in black in the figure) was the analogous for H β +[OIII] OTELO emitters, that is, the set of objects having $0.79 < z_{spec} < 0.91$. For both contours, we calculated their degree of completeness by checking how many sources within the requested redshift range were actually found inside them. For the first one, we saw that more than 90% of the sources having $0.36 < z_{spec} < 0.41$ fell inside the contour. For the other one, the number was even higher: more than 93% of the sources with $0.79 < z_{spec} < 0.91$ were found inside it. The degree of cross-contamination between both contours was negligible: less than 1% in both cases.

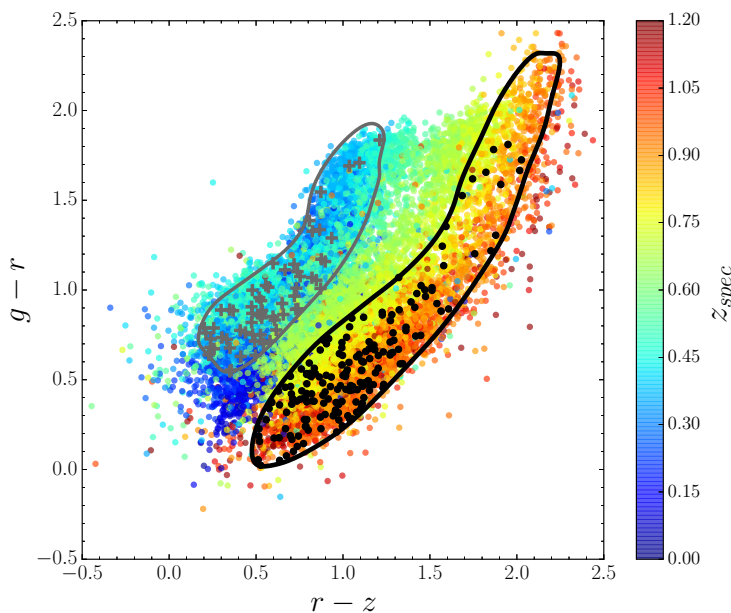


Figure 5.18: Colour-colour diagram of AEGIS and zCOSMOS spectroscopic sources up to $z \sim 1.20$. The grey line represents the 1σ contour of the sources having $0.36 < z_{spec} < 0.41$, while the black contour encloses those with $0.79 < z_{spec} < 0.91$. The grey crosses are the emitting sources from OTELO that fall inside the first contour and thus are potential H α emitters. The black dots are the emitting sources from OTELO that fall inside the second contour and thus are potential H β +[OIII] emitters.

We then plotted OTELO's emitting sources in the colour-colour diagram, in order to determine which of them fell inside each one of the contours. We found 53 emitting objects within the first contour, i.e, liable to have a redshift in the range of H α emitters. Of those, 32 were not selected before and were added to the sample of H α candidates. As for the second contour, we found 180 emitters inside of it, thus potential H β +[OIII] emitters. Those H α and H β +[OIII] emitters candidates, which are plotted in Fig. 5.18 as grey crosses and black dots, respectively, were later analysed in depth to confirm the emission (see sub-section 5.3 for the H α case).

5.2.4 Narrow-band excess

A last diagram was made in order to rescue possible emitting objects not identified as such with their pseudo-spectra but presenting a narrow-band excess. We followed the methodology developed by Bunker et al. (1995), which has been used in a large number of works such as the ones by Sobral et al. (2013) or Matthee et al. (2017). This strategy targets the objects showing an excess of flux in a narrow-band (NB) when compared to a broad-band (BB), i.e, having positive colours: BB – NB > 0.

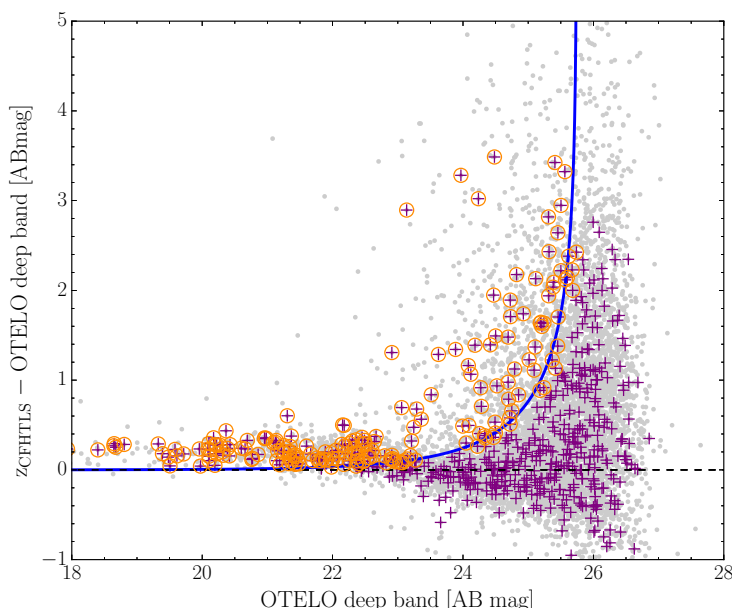


Figure 5.19: Narrow-band excess as a function of narrow-band magnitude for OTELO sources. OTELO deep band corresponds to the flux measured in the deep image, that is, OTELO's integrated flux. Colour is defined using the z -CFHTLS band as the broad band and OTELO deep band as the narrow band. Light grey dots represent all the OTELO sources, while purple crosses are those with $0.30 < z_{phot} < 0.50$, corresponding to the range of H α emission in OTELO survey. The blue line shows the limit $\Sigma > 3$. The orange circled sources are the sources presenting a narrow-band excess and having a photometric redshift compatible with an H α emission.

We used the integrated flux of OTELO (or deep band) as the narrow-band (FWHM of ~ 210 Å) and the z -band from the CFHTLS catalogue as the broad band (FWHM of ~ 200 nm). To distinguish real emitters

from objects having an excess of colour due to the random scatter in the photometry, the excess significance parameter, Σ , is used. It quantifies the number of standard deviations between the counts measured in the broad-band and the ones expected for a source with zero colour ($BB - NB = 0$) as a function of the narrow-band magnitude :

$$\Sigma = \frac{1 - 10^{-0.4(BB-NB)}}{10^{-0.4(ZP-NB)} \sqrt{\pi r_{ap}^2 (\sigma_{NB}^2 + \sigma_{BB}^2)}} \quad (5.2)$$

In this formula, ZP represents OTELO's deep image zero-point (30.504 in AB magnitudes), r_{ap} is the aperture radius in pixels (considering the standard 3 arcsec aperture to measure the total flux of sources, this gives: $1.5 \text{ arcsec} \div 0.254 \text{ arcsec/pixel} = 5.91 \text{ pixels}$) and σ_{NB} and σ_{BB} are the median RMS of background noise in each image (2.49 and 0.56, respectively).

We plotted the narrow-band excess ($BB - NB$) as a function of the narrow-band magnitude for all the sources in OTELO's catalogue, paying special attention to those having $0.30 < z_{phot} < 0.50$, which could be potential H α emitters (see Fig. 5.19). We considered as emitting candidates those having an excess significance above $\Sigma > 3$. In total, 237 objects presented such a narrow-band excess and had at the same time a photometric redshift in the considered range. From those, 38 had already been classified as emitters by their pseudo-spectra and selected as H α candidates. The other 199 were analysed visually one by one in order to check if an emitting line could actually be seen in the pseudo-spectrum. Finally, 27 new candidates were added to the sample of candidates.

Final sample of H α emitters candidates

In summary, the final sample of H α emitters candidates was composed of all the objects selected by the different methods previously described as possible H α emitters: by their spectroscopic or photometric redshifts, location in the colour-colour diagram and/or narrow-band excess. This preselection was deliberately broad so as to make sure to select a sample as complete as possible of the existing H α emitters in OTELO's catalogue. Additionally, 31 emitters that did not fulfill any of the previously mentioned conditions, but whose pseudo-spectra showed signs of a possible H α +[NII] emission, such as the first object in Fig. 5.6, were also included in the sample. In total, the final sample of candidates comprised 202 objects. Table 5.1 summarises the different selection criteria used to build it. In the next section, the process of identifying the H α emitters from the candidates sample is described.

Table 5.1: Selection of H α candidates sample. Column 1: criterion used for the selection of the candidate. Column 2: number of candidates selected with that criterion. Some objects may have been selected by more than one criterion but they are only included in one category, following the order of the table's list from top to bottom.

Criterion	N
with $0.37 \leq z_{spec} \leq 0.42$	4
with $0.30 \leq z_{phot} \leq 0.50$	108
selected by color	32
selected by narrow-band excess	27
selected by appearance	31
TOTAL	202

Este documento incorpora firma electrónica, y es copia auténtica de un documento electrónico archivado por la ULL según la Ley 39/2015. Su autenticidad puede ser contrastada en la siguiente dirección https://sede.ull.es/validacion/		
Identificador del documento: 969870	Código de verificación: 8KFVZkZp	
Firmado por: MARINA RAMÓN PÉREZ UNIVERSIDAD DE LA LAGUNA		Fecha: 28/06/2017 21:15:24
ANGEL MANUEL BONGIOVANNI PÉREZ UNIVERSIDAD DE LA LAGUNA		29/06/2017 09:30:15
JORGE CEPA NOGUE UNIVERSIDAD DE LA LAGUNA		29/06/2017 09:33:05
ANA MARIA PÉREZ GARCIA UNIVERSIDAD DE LA LAGUNA		29/06/2017 11:12:35
ERNESTO PEREDA DE PABLO UNIVERSIDAD DE LA LAGUNA		04/07/2017 18:28:07

5.3 Identification of H α emitters

The identification of H α emitters was made by four different collaborators separately, including the PhD candidate, with the use of a questionnaire specifically designed by M.Cerviño for the analysis of OTELO's objects. The questionnaire gathers all of the available information about an object with the purpose of classifying it. It includes three main sections: **1**) general analysis (information about OTELO's pseudo-spectrum), **2**) image analysis (information and images of the object in additional bands) and **3**) photo-z analysis (information about LePhare fit and other redshifts, if available), which we describe in detail below.

The first section of the questionnaire (see Fig. 5.20) shows the basic information of the object: OTELO ID, deep magnitude, stellarity index from SExtractor, selection type as in table 5.1 and emitter type (as in section 5.1.2). The pseudo-spectrum is displayed and analysed in order to see whether it shows an absorption or emitting line, and its characteristics: truncated line, double-peaked, blended, etc. The questionnaire also allows us to discard the object as an spurious one or to select it as a good candidate for general presentations of the survey. Finally, a comment can be made on the appearance of the object's pseudo-spectrum.

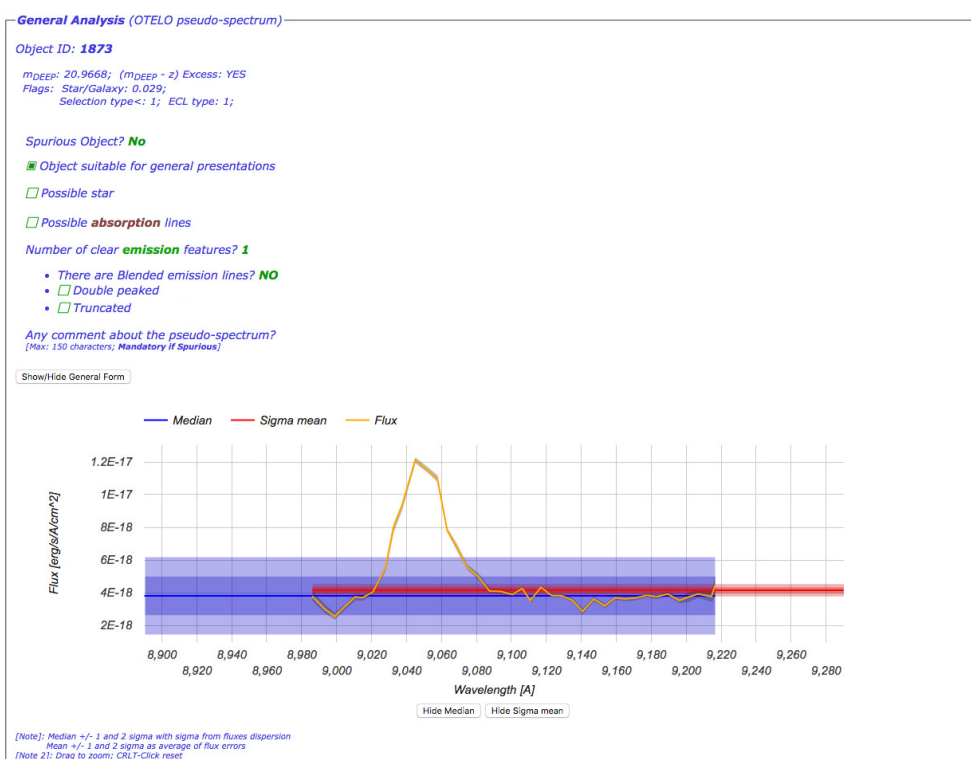


Figure 5.20: First section of the analysis questionnaire about the pseudo-spectrum of the object. The basic information of the object is displayed: OTELO ID, deep magnitude and flags (stellarity index from SExtractor, selection type and emitter type). The general appearance of the PS is analysed: emission and absorption features, truncated or blended lines, etc.

Este documento incorpora firma electrónica, y es copia auténtica de un documento electrónico archivado por la ULL según la Ley 39/2015. Su autenticidad puede ser contrastada en la siguiente dirección https://sede.ull.es/validacion/	
Identificador del documento: 969870	Código de verificación: 8KFVZkZp
Firmado por: MARINA RAMÓN PÉREZ UNIVERSIDAD DE LA LAGUNA	Fecha: 28/06/2017 21:15:24
ANGEL MANUEL BONGIOVANNI PEREZ UNIVERSIDAD DE LA LAGUNA	29/06/2017 09:30:15
JORGE CEPA NOGUE UNIVERSIDAD DE LA LAGUNA	29/06/2017 09:33:05
ANA MARIA PEREZ GARCIA UNIVERSIDAD DE LA LAGUNA	29/06/2017 11:12:35
ERNESTO PEREDA DE PABLO UNIVERSIDAD DE LA LAGUNA	04/07/2017 18:28:07

The second section of the questionnaire (see Fig. 5.21) analyses the appearance of the object in the different images available. In particular, the object is shown in OTELO's deep image and also in the u , g , r , i , z , J , H , Ks , IRAC 3.6 μm , IRAC 4.5 μm , HST 606W, and HST 814W bands. The questionnaire allows to change the contrast and size of the images, and to show the positions of nearby objects, the segmentation map and its ellipses. This is useful to: first, discard possible spurious objects (when only seen in OTELO's deep image) and second, make a preliminary visual analysis of the object's morphology based on the high resolution images of the HST. Finally, a comment can be made whenever the morphology presents some kind of complexity: multiple components, possible mergers or interactions, etc.

Image Analysis (OTELO resolution: 8x8 arc sec)

Normal size Size x2 Size x4 (max) Hide Positions Show Catalog Positions Hide Segmentation Map Show Ellipses seg. Map Change contrast

Comments about Low Resolution Images
[Max: 150 characters]

Bands where the object is NOT visible

- i
- H
- J
- HST 606W (low)
- HST 814W (low)
- r
- z
- Ks
- OTELO
- IRAC 3.6
- IRAC 4.5
- HST 606W (high)
- HST 814W (high)

Environment:

- Nearby objects (maybe cluster)
- Possible blending

Observation Issues:

- Object in border of OTELO field
- Truncated Object?

High resolution HST-data (F606W & F814W)

HST images Structure?

- Clumpiness, foci
- Multiple objects in high resolution image

Morphology class:

- Spheroid; all ellipticities

Comments [Unclassifiable morphology; number of components if multiple; possible interactions, merging, dynamical structures...]
[Max: 200 characters]

Figure 5.21: Second section of the analysis questionnaire about the appearance of the object in OTELO's deep image and in each image of the complementary data: u , g , r , i , z , J , H , Ks , IRAC 3.6 μm , IRAC 4.5 μm , HST 606W, and HST 814W. The questionnaire allows to change the size and contrast of the images, and to show the positions of nearby objects, the segmentation map and its ellipses. The morphology of the object is also analysed by means of the HST information.

Este documento incorpora firma electrónica, y es copia auténtica de un documento electrónico archivado por la ULL según la Ley 39/2015. Su autenticidad puede ser contrastada en la siguiente dirección https://sede.ull.es/validacion/	
Identificador del documento: 969870	Código de verificación: 8KfvZkZp
Firmado por: MARINA RAMÓN PÉREZ UNIVERSIDAD DE LA LAGUNA	Fecha: 28/06/2017 21:15:24
ANGEL MANUEL BONGIOVANNI PEREZ UNIVERSIDAD DE LA LAGUNA	29/06/2017 09:30:15
JORGE CEPA NOGUE UNIVERSIDAD DE LA LAGUNA	29/06/2017 09:33:05
ANA MARIA PEREZ GARCIA UNIVERSIDAD DE LA LAGUNA	29/06/2017 11:12:35
ERNESTO PEREDA DE PABLO UNIVERSIDAD DE LA LAGUNA	04/07/2017 18:28:07

The third section of the questionnaire (see Fig. 5.22) focuses on the photo-z analysis of the object. First, LePhare's different fits are shown for each set of templates (galaxy, QSO, star and FIR component). The photometric points, taken from OTELO's multiwavelength catalogue, are also displayed in order to evaluate the goodness of the fits. A table summarises all the redshift information of the object (best LePhare's photo-z for each library, CFHTLS photo-z and DEEP2 spectroscopic redshift, whenever available). The probability distribution of LePhare's photo-z is displayed in another graph. Finally, a dynamic tool specifically designed for our purpose allows us to assign a certain redshift to the PS feature of our choice, so as to see which emission or absorption line would correspond to it. The opposite test can also be made: to chose an specific line (H α , H β ...) and see at what redshift it would be seen for it to coincide with the PS feature of our choice. To help the identification of the spectral feature, a last table indicates the most relevant spectral lines in the range of the chosen redshift, along with their approximate intensity depending on the type of object.



Figure 5.22: Third section of the analysis questionnaire about the photo-z analysis of the object. LePhare's different fits are shown for each type of template (galaxy, QSO, star and FIR component), as well as the object's photometric points (top left). A table displays the different redshifts obtained with OTELO's multiwavelength catalogue and the ones from DEEP2 and CFHTLS (top right). The middle graph shows the probability distribution of LePhare's photo-z. At the bottom, a dynamic tool allows to assign a certain redshift to the PS feature of our choice, so as to see which emitting or absorption line would correspond. The bottom left table shows the most relevant spectral lines in the range of the chosen redshift, along with their approximate intensity depending on the type of object.

Este documento incorpora firma electrónica, y es copia auténtica de un documento electrónico archivado por la ULL según la Ley 39/2015.
Su autenticidad puede ser contrastada en la siguiente dirección <https://sede.ull.es/validacion/>

Identificador del documento: 969870

Código de verificación: 8KFVZkZp

Fecha: 28/06/2017 21:15:24

Firmado por: MARINA RAMÓN PÉREZ
UNIVERSIDAD DE LA LAGUNA

ANGEL MANUEL BONGIOVANNI PEREZ
UNIVERSIDAD DE LA LAGUNA

JORGE CEPA NOGUE
UNIVERSIDAD DE LA LAGUNA

ANA MARIA PEREZ GARCIA
UNIVERSIDAD DE LA LAGUNA

ERNESTO PEREDA DE PABLO
UNIVERSIDAD DE LA LAGUNA

29/06/2017 09:30:15

29/06/2017 09:33:05

29/06/2017 11:12:35

04/07/2017 18:28:07

Each object in the sample of H α candidates was analysed using this questionnaire by four independent collaborators. At the end of the individual analysis, the goal was to assign to the emitting object up to three possible values of redshift with a corresponding degree of confidence (C) in the form of a number ranging from 5 (highly reliable redshift) to 1 (possible but not very reliable). In order to compare the results obtained from the different individual analysis, each suggested value of z was given a score S such as:

$$S = 2^{C-1} \quad (5.3)$$

This expression takes into account the fact that a subjective appreciation is generally non linear and that a power law is the easiest way to model this behaviour. By using it in base 2, we suppose that two people assigning a degree of confidence C is equivalent to a single person assigning $C + 1$, which is a reasonable approximation. This is specially sensible when dealing with ranges of z instead of exact values, as was the case here.

Two comparison groups were made for the analysis: one for those z falling in the H α window of OTELO and another one for the rest. All the different scores of the z values in each group were summed up. Whenever someone selected the option “can not find a reliable z ” in the questionnaire, a score of $S = 2^2$ (i.e., a confidence value of 3) was added to the second group (“ z not belonging to the H α range”). The selection of H α emitters was made by comparing the final score of both groups. If the total score of the first group was higher than that of the second group, the object was considered as a reliable H α emitter. Considering all of this, 46 out of the 202 candidates were finally selected as true H α emitters.

Este documento incorpora firma electrónica, y es copia auténtica de un documento electrónico archivado por la ULL según la Ley 39/2015.
Su autenticidad puede ser contrastada en la siguiente dirección <https://sede.ull.es/validacion/>

Identificador del documento:	969870	Código de verificación:	8KFVZkZp
Firmado por:	MARINA RAMÓN PÉREZ UNIVERSIDAD DE LA LAGUNA	Fecha:	28/06/2017 21:15:24
	ANGEL MANUEL BONGIOVANNI PEREZ UNIVERSIDAD DE LA LAGUNA		29/06/2017 09:30:15
	JORGE CEPA NOGUE UNIVERSIDAD DE LA LAGUNA		29/06/2017 09:33:05
	ANA MARIA PEREZ GARCIA UNIVERSIDAD DE LA LAGUNA		29/06/2017 11:12:35
	ERNESTO PEREDA DE PABLO UNIVERSIDAD DE LA LAGUNA		04/07/2017 18:28:07

Este documento incorpora firma electrónica, y es copia auténtica de un documento electrónico archivado por la ULL según la Ley 39/2015.
Su autenticidad puede ser contrastada en la siguiente dirección <https://sede.ull.es/validacion/>

Identificador del documento: 969870

Código de verificación: 8KFVZkZp

Fecha: 28/06/2017 21:15:24

Firmado por: MARINA RAMÓN PÉREZ
UNIVERSIDAD DE LA LAGUNA

ANGEL MANUEL BONGIOVANNI PEREZ
UNIVERSIDAD DE LA LAGUNA

JORGE CEPA NOGUE
UNIVERSIDAD DE LA LAGUNA

ANA MARIA PEREZ GARCIA
UNIVERSIDAD DE LA LAGUNA

ERNESTO PEREDA DE PABLO
UNIVERSIDAD DE LA LAGUNA

29/06/2017 09:30:15

29/06/2017 09:33:05

29/06/2017 11:12:35

04/07/2017 18:28:07

6

SELECTION OF AGN

In this Chapter, we describe the selection among the objects in OTELO's catalogue of galaxies having active galactic nuclei. Different methods are used for this purpose, each selecting a different population of AGN. We use the information of emission lines in the optical, but also the X-rays and mid-infrared data gathered in OTELO's multiwavelength catalogue.

Active galactic nuclei are a special astronomical phenomenon showing characteristic spectral signatures in different wavelength bands. They can be selected with different techniques targeting each one of those specific marks. However, due to the diversity of AGN types, a specific technique may correctly select an AGN population while missing others. For instance, a selection based on X-ray or optical emission can miss the population of obscured (either by interstellar gas or by dust) AGN, unlike an infrared photometry based method. On the other hand, X-ray emission is a powerful tool to select low-luminosity AGN or AGN hiding behind larger Hydrogen column densities than those found by optical methods.

In view of this, and in order to take advantage of the multiwavelength data available for OTELO sources, we used three different techniques to select AGN. The first one targets the AGN optical emission and uses a diagnostic diagram to separate them from star-forming galaxies. The second one employs the X-ray-to-optical flux ratio (X/O). Finally, the third one uses MIR colour-colour diagrams.

6.1 AGN at $z \sim 0.40$

The first method to select AGN takes advantage of the potential of OTELO survey to identify emitting objects, as already discussed in previous chapters. Despite lacking any spectroscopic measurement, the pseudo-spectrum built for every object in OTELO's catalogue, together with all the additional information, allows us to identify emission lines (see chapter 5). In the case of the H α line at $z \sim 0.40$, the PS also enables the measurement of fluxes and equivalent widths (Lara-López et al. 2011). This makes it possible to use optical diagnostic diagrams, such as the one by Cid Fernandes et al. (2010), to discriminate between AGN and starburst galaxies.

Este documento incorpora firma electrónica, y es copia auténtica de un documento electrónico archivado por la ULL según la Ley 39/2015.
Su autenticidad puede ser contrastada en la siguiente dirección <https://sede.ull.es/validacion/>

Identificador del documento:	969870	Código de verificación:	8KFVZkZp
Firmado por:	MARINA RAMÓN PÉREZ UNIVERSIDAD DE LA LAGUNA	Fecha:	28/06/2017 21:15:24
	ANGEL MANUEL BONGIOVANNI PEREZ UNIVERSIDAD DE LA LAGUNA		29/06/2017 09:30:15
	JORGE CEPA NOGUE UNIVERSIDAD DE LA LAGUNA		29/06/2017 09:33:05
	ANA MARIA PEREZ GARCIA UNIVERSIDAD DE LA LAGUNA		29/06/2017 11:12:35
	ERNESTO PEREDA DE PABLO UNIVERSIDAD DE LA LAGUNA		04/07/2017 18:28:07

6.1.1 Broad-Line AGN

First of all, we selected broad-line AGN (BLAGN) from our sample of H α emitters. BLAGN are active galactic nuclei showing permitted lines with widths of thousands of kilometers per second. In comparison, narrow-line AGN (NLAGN) have line widths of only a few hundred kilometers per second or less. Their selection is described in subsection 6.1.3.

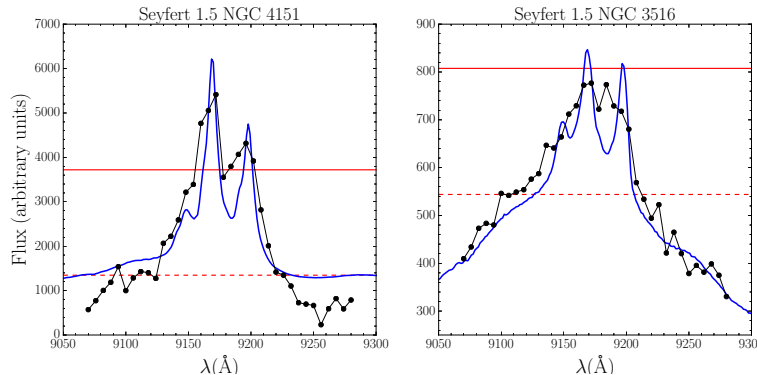


Figure 6.1: Spectra of real BLAGN showing H α +[NII] emission redshifted to $z = 0.39$ (blue lines) and their simulated pseudo-spectra as seen with OTELO's tunable filters (black dots). The red dashed line represents the pseudo-continuum, f_{cont} , defined as the median value of the pseudo-spectrum points which remain within 2σ around the median value of the whole pseudo-spectrum. The red continuous line represents $f_{cont} + 2\sigma_{cont}$, where σ_{cont} is the standard deviation of the pseudo-continuum points. As explained in Chapter 5, NGC 3516 would not have been selected as an emitter in the first round.

In order to check the aspect of broad-lines when observed through OSIRIS tunable filters, we performed a simulation using two real spectra of BLAGN: the Seyferts 1.5 NGC 3516 (Arribas et al. 1997) and NGC 4151 (Kaspi et al. 1996). We redshifted their spectra to $z = 0.39$ so that the H α component would fall in OTELO's spectral window and convolved them with our TF transmission profile (equation 2.3). A noise component was also added, corresponding to random values drawn from a normal distribution with zero mean value and a standard deviation of 10% the difference between the highest value of the pseudo-spectrum and its median.

In Fig. 6.1, both spectra and their simulated pseudo-spectra are shown. The values of f_{cont} and $f_{cont} + 2\sigma_{cont}$, as defined in Chapter 5, are also indicated. It can be seen that, even if the H α +[NII] emission is well reproduced in both examples, in the case of NGC 3516 the line is so broad that it becomes diluted after the convolution and the object would fail the automatic test described in section 5.1.1 for the detection of emission lines.

In order to estimate the maximum line width that a BLAGN can have to be selected by our algorithm, we performed simulations assuming two gaussians of variable width (H α and [NII]) at a redshift of ~ 0.398 , so that the H α component would be centered at 9175 Å, in the OTELO wavelength window. Then, we convolved the simulated spectra to the TF response, adding a noise component and checking whether the resulting pseudo-spectrum would have been recognised as an emitting candidate. Finally, the pseudo-spectra were fitted to a single gaussian in order to estimate the FWHM. Two examples of such simulations can be seen in Fig. 6.2. We found that the automatic algorithm for the detection of emitting lines starts to fail when the FWHM of the resulting gaussian fit is beyond ~ 83 Å, which corresponds to a width of ~ 2700 km/s at that redshift. This gaussian fit includes both H α +[NII] lines, but since [NII] is a narrow line, most of the contribution would

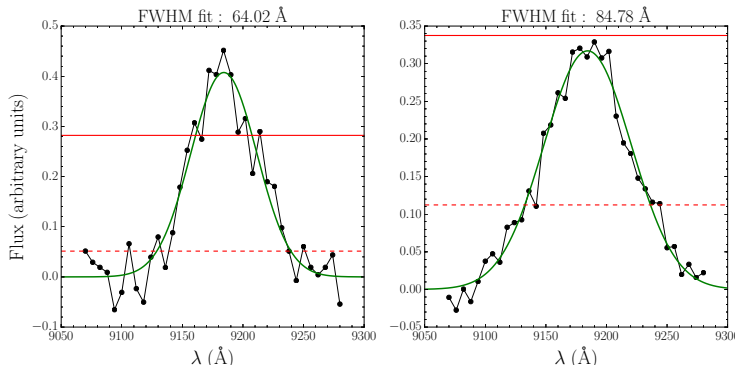


Figure 6.2: Simulated pseudo-spectra (black dots) of $\text{H}\alpha$ +[NII] lines with different widths after being convolved to the TF spectral response. The green lines represent the best gaussian fit to each pseudo-spectrum and the texts in the top left corners describe the corresponding FWHM. The red dashed lines represent the pseudo-continuum, f_{cont} , defined as the median value of the pseudo-spectrum points which remain within 2σ around the median value of the whole pseudo-spectrum. The red continuous lines represent $f_{\text{cont}} + 2\sigma_{\text{cont}}$, where σ_{cont} is the standard deviation of the pseudo-continuum points. The automatic algorithm described in Chapter 5 efficiently detects broad-lines as emitting lines for widths up to $\sim 83\text{\AA}$. In the left panel, with a FWHM of 64.02\AA , the broad line is detected. On the contrary, the line in the right panel is so broad (FWHM of 84.78\AA) that it is not recognised.

belong to $\text{H}\alpha$. This result is consistent with the conclusion of the simulation carried out in section 5.2.1, where we found an approximate detection limit at $\sim 60\text{\AA}$ for the FWHM of the input gaussian ($\text{H}\alpha$), corresponding to $\sim 84\text{\AA}$ at $z = 0.398$. The situation improves when the lines are not centered in the OTELO wavelength window, as can be seen in Fig. 6.3. In those cases, when the line appears close to the limiting edges of the spectral window, the pseudo-continuum is more realistically reproduced by the algorithm, favouring the detection.

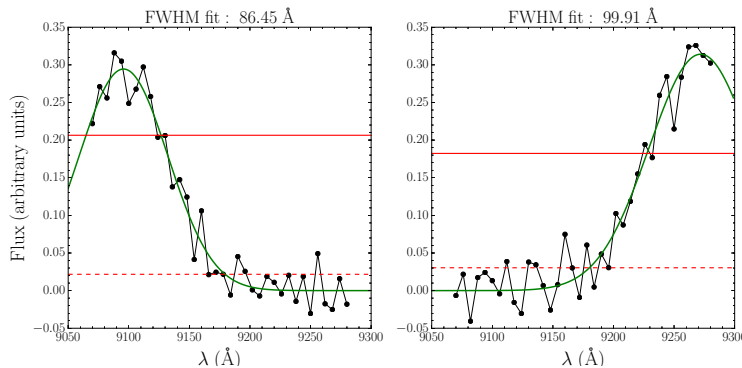


Figure 6.3: Simulated pseudo-spectra of $\text{H}\alpha$ +[NII] lines not centered in OTELO wavelength window after being convolved to the TF spectral response. The symbols and colours are as in Fig. 6.2. The automatic algorithm described in Chapter 5 detects broader lines as emitting ones when they are not centered in OTELO wavelength window. In this case, lines with FWHM of 86.45\AA and 99.91\AA are easily detected by the algorithm.

Este documento incorpora firma electrónica, y es copia auténtica de un documento electrónico archivado por la ULL según la Ley 39/2015. Su autenticidad puede ser contrastada en la siguiente dirección https://sede.ull.es/validacion/		
Identificador del documento:	969870	Código de verificación: 8KFVZkZp
Firmado por:	MARINA RAMÓN PÉREZ UNIVERSIDAD DE LA LAGUNA	Fecha: 28/06/2017 21:15:24
	ANGEL MANUEL BONGIOVANNI PEREZ UNIVERSIDAD DE LA LAGUNA	29/06/2017 09:30:15
	JORGE CEPA NOGUE UNIVERSIDAD DE LA LAGUNA	29/06/2017 09:33:05
	ANA MARIA PEREZ GARCIA UNIVERSIDAD DE LA LAGUNA	29/06/2017 11:12:35
	ERNESTO PEREDA DE PABLO UNIVERSIDAD DE LA LAGUNA	04/07/2017 18:28:07

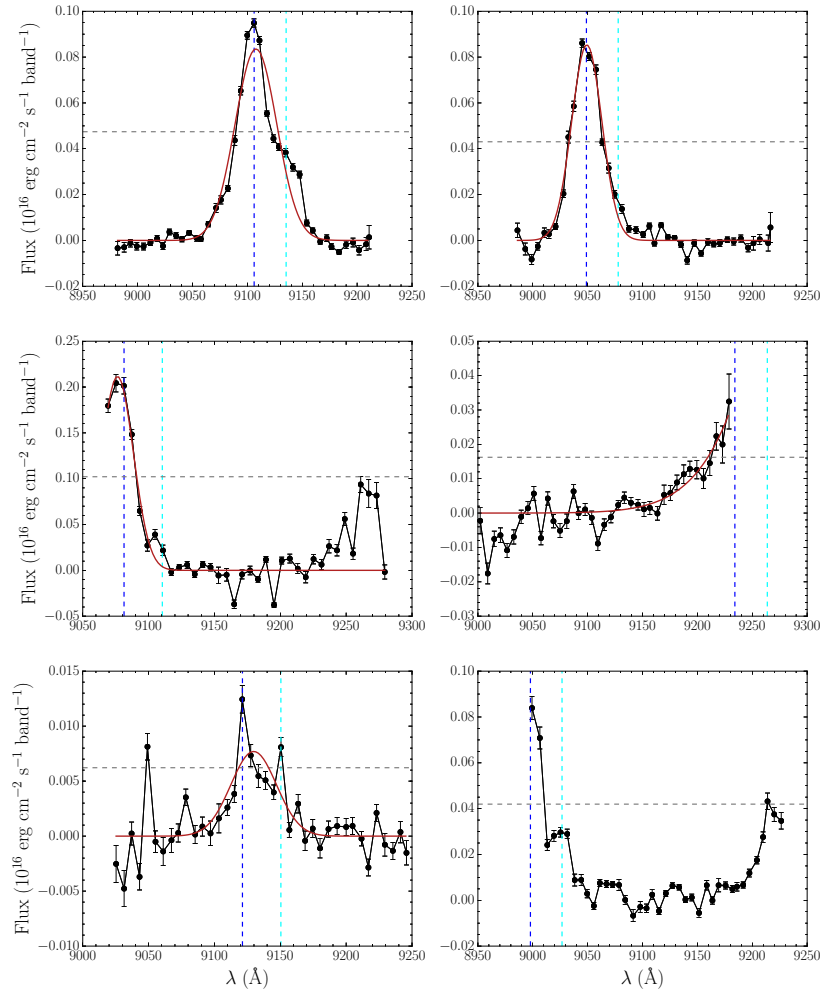


Figure 6.4: Objects from OTELO survey showing H α +[NII] emission and classified as BLAGN. The red lines show the best fit to a gaussian profile, while the grey dashed lines represent half the maximum value of the pseudo-spectra. The blue and cyan vertical lines mark the positions of the H α and [NII] emission lines, respectively. In the last case, no fitting could be made due to the truncation of the line. However, the object was included in the final sample because its width is comparable to the rest of the objects selected as BLAGN.

Este documento incorpora firma electrónica, y es copia auténtica de un documento electrónico archivado por la ULL según la Ley 39/2015.
Su autenticidad puede ser contrastada en la siguiente dirección <https://sede.ull.es/validacion/>

Identificador del documento: 969870

Código de verificación: 8KFVZkZp

Fecha: 28/06/2017 21:15:24

Firmado por: MARINA RAMÓN PÉREZ
UNIVERSIDAD DE LA LAGUNA

29/06/2017 09:30:15

ANGEL MANUEL BONGIOVANNI PEREZ
UNIVERSIDAD DE LA LAGUNA

29/06/2017 09:33:05

JORGE CEPA NOGUE
UNIVERSIDAD DE LA LAGUNA

29/06/2017 11:12:35

ANA MARIA PÉREZ GARCIA
UNIVERSIDAD DE LA LAGUNA

04/07/2017 18:28:07

ERNESTO PEREDA DE PABLO
UNIVERSIDAD DE LA LAGUNA

In this work, we considered as BLAGN those objects having a FWHM greater than 1000 km/s, in order to distinguish them from NLAGN which have smaller widths (typically only hundreds of km/s). Also, from the previous simulations, we do not expect to find BLAGN in our survey with widths larger than ~ 2700 km/s. BLAGN were selected on the basis of two different but equivalent criteria. The first one consisted in fitting the pseudo-spectrum to a gaussian and determining the FWHM of the fit (as in Fig. 6.2). After visual inspection to discard incorrect or unclear fits, we selected as BLAGN those objects having a resulting FWHM greater than ~ 30 Å (corresponding to ~ 1000 km/s at $z \sim 0.40$).

The second criteria was used whenever the pseudo-spectrum could not be fitted. In those cases, we calculated the number of PS points around the maximum that exceeded half its value. Two different maxima were considered: 1) the real PS maximum and 2) the closest PS point to the H α line maximum, given the redshift. If at least 5 points around one of these maxima had a value higher than max/2, the object was considered a BLAGN. Taking into account that the sampling interval of OTELO is 6Å, both this criterium and the previous one are equivalent. In total, 6 H α emitters were selected as BLAGN by one or both of these criteria. They are shown in Fig. 6.4. One of these objects (the last one in the figure) showed a truncated line which prevented the fitting and the analysis. However, it was included in the final sample of BLAGN because its width is comparable to the rest of the objects selected as BLAGN, if we assume a symmetrical line.

6.1.2 Measurement of H α and [NII] fluxes and EW

Once BLAGN were selected, we focused on the search of NLAGN. To do so, H α and [NII] fluxes and EW were calculated. The first step in this process was to subtract a linear continuum to the pseudo-spectra. This was done by performing a linear fit to all the PS points except those belonging to the emission line. The fits were then verified visually. In some cases, when the continuum fit was not good enough and included part of the emission line, the continuum level was subtracted manually. The H α and [NII] fluxes ($f(H\alpha)$ and $f([NII])$, respectively) were derived following the procedure described in Sánchez-Portal et al. (2015), that assumes infinitely thin lines. For each object, the wavelength position of both lines is known given the redshift. The fluxes measured in the closest scan slices to these positions ($f_{H\alpha}$ and $f_{[NII]}$, respectively), correspond to a combination of both line fluxes such as:

$$\begin{aligned} f_{H\alpha} &= T_{H\alpha}(H\alpha)f(H\alpha) + T_{H\alpha}([NII])f([NII]) \\ f_{[NII]} &= T_{[NII]}(H\alpha)f(H\alpha) + T_{[NII]}([NII])f([NII]) \end{aligned} \quad (6.1)$$

In the previous equations, T_{slice} ('line') represents the TF transmission of a given slice at a given line wavelength. It can be determined from the approximate TF expression of equation 2.3. The real H α and [NII] fluxes can then be derived from the previous equations with a little bit of calculus, yielding:

$$f(H\alpha) = \frac{f_{H\alpha}T_{[NII]}([NII]) - f_{[NII]}T_{H\alpha}([NII])}{T_{H\alpha}(H\alpha)T_{[NII]}([NII]) - T_{H\alpha}([NII])T_{[NII]}(H\alpha)}, \quad (6.2)$$

and a similar equation for $f([NII])$. EW were then converted to rest-frame using the redshift information. The distribution of H α fluxes calculated for our sample of H α sources in this way can be seen in Fig. 6.5. The median error was $\sim 12\%$, in agreement with the results of a simulation performed by Lara-López et al. (2011), which yielded errors below 20% for a FWHM of the OSIRIS TF of 12Å and a sampling of 6Å. However, our errors in the measurement of the [NII] line were much higher, with 60% of the objects having errors above 50%.

Este documento incorpora firma electrónica, y es copia auténtica de un documento electrónico archivado por la ULL según la Ley 39/2015.
Su autenticidad puede ser contrastada en la siguiente dirección <https://sede.ull.es/validacion/>

Identificador del documento: 969870	Código de verificación: 8KFVZkZp
Firmado por: MARINA RAMÓN PÉREZ UNIVERSIDAD DE LA LAGUNA	Fecha: 28/06/2017 21:15:24
ANGEL MANUEL BONGIOVANNI PEREZ UNIVERSIDAD DE LA LAGUNA	29/06/2017 09:30:15
JORGE CEPA NOGUE UNIVERSIDAD DE LA LAGUNA	29/06/2017 09:33:05
ANA MARIA PEREZ GARCIA UNIVERSIDAD DE LA LAGUNA	29/06/2017 11:12:35
ERNESTO PEREDA DE PABLO UNIVERSIDAD DE LA LAGUNA	04/07/2017 18:28:07

This, inevitably, was to be expected since the [NII] line is usually fainter than the H α one¹ and, in addition, the object's selection is made on the basis of the detection of the latter.

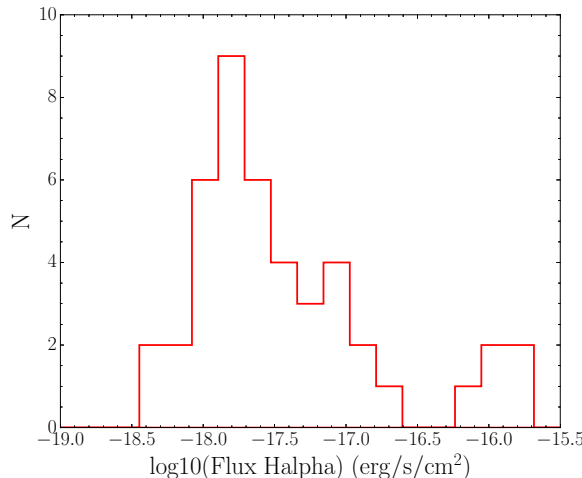


Figure 6.5: Histogram of H α fluxes of the sources selected as H α emitters (see Chapter 5) and derived using the procedure described in the text.

6.1.3 Discrimination between SFG and AGN

Optical diagnostic diagrams based on fluxes of emission lines are a key tool when it comes to distinguish between star-forming galaxies (SFG) and AGN. The comparison of the intensities of different emission lines gives information about the ionization mechanism of the gas. The photoionization can be due to the radiation produced by young (O and B) stars in the case of SFG or by a harder radiation field (a power-law continuum source), as in the case of AGN.

One of the most classical and used diagnostic diagrams is the Baldwin, Phillips & Terlevich diagram (1981), known as the “BPT diagram”, which uses the ratios of [OIII]/H β and [NII]/H α emission lines. Other flux ratios, such as [SII](λ 6716+ λ 6731)/H α or [OI] λ 6300/H α are also useful for this purpose (Baldwin et al. 1981, Veilleux & Osterbrock 1987). Unfortunately, those lines are not always available, neither can their fluxes always be measured. More humble diagnostic diagrams are thus needed to separate distinct classes of objects. An alternative is to use the EW α n2 diagram, in which the [OIII]/H β ratio of the BPT diagram is replaced with the equivalent width of H α at rest-frame (Cid Fernandes et al. 2010).

In the EW α n2 diagram, star-forming and active galaxies occupy separate regions along the horizontal axis, while Seyferts and LINERs are differently distributed along the vertical axis (see Fig. 6.6). Several criteria can be used in order to select AGN. Stasińska et al. (2006), for instance, defines pure star-forming galaxies as those objects lying in the $\log [\text{NII}]/\text{H}\alpha \leq -0.4$ region and AGN as those with $\log [\text{NII}]/\text{H}\alpha > -0.2$. In the intermediate region, hybrid objects having both star-formation and nuclear activity are located. A similar classification for AGN is proposed by Ho et al. (1997), while Kewley et al. (2001) are a bit more restrictive and

¹At least for star-forming galaxies, which are the majority, as will be seen in the next subsection.

consider as pure AGN those objects having $\log [\text{NII}]/\text{H}\alpha > -0.1$. Moreover, a separation between LINERs and Seyferts can be traced at $\text{EW}(\text{H}\alpha) = 6\text{\AA}$ (rest-frame), according to Kewley et al. (2006).

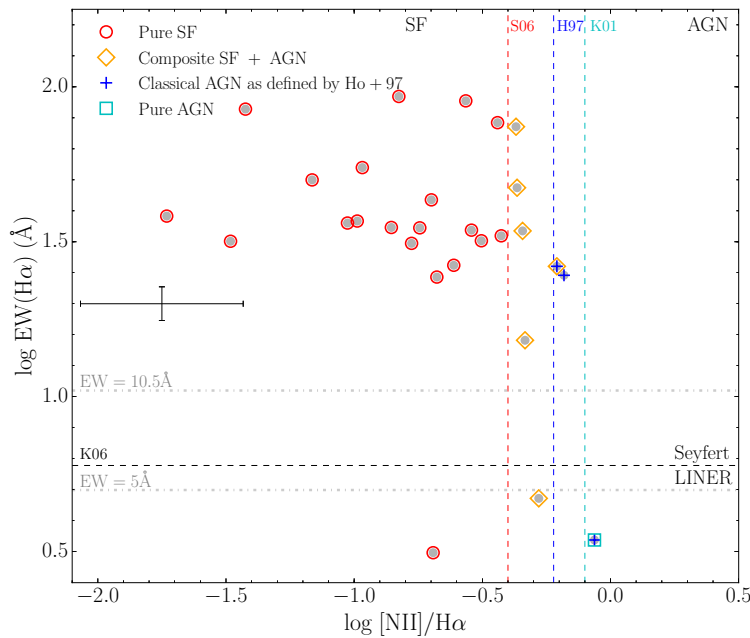


Figure 6.6: $\text{EW}\alpha\text{n}2$ diagnostic diagram defined by Cid Fernandes et al. (2010) in order to distinguish star-forming galaxies from AGN. Pure star-forming galaxies (red circles) are separated from composite objects (SF+AGN, orange diamonds) according to Stasińska et al. (2006) (red dashed vertical line). Classical AGN as defined by Ho et al. (1997) (blue dashed vertical line) are displayed with blue crosses. Pure AGN according to Kewley et al. (2001) (cyan dashed vertical line) are represented in cyan squares. The black dashed horizontal line corresponds to the Seyfert/LINER separation criterion by Kewley et al. (2006). The two grey dashed-dotted horizontal lines mark our minimum detected $\text{EW}(\text{H}\alpha)$ with a probability threshold of $p \geq 0.95$ for objects with a PS continuum up to $\sim 10^{-18} \text{ erg/s/cm}^2/\text{\AA}$, and the one with $p \geq 0.50$ for objects with a PS continuum up to $\sim 10^{-19} \text{ erg/s/cm}^2/\text{\AA}$ (see simulation in subsection 5.2.1). The error bars in the middle left of the plot represent the median errors in our $\text{H}\alpha$ sample.

Fig. 6.6 shows the $\text{EW}\alpha\text{n}2$ diagram for our sample of $\text{H}\alpha$ emitters. The different criteria previously described are shown. We have also traced our minimum detected $\text{EW}(\text{H}\alpha)$ with a probability threshold of $p \geq 0.95$ and $p \geq 0.50$, according to the simulation described in subsection 5.2.1. In order to ensure the selection, the objects with EW below the $p \geq 0.95$ limit, including two possible LINERs, were discarded from the analysis. Accordingly, all the selected AGN are presumably Seyfert galaxies with $\text{EW}(\text{H}\alpha) > 0.6$. We have selected all galaxies showing evidence of nuclear activity, either in hybrid galaxies or in pure active ones, following the criterion by Stasińska et al. (2006). In this way, 6 $\text{H}\alpha$ emitters have been selected as NLAGN. However, due to the large uncertainties in the [NII] line flux measurements, the [NII]/ $\text{H}\alpha$ ratios have also large errors (the mean relative error in the sample was 32%, see error bars in Fig. 6.6) and so the selection of NLAGN with this procedure should be taken with caution.

Este documento incorpora firma electrónica, y es copia auténtica de un documento electrónico archivado por la ULL según la Ley 39/2015. Su autenticidad puede ser contrastada en la siguiente dirección https://sede.ull.es/validacion/		
Identificador del documento:	969870	Código de verificación: 8KFVZkZp
Firmado por:	MARINA RAMÓN PÉREZ UNIVERSIDAD DE LA LAGUNA	Fecha: 28/06/2017 21:15:24
	ANGEL MANUEL BONGIOVANNI PEREZ UNIVERSIDAD DE LA LAGUNA	29/06/2017 09:30:15
	JORGE CEPA NOGUE UNIVERSIDAD DE LA LAGUNA	29/06/2017 09:33:05
	ANA MARIA PEREZ GARCIA UNIVERSIDAD DE LA LAGUNA	29/06/2017 11:12:35
	ERNESTO PEREDA DE PABLO UNIVERSIDAD DE LA LAGUNA	04/07/2017 18:28:07

6.2 X-ray selection

The X-rays emission is a good indicator of nuclear activity in galaxies. In fact, AGN are believed to be the prevailing astronomical objects contributing to the cosmic X-ray background (Della Ceca et al. 2004). In the surveys carried out with the Chandra and XMM-Newton spatial observatories, for instance, the majority of the extragalactic X-ray sources that were found were AGN (Brandt et al. 2004). The strong X-ray emission of those objects is produced in the central regions of the accretion disk surrounding the black hole.

As already noted by Maccacaro et al. (1988), a good way to distinguish AGN from other X-ray emitting sources is to use the X-ray-to-optical flux ratio (X/O). As both our X-ray sources from Pović et al. (2009) and the ones from Laird et al. (2009) in OTELLO's catalogue had information in the soft 0.5-2 keV band, we used the definition of X/O by Szokoly et al. (2004):

$$X/O \equiv \log_{10}(f_X/f_O) \equiv \log_{10}(f_X) + 0.4R + 5.71 \quad (6.3)$$

where f_X is the X-ray flux in the 0.5-2 keV band ($\text{erg/cm}^2/\text{s}$) and R is the optical magnitude in Vega magnitudes. According to numerous authors such as the already mentioned and also Stocke et al. (1991) or Alexander et al. (2001), AGN are typically located in the range:

$$-1 < X/O < 1 \quad (6.4)$$

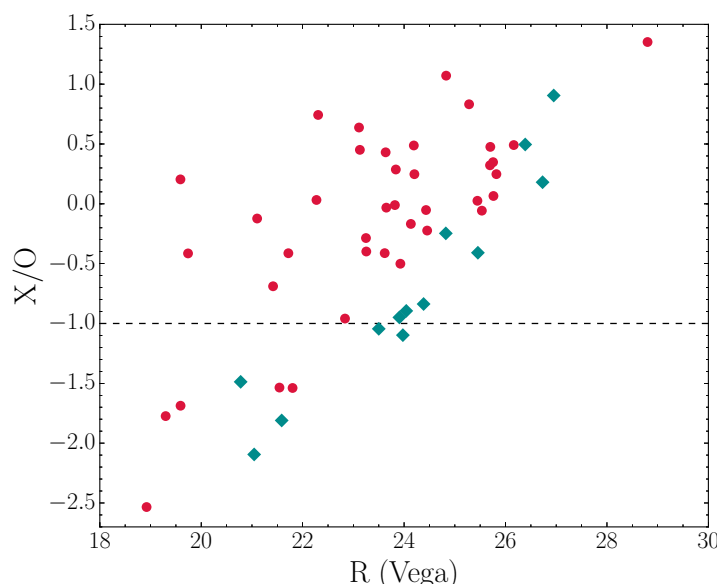


Figure 6.7: X-ray-to-optical flux ratio (X/O) as a function of the optical band (R in Vega magnitudes) of the X-ray emitting sources in OTELLO's catalogue. Red dots correspond to the sources from the original catalogue of Pović et al. (2009) with information in the soft band (0.5-2 keV), while the green diamonds are the ones from the catalogue of Laird et al. (2009). The adopted criterion to select AGN is $X/O > -1$, which results in 42 findings.

At very high values of X/O we can find not only types 1 and 2 AGN, but also clusters of galaxies at high redshift and extreme BL Lac objects. On the other hand, low values of X/O ($X/O < -1$) are characteristic of coronal emitting stars, early-type and star-forming galaxies and nearby heavily absorbed (Compton thick) AGN. For our purpose, objects with nuclear activity and those with star-formation can be separated with the $X/O = -1$ limit.

In Fig. 6.7 we have plotted the X/O ratio as a function of the optical magnitude, for the sources in OTELO's catalogue that show an X-ray emission and have information in the soft band (53 out of 56). We have selected as AGN 42 sources having $X/O > -1$.

6.3 Mid-infrared selection

One of the main features of AGN is the power-law continuum that generally dominates their spectrum from UV to $\sim 5\mu\text{m}$. On the contrary, star-forming galaxies exhibit a blackbody shaped continuum due to their stellar populations in this range, with a peak around $\sim 1.6\mu\text{m}$. As a consequence, AGN tend to be redder than normal galaxies in the mid-infrared. By using infrared colours, one can obtain information about the underlying continuum in a spectrum and detect objects whose SED do not decline in the *red* side of the stellar peak.

The great advantage of mid-infrared selection of AGN is that it permits to detect even those objects obscured by interstellar gas or by dust that can not be seen in X-rays or in the optica However, when compared to other bands, images in the infrared may sometimes suffer from poorer spatial resolution.

Diagnostic diagrams to distinguish AGN from star-forming galaxies using infrared colours are very common. One of the most famous is the empirical criterion proposed by Stern et al. (2005). It uses the four IRAC bands (at 3.6, 4.5, 5.8 and 8.0 μm) to build a colour-colour diagram, and then defines an empirical region where most of the AGN are located. In this way, 90% of their spectroscopically identified type 1 AGN, and 40% of their type 2 AGN were selected. Nevertheless, the authors also claim that this method may omit AGN at $z \sim 0.8$ and 2. Thus, it is not convenient in OTELO's case, where sources have no constrains in redshift.

In 2012, Donley et al. proposed the "IRAC revised criteria" in order to improve the previous method and reduce the contamination by star-forming galaxies at high redshift ($z > 0.5$). Their philosophy is similar to that of Stern et al. (2005), but the criteria are more restrictive. It also makes use of the fluxes in the four IRAC bands and defines an empirical region where AGN are found:

$$\begin{aligned} x &\geq 0.08 \\ y &\geq 0.15 \\ y &\geq 1.21 \times x - 0.27 \\ y &\leq 1.21 \times x + 0.27, \end{aligned} \tag{6.5}$$

where $x = \log_{10}(f_{5.8\mu\text{m}}/f_{3.6\mu\text{m}})$ and $y = \log_{10}(f_{8.0\mu\text{m}}/f_{4.5\mu\text{m}})$. We used this method to select AGN based on their MIR colours. As can be seen in Fig. 6.8, 15 AGN were found in this way.

In addition, we used an alternative second MIR criterion to select AGN in the field (the "KIM" criterion), based on the work by Messias et al. (2012). This criterion not only takes the IRAC bands into account, but also the K_s and the 24 μm bands, which are also contained in OTELO's multiwavelength catalogue. The authors first define the KI criterion (K_s +IRAC), an alternative to Stern et al. (2005) and Lacy et al. (2004, 2007) methods, with less contamination from normal galaxies at $z < 2.5$ and no loss of completeness:

Este documento incorpora firma electrónica, y es copia auténtica de un documento electrónico archivado por la ULL según la Ley 39/2015. Su autenticidad puede ser contrastada en la siguiente dirección https://sede.ull.es/validacion/		
Identificador del documento: 969870	Código de verificación: 8KFVZkZp	Fecha: 28/06/2017 21:15:24
Firmado por: MARINA RAMÓN PÉREZ UNIVERSIDAD DE LA LAGUNA		29/06/2017 09:30:15
ANGEL MANUEL BONGIOVANNI PÉREZ UNIVERSIDAD DE LA LAGUNA		29/06/2017 09:33:05
JORGE CEPA NOGUE UNIVERSIDAD DE LA LAGUNA		29/06/2017 11:12:35
ANA MARIA PÉREZ GARCIA UNIVERSIDAD DE LA LAGUNA		04/07/2017 18:28:07
ERNESTO PEREDA DE PABLO UNIVERSIDAD DE LA LAGUNA		

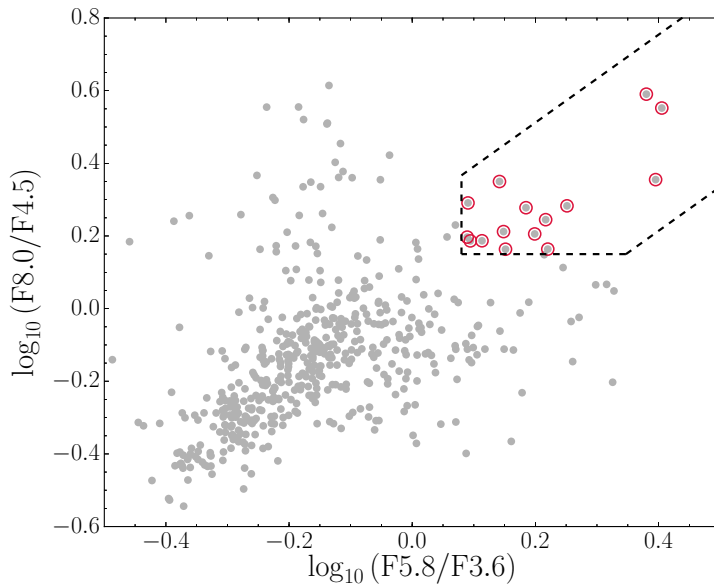


Figure 6.8: Revised IRAC criteria from Donley et al. (2012) to separate AGN from star-forming galaxies. The x axis shows the ratio between the flux in the $5.8\mu\text{m}$ band and the flux in the $3.6\mu\text{m}$ band, while the y axis depicts the ratio between the flux in the $8.0\mu\text{m}$ band and the flux in the $4.5\mu\text{m}$ band. Grey dots are all the sources in OTELO's catalogue with information in the four IRAC bands. Black dashed lines correspond to the limits set by Donley et al. (2012) to select AGN. Red circled sources are the 15 sources selected as AGN in this way.

$$\begin{aligned} K_s - [4.5] &> 0 \\ [4.5] - [8.0] &> 0 \end{aligned} \quad (6.6)$$

Then, they extend this criterion to high redshifts ($z > 1$) with the IM criterion (IRAC+MIPS):

$$\begin{aligned} [8.0] - [24] &> -2.9 \times ([4.5] - [8.0]) + 2.8 \\ [8.0] - [24] &> 0.5, \end{aligned} \quad (6.7)$$

although these last criteria fail at $z < 1$ because AGN and star-forming galaxies occupy the same region in the colour-colour space. Finally, a combination of both criteria (KI+IM) is proposed. The so-called KIM (K_s +IRAC+MIPS) criterion satisfies equations 6.7 and $K_s - [4.5] > 0$, the first equation of 6.6. It minimises contamination at low redshifts from normal galaxies while effectively separating AGN from star-forming galaxies at high redshifts, and thus can be used at all ranges of z . In Fig. 6.9, we have plotted the $[8.0] - [24]$ versus $[4.5] - [8.0]$ colours, and have selected the sources fulfilling the IM criterion plus those that satisfy, in addition, $K_s - [4.5] > 0$. Given that OTELO has no contrains in redshift, we used the KIM criteria and selected

Identificador del documento:	969870	Código de verificación:	8KFVZkZp
Firmado por:	MARINA RAMÓN PÉREZ UNIVERSIDAD DE LA LAGUNA	Fecha:	28/06/2017 21:15:24
	ANGEL MANUEL BONGIOVANNI PEREZ UNIVERSIDAD DE LA LAGUNA		29/06/2017 09:30:15
	JORGE CEPA NOGUE UNIVERSIDAD DE LA LAGUNA		29/06/2017 09:33:05
	ANA MARIA PEREZ GARCIA UNIVERSIDAD DE LA LAGUNA		29/06/2017 11:12:35
	ERNESTO PEREDA DE PABLO UNIVERSIDAD DE LA LAGUNA		04/07/2017 18:28:07

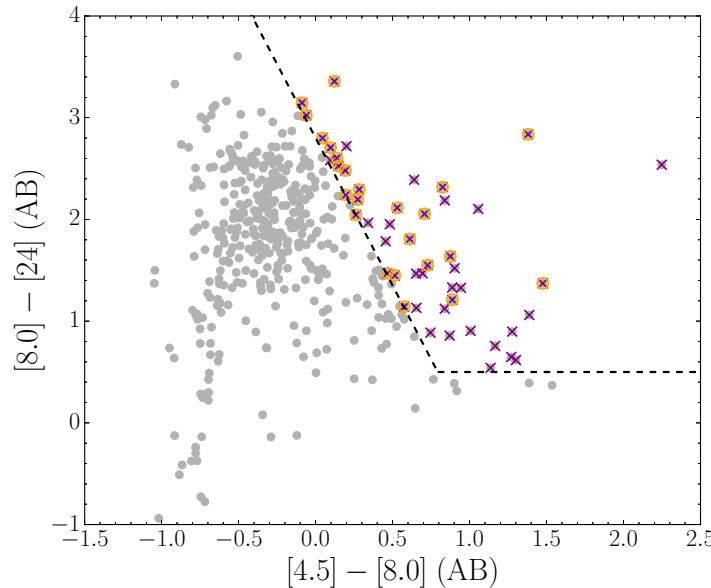


Figure 6.9: IRAC+MIPS (IM) infrared criteria by Messias et al. (2012) to select AGN. Grey dots are all the OTELO sources with information in the four IRAC bands as well as in the K_s and [24] μm bands. Black dashed lines are the limits of the IM criteria (see equations 6.7). Purple crosses represent the objects fulfilling the IM criteria. Orange circled sources represent the sources satisfying, in addition, that $K_s - [4.5] > 0$, i.e., the KIM (K_s +IRAC+MIPS) criteria. These are the objects selected as AGN by the KIM criteria (24 sources).

the latter (24 sources) as AGN. From those, 10 had already been selected by Donley et al. (2012) criteria and 14 were new. In total, 29 AGN were selected by infrared methods.

Final sample of AGN

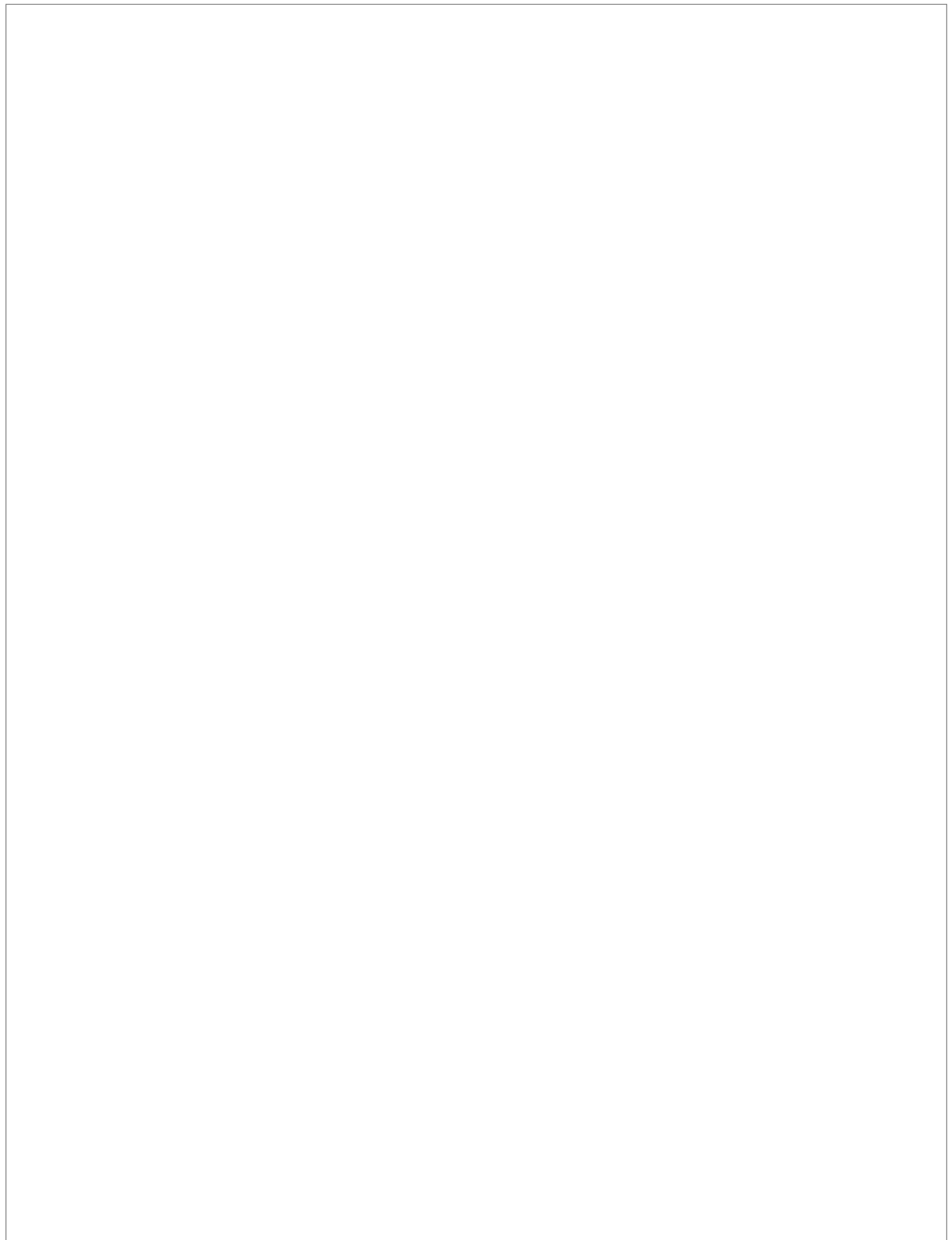
The following table summarises the different criteria used for the selection of AGN, and the number of objects selected in each case. In total, 72 objects were classified as AGN.

Table 6.1: Summary of AGN selection. Column 1: criterion used for the identification of AGN. Column 2: number of AGN selected using that criterion.

Criterion	Total detections
X-rays	31
Mid-infrared	18
X-rays & MIR	11
NLAGN ($z = 0.40$)	6
BLAGN ($z = 0.40$)	6
TOTAL	72

Este documento incorpora firma electrónica, y es copia auténtica de un documento electrónico archivado por la ULL según la Ley 39/2015.
Su autenticidad puede ser contrastada en la siguiente dirección <https://sede.ull.es/validacion/>

Identificador del documento: 969870	Código de verificación: 8KFVZkZp
Firmado por: MARINA RAMÓN PÉREZ UNIVERSIDAD DE LA LAGUNA	Fecha: 28/06/2017 21:15:24
ANGEL MANUEL BONGIOVANNI PEREZ UNIVERSIDAD DE LA LAGUNA	29/06/2017 09:30:15
JORGE CEPA NOGUE UNIVERSIDAD DE LA LAGUNA	29/06/2017 09:33:05
ANA MARIA PEREZ GARCIA UNIVERSIDAD DE LA LAGUNA	29/06/2017 11:12:35
ERNESTO PEREDA DE PABLO UNIVERSIDAD DE LA LAGUNA	04/07/2017 18:28:07



Este documento incorpora firma electrónica, y es copia auténtica de un documento electrónico archivado por la ULL según la Ley 39/2015. <i>Su autenticidad puede ser contrastada en la siguiente dirección https://sede.ull.es/validacion/</i>		
Identificador del documento:	969870	Código de verificación: 8KFVZkZp
Firmado por:	MARINA RAMÓN PÉREZ UNIVERSIDAD DE LA LAGUNA	Fecha: 28/06/2017 21:15:24
	ANGEL MANUEL BONGIOVANNI PEREZ UNIVERSIDAD DE LA LAGUNA	29/06/2017 09:30:15
	JORGE CEPA NOGUE UNIVERSIDAD DE LA LAGUNA	29/06/2017 09:33:05
	ANA MARIA PEREZ GARCIA UNIVERSIDAD DE LA LAGUNA	29/06/2017 11:12:35
	ERNESTO PEREDA DE PABLO UNIVERSIDAD DE LA LAGUNA	04/07/2017 18:28:07

7

ANALYSIS OF AGN

In this Chapter, the analysis of the galaxies found in OTELO survey which show AGN signatures is described. First, a demographic study over the AGN population is done on the basis of the different methods of selection. Then, a morphological classification is performed with the use of the HST images, and the fraction of luminous and ultra-luminous infrared galaxies is estimated. Finally, the environments of AGN at $z \sim 0.40$ are studied and a luminosity function is derived for objects at that redshift.

Once the AGN population in OTELO survey is isolated from the rest of objects (see previous Chapter), a first analysis is performed in order to know more about its general characteristics, such as its demography and morphology. Also, the fraction of LIRGs and ULIRGs is studied. Finally, an inceptive analysis is performed for the subpopulation of AGN at $z \sim 0.40$, which includes the study of the sources environments and the construction of a luminosity function at this redshift. However, it should be noted from the very beginning that we are dealing in that case with small number statistics, therefore any generalization should be made with caution.

7.1 Demography

The AGN population found in OTELO with the methods described in this work comprises 72 objects and represents a very small fraction of the total number of objects in the catalogue (less than 1%). Their distribution in redshift, as obtained with LePhare (see Chapter 5), can be seen in Fig. 7.1, together with that of the total and selected emitters (ELC) populations. It can be seen that there are more ELCs and AGNs at the redshifts corresponding to the more intense optical emission lines, which is a characteristic bias of emission line surveys. In particular, the AGN population exhibits a peak at $z = 0.40$, as this is the redshift at which the H α line appears in OTELO and we have focused on the search of those AGN. Thus, this is not indicative of a redshift preference but rather a selection effect. As a matter of fact, other emission lines, such as [NeV], could also be an indicator of activity. The search of AGN by focusing in other emission lines will be performed in the future. It should also be noted that the proportion of AGN over the total sample of objects is higher at higher redshifts. This is expected since AGN are very luminous objects and thus can be detected at higher redshifts than passive galaxies.

Este documento incorpora firma electrónica, y es copia auténtica de un documento electrónico archivado por la ULL según la Ley 39/2015.
Su autenticidad puede ser contrastada en la siguiente dirección <https://sede.ull.es/validacion/>

Identificador del documento:	969870	Código de verificación:	8KFVZkZp
Firmado por:	MARINA RAMÓN PÉREZ UNIVERSIDAD DE LA LAGUNA	Fecha:	28/06/2017 21:15:24
	ANGEL MANUEL BONGIOVANNI PEREZ UNIVERSIDAD DE LA LAGUNA		29/06/2017 09:30:15
	JORGE CEPA NOGUE UNIVERSIDAD DE LA LAGUNA		29/06/2017 09:33:05
	ANA MARIA PEREZ GARCIA UNIVERSIDAD DE LA LAGUNA		29/06/2017 11:12:35
	ERNESTO PEREDA DE PABLO UNIVERSIDAD DE LA LAGUNA		04/07/2017 18:28:07

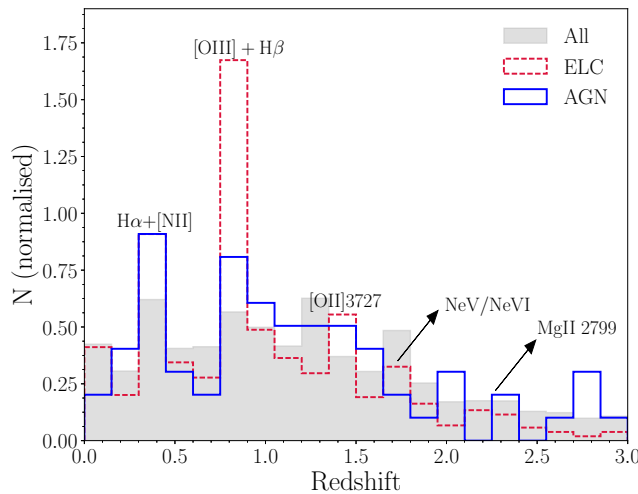


Figure 7.1: Distribution of redshifts (obtained with LePhare as described in Chapter 5) for the whole sample of OTELO (gray), the 1030 emitting-line candidates (ELC, shown in red) selected in Chapter 5 and the AGN sample selected in Chapter 6 (shown in blue). Some of the most intense emission lines in this spectral interval are displayed.

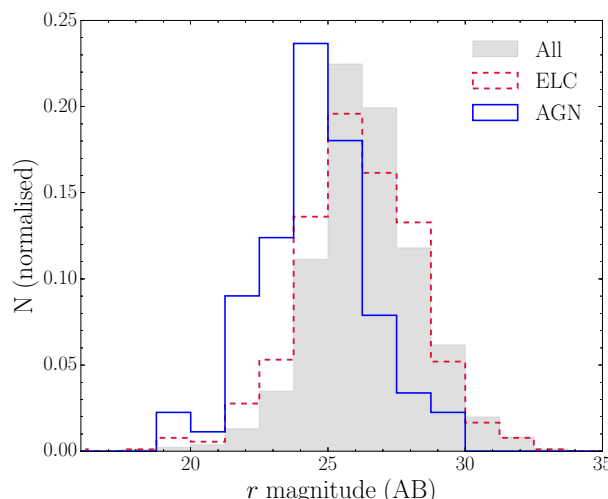


Figure 7.2: Magnitude distribution in the r band of all the objects in OTELO's catalogue (gray), the selected emitters (red dashed line) and the population of AGN (blue solid line). The AGN distribution peaks at 24.5 mag, one magnitude and a half brighter than the other two distributions.

Este documento incorpora firma electrónica, y es copia auténtica de un documento electrónico archivado por la ULL según la Ley 39/2015.
Su autenticidad puede ser contrastada en la siguiente dirección <https://sede.ull.es/validacion/>

Identificador del documento: 969870

Código de verificación: 8KFVZkZp

Fecha: 28/06/2017 21:15:24

Firmado por: MARINA RAMÓN PÉREZ
UNIVERSIDAD DE LA LAGUNA

29/06/2017 09:30:15

ANGEL MANUEL BONGIOVANNI PEREZ
UNIVERSIDAD DE LA LAGUNA

29/06/2017 09:33:05

JORGE CEPA NOGUE
UNIVERSIDAD DE LA LAGUNA

29/06/2017 11:12:35

ANA MARIA PEREZ GARCIA
UNIVERSIDAD DE LA LAGUNA

04/07/2017 18:28:07

ERNESTO PEREDA DE PABLO
UNIVERSIDAD DE LA LAGUNA

Fig. 7.2 represents the distribution of magnitudes in the r band, comparing the whole sample of OTELO with the selected emitters and the AGN. As can be seen, the total and the ELC population show very similar distributions. Their median magnitudes are 26.4 and 26.0 ± 2.2 , respectively. In the case of the AGN population, the distribution peaks at brighter magnitudes, the median being 24.5 ± 2.0 .

Our sample of AGN has been selected with various methods targeting different spectral ranges, as seen in Chapter 6. Some of the AGN have been selected with one method only, while others have been classified twice as active galactic nuclei, thus increasing their reliability. A summary of this is shown in Fig. 7.1. We now discuss some of the characteristics of each group.

Table 7.1: Classification of AGN according to the way they have been selected. The first column indicates the number of objects in a group. The following columns specify the selection methods: X-rays, MIR, NLAGN at $z = 0.40$ or BLAGN at $z = 0.40$ (see Chapter 6 for more details). The green checkmark means that an object at any redshift has been selected as AGN by the corresponding method, while the red cross indicates that the object has not been selected by that method. Each row shows a subgroup of AGN detected by one or more methods. The last row, in bold, indicates the total number of AGN in each group.

Number of objects	X-rays	MIR	NLAGN ($z = 0.40$)	BLAGN ($z = 0.40$)
31	✓	✗	✗	✗
11	✓	✓	✗	✗
18	✗	✓	✗	✗
6	✗	✗	✓	✗
6	✗	✗	✗	✓
72	42	29	6	6

X-ray-detected AGN

X-ray surveys are an efficient method to select AGN, as can be deduced from Table 7.1. 43% of our AGN (31) have been selected exclusively using the X/O ratio described in section 6.2. In total, this method has selected 58% of the whole sample of AGN (42). Moreover, of the 52 sources with X/O information, 81% turned out to be AGN, thus signaling that active galaxies could be responsible for the majority of the X-ray emission.

aa

X-ray-selected AGN can be divided in two groups, according to their level of obscuration, caused by large columns of gas along the line of sight ($N_H > 10^{22} \text{ cm}^{-2}$). In order to distinguish between unobscured and obscured X-rays AGN, we used an useful parameter from the catalogue of Pović et al. (2009): the hardness ratio. It is defined as follows:

$$\text{HR}(\Delta E_1 / \Delta E_2) = \frac{\text{CR}(\Delta E_1) - \text{CR}(\Delta E_2)}{\text{CR}(\Delta E_1) + \text{CR}(\Delta E_2)} \quad (7.1)$$

where ΔE_1 and ΔE_2 are two different energy bands, in our case $\Delta E_1 = 2 - 4.5 \text{ keV}$ (hard2 band) and $\Delta E_2 = 0.5 - 2 \text{ keV}$ (soft band), and $\text{CR}(\Delta E_n)$ is the count rate in the corresponding band. Caccianiga et al. (2004) proposed that the limit $\text{HR} = -0.30$ separates unobscured type 1 (with both narrow and broad emission lines in their spectra) from obscured type 2 (showing only narrow lines) AGN. Della Ceca et al. (2004) claimed that 90% of their type 1 AGN fell inside a narrow limit: $-0.75 < \text{HR} < -0.35$, while type 2 sources occupied

Este documento incorpora firma electrónica, y es copia auténtica de un documento electrónico archivado por la ULL según la Ley 39/2015. Su autenticidad puede ser contrastada en la siguiente dirección https://sede.ull.es/validacion/		
Identificador del documento: 969870	Código de verificación: 8KFVZkZp	
Firmado por: MARINA RAMÓN PÉREZ UNIVERSIDAD DE LA LAGUNA		Fecha: 28/06/2017 21:15:24
ANGEL MANUEL BONGIOVANNI PEREZ UNIVERSIDAD DE LA LAGUNA		29/06/2017 09:30:15
JORGE CEPA NOGUE UNIVERSIDAD DE LA LAGUNA		29/06/2017 09:33:05
ANA MARIA PEREZ GARCIA UNIVERSIDAD DE LA LAGUNA		29/06/2017 11:12:35
ERNESTO PEREDA DE PABLO UNIVERSIDAD DE LA LAGUNA		04/07/2017 18:28:07

a broader range with $\text{HR} > -0.35$. We have adopted those limits to separate our AGN into different types (see Fig. 7.3).

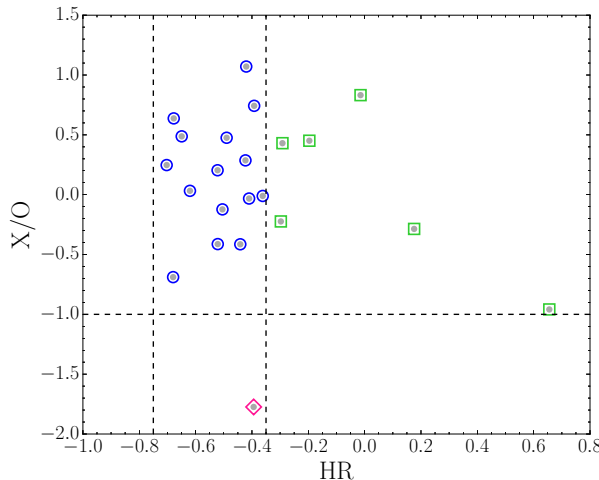


Figure 7.3: X-ray-to-optical flux ratio (X/O) as a function of the hardness ratio, for the sources of Pović et al. (2009) (grey dots) in OTELO's catalogue. The horizontal line corresponds to the limit $X/O = -1$, which separates AGN ($X/O > -1$) from star-forming galaxies ($X/O < -1$). The two vertical lines correspond to the limits set by Della Ceca et al. (2004) which encloses type 1 AGN ($-0.75 < \text{HR} < -0.35$), represented here as blue circles. Green squares are sources with $\text{HR} > -0.35$, i.e., type 2 AGN. The pink diamond represents probably a non-AGN source, which could be a coronal emitting star, a star-forming or early-type galaxy or a heavily absorbed (Compton thick) AGN.

In total, 21 out of our 42 X-ray-selected AGN included the hardness ratio information in their catalogue. With the above described method, 15 sources were selected in the first category and 6 in the second one. This represents a fraction of 71% unobscured and 29% obscured X-ray AGN over the total subsample of those objects possessing information of their hardness ratio. This is in agreement with what was found by Marchesi et al. (2016), where 69% and 31% of their whole sample of X-rays AGN (both type 1 and type 2) were unobscured and obscured, respectively.

MIR-selected AGN

The MIR selection methods described in section 6.3 effectively selected 29 AGN, 40% of the sample. Besides, 18 of those objects, i.e. a quarter of the AGN sample, have not been selected by any other method. This implies that MIR selection is an effective method to select AGN. However, the fraction of infrared AGN over the total infrared population is quite small. In fact, barely 1% of the objects having information in the 4 IRAC bands were selected as AGN using the revised IRAC criteria from Donley et al. (2012). Similarly, of the objects possessing information in the 4.5 and $8.0\mu\text{m}$ bands from IRAC and in the $24\mu\text{m}$ band from MIPS, only 3% were classified as AGN according to the KIM criteria of Messias et al. (2012). The striking difference in the number of AGN versus the total population of X-rays and MIR sources is also seen in the work of Cowley et al. (2016), who performed a similar multiwavelength AGN selection (compare their Fig. 3 and 4).

Identificador del documento:	969870	Código de verificación:	8KFVZkZp
Firmado por:	MARINA RAMÓN PÉREZ UNIVERSIDAD DE LA LAGUNA	Fecha:	28/06/2017 21:15:24
	ANGEL MANUEL BONGIOVANNI PEREZ UNIVERSIDAD DE LA LAGUNA		29/06/2017 09:30:15
	JORGE CEPA NOGUE UNIVERSIDAD DE LA LAGUNA		29/06/2017 09:33:05
	ANA MARIA PEREZ GARCIA UNIVERSIDAD DE LA LAGUNA		29/06/2017 11:12:35
	ERNESTO PEREDA DE PABLO UNIVERSIDAD DE LA LAGUNA		04/07/2017 18:28:07

As already said, the great advantage of MIR selection is that it allows us detecting even those AGN heavily obscured in X-rays. Consequently, by comparing the objects selected with MIR and X-rays methods, we can determine the fraction of obscured AGN whose X-ray emission has been heavily absorbed by the surrounding interstellar gas or dust and re-emitted at infrared wavelengths. In our case, 11 objects were selected both with MIR and X-rays methods while 18 were only selected with the former. This implies that 38% of our infrared AGN are unobscured or moderately obscured and the rest (62%) are heavily obscured. In their work, Mateos et al. (2012) selected AGN with infrared methods over the BUXS¹ field and found that 38.5% had an X-ray counterpart, meaning they were not heavily obscured. This is in agreement with our findings.

AGN at $z \sim 0.40$

As seen in Chapter 5, our final sample of H α emitters at $z \sim 0.40$ was composed of 46 objects. From those, 12 were optically selected as AGN (half of them being BLAGN and half NLAGN) with the techniques described in Chapter 6. From the rest of the AGN sample, only one object (X-ray-selected) fell at that redshift. In total, we have 13 AGN at $z \sim 0.40$.

In order to evaluate the proportion of line-emitters and AGN at that redshift, we first estimated the total number of objects found at $z \sim 0.40$ in OTELO. Considering an error of ~ 0.1 in the redshifts calculated with LePhare, we focused our search on the spectral window $0.37 < z < 0.42$, which covers the H α and [NII] lines in OTELO ± 0.1 in redshift. To these objects, we added the H α emitters selected in Chapter 5 which did not have a redshift in that interval but were classified as $z \sim 0.40$ emitters by alternative methods. We avoided stars by discarding bright objects (with an AB magnitude in the deep image < 24) having an stellarity index > 0.95 from SExtractor. In total, the population of sources at $z \sim 0.40$ in OTELO was estimated in ~ 186 objects. This would imply that $\sim 25\%$ of the objects at $z \sim 0.40$ are line-emitters, while $\sim 7\%$ are AGN. However, due to the small numbers that are being managed here, this statistic may not be significant. Furthermore, the fraction of optically-selected AGN (NLAGN or BLAGN) over the sample of H α emitters is 26% (see Table 7.2).

Table 7.2: OTELO sources at $z \sim 0.40$ and fraction of emitters and AGN. First column: total number of OTELO sources at $z \sim 0.40$ (see text for details). Second column: total number of H α selected emitters (see Chapter 5). Third and fourth columns: number of optically-selected and X-rays-selected AGN at that redshift (see Chapter 5). Fifth column: total number of AGN at that redshift. The second row shows the proportion of emitters and AGN over the total sample of objects at that redshift. The third row indicates the proportion of optically-selected AGN (NLAGN or BLAGN) over the sample of emitters. Due to the small numbers that are being managed here, and the uncertainty in the estimation of the total number of sources at $z \sim 0.40$, these numbers, specially those in the second row, should be taken with caution.

Objects at $z \sim 0.4$	H α Emitters	AGN		
		Optical	X-Rays	Total
~ 186	46	12	1	13
100%	$\sim 25\%$			$\sim 7\%$
	100%	26%		

While the total number of sources at $z \sim 0.40$ may be subject to errors due to the uncertainty in our photo-z calculations, specially for the faintest sources, the sample of H α emitters, on the other hand, has been carefully inspected by different collaborators as described in Chapter 5, and thus we fully rely on them. In their recent

¹Bright Ultra-hard XMM-Newton Survey.

Este documento incorpora firma electrónica, y es copia auténtica de un documento electrónico archivado por la ULL según la Ley 39/2015. Su autenticidad puede ser contrastada en la siguiente dirección https://sede.ull.es/validacion/		
Identificador del documento:	969870	Código de verificación: 8KFVZkZp
Firmado por:	MARINA RAMÓN PÉREZ UNIVERSIDAD DE LA LAGUNA	Fecha: 28/06/2017 21:15:24
	ANGEL MANUEL BONGIOVANNI PÉREZ UNIVERSIDAD DE LA LAGUNA	29/06/2017 09:30:15
	JORGE CEPA NOGUE UNIVERSIDAD DE LA LAGUNA	29/06/2017 09:33:05
	ANA MARIA PÉREZ GARCIA UNIVERSIDAD DE LA LAGUNA	29/06/2017 11:12:35
	ERNESTO PEREDA DE PABLO UNIVERSIDAD DE LA LAGUNA	04/07/2017 18:28:07

work from the HSC-SSP², Hayashi et al. (2017) found 14513 H α emitters in a total comoving volume of $9,77 \times 10^5$ Mpc 3 , using the NB921 filter to select the objects. This volume is 508 times bigger than the one covered by OTELO's field in the redshift range $0.37 < z < 0.42$, which is $1924,31$ Mpc 3 . According to these results, we would expect to find ~ 29 H α emitters in our field. This means we have found a non-negligible one third more emitters in the OTELO survey. This difference may be attributed to the limiting line flux reached by the Subaru team (1.5×10^{-17} erg/s/cm 2), which is higher than ours ($\sim 1.6 \times 10^{-18}$ erg/s/cm 2 , see Fig. 7.4), and also to the fact that their detection method, based only in a colour-colour diagram as the one in Fig. 5.18, is less efficient. As a matter of fact, with this method they are only able to select objects with an observed EW $> 25\text{\AA}$ for the NB921 filter, while our restrictions in EW go much lower (see section 5.2.1).

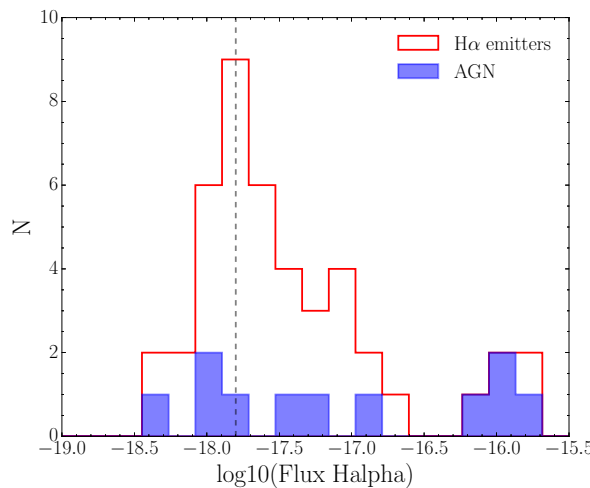


Figure 7.4: Histogram of H α fluxes of the sources selected as H α emitters (red line) and the optically-selected AGN at $z \sim 0.40$ (blue). The gray dashed line marks the peak of the distribution, corresponding to a flux of $\sim 1.6 \times 10^{-18}$ erg/s/cm 2 .

Sobral et al. (2013) also conducted a survey to find H α emitters at $z \sim 0.40$ using the NB921 filter and the same colour-colour diagram technique with an identical EW cut as the Subaru team. They found 1742 emitters over a cosmic volume of 8.8×10^4 Mpc 3 , 46 times bigger than our own. Translated to the OTELO volume, this would imply 38 emitters in our field, a value closer to what we find but still smaller. It is clear from these two comparisons the potential of OTELO's pseudo-spectra to select emitters.

As for the AGN fraction, Sobral et al. (2013) and other authors estimated an AGN contribution to the H α population of $\sim 10\text{--}15\%$, up to $z \sim 1$. However, in a more recent work, the same author found that the AGN fraction strongly correlates with the H α luminosity (Sobral et al. 2016). While for low luminosities the previous estimation is acceptable, for higher luminosities the AGN fraction increases strongly. They estimated it in 30% and found that the most luminous H α emitters at any cosmic time are BLAGN. In our case, we find a higher mean proportion of optically-selected AGN (26% of the overall H α population, at any luminosity) although given our small numbers this is within the uncertainties (see Table 7.2). On the other hand, our fraction of

²Hyper Suprime-Cam (HSC) Subaru Strategic Program (SSP). See <http://hsc.mtk.nao.ac.jp/ssp/>.

Este documento incorpora firma electrónica, y es copia auténtica de un documento electrónico archivado por la ULL según la Ley 39/2015. Su autenticidad puede ser contrastada en la siguiente dirección https://sede.ull.es/validacion/		
Identificador del documento: 969870	Código de verificación: 8KFVZkZp	
Firmado por: MARINA RAMÓN PÉREZ UNIVERSIDAD DE LA LAGUNA		Fecha: 28/06/2017 21:15:24
ANGEL MANUEL BONGIOVANNI PEREZ UNIVERSIDAD DE LA LAGUNA		29/06/2017 09:30:15
JORGE CEPA NOGUE UNIVERSIDAD DE LA LAGUNA		29/06/2017 09:33:05
ANA MARIA PEREZ GARCIA UNIVERSIDAD DE LA LAGUNA		29/06/2017 11:12:35
ERNESTO PEREDA DE PABLO UNIVERSIDAD DE LA LAGUNA		04/07/2017 18:28:07

AGN is almost 100% at the highest luminosities, as shown in Fig. 7.4, in agreement with Sobral et al. (2016). Moreover, our brightest AGN are the broad-line ones, as also found in the mentioned work.

7.2 Morphology

We studied the morphology of our AGN using the software GALAPAGOS (Barden et al. 2012), which combines the detection of objects with SExtractor and their light profile modelling with GALFIT (Peng et al. 2002). GALAPAGOS was run over the high resolution images from the Hubble Space Telescope (F606W and F814W filters) corresponding to OTELO’s field of view. The HST images cover the whole field of OTELO except for a ~ 3.1 arcmin 2 region in the lower left corner. The objects detected in this way were matched to the sources in OTELO’s catalogue. GALFIT then obtained a light model with a Sérsic profile (Sérsic 1963) for each of the detected components, starting by the brightest ones:

$$I(r) = I_0 \exp\left(-\frac{r}{\alpha}\right)^{1/n} \quad (7.2)$$

This expression describes the intensity I of a galaxy as a function of its radius r , I_0 being the central intensity, α the scale length (the radius at which the intensity drops by e^{-1}) and n the so called Sérsic index. This model was then subtracted to the original image in order to obtain a residual image, showing possible hidden subcomponents of the object. Several examples of this procedure (original HST images used for the detection, Sérsic profile modelled by GALFIT and residual images) are shown in Appendix A.

Of the total sample of 72 AGN, a GALFIT model with one or more components was obtained for 56 objects. For the rest of them, either the source was so dim that it could not be fitted, or no HST image was available. We performed a visual classification of those objects by four collaborators, based on the following parameters: 1) the appearance of the object in the HST images, 2) the GALFIT model and, in particular, the value of the Sérsic index of the main component, n , 3) the existence (or not) of a residual after subtracting the model to the original image (revealing possible spiral arms, bars and hidden structures) and 4) the relative colour of the source in a colour-colour diagram (such as $u - K_s$ vs. $z - K_s$, for instance). Based on that, each object was classed in one of the following categories: 1) point-like sources, 2) early-type sources (spheroidal objects, including ellipticals, E, and lenticulars, S0), 3) late-type sources (objects with disk, including spirals, S, and irregulars, Irr) and 4) unclassifiable objects. A summary of this classification is shown in Table 7.3.

Table 7.3: Morphological classification of OTELO’s AGN. The different types of AGN, according to their selection method (X-Rays, MIR, or BLAGN/NLAGN at $z \sim 0.40$) are divided in 4 morphological categories: point-like sources, early-type (including ellipticals and lenticulars), late-type (including spirals and irregulars), and unclassifiable galaxies.

	X-Rays	X-Rays + MIR (unobscured)	MIR (obscured)	BLAGN at $z \sim 0.40$	NLAGN at $z \sim 0.40$	Total
Point-like	3	2	2	0	0	7
Early-type	5	2	0	0	1	8
Late-type	14	6	11	5	0	36
Unclassifiable	3	0	1	0	1	5
Total	25	10	14	5	2	56

Este documento incorpora firma electrónica, y es copia auténtica de un documento electrónico archivado por la ULL según la Ley 39/2015.
Su autenticidad puede ser contrastada en la siguiente dirección <https://sede.ull.es/validacion/>

Identificador del documento: 969870	Código de verificación: 8KFVZkZp
Firmado por: MARINA RAMÓN PÉREZ UNIVERSIDAD DE LA LAGUNA	Fecha: 28/06/2017 21:15:24
ANGEL MANUEL BONGIOVANNI PEREZ UNIVERSIDAD DE LA LAGUNA	29/06/2017 09:30:15
JORGE CEPA NOGUE UNIVERSIDAD DE LA LAGUNA	29/06/2017 09:33:05
ANA MARIA PEREZ GARCIA UNIVERSIDAD DE LA LAGUNA	29/06/2017 11:12:35
ERNESTO PEREDA DE PABLO UNIVERSIDAD DE LA LAGUNA	04/07/2017 18:28:07

The majority of our AGN were classified as late-type objects (64%). Of those, 12 were clearly spirals (21%) such as the ones shown in Figures A.1 and A.2, and 9 were irregulars (16%) (see, for instance, Fig. A.13). On the other hand, 14% of our AGN were classified as early-type objects, including two possible lenticulars as the one shown in Fig. A.9. Finally, 12.5% of the sample were point-like sources and thus possible QSOs (see, as an example, the objects in Fig. A.8 and A.11) and 9% could not be classified (as the one in Fig. A.4). In addition to that, 9 of the AGN were flagged as multiple objects (16%), meaning that what was seen as a single object in OTELO was actually a system of multiple components as revealed by the HST images (see Fig. A.3) and 9 (16%) were flagged as having a possible interactions or mergers (see Fig. A.6 or A.12).

If we study the morphological classification of our AGN according to the selection methods, we can see that 4/5 of the BLAGN at $z \sim 0.40$ are in spiral galaxies, while the only NLAGN that was classified at that same redshift is an early-type instead. On the other hand, X-ray and MIR selected AGN seem to share similar morphologies, although the fraction of late-type galaxies among the X-ray selected AGN (56%) is smaller than among the MIR ones (79%). This is in agreement with Griffith & Stern (2010), who found that their MIR selected AGN had a slightly higher incidence of being hosted by disk galaxies than the X-ray selected ones, although both had in general similar morphologies. They explained this according to the scenario proposed by Gabor et al. (2009), where AGN represent an intermediate stage between disk-dominated and bulge-dominated galaxies. Hickox et al. (2009) also found results in agreement with this evolutionary scenario, where galaxies evolve from blue, disk-dominated types with radiatively efficient AGN (optical- and IR-bright) to red, bulge-dominated ones with less efficient AGN (optically faint, radio-bright) following the growth of the stellar bulge and a quasar phase. In this context, AGN tend to be selected in MIR when the accretion to the SMBH is more effective and the reprocessing of UV photons to MIR by the dust torus is significant, while they are better selected in X-rays when the accretion is less efficient.

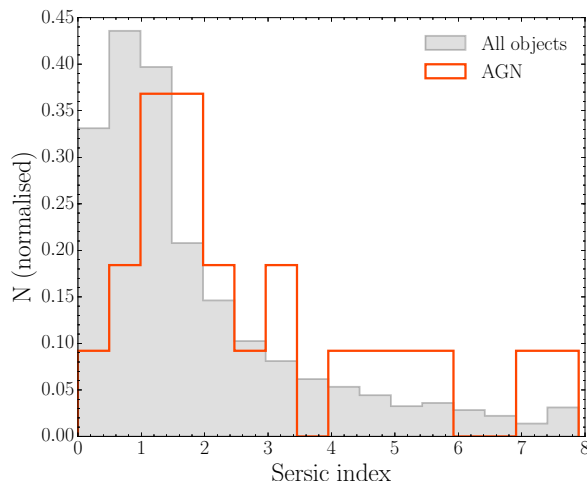


Figure 7.5: Sersic indices from the GALFIT models obtained for objects having unique components. The grey distribution represents the whole sample of OTELO's sources that have been modelled as a single component (3286 objects). The orange distribution represents the AGN subpopulation.

We also analysed the distribution of Sérsic indices obtained with the GALFIT models. According to Eq. 7.2, higher indices imply more concentrated objects with a steeper decrement in brightness. For that purpose, we used only the objects modelled by GALFIT as a single component and discarded the multiple ones, which would require a deeper and detailed analysis. In Fig. 7.5 the distribution of Sersic indices is shown, both for the whole sample of OTELO's objects and for the AGN subpopulation. For the total population of OTELO's objects, the distribution peaks at $n \sim 1$ and decreases steadily up to the maximum value of $n = 8$. The AGN distribution peaks at slightly higher indices and seems to have a higher proportion of concentrated objects. However, due to the small numbers being managed in the AGN sample, these variations may be attributed to statistical differences. As a matter of fact, Fan et al. (2014) performed a similar analysis over a sample of X-rays selected AGN at $z \sim 2$ and found AGN and non-AGN distributions very similar to ours (see their Fig. 2). Their numbers were also small (35 AGN) and they concluded that there was no statistical difference between the AGN and the control sample. In any case, the distribution of Sersic indices agrees with our previous findings about the predominance of late-type galaxies with a disk among the AGN.

7.3 Luminous and ultra-luminous infrared galaxies

Luminous and ultra-luminous infrared galaxies are among the brightest galaxies in the Universe. As their names suggest, they emit most of their radiation in the infrared, their luminosity in this range being superior to 10^{11} and $10^{12} L_\odot$, respectively. The power source responsible for this emission is believed to be a starburst and/or an AGN. In order to look for these objects in OTELO, we first derived the infrared luminosity (L_{IR}) of our sources. This luminosity is defined as the emission in the spectral range from 8 to $1000\mu\text{m}$. LePhare calculates it by integrating the emission in this range from the best FIR SED fitted to each galaxy (see section 5.2.2):

$$L_{\text{IR}} = \int_{8\mu\text{m}}^{1000\mu\text{m}} L_\lambda d\lambda \quad (7.3)$$

Other methods estimate L_{IR} using a single photometric point from MIPS or PACS. An example is the method by Wuyts et al. (2011), who obtained a set of conversion factors dependent on redshift in order to convert the $24\mu\text{m}$ flux from MIPS or the 70, 100 or $160\mu\text{m}$ ones from PACS to IR luminosity, using a single IR template built for the occasion³. We compared our infrared luminosity by LePhare with the one obtained with Wuyts et al. (2011)'s method for objects having MIPS photometry.

As can be seen in Fig. 7.6, both methods give concordant results within the errors, although for sources having more infrared photometric points than just the MIPS one, Wuyts et al. (2011)'s method seems to obtain systematically lower luminosities than LePhare's. An analysis performed by Lee et al. (2010) concluded that, at higher redshifts, the opposite happens and infrared luminosities calculated by extrapolating the $24\mu\text{m}$ flux without taking into account other FIR fluxes overestimate the real L_{IR} . In this work, we took advantage of our multiwavelength catalogue and the fact that our sources may have not only MIPS photometry but also fluxes in the 100 and $160\mu\text{m}$ PACS bands and in the 250, 350 and $500\mu\text{m}$ bands from SPIRE. Moreover, the fact that LePhare uses the best FIR template for each source instead of a single general template increases the reliability of the L_{IR} calculation.

The distributions of infrared luminosities obtained in this way are shown in Fig. 7.7. As can be seen, at higher luminosities the proportion of AGN contributing to the total L_{IR} is greater. We can also deduce from the figure that the proportion of LIRGs and ULIRGs among AGN is significant. However, in order to draw conclusions, we need to estimate the redshift up to which the sample of LIRGs and ULIRGs is complete. To

³See http://www.mpe.mpg.de/~swuyts/Site/Lir_template.html.

Este documento incorpora firma electrónica, y es copia auténtica de un documento electrónico archivado por la ULL según la Ley 39/2015. Su autenticidad puede ser contrastada en la siguiente dirección https://sede.ull.es/validacion/		
Identificador del documento:	Código de verificación:	
Firmado por: MARINA RAMÓN PÉREZ UNIVERSIDAD DE LA LAGUNA	8KFVZkZp	Fecha: 28/06/2017 21:15:24
ANGEL MANUEL BONGIOVANNI PEREZ UNIVERSIDAD DE LA LAGUNA		29/06/2017 09:30:15
JORGE CEPA NOGUE UNIVERSIDAD DE LA LAGUNA		29/06/2017 09:33:05
ANA MARIA PEREZ GARCIA UNIVERSIDAD DE LA LAGUNA		29/06/2017 11:12:35
ERNESTO PEREDA DE PABLO UNIVERSIDAD DE LA LAGUNA		04/07/2017 18:28:07

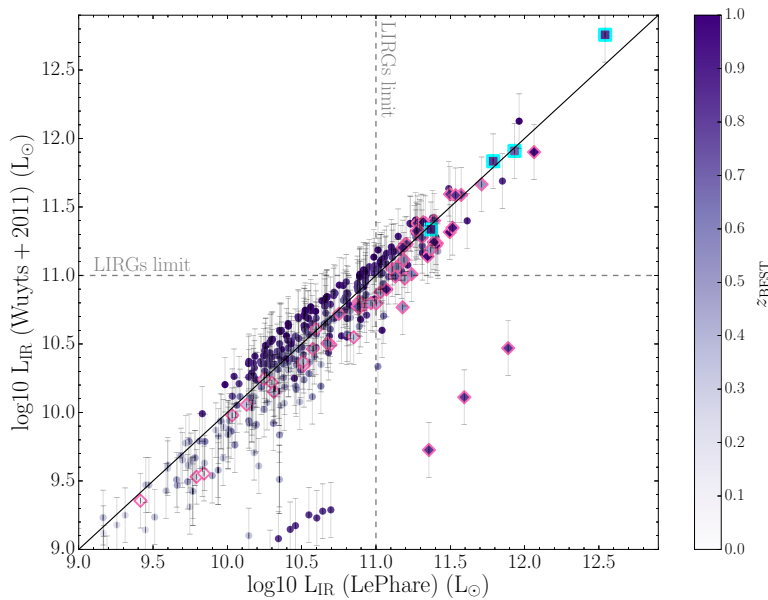


Figure 7.6: Comparison of methods to calculate the infrared luminosity for OTELO objects up to $z = 1$ having $24\mu\text{m}$ photometry. Infrared luminosity calculated with LePhare is shown in the x axis, and the one obtained with the conversion factors from Wuyts et al. (2011) in the y axis. Gray error bars indicate the scatter in the L_{IR} calculation of the latter, with respect to the L_{IR} obtained from PACS photometry using the same method. Pink diamonds indicate the sources with at least one extra PACS point (100 or $160\mu\text{m}$). Cyan squares are the sources with MIPS, PACS and SPIRE photometry (24 , 100 , 160 , 250 , 300 and $500\mu\text{m}$). The colour intensity of the points indicates their photometric redshift according to the scale at the right side of the figure.

do so, we used the minimum $24\mu\text{m}$ MIPS flux detected in OTELO (21.95 AB) and a FIR SED template from Chary & Elbaz (2001). The template was redshifted from $z = 0$ to 2.5 and re-escalated so that the minimum flux would correspond to the MIPS photometric point. Then, the infrared luminosity was obtained by integrating the SED flux from 8 to $1000\mu\text{m}$. The results are shown in Fig. 7.8. As expected (see, for instance, Fig. 4 from Elbaz et al. 2011), the minimum detectable L_{IR} increases with redshift. Given our sensitivity limits, we are able to detect all the LIRGs up to $z \sim 1.6$, while the ULIRGs sample is complete at all redshifts.

The distribution of all the LIRGs and ULIRGs found in OTELO, as a function of redshift, is shown in Fig. 7.9. It can be seen that the number of LIRGs is very superior to that of ULIRGs at low redshifts, and that it increases with z (as also found by Magnelli et al. 2013, see its Fig. 12) up to $z \sim 1.5$, from where it starts to decrease as a consequence of our detection limits and in agreement with the previous estimation. At high redshifts, on the other hand, the number of ULIRGs prevails. Our distributions of LIRGs and ULIRGs over redshift are in agreement with what was found by Lin et al. (2016) and Malek et al. (2017).

Table 7.4 details the number of (ultra) luminous infrared galaxies found over the total sample of OTELO objects with L_{IR} , as well as among the AGN and non-AGN galaxies. We found that the fraction of LIRGs and ULIRGs is higher among the AGN population than among the rest of the galaxies, and that this difference

Este documento incorpora firma electrónica, y es copia auténtica de un documento electrónico archivado por la ULL según la Ley 39/2015. Su autenticidad puede ser contrastada en la siguiente dirección https://sede.ull.es/validacion/		
Identificador del documento: 969870	Código de verificación: 8KFVZkZp	
Firmado por: MARINA RAMÓN PÉREZ UNIVERSIDAD DE LA LAGUNA		Fecha: 28/06/2017 21:15:24
ANGEL MANUEL BONGIOVANNI PEREZ UNIVERSIDAD DE LA LAGUNA		29/06/2017 09:30:15
JORGE CEPA NOGUE UNIVERSIDAD DE LA LAGUNA		29/06/2017 09:33:05
ANA MARIA PEREZ GARCIA UNIVERSIDAD DE LA LAGUNA		29/06/2017 11:12:35
ERNESTO PEREDA DE PABLO UNIVERSIDAD DE LA LAGUNA		04/07/2017 18:28:07

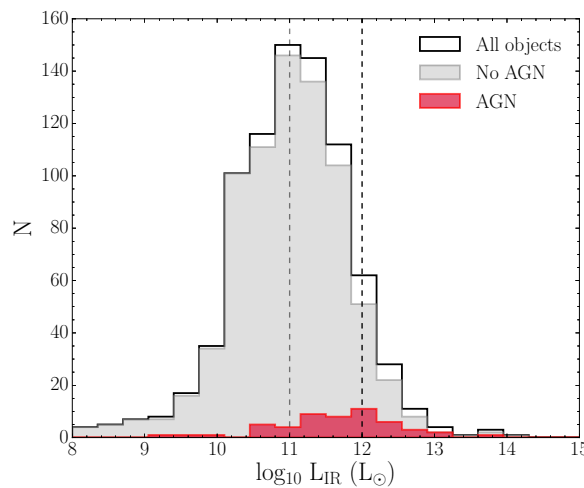


Figure 7.7: Distribution of infrared luminosities for the whole sample of OTELO sources having $24\mu\text{m}$ photometry (black solid line), the objects not detected as AGN (gray) and the selected AGN (red). The gray and black dashed lines indicate the LIRGs and ULIRGs limit, respectively: 10^{11} and $10^{12} L_{\odot}$.

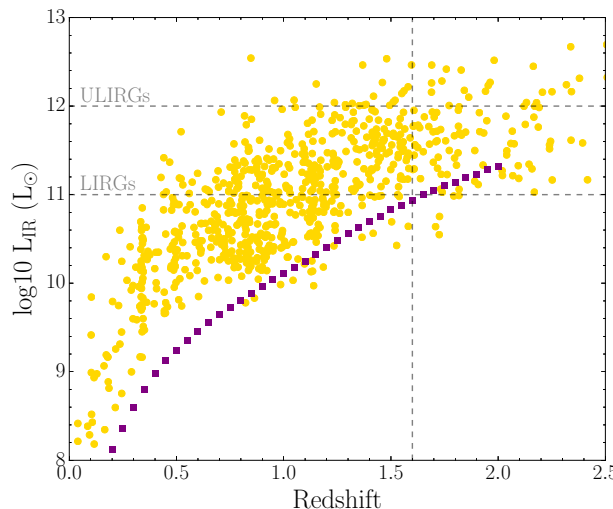


Figure 7.8: Infrared luminosity in OTELO, as a function of redshift. Yellow dots represent the infrared luminosity of OTELO sources having $24\mu\text{m}$ photometry. Purple squares represent the minimum detectable L_{IR} given the sensitivity limits in our catalogue (see text for details). Horizontal lines indicate the LIRGs and ULIRGs limits. The vertical line shows the redshift up to which the sample of LIRGs is complete in our survey ($z = 1.6$).

Este documento incorpora firma electrónica, y es copia auténtica de un documento electrónico archivado por la ULL según la Ley 39/2015. Su autenticidad puede ser contrastada en la siguiente dirección https://sede.ull.es/validacion/		
Identificador del documento:	969870	Código de verificación: 8KFVZkZp
Firmado por:	MARINA RAMÓN PÉREZ UNIVERSIDAD DE LA LAGUNA	Fecha: 28/06/2017 21:15:24
	ANGEL MANUEL BONGIOVANNI PEREZ UNIVERSIDAD DE LA LAGUNA	29/06/2017 09:30:15
	JORGE CEPA NOGUE UNIVERSIDAD DE LA LAGUNA	29/06/2017 09:33:05
	ANA MARIA PEREZ GARCIA UNIVERSIDAD DE LA LAGUNA	29/06/2017 11:12:35
	ERNESTO PEREDA DE PABLO UNIVERSIDAD DE LA LAGUNA	04/07/2017 18:28:07

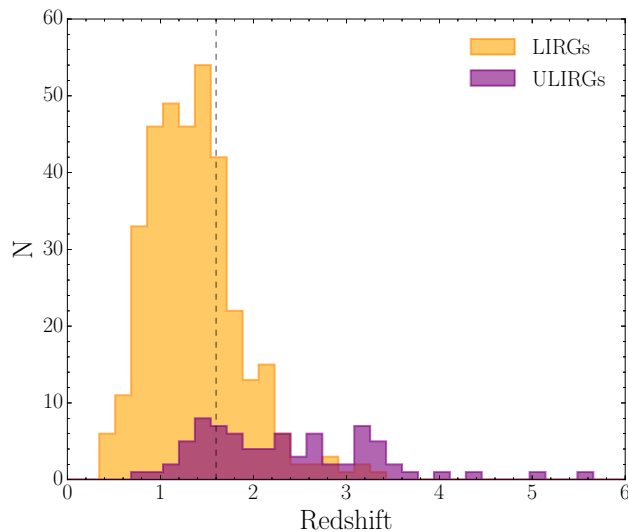


Figure 7.9: Distribution of redshifts for luminous and ultra-luminous infrared galaxies (orange and purple, respectively). The gray dashed line indicates $z = 1.6$, the redshift up to which the sample of LIRGs is complete.

is specially remarkable for the ULIRGs: 57% (40%) of AGN (non-AGN) are LIRGs, while 33% (8%) are ULIRGs.

We also found that 8% of LIRGs up to $z = 1.6$ are active galaxies and that this number increases to 22% for ULIRGs. This result is in agreement with Małek et al. (2017), who found that ULIRGs are characterised by a higher fraction of AGN than LIRGs. Among the 17 ULIRGs that are AGN, all but one (21%) were selected with MIR methods. This coincides with what was found by Veilleux et al. (1997), who affirmed that 25-30% of their ULIRGs showed signs of activity in the optical or near-infrared.

Table 7.4: Number of LIRGs and ULIRGs found among the AGN and non-AGN population, as well as the whole sample of OTELO sources having L_{IR} . The numbers in brackets represent the fraction of these kind of objects over the given population. (*): The LIRGs sample is studied only up to $z = 1.6$ for completeness purposes (see text for details), while the ULIRGs sample covers all redshifts.

	LIRGs*	ULIRGs	ULIRGs
	($z < 1.6$)	($z < 1.6$)	(all z)
AGN	21 (57%)	6 (16%)	17 (33%)
No AGN	243 (39%)	15 (2.4%)	60 (7.9%)
Total	264 (40%)	21 (3.2%)	77 (9.5%)

7.4 Analysis of AGN at $z \sim 0.40$

Once a general analysis of the AGN found in OTEL0 has been done, we focus on the population of objects at $z \sim 0.40$. We study the environments of AGN at this redshift in an attempt to determine if they tend to be in high or low density environments. After that, we obtain a luminosity function at $z \sim 0.40$ and examine the contribution of AGN to the total H α luminosity.

7.4.1 Environment and density

AGN environment

The role of environment in AGN triggering is one of the most important open questions in the field. Not only the local environment but also the large-scale one seems to be decisive in the evolution and properties of galaxies. In this work, we attempted to study the environments of AGN at $z \sim 0.40$. The spatial distribution of all the sources at this redshift is shown in Fig. 7.10, along with that of the H α emitters and the AGN.

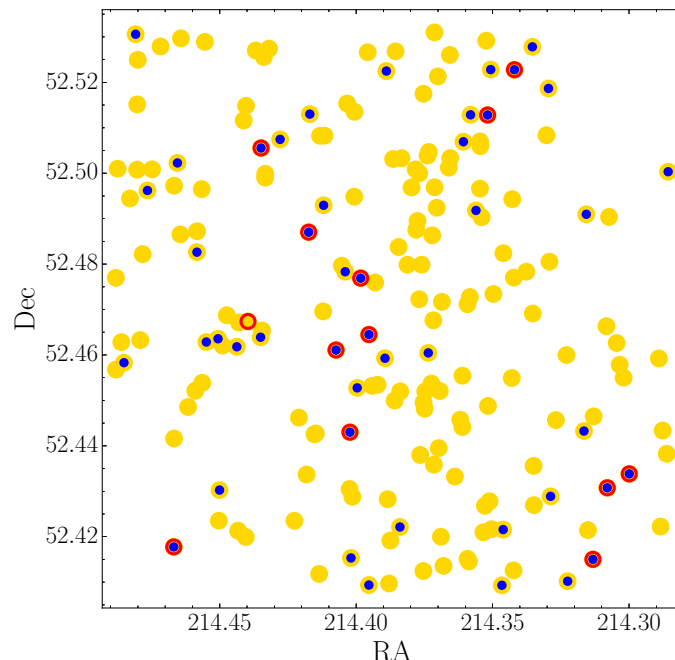


Figure 7.10: Distribution of sources at $z \sim 0.40$ in OTEL0. Yellow dots represent all the sources at that redshift. Blue dots are the H α emitters, while red circles are the selected AGN.

We studied the surface density by means of the projected fifth-nearest-neighbour distance (D_5) of each source. This method provides the most accurate estimate of local galaxy density when compared to other

Este documento incorpora firma electrónica, y es copia auténtica de un documento electrónico archivado por la ULL según la Ley 39/2015. Su autenticidad puede ser contrastada en la siguiente dirección https://sede.ull.es/validacion/		
Identificador del documento:	969870	Código de verificación: 8KFVZkZp
Firmado por:	MARINA RAMÓN PÉREZ UNIVERSIDAD DE LA LAGUNA	Fecha: 28/06/2017 21:15:24
	ANGEL MANUEL BONGIOVANNI PEREZ UNIVERSIDAD DE LA LAGUNA	29/06/2017 09:30:15
	JORGE CEPA NOGUE UNIVERSIDAD DE LA LAGUNA	29/06/2017 09:33:05
	ANA MARIA PEREZ GARCIA UNIVERSIDAD DE LA LAGUNA	29/06/2017 11:12:35
	ERNESTO PEREDA DE PABLO UNIVERSIDAD DE LA LAGUNA	04/07/2017 18:28:07

techniques such as the use of counts in a fixed aperture or the Voronoi volume, according to Cooper et al. (2005). We used the edge correction by Kovač et al. (2010) to avoid obtaining artificially lower densities in the regions close to the edges of the field. The surface density is calculated as:

$$\Sigma_5 = \frac{5}{\pi D_5^2} \quad (7.4)$$

We compared the distributions of the surface density parameter for the sample of AGN at $z \sim 0.40$ (13 objects) and for a control sample of 13 non-AGN randomly chosen at the same redshift. As can be seen in Fig. 7.11, galaxies tend to concentrate in low density environments. The AGN and non-AGN distributions are very similar, and seem to be in agreement with the density distribution of the overall population. We performed the analysis for different control samples and obtained analogous results every time.

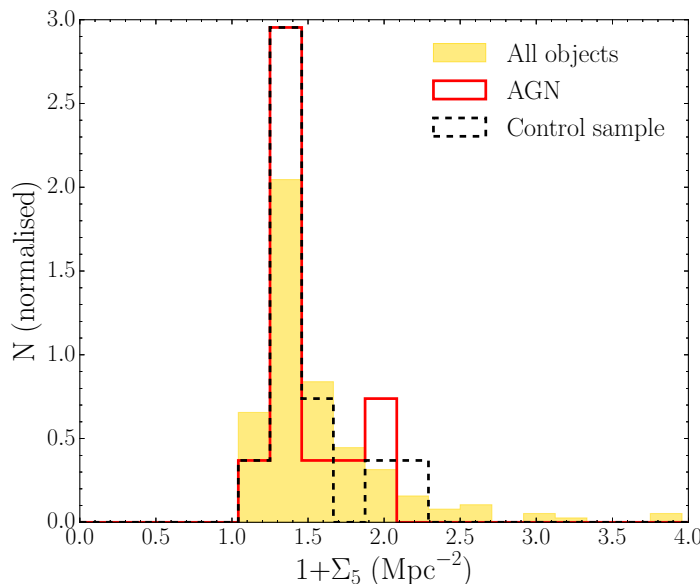


Figure 7.11: Distribution of the surface density parameter (Σ_5) for the whole sample of OTELO objects at $z \sim 0.40$ (yellow), the AGN (red) and a random control sample of non-AGN (black).

To further analyse the environmental differences between the AGN and the control sample, we looked at the distance parameter, D_5 , in each sample. The distance from a randomly chosen source to the fifth-nearest other object follows an homogenous Poisson process (Martínez & Saar 2002) whose probability distribution function in 2D is given by:

$$G(D_5) = 1 - \exp(-\rho \pi D_5^2) \quad , \quad (7.5)$$

where ρ is the intensity of the process, or the expected value of D_5 . We fitted the cumulative distributions of D_5 in each sample to this function, assuming statistical errors of Poissonian nature, and compared it to the distribution of the overall population, composed of all the objects at $z \sim 0.40$. The results are shown in Fig.

Este documento incorpora firma electrónica, y es copia auténtica de un documento electrónico archivado por la ULL según la Ley 39/2015. Su autenticidad puede ser contrastada en la siguiente dirección https://sede.ull.es/validacion/		
Identificador del documento:	969870	Código de verificación: 8KFVZkZp
Firmado por:	MARINA RAMÓN PÉREZ UNIVERSIDAD DE LA LAGUNA	Fecha: 28/06/2017 21:15:24
	ANGEL MANUEL BONGIOVANNI PEREZ UNIVERSIDAD DE LA LAGUNA	29/06/2017 09:30:15
	JORGE CEPA NOGUE UNIVERSIDAD DE LA LAGUNA	29/06/2017 09:33:05
	ANA MARIA PEREZ GARCIA UNIVERSIDAD DE LA LAGUNA	29/06/2017 11:12:35
	ERNESTO PEREDA DE PABLO UNIVERSIDAD DE LA LAGUNA	04/07/2017 18:28:07

7.12. It is clear from this figure that the AGN population and the control group do not statistically differ. This indicates that AGN in OTELO field at $z \sim 0.40$ are found in identical density environments as non-AGN.

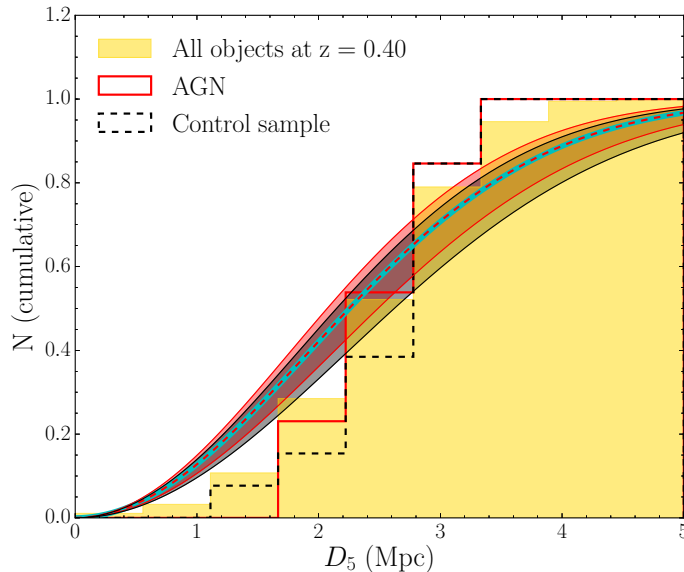


Figure 7.12: Cumulative and normalised distributions of D_5 for the total sample of OTELO's objects, the AGN and the control sample (non-AGN). The yellow distribution is the distribution of all the objects at $z \sim 0.40$ and the cyan solid line its Poissonian fit. The step histograms in red and black represent the distributions of D_5 for the AGN and non-AGN sample, respectively, while the corresponding dashed lines are their Poissonian fits. The filled bands show the propagation of statistical errors in the Poissonian fit.

Density distributions

We then performed a similar analysis for the complete sample of OTELO objects at $z \sim 0.40$ (186 objects), the 46 H α emitters and the remaining 140 passive galaxies without emission lines. The sample of H α emitters was in turn divided into the selected AGN and the rest, presumably star-forming galaxies (SFG). We studied these populations independently, unlike the previous analysis, i.e., by looking for neighbours of the same category as the considered source.

The distributions of Σ_5 for the different samples are shown in Fig. 7.13. Fig. 7.14 shows the cumulative distributions of D_5 for each population, as well as the corresponding fits considering Poisson processes (Eq. 7.5). It can be seen that AGN and passive galaxies are the groups deviating the most from the general trend of the overall population at $z \sim 0.40$.

Este documento incorpora firma electrónica, y es copia auténtica de un documento electrónico archivado por la ULL según la Ley 39/2015.
Su autenticidad puede ser contrastada en la siguiente dirección <https://sede.ull.es/validacion/>

Identificador del documento: 969870

Código de verificación: 8KFVZkZp

Firmado por: MARINA RAMÓN PÉREZ
UNIVERSIDAD DE LA LAGUNA

Fecha: 28/06/2017 21:15:24

ANGEL MANUEL BONGIOVANNI PEREZ
UNIVERSIDAD DE LA LAGUNA

29/06/2017 09:30:15

JORGE CEPA NOGUE
UNIVERSIDAD DE LA LAGUNA

29/06/2017 09:33:05

ANA MARIA PEREZ GARCIA
UNIVERSIDAD DE LA LAGUNA

29/06/2017 11:12:35

ERNESTO PEREDA DE PABLO
UNIVERSIDAD DE LA LAGUNA

04/07/2017 18:28:07

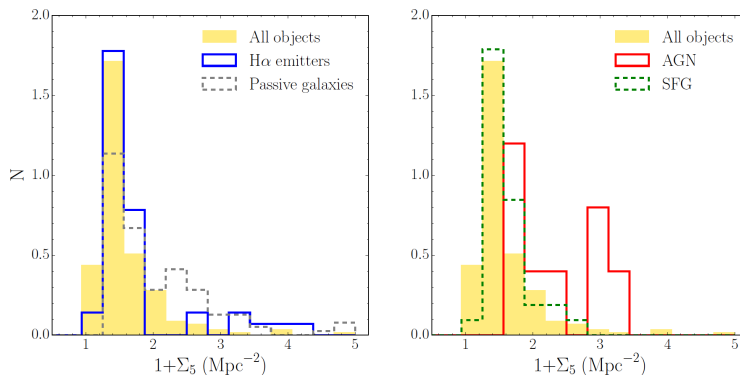


Figure 7.13: Distribution of the surface density parameter (Σ_5) for the whole sample of OTELO objects at $z \sim 0.40$ (yellow), the H α emitters (blue), the passive galaxies (gray), the selected AGN (red) and the star-forming galaxies (green).

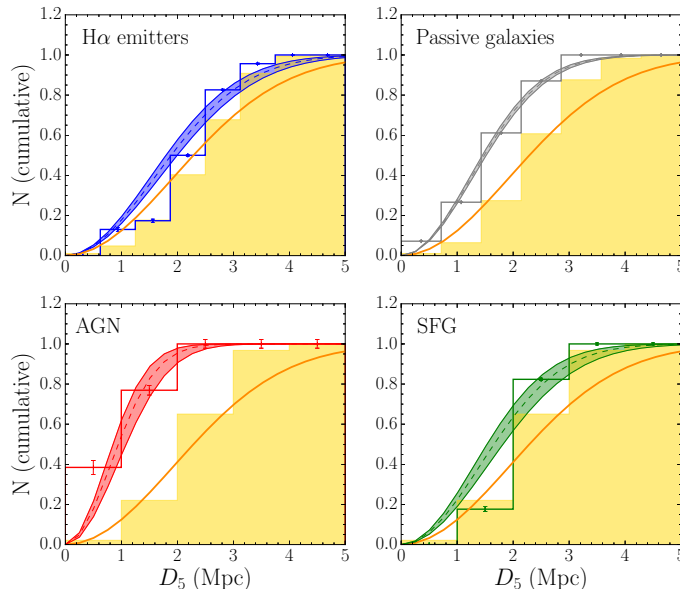


Figure 7.14: Cumulative and normalised distributions of D_5 for the sample of H α emitters, passive galaxies, AGN and star-forming galaxies (from top to bottom and from left to right). The yellow distribution is the distribution of all the objects at $z \sim 0.40$ and the orange solid line its Poissonian fit. The step histograms in different colours represent the distribution of D_5 for the rest of the samples, while the corresponding dashed lines are their Poissonian fits. The error bars correspond to statistical errors given the number of objects in each bin. The filled bands show the propagation of those statistical errors in the Poissonian fit.

Este documento incorpora firma electrónica, y es copia auténtica de un documento electrónico archivado por la ULL según la Ley 39/2015.
Su autenticidad puede ser contrastada en la siguiente dirección <https://sede.ull.es/validacion/>

Identificador del documento: 969870

Código de verificación: 8KFVZkZp

Firmado por: MARINA RAMÓN PÉREZ
UNIVERSIDAD DE LA LAGUNA

Fecha: 28/06/2017 21:15:24

ANGEL MANUEL BONGIOVANNI PEREZ
UNIVERSIDAD DE LA LAGUNA

29/06/2017 09:30:15

JORGE CEPA NOGUE
UNIVERSIDAD DE LA LAGUNA

29/06/2017 09:33:05

ANA MARIA PEREZ GARCIA
UNIVERSIDAD DE LA LAGUNA

29/06/2017 11:12:35

ERNESTO PEREDA DE PABLO
UNIVERSIDAD DE LA LAGUNA

04/07/2017 18:28:07

A way to better compare the behaviours of each group is to use the J function, first proposed by Lieshout & Baddeley (1996), which is particularly useful when applied to galaxy data (Kerscher et al. 1999):

$$J(D_5) = \frac{1 - G(D_5)}{1 - F(D_5)} \quad (7.6)$$

In our case, $G(D_5)$ are the Poissonian fits obtained for each sample (Eq. 7.5) and $F(D_5)$ is the corresponding fit to the overall population of galaxies at $z \sim 0.40$, that we use as comparison sample. Positive values of $J(D_5)$ indicate regular point distributions, while negative values show clustered patterns. The results that we obtained are shown in Fig. 7.15. At small scales, the deviations are minimal, but they grow with the distance. At large-scales, each subpopulation tends to be more clustered than the overall population. AGN and passive galaxies are the groups deviating the most, specially AGN which is the most clustered group. Although these results are interesting, they should be taken with caution due to our very small number of sources (specially in the AGN sample), that may introduce large errors and biases. A study with more statistical significance should be made in order to confirm these results.

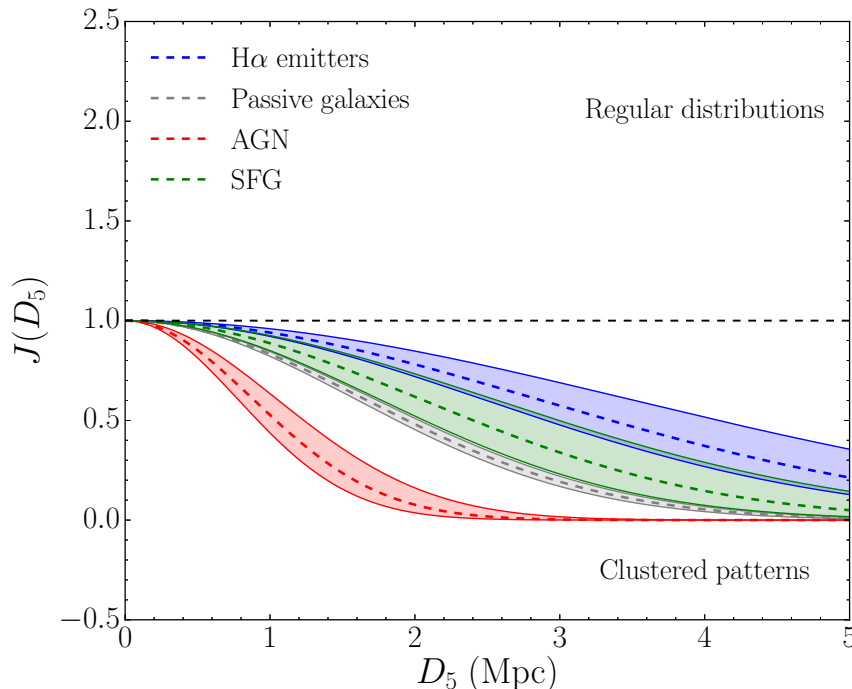


Figure 7.15: $J(D_5)$ function that compares the D_5 distributions of the different samples ($H\alpha$ emitters, passive galaxies, AGN and SFG) with the distribution of the overall population at $z \sim 0.40$. The filled bands correspond to the propagation of the statistical errors in the different Poissonian fits. $J(D_5) < 0$ indicates that the given distribution is more clustered than the comparison sample, while $J(D_5) > 0$ indicates the opposite (a more regular distribution).

7.4.2 Luminosity function at z~0.40

The luminosity function (LF), which gives the distribution of astrophysical objects per luminosity interval, is an empirical and essential tool to derive the distribution of galaxies in the Universe at different cosmological times and hence to understand their origin and evolution. In this work, we obtain the H α LF at $z \sim 0.40$ that we use to study the AGN contribution to the total luminosity at that redshift. The main advantage of OTELO, when compared to other surveys, is that emitters and AGN at $z \sim 0.40$ have been carefully inspected and selected, so the AGN contribution in each luminosity interval is exactly known and not only estimated, as in other works (see, for instance, Shioya et al. 2008 or Sobral et al. 2013).

One of the main difficulties when deriving the LF is to estimate (and correct) the incompleteness of the sample of objects. In our case, we took advantage of the simulations carried out in Chapter 5, which evaluated the detection probability of an H α emission line at $z \sim 0.40$ in OTELO. We calculated the mean detection probability as a function of the line flux, for the simulated objects having $p \geq 0.50$, which is the completeness cut that we adopted. The result is shown in Fig. 7.16. We then fitted the data to a sigmoid function such as:

$$d = \frac{aF_l}{\sqrt{c - F_l^2}} , \quad (7.7)$$

where $F_l = \log(f_l) - b$, f_l is the line flux. The values obtained from a least-squared fitting using the Levenberg-Marquardt algorithm implementation in IDL were $a = 0.916 \pm 0.005$, $b = 19.187 \pm 0.047$ and $c = 0.072 \pm 0.023$. This function was used as our LF completeness correction.

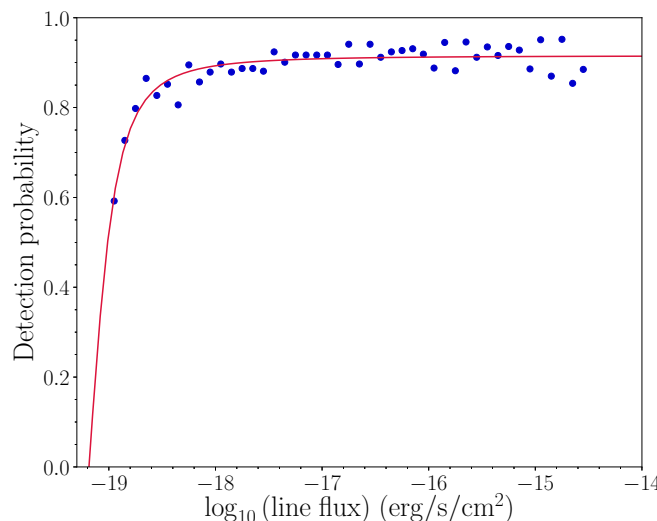


Figure 7.16: Mean detection probability as a function of H α line flux (blue dots), for simulated objects having $p \geq 0.50$ (see Chapter 5). The red line indicates the best least-squared fitting of a sigmoid function (Eq. 7.7).

The LF calculation starts by computing the number Φ of galaxies per unit volume and per unit of H α luminosity, in bins of $\log L(\text{H}\alpha) \pm 0.5 \times \Delta[\log L(\text{H}\alpha)]$. We have used the V_{\max} method (Schmidt 1968; see, for instance, Eq. 2 in Bongiovanni et al. 2005 or Eq. 8 in Hayashi et al. 2017), with the following adapted expression:

$$\Phi[\log L(\text{H}\alpha)] = \kappa \frac{4\pi}{\Omega} \sum_i \frac{1}{d_i} , \quad (7.8)$$

which takes into account the volume of Universe surveyed and the completeness bias in our survey: d_i is the detection probability defined in eq. 7.7 for the i -th galaxy, Ω is the surveyed solid angle ($\sim 4.7 \times 10^{-6}$ str) and κ is a normalisation factor proportional to V_{\max}^{-1} ($\kappa = V_{\max}^{-1} \times \Delta[\log L(\text{H}\alpha)]^{-1}$), the comoving volume limited by the H α line redshift in OTELO ($\sim 1.6 \times 10^3$ Mpc 3).

The Schechter function (Schechter 1976), ϕ , is usually used to describe the luminosity function such as:

$$\Phi[\log L(\text{H}\alpha)] d\log L = \phi(L) dL , \quad (7.9)$$

where:

$$\phi(L) dL \equiv \phi^* \left(\frac{L}{L^*} \right)^\alpha \exp \left(-\frac{L}{L^*} \right) d \left(\frac{L}{L^*} \right) \quad (7.10)$$

The parameters L^* , ϕ^* and α define the luminosity function. L^* is the characteristic luminosity, which separates the high and the low luminosity regimes in the LF, with exponential and power-law forms, respectively. ϕ^* is the number density at L^* and α represents the slope of the faint end of the LF. Accordingly, the integrated H α luminosity, $\mathcal{L}(\text{H}\alpha)$, has the following analytical value:

$$\mathcal{L}(\text{H}\alpha) = \int_0^\infty \phi(L) L dL = \phi^* L^* \Gamma(2 + \alpha) , \quad (7.11)$$

In this work, our sample of H α emitters was composed of the 46 OTELO sources selected at $z \sim 0.40$, of which 12 were optically classified as narrow- or broad-line AGNs. The sample was corrected from completeness following the expression in eq. 7.7 and also from dust attenuation, using the reddening value given by the best LePhare's fit for each galaxy (see Chapter 5). We used the empirical relation by Ly et al. (2012), which connects the dust reddening $E(B-V)$ and the extinction $A_{\text{H}\alpha}$ for galaxies at $z \sim 0.50$:

$$A_{\text{H}\alpha} = 1.85 \times E(B-V) \times k(\text{H}\alpha) , \quad (7.12)$$

where $k(\text{H}\alpha) = 3.33$ and the proportionality factor comes from the ratio between stellar and nebular reddening: $E(B-V)_{\text{gas}} = 1.85 \times E(B-V)$ (Calzetti et al. 2000).

Este documento incorpora firma electrónica, y es copia auténtica de un documento electrónico archivado por la ULL según la Ley 39/2015. Su autenticidad puede ser contrastada en la siguiente dirección https://sede.ull.es/validacion/		
Identificador del documento: 969870	Código de verificación: 8KFVZkZp	
Firmado por: MARINA RAMÓN PÉREZ UNIVERSIDAD DE LA LAGUNA		Fecha: 28/06/2017 21:15:24
ANGEL MANUEL BONGIOVANNI PÉREZ UNIVERSIDAD DE LA LAGUNA		29/06/2017 09:30:15
JORGE CEPA NOGUE UNIVERSIDAD DE LA LAGUNA		29/06/2017 09:33:05
ANA MARIA PEREZ GARCIA UNIVERSIDAD DE LA LAGUNA		29/06/2017 11:12:35
ERNESTO PEREDA DE PABLO UNIVERSIDAD DE LA LAGUNA		04/07/2017 18:28:07

Using the aforementioned expressions, an H α luminosity function at $z \sim 0.40$ was obtained for OTELO's complete dataset (46 objects) and for OTELO's star-forming galaxies sample (34 objects). Both are shown in Fig. 7.17, along with the luminosity functions obtained by previous works for H α emitters at the same redshift. The errors in our LFs are of statistical nature only, as these weight more in the estimation of the LF than the flux errors and the dispersion of the detection probability function fit.

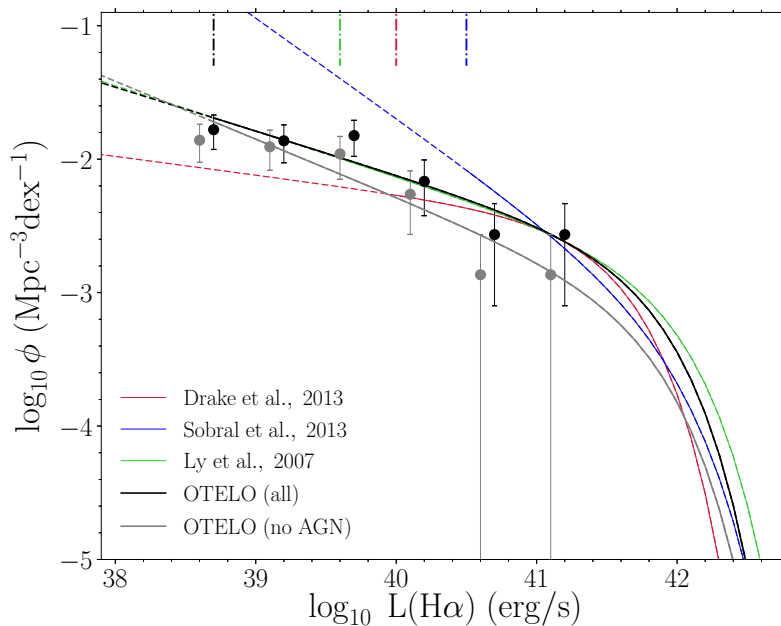


Figure 7.17: H α luminosity function at $z \sim 0.40$. The black line corresponds to the LF fitting for the whole sample of OTELO's emitters at that redshift, which are represented with black dots, while the gray line is the LF fitting for the non AGN population (gray circles). For the sake of clarity, gray circles are displaced -0.1 dex in luminosity with respect to black ones. Error bars (statistical only) are subject to an assumed Poissonian process. The H α luminosity functions of Drake et al. (2013), Sobral et al. (2013) and Ly et al. (2007) are plotted in red, blue and green, respectively. In each case, the solid line represents their sampled luminosity interval, while the dashed line is the extrapolation of their Schechter function fit. Vertical dotted-dashed lines in the upper part of the graph represent the corresponding luminosity limits for the construction of the LF in each survey, in the corresponding colour.

The characteristics of OTELO survey makes it very competitive in terms of depth and recovery of the LF faint end. As can be seen in the figure, OTELO's data reach luminosities almost 1 dex fainter than the faintest limit of the deepest survey (Ly et al. 2007). However, due to its small angular coverage and number statistics, OTELO's LF bright end is poorly sampled. That is why we decided to fix the L^* parameter and take the mean value from the luminosity functions of Drake et al. (2013), Sobral et al. (2013) and Ly et al. (2007): $L^* = 41.81$ erg/s. The dispersion in L^* obtained in those works is very small, reinforcing our assumption. Besides, the strength of OTELO resides in its depth, and hence in determining the slope at the faint end, α . This parameter

and ϕ^* were obtained by fitting the Schechter function to our datapoints. Their values, as well as those obtained by the already mentioned works, are shown in Table 7.5.

Table 7.5: Schechter parameters of the H α luminosity functions at $z \sim 0.4$ for the OTELO survey and earlier works. The first columns indicate the number of objects used to build the LF (N) and the limiting luminosity in each case (L_{lim}).

	N	$\log_{10} L_{lim}$	$\log_{10} \phi^*$	$\log_{10} L^*$	α	$\log_{10} \mathcal{L}$
Ly et al. (2007)	391	39.6	-2.75±0.16	41.93±0.19	-1.34±0.06	39.31±0.08
Drake et al. (2013)	271	40	—	41.55±0.12	—	39.15±0.10
Sobral et al. (2013)	797	40.5	-3.12±0.22	41.95±0.29	-1.75±0.20	39.55±0.22
OTELO (all galaxies)	42 (< L_*)	38.7	-2.68±0.17	41.81	-1.33±0.08	39.26±0.19
OTELO (non AGN)	33 (< L_*)	38.7	-3.03±0.21	41.81	-1.43±0.10	38.98±0.23

OTELO's luminosity functions not only are in agreement with the findings of previous works, specially with Ly et al. (2007), but they allow us to extend the luminosity range almost 1 dex fainter than theirs. The luminosity function of Sobral et al. (2013) seems to deviate from the rest at faint luminosities, overestimating the number of low-luminosity objects. However, given the luminosity limits of their survey, this should not be surprising. The work of Sobral et al. is, nevertheless, a good reference for the bright end of the LF, as their survey covers a field of view of ~ 2 deg 2 . It is also worth noticing the potential of OTELO survey to recover and extend the LF, in spite of the small number of objects under study in our sample. As a matter of fact, the samples of Drake et al. (2013), Sobral et al. (2013) and Ly et al. (2007)'s works have 6.5, 19 and 9 times more galaxies than our own (see Table 7.5).

A work comparable to OTELO, both in terms of number statistics and depth, is the one by Gómez-Guijarro et al. (2016), who used data from the ultra-deep VLT/HAWK-I narrow-band observations in the GOODS-S field. They obtained the H α LF at $z \sim 0.62$ with only 28 objects in their sample and reached a luminosity limit of $\log_{10} L \sim 39.8$ erg/s after the extinction correction, which allowed them to trace the faint-end of the LF at that redshift. They were able to detect extremely faint H α emitters, with a minimum flux of $> 1.7 \times 10^{-18}$ erg/s/cm 2 . However, as can be seen in Fig. 7.4, the minimum H α fluxes detected in OTELO are still fainter, with 6 objects below 10^{-19} erg/s/cm 2 .

The objects in our sample of H α emitters which were not selected as AGN are presumably star-forming galaxies (see Chapter 6). By studying their luminosity function, the star-formation rate (SFR) can be derived following the standard calibration of Kennicutt (1998), which assumes a Salpeter initial mass function (IMF) with masses between 0.1 and 100 M $_{\odot}$:

$$\text{SFR}(\text{M}_{\odot} \text{ year}^{-1}) = 7.9 \times 10^{-42} \mathcal{L}(\text{H}\alpha) \text{ (erg/s)} \quad (7.13)$$

Using our value of $\log_{10} \mathcal{L}(\text{H}\alpha) = 38.98$, we obtain a SFR density of $\rho_{SFR} = 0.0075 \pm 0.0042 \text{ M}_{\odot} \text{ yr}^{-1} \text{ Mpc}^{-3}$ at $z \sim 0.40$, a value slightly smaller than those obtained by previous works (see Table 7.6), although in consistency with them. As expected, our SFR is closer to that of Ly et al. (2007) and Drake et al. (2013), while the value obtained by Sobral et al. (2013) departs from the rest and tends to overestimate the SFR due to the aforementioned reasons.

Este documento incorpora firma electrónica, y es copia auténtica de un documento electrónico archivado por la ULL según la Ley 39/2015. Su autenticidad puede ser contrastada en la siguiente dirección https://sede.ull.es/validacion/		
Identificador del documento: 969870		Código de verificación: 8KFVZkZp
Firmado por: MARINA RAMÓN PÉREZ UNIVERSIDAD DE LA LAGUNA	Fecha: 28/06/2017 21:15:24	
ANGEL MANUEL BONGIOVANNI PEREZ UNIVERSIDAD DE LA LAGUNA	29/06/2017 09:30:15	
JORGE CEPA NOGUE UNIVERSIDAD DE LA LAGUNA	29/06/2017 09:33:05	
ANA MARIA PEREZ GARCIA UNIVERSIDAD DE LA LAGUNA	29/06/2017 11:12:35	
ERNESTO PEREDA DE PABLO UNIVERSIDAD DE LA LAGUNA	04/07/2017 18:28:07	

Table 7.6: Star formation rate density at $z \sim 0.40$ for OTELO survey and earlier works.

	ρ_{SFR} ($M_\odot \text{ yr}^{-1} \text{ Mpc}^{-3}$)
Ly et al. (2007)	0.016
Drake et al. (2013)	0.0113 ± 0.0005
Sobral et al. (2013)	0.03 ± 0.01
OTELO	0.0075 ± 0.0042

Finally, the AGN contribution to the total H α luminosity at $z \sim 0.40$ can be estimated by comparing the OTELO LF obtained for the complete sample of emitters and the one obtained for the sample of star-forming galaxies only, both represented in Fig. 7.17. We obtained the difference in the LFs (see Fig. 7.18) and fitted the resulting data points to a linear function with the following parameters:

$$\Delta \log_{10} \phi = a \times \log_{10} L(\text{H}\alpha) + b \quad (7.14)$$

$$a = 0.0814 \pm 0.0404$$

$$b = -3.1054 \pm 1.5893$$

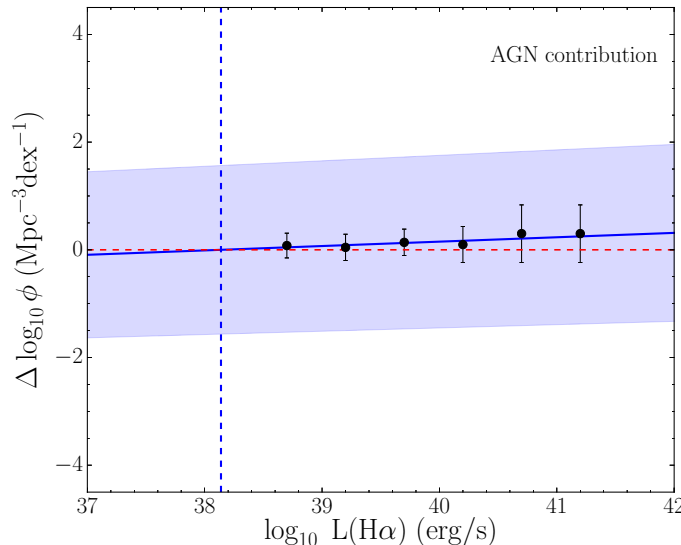


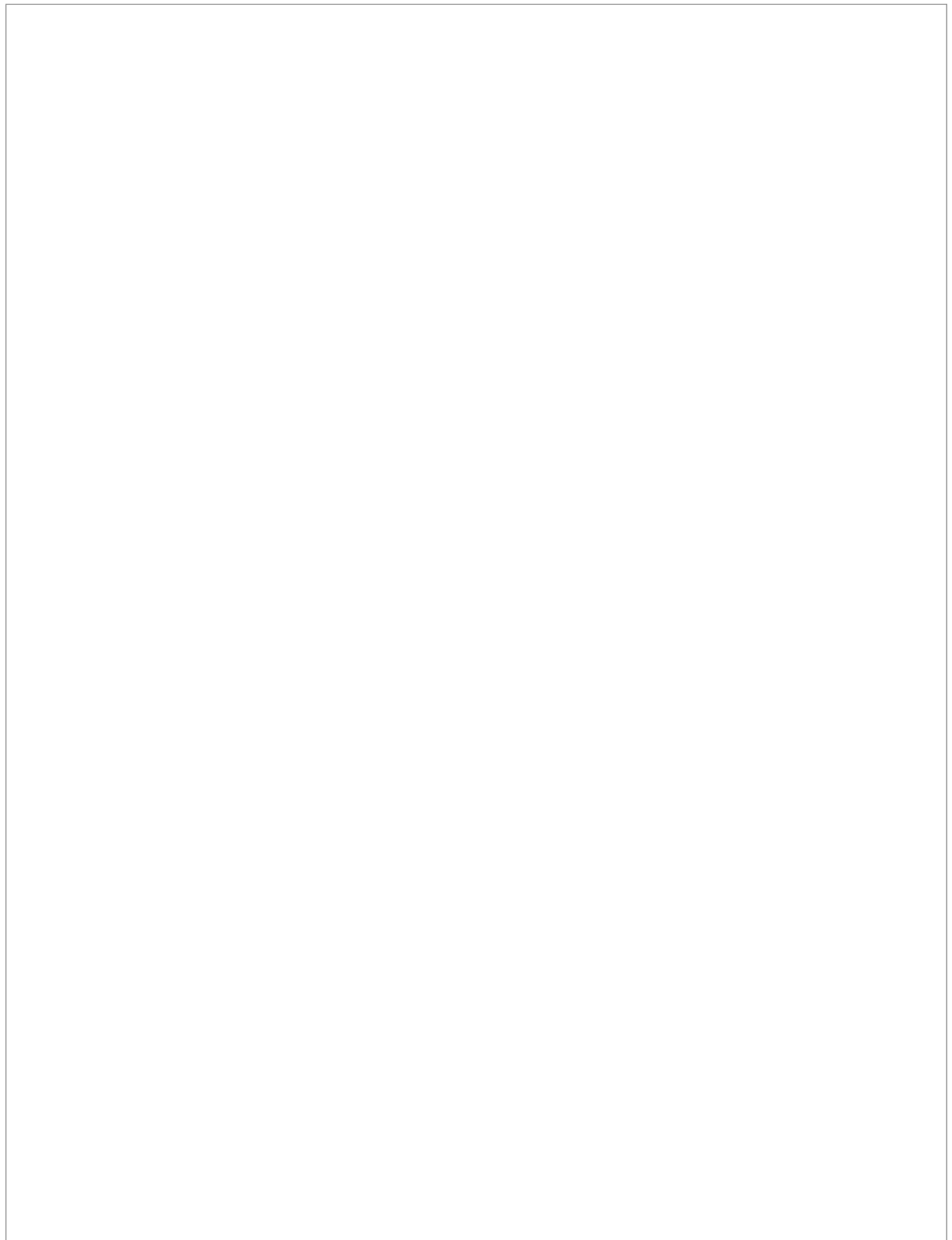
Figure 7.18: Difference between the OTELO H α LF of the total sample of emitters at $z \sim 0.40$ and that of the star-forming galaxies only. Black dots are the empirical data. The blue solid line corresponds to a linear fitting to these points. The red horizontal line corresponds to a null difference ($\Delta \log_{10} \phi = 0$). The blue dashed vertical line represents the luminosity above which the AGN contribution becomes relevant ($\Delta \log_{10} \phi > 0$).

The large errors in the parameters are mainly due to the small number of data points available for the fitting, and also to the statistical errors in the construction of the LFs. The AGN contribution to the total H α luminosity dominates when the difference in the LFs is positive, i.e, for luminosities greater than $\log_{10}L(H\alpha) > 38.14$ erg/s. Therefore, it would not be expected to find optical AGN at that redshift below that luminosity threshold. Above that value, the AGN contribution grows with the luminosity as in eq. 7.14.

Given the small number of objects in our samples for the construction of the LFs, the above conclusions about the AGN contribution should be taken with caution. However, it is worth noticing that the general procedure in other works (such as the ones used as a comparison here) is to roughly estimate the fraction of AGN as a percentage over the total population, and correct the sample of galaxies accordingly in order to build the LF. OTELO survey, in contrast, has allowed us to obtain a complete sample of H α emitters, for which the AGN fraction is known at each luminosity interval, and to derive a LF and SFR with a number of objects much smaller than in other surveys.

Este documento incorpora firma electrónica, y es copia auténtica de un documento electrónico archivado por la ULL según la Ley 39/2015.
Su autenticidad puede ser contrastada en la siguiente dirección <https://sede.ull.es/validacion/>

Identificador del documento:	969870	Código de verificación:	8KFVZkZp
Firmado por:	MARINA RAMÓN PÉREZ UNIVERSIDAD DE LA LAGUNA	Fecha:	28/06/2017 21:15:24
	ANGEL MANUEL BONGIOVANNI PEREZ UNIVERSIDAD DE LA LAGUNA		29/06/2017 09:30:15
	JORGE CEPA NOGUE UNIVERSIDAD DE LA LAGUNA		29/06/2017 09:33:05
	ANA MARIA PEREZ GARCIA UNIVERSIDAD DE LA LAGUNA		29/06/2017 11:12:35
	ERNESTO PEREDA DE PABLO UNIVERSIDAD DE LA LAGUNA		04/07/2017 18:28:07



Este documento incorpora firma electrónica, y es copia auténtica de un documento electrónico archivado por la ULL según la Ley 39/2015. <i>Su autenticidad puede ser contrastada en la siguiente dirección https://sede.ull.es/validacion/</i>		
Identificador del documento:	969870	Código de verificación:
Firmado por:	MARINA RAMÓN PÉREZ UNIVERSIDAD DE LA LAGUNA	Fecha: 28/06/2017 21:15:24
	ANGEL MANUEL BONGIOVANNI PEREZ UNIVERSIDAD DE LA LAGUNA	29/06/2017 09:30:15
	JORGE CEPA NOGUE UNIVERSIDAD DE LA LAGUNA	29/06/2017 09:33:05
	ANA MARIA PEREZ GARCIA UNIVERSIDAD DE LA LAGUNA	29/06/2017 11:12:35
	ERNESTO PEREDA DE PABLO UNIVERSIDAD DE LA LAGUNA	04/07/2017 18:28:07

SUMMARY AND CONCLUSIONS

This work has focused on the OTELO survey, an emission-line object survey done using the red tunable filters of the OSIRIS instrument at the GTC. The data have been reduced and calibrated using specifically designed procedures. 11237 sources have been extracted in the field and their photometry has been performed in order to obtain a catalogue of objects. Also, a pseudo-spectrum has been built for every source, using the potential of TFs to perform 2D low-resolution spectroscopy. The use of complementary data from X-rays to FIR has allowed us to obtain the final multiwavelength catalogue of OTELO, the basic tool for the following analysis.

After that, we have focused on the search of emission-line objects, specially H α emitters at $z \sim 0.40$. 1030 sources have been classified as emitters after an analysis involving both an automatic algorithm and visual selection using the pseudo-spectra. Photometric redshifts have been obtained for every source in the catalogue, allowing the discrimination between different emission lines. In particular, we have selected the H α emitters in the field by means of a careful analysis using all the information gathered from the catalogue and in the pseudo-spectra.

The next step has been the identification of AGN in OTELO's field. To do that, we have used several methods targeting distinct spectral ranges (X-rays and MIR) to select different populations of AGN. We have also taken advantage of the previous H α emitters selection in order to measure the H α +[NII] fluxes and used an optical selection diagram to discriminate AGN from star-forming galaxies.

The final step of this work has been the analysis of the OTELO AGN sample. We have studied the demography of AGN, their morphology and the LIRGs/ULIRGs population. We have then focused on the subpopulation of AGN at $z \sim 0.40$. We have characterised their environments and obtained the H α luminosity function, both for the whole sample of emitters and for the non-AGN only. In this way, we have estimated the AGN contribution to the total luminosity. We have also obtained a value for the star-formation rate of galaxies at that redshift.

Starting from the objectives of this thesis summarised in Chapter 1, we present in what follows the main conclusions of this work:

- A deep, multiwavelength catalogue of objects in the field (11237) and of emitting objects (1030) in the OTELO survey has been obtained. We have reached a limiting flux of 6.8×10^{-18} erg/s/cm 2 at 3σ , corresponding to a limiting AB magnitude of 26.50. The completeness flux is 1.08×10^{-17} , i.e., an AB magnitude of 26. For all the sources, the catalogue contains precise photometric measurements from

Este documento incorpora firma electrónica, y es copia auténtica de un documento electrónico archivado por la ULL según la Ley 39/2015. Su autenticidad puede ser contrastada en la siguiente dirección https://sede.ull.es/validacion/		
--	--	--

Identificador del documento: 969870	Código de verificación: 8KFVZkZp
-------------------------------------	----------------------------------

Fecha: 28/06/2017 21:15:24

Firmado por: MARINA RAMÓN PÉREZ UNIVERSIDAD DE LA LAGUNA

29/06/2017 09:30:15

ANGEL MANUEL BONGIOVANNI PEREZ UNIVERSIDAD DE LA LAGUNA
--

29/06/2017 09:33:05

JORGE CEPA NOGUE UNIVERSIDAD DE LA LAGUNA
--

29/06/2017 11:12:35

ANA MARIA PEREZ GARCIA UNIVERSIDAD DE LA LAGUNA
--

04/07/2017 18:28:07

ERNESTO PEREDA DE PABLO UNIVERSIDAD DE LA LAGUNA

OTELO's deep image and from 10 additional images: u, g, r, i, z from the CFHTLS, V and I from the HST-ACS and J, H and Ks from WIRDS. Moreover, this nuclear catalogue has been cross-matched to 8 complementary catalogues: 6 with information from X-rays to FIR, and 2 with photo- z and spec- z information. This catalogue represents the deepest catalogue of emitting objects to date. Regarding the H α emitters studied in this thesis, we have reached line fluxes below 10^{-19} erg/s/cm 2 , exceeding, for instance, the ultra-deep observations carried out with the VLT/HAWK-I in narrow band (Gómez-Guijarro et al. 2016).

- A selection of emission-line objects has been performed in OTELO survey, yielding 1030 candidates and 46 secure H α emitters in the field. The analysis has been done using all the information gathered in the multiwavelength catalogue (specially the photometric redshifts), as well as the pseudo-spectra of the sources. The potential of OTELO survey to select emitters, and in particular H α sources, has been demonstrated in two ways:
 - in a theoretical way, with a simulation performed in order to obtain OTELO's detection limits. This proved that OTELO is able to recover, with a probability of $p \geq 0.50$, H α emitters at $z \sim 0.40$ down to an equivalent width of $\sim 5\text{\AA}$, allowing the detection of 1 out of 5 elliptical galaxies with $\text{EW} = 6\text{\AA}$ and more than 75% of spiral galaxies with $\text{EW} \geq 60\text{\AA}$.
 - in an empirical way, by comparing the density of H α emitters found in OTELO survey with that of other important surveys such as the HSC-SSP and HIZELS. OTELO reaches deeper fluxes and our selection methods, based mainly in photo- z estimations and in the TFs pseudo-spectra of the sources, are more efficient and add less contaminants. As a matter of fact, we find a non-negligible one third more H α emitters in OTELO than in the HSC-SSP survey.
- We have obtained a sample of 72 AGN in OTELO's field, selected with 4 different methods: an optical diagnostic diagram based on the H α +[NII] fluxes of the emitters at $z \sim 0.40$, a selection of BLAGN at the same redshift based on the width of the emission line as seen in the pseudo-spectra, an X-ray selection and two diagnostic diagrams in the MIR.
- An analysis has been performed on OTELO's AGN population in order to characterize them. These are the main results from the analysis:
 - X-ray emission is the most efficient method to select AGN. This method has selected 58% of the whole sample of AGN in OTELO.
 - From the X-ray-selected AGN, around one third are obscured while the rest are unobscured AGN.
 - MIR diagnostic diagrams are also very effective, selecting 40% of the OTELO AGN sample.
 - From the MIR selected AGN, the proportion of obscured and unobscured AGN is 62% and 38%, respectively. This is roughly the opposite as in the X-ray-selected case.
 - At $z \sim 0.40$ we have found 13 AGN, which represent a 26% of the total of H α emitters at that redshift.
 - The majority of our AGN (64%) were classified as late-type galaxies, 16% as irregulars, 14% as early-type and 12.5% as point-like sources.
 - Most of the BLAGN at $z \sim 0.40$ are spiral galaxies (4 out of 5).

Este documento incorpora firma electrónica, y es copia auténtica de un documento electrónico archivado por la ULL según la Ley 39/2015.
Su autenticidad puede ser contrastada en la siguiente dirección <https://sede.ull.es/validacion/>

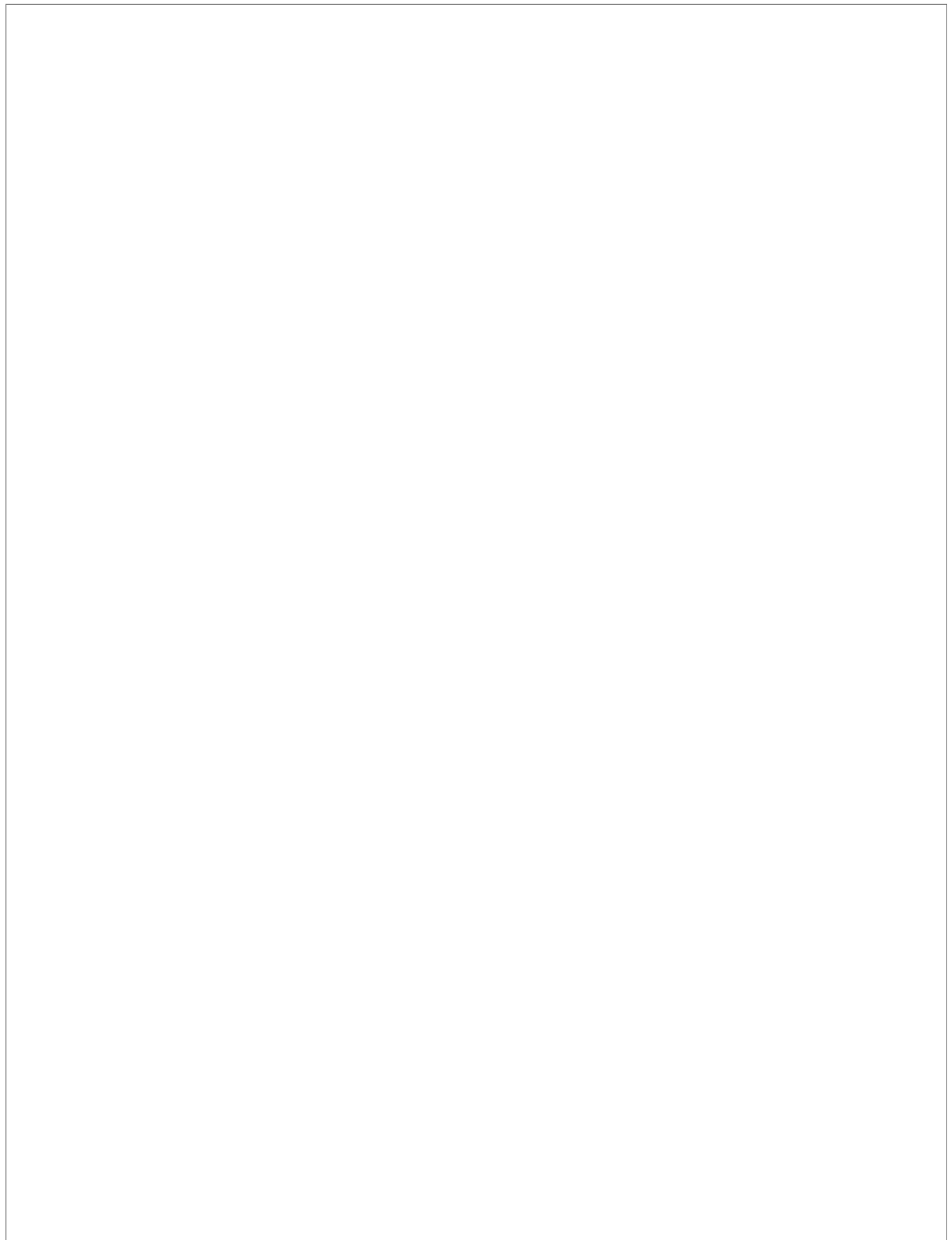
Identificador del documento:	Código de verificación:
969870	8KFVZkZp
Firmado por: MARINA RAMÓN PÉREZ UNIVERSIDAD DE LA LAGUNA	Fecha: 28/06/2017 21:15:24
ANGEL MANUEL BONGIOVANNI PÉREZ UNIVERSIDAD DE LA LAGUNA	29/06/2017 09:30:15
JORGE CEPA NOGUE UNIVERSIDAD DE LA LAGUNA	29/06/2017 09:33:05
ANA MARIA PEREZ GARCIA UNIVERSIDAD DE LA LAGUNA	29/06/2017 11:12:35
ERNESTO PEREDA DE PABLO UNIVERSIDAD DE LA LAGUNA	04/07/2017 18:28:07

- The fraction of late-type galaxies among the X-rays selected AGN (56%) is smaller than among the MIR ones (79%).
 - Signs of interactions or mergers are found in 16% of AGN.
 - We are able to recover all the LIRGs in OTELO's field up to $z \sim 1.6$.
 - The fraction of LIRGs and ULIRGs is higher among the AGN population than among the rest of the galaxies, and this difference is specially remarkable for the ultra-luminous type.
 - ULIRGs are characterised by a higher fraction of AGN than LIRGs.
 - AGN in OTELO field at $z \sim 0.40$ are found in identical environments as non-AGN.
 - The subpopulation of AGN at $z \sim 0.40$ is the most clustered group when compared to passive galaxies, SFG and H α emitters.
- An H α luminosity function at $z \sim 0.40$ has been obtained, using the completeness correction from our simulation and an extinction correction from the photo-z estimation. These are the main conclusions:
 - Using the mean value of $\log_{10} L^*$ from previous works (41.81), we fitted our data points to a Schechter function with the following parameters for the whole sample of H α emitters: $\log_{10} \phi^* = -2.68 \pm 0.17$ and $\alpha = -1.33 \pm 0.08$.
 - Removing the AGN from the previous sample, we obtain a second luminosity function for non-AGN only, with the following parameters: $\log_{10} \phi^* = -3.03 \pm 0.21$ and $\alpha = -1.43 \pm 0.10$.
 - When compared to previous works, our luminosity functions extend the faint-end almost 1 dex, reaching luminosities of $\log_{10} L_{lim} = 38.7$.
 - The AGN contribution to the total H α luminosity has been estimated. We find that no AGN should be expected below a luminosity of $\log_{10} L = 38.14$ erg/s. Above that value, the AGN contribution grows with the luminosity. Again, given our small sample of AGN at $z \sim 0.40$, a study with more statistical significance should be made in order to confirm this result.
 - A star-formation rate has been obtained for the sample of non-AGN (presumably, star-forming galaxies) at $z \sim 0.40$: $SFR(M_\odot \text{ year}^{-1}) = 7.9 \times 10^{-42} \mathcal{L}(H\alpha)$ (erg/s), yielding a star formation rate density of $\rho_{SFR} = 0.0075 \pm 0.0042 M_\odot \text{ yr}^{-1} \text{ Mpc}^{-3}$.

Summarizing, in this work we have performed the first exploitation of OTELO's data, that included the obtention of the deepest catalogue of emitting objects to date. We have gathered the faintest sample of H α emitters ever compiled, with line fluxes below 10^{-19} erg/s/cm 2 , that has allowed us to extend the faint-end of the LF at $z \sim 0.40$ almost 1 dex when compared to other works. The subsequent analysis of other emission lines in OTELO will allow us to explore volumes of Universe in a never known depth, as well as detect new AGN based on other emission lines.

Este documento incorpora firma electrónica, y es copia auténtica de un documento electrónico archivado por la ULL según la Ley 39/2015.
Su autenticidad puede ser contrastada en la siguiente dirección <https://sede.ull.es/validacion/>

Identificador del documento:	Código de verificación:
969870	8KFVZkZp
Firmado por: MARINA RAMÓN PÉREZ UNIVERSIDAD DE LA LAGUNA	Fecha: 28/06/2017 21:15:24
ANGEL MANUEL BONGIOVANNI PEREZ UNIVERSIDAD DE LA LAGUNA	29/06/2017 09:30:15
JORGE CEPA NOGUE UNIVERSIDAD DE LA LAGUNA	29/06/2017 09:33:05
ANA MARIA PEREZ GARCIA UNIVERSIDAD DE LA LAGUNA	29/06/2017 11:12:35
ERNESTO PEREDA DE PABLO UNIVERSIDAD DE LA LAGUNA	04/07/2017 18:28:07



Este documento incorpora firma electrónica, y es copia auténtica de un documento electrónico archivado por la ULL según la Ley 39/2015. <i>Su autenticidad puede ser contrastada en la siguiente dirección https://sede.ull.es/validacion/</i>		
Identificador del documento:	969870	Código de verificación:
Firmado por:	MARINA RAMÓN PÉREZ UNIVERSIDAD DE LA LAGUNA	Fecha: 28/06/2017 21:15:24
	ANGEL MANUEL BONGIOVANNI PEREZ UNIVERSIDAD DE LA LAGUNA	29/06/2017 09:30:15
	JORGE CEPA NOGUE UNIVERSIDAD DE LA LAGUNA	29/06/2017 09:33:05
	ANA MARIA PEREZ GARCIA UNIVERSIDAD DE LA LAGUNA	29/06/2017 11:12:35
	ERNESTO PEREDA DE PABLO UNIVERSIDAD DE LA LAGUNA	04/07/2017 18:28:07

A

AGN MORPHOLOGIES (EXAMPLES)

In this Appendix, the morphologies of some of the AGN found in OTELO are shown as representative examples:

- Broad-line AGN at $z \sim 0.40$: Figures A.1, A.2 and A.3.
- Narrow-line AGN at $z \sim 0.40$: Figures A.4 and A.5.
- X-rays selected AGN: Figures A.6-A.9.
- Unobscured AGN (MIR+X-rays selection): Figure A.10 and A.11.
- Obscured AGN (MIR selection only): Figures A.12-A.15.

The figures display the object in the original HST images along with their GALFIT model and residual, both described in section 7.2.

Este documento incorpora firma electrónica, y es copia auténtica de un documento electrónico archivado por la ULL según la Ley 39/2015.
Su autenticidad puede ser contrastada en la siguiente dirección <https://sede.ull.es/validacion/>

Identificador del documento:	969870	Código de verificación:	8KFVZkZp
Firmado por:	MARINA RAMÓN PÉREZ UNIVERSIDAD DE LA LAGUNA	Fecha:	28/06/2017 21:15:24
	ANGEL MANUEL BONGIOVANNI PEREZ UNIVERSIDAD DE LA LAGUNA		29/06/2017 09:30:15
	JORGE CEPA NOGUE UNIVERSIDAD DE LA LAGUNA		29/06/2017 09:33:05
	ANA MARIA PEREZ GARCIA UNIVERSIDAD DE LA LAGUNA		29/06/2017 11:12:35
	ERNESTO PEREDA DE PABLO UNIVERSIDAD DE LA LAGUNA		04/07/2017 18:28:07

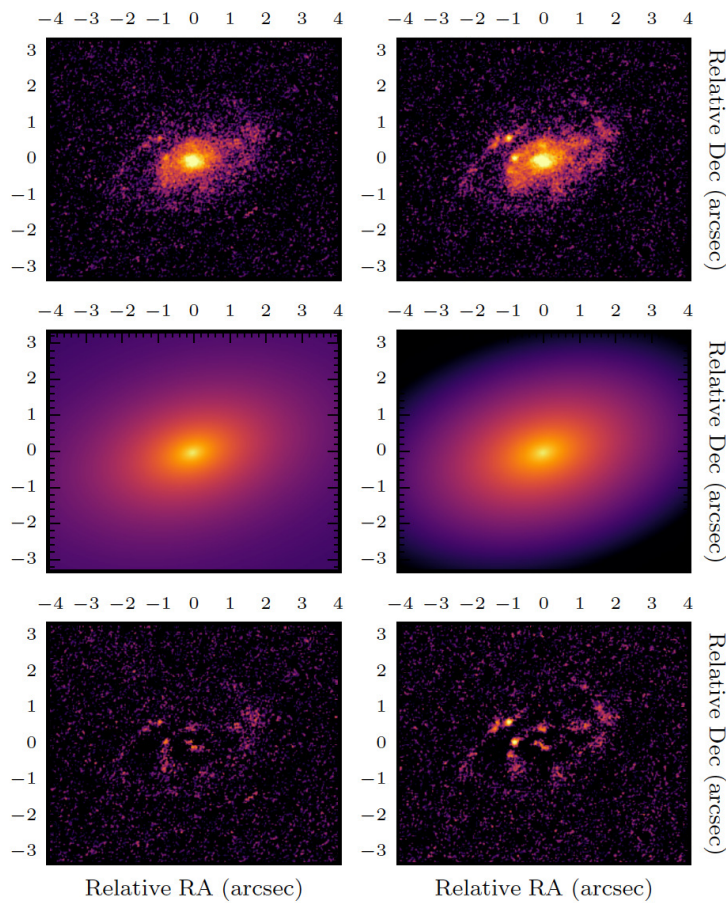


Figure A.1: Morphology of the object #1873. This object was classified as a BLAGN at $z \sim 0.40$ and is clearly a spiral galaxy (S, late-type). The spiral arms are visible in the residual. First row: HST images of the object. Second row: GALFIT models. Third row: GALFIT residuals obtained by subtracting its model to the original image. The first column shows the V filter of HST (F814W) and the second one the I filter (F606W).

Este documento incorpora firma electrónica, y es copia auténtica de un documento electrónico archivado por la ULL según la Ley 39/2015.
Su autenticidad puede ser contrastada en la siguiente dirección <https://sede.ull.es/validacion/>

Identificador del documento: 969870

Código de verificación: 8KFVZkZp

Fecha: 28/06/2017 21:15:24

Firmado por: MARINA RAMÓN PÉREZ
UNIVERSIDAD DE LA LAGUNA

29/06/2017 09:30:15

ANGEL MANUEL BONGIOVANNI PEREZ
UNIVERSIDAD DE LA LAGUNA

29/06/2017 09:33:05

JORGE CEPA NOGUE
UNIVERSIDAD DE LA LAGUNA

29/06/2017 11:12:35

ANA MARIA PEREZ GARCIA
UNIVERSIDAD DE LA LAGUNA

04/07/2017 18:28:07

ERNESTO PEREDA DE PABLO
UNIVERSIDAD DE LA LAGUNA

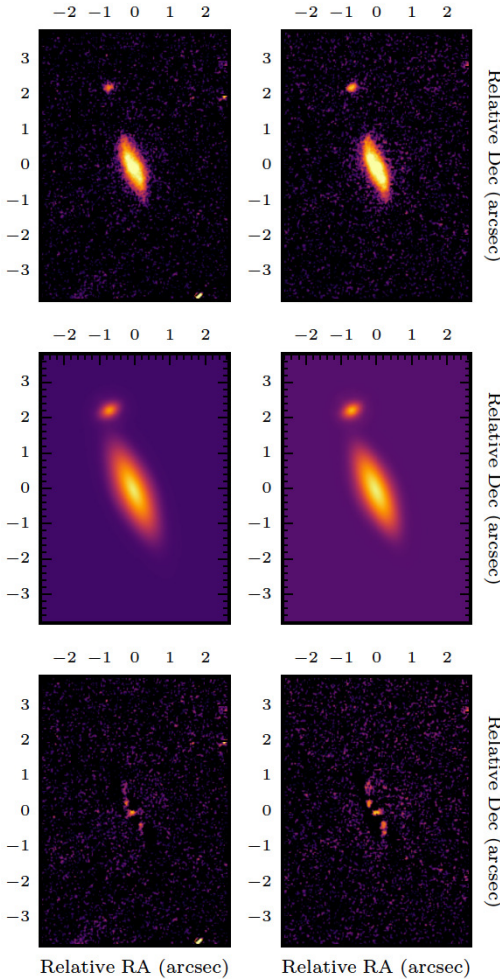


Figure A.2: Morphology of the object #8762. This object is a BLAGN at $z \sim 0.40$. It is a barred spiral galaxy (SB), whose bar appears visible in the residual images. First row: HST images of the object. Second row: GALFIT models. Third row: GALFIT residuals obtained by subtracting its model to the original image. The first column shows the V filter of HST (F814W) and the second one the I filter (F606W)..

Este documento incorpora firma electrónica, y es copia auténtica de un documento electrónico archivado por la ULL según la Ley 39/2015.
Su autenticidad puede ser contrastada en la siguiente dirección <https://sede.ull.es/validacion/>

Identificador del documento: 969870

Código de verificación: 8KFVZkZp

Fecha: 28/06/2017 21:15:24

Firmado por: MARINA RAMÓN PÉREZ
UNIVERSIDAD DE LA LAGUNA

ANGEL MANUEL BONGIOVANNI PEREZ
UNIVERSIDAD DE LA LAGUNA

JORGE CEPA NOGUE
UNIVERSIDAD DE LA LAGUNA

ANA MARIA PEREZ GARCIA
UNIVERSIDAD DE LA LAGUNA

ERNESTO PEREDA DE PABLO
UNIVERSIDAD DE LA LAGUNA

29/06/2017 09:30:15

29/06/2017 09:33:05

29/06/2017 11:12:35

04/07/2017 18:28:07

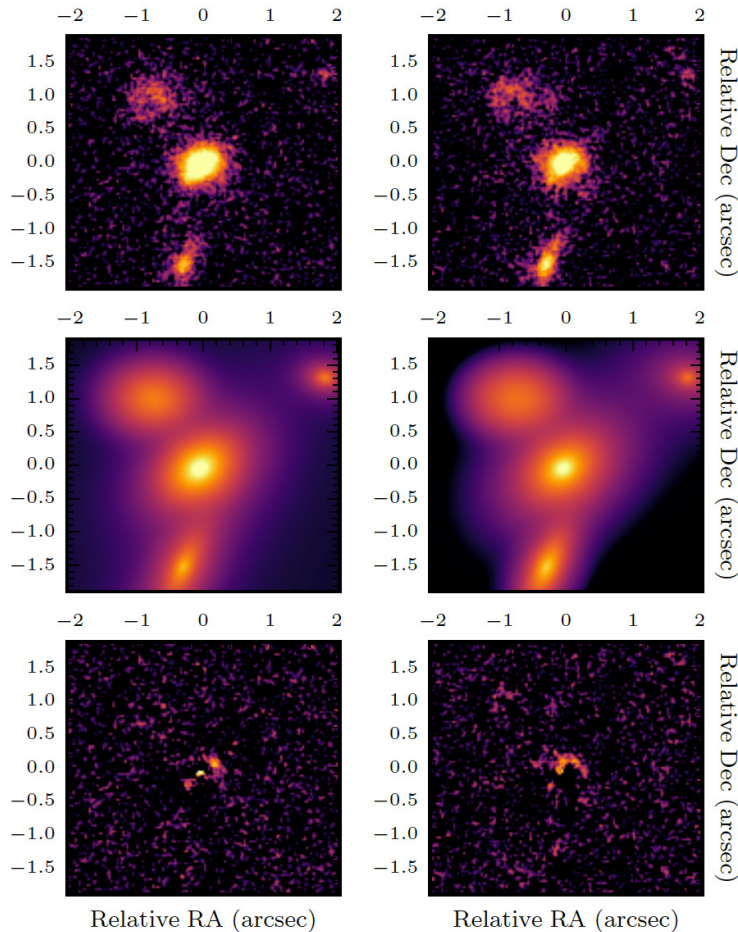


Figure A.3: Morphology of the object #2146. This object is a BLAGN at $z \sim 0.40$. It was classified as a late-type and flagged as a multiple object. First row: HST images of the object. Second row: GALFIT models. Third row: GALFIT residuals obtained by subtracting its model to the original image. The first column shows the V filter of HST (F814W) and the second one the I filter (F606W)..

Este documento incorpora firma electrónica, y es copia auténtica de un documento electrónico archivado por la ULL según la Ley 39/2015.
Su autenticidad puede ser contrastada en la siguiente dirección <https://sede.ull.es/validacion/>

Identificador del documento: 969870

Código de verificación: 8KFVZkZp

Firmado por: MARINA RAMÓN PÉREZ
UNIVERSIDAD DE LA LAGUNA

Fecha: 28/06/2017 21:15:24

ANGEL MANUEL BONGIOVANNI PEREZ
UNIVERSIDAD DE LA LAGUNA

29/06/2017 09:30:15

JORGE CEPA NOGUE
UNIVERSIDAD DE LA LAGUNA

29/06/2017 09:33:05

ANA MARIA PEREZ GARCIA
UNIVERSIDAD DE LA LAGUNA

29/06/2017 11:12:35

ERNESTO PEREDA DE PABLO
UNIVERSIDAD DE LA LAGUNA

04/07/2017 18:28:07

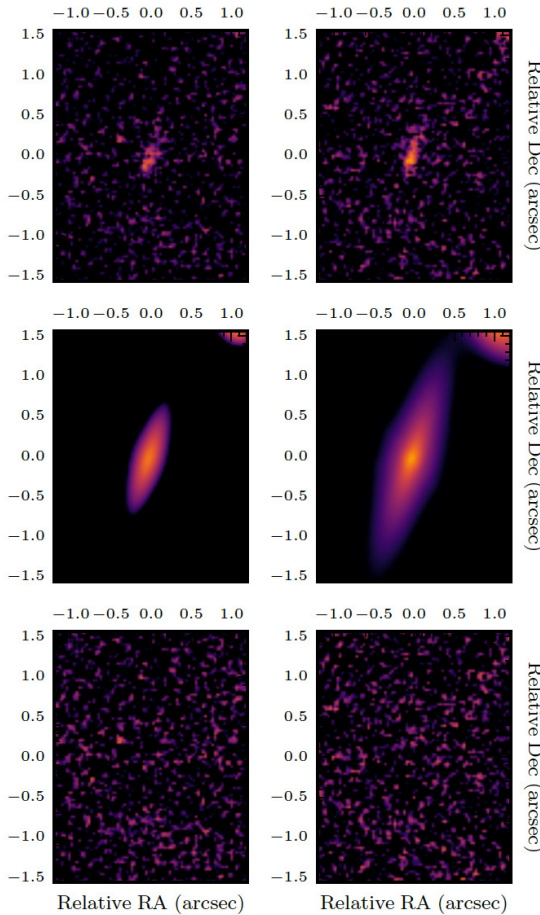


Figure A.4: Morphology of the object #3854. This object was classified as a NLAGN at $z \sim 0.40$ and was not assigned any morphological type (unclassifiable). First row: HST images of the object. Second row: GALFIT models. Third row: GALFIT residuals obtained by subtracting its model to the original image. The first column shows the V filter of HST (F814W) and the second one the I filter (F606W).

Este documento incorpora firma electrónica, y es copia auténtica de un documento electrónico archivado por la ULL según la Ley 39/2015.
Su autenticidad puede ser contrastada en la siguiente dirección <https://sede.ull.es/validacion/>

Identificador del documento: 969870

Código de verificación: 8KFVZkZp

Fecha: 28/06/2017 21:15:24

Firmado por: MARINA RAMÓN PÉREZ
UNIVERSIDAD DE LA LAGUNA

29/06/2017 09:30:15

ANGEL MANUEL BONGIOVANNI PEREZ
UNIVERSIDAD DE LA LAGUNA

29/06/2017 09:33:05

JORGE CEPA NOGUE
UNIVERSIDAD DE LA LAGUNA

29/06/2017 11:12:35

ANA MARIA PEREZ GARCIA
UNIVERSIDAD DE LA LAGUNA

04/07/2017 18:28:07

ERNESTO PEREDA DE PABLO
UNIVERSIDAD DE LA LAGUNA

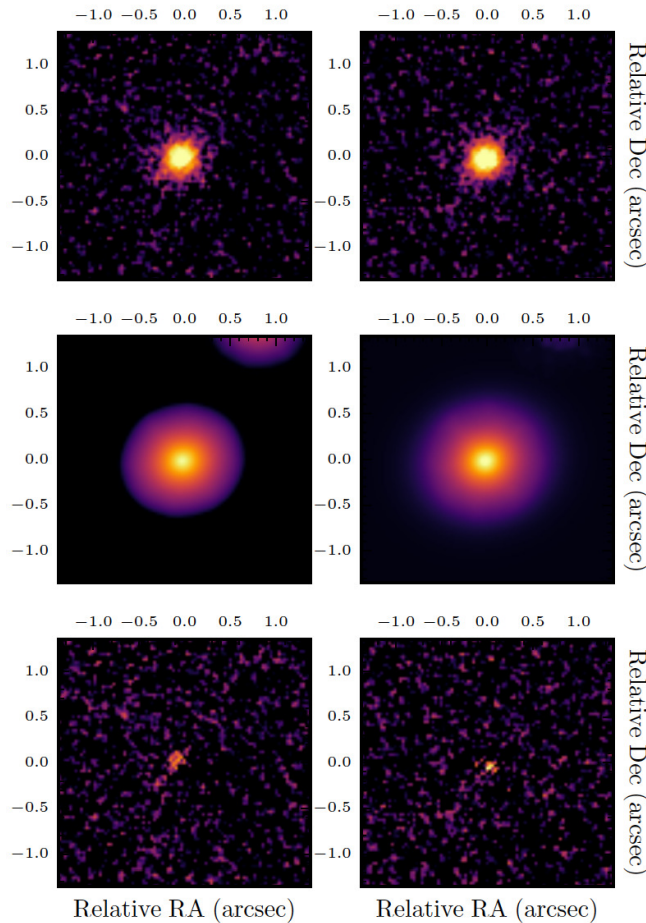


Figure A.5: Morphology of the object #6395. This object was classified as a NLAGN at $z \sim 0.40$ with a spheroidal morphology (early-type). First row: HST images of the object. Second row: GALFIT models. Third row: GALFIT residuals obtained by subtracting its model to the original image. The first column shows the V filter of HST (F814W) and the second one the I filter (F606W).

Este documento incorpora firma electrónica, y es copia auténtica de un documento electrónico archivado por la ULL según la Ley 39/2015.
Su autenticidad puede ser contrastada en la siguiente dirección <https://sede.ull.es/validacion/>

Identificador del documento: 969870

Código de verificación: 8KFVZkZp

Fecha: 28/06/2017 21:15:24

Firmado por: MARINA RAMÓN PÉREZ
UNIVERSIDAD DE LA LAGUNA

ANGEL MANUEL BONGIOVANNI PEREZ
UNIVERSIDAD DE LA LAGUNA

JORGE CEPA NOGUE
UNIVERSIDAD DE LA LAGUNA

ANA MARIA PEREZ GARCIA
UNIVERSIDAD DE LA LAGUNA

ERNESTO PEREDA DE PABLO
UNIVERSIDAD DE LA LAGUNA

29/06/2017 09:30:15

29/06/2017 09:33:05

29/06/2017 11:12:35

04/07/2017 18:28:07

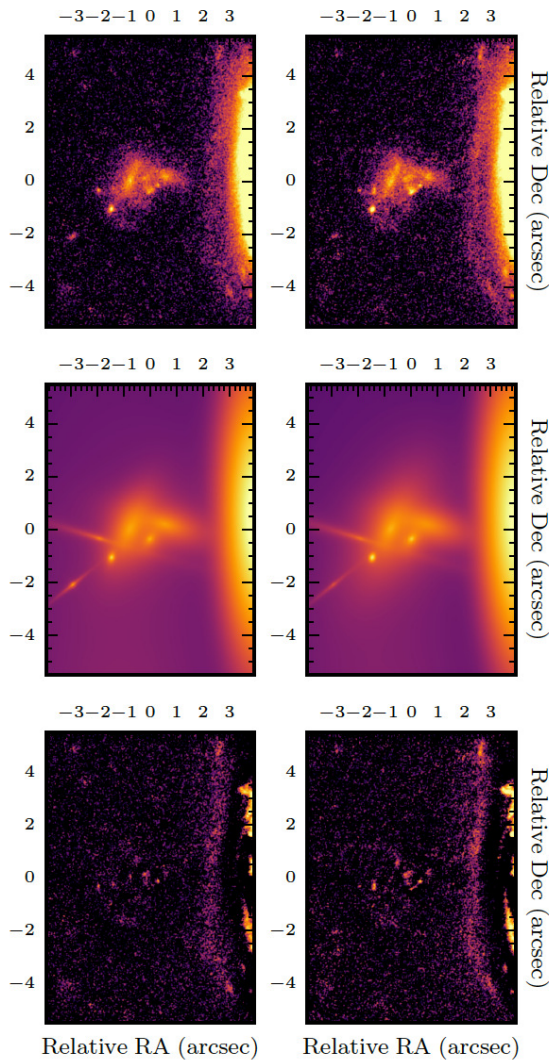


Figure A.6: Morphology of the object #5662. This object, selected as AGN by its X-rays emission, is part of a system with multiple interacting components. Due to its complexity, it was not assigned any morphological type (unclassifiable). First row: HST images of the object. Second row: GALFIT models. Third row: GALFIT residuals obtained by subtracting its model to the original image. The first column shows the V filter of HST (F814W) and the second one the I filter (F606W).

Este documento incorpora firma electrónica, y es copia auténtica de un documento electrónico archivado por la ULL según la Ley 39/2015.
Su autenticidad puede ser contrastada en la siguiente dirección <https://sede.ull.es/validacion/>

Identificador del documento: 969870

Código de verificación: 8KFVZkZp

Firmado por: MARINA RAMÓN PÉREZ
UNIVERSIDAD DE LA LAGUNA

Fecha: 28/06/2017 21:15:24

ANGEL MANUEL BONGIOVANNI PEREZ
UNIVERSIDAD DE LA LAGUNA

29/06/2017 09:30:15

JORGE CEPA NOGUE
UNIVERSIDAD DE LA LAGUNA

29/06/2017 09:33:05

ANA MARIA PEREZ GARCIA
UNIVERSIDAD DE LA LAGUNA

29/06/2017 11:12:35

ERNESTO PEREDA DE PABLO
UNIVERSIDAD DE LA LAGUNA

04/07/2017 18:28:07

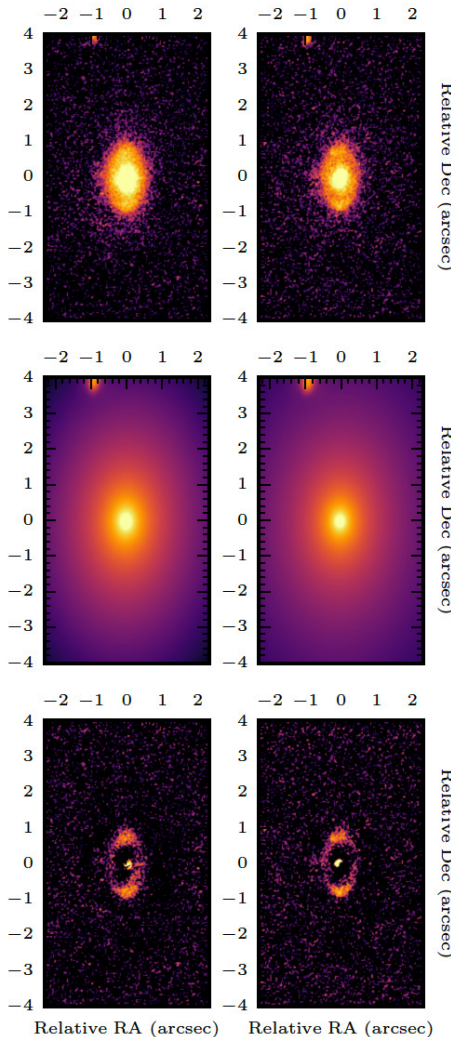


Figure A.7: Morphology of the object #3216. This object is an X-rays selected AGN. It is a face-on spiral, whose arms are visible in the residual images (late-type). First row: HST images of the object. Second row: GALFIT models. Third row: GALFIT residuals obtained by subtracting its model to the original image. The first column shows the V filter of HST (F814W) and the second one the I filter (F606W).

Este documento incorpora firma electrónica, y es copia auténtica de un documento electrónico archivado por la ULL según la Ley 39/2015.
Su autenticidad puede ser contrastada en la siguiente dirección <https://sede.ull.es/validacion/>

Identificador del documento: 969870

Código de verificación: 8KFVZkZp

Fecha: 28/06/2017 21:15:24

Firmado por: MARINA RAMÓN PÉREZ
UNIVERSIDAD DE LA LAGUNA

ANGEL MANUEL BONGIOVANNI PEREZ
UNIVERSIDAD DE LA LAGUNA

JORGE CEPA NOGUE
UNIVERSIDAD DE LA LAGUNA

ANA MARIA PEREZ GARCIA
UNIVERSIDAD DE LA LAGUNA

ERNESTO PEREDA DE PABLO
UNIVERSIDAD DE LA LAGUNA

29/06/2017 09:30:15

29/06/2017 09:33:05

29/06/2017 11:12:35

04/07/2017 18:28:07

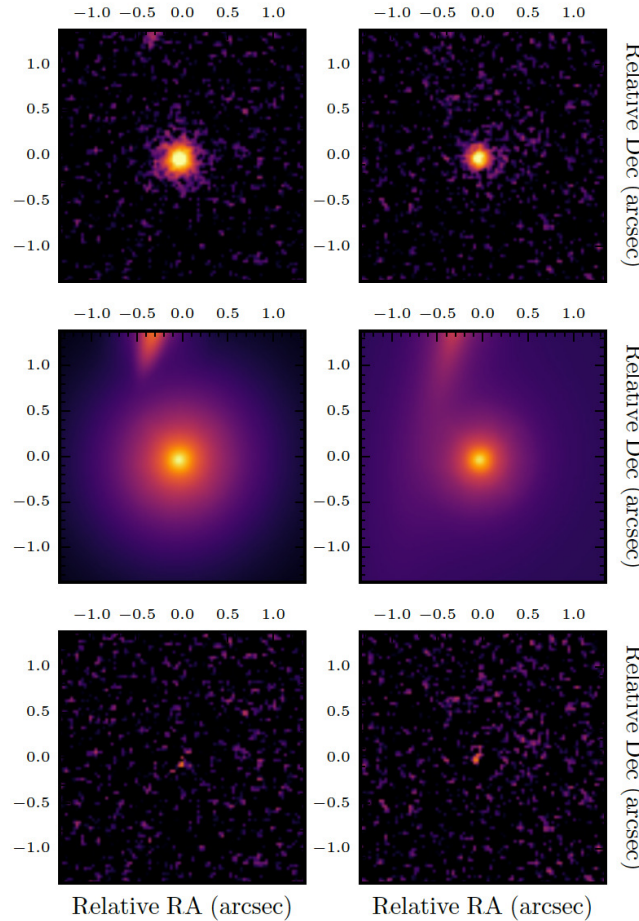


Figure A.8: Morphology of the object #6173. This object is an X-rays selected AGN. It has a point-like appearance, and is probably a QSO, just like the object #8351, shown in Fig. A.11. First row: HST images of the object. Second row: GALFIT models. Third row: GALFIT residuals obtained by subtracting its model to the original image. The first column shows the V filter of HST (F814W) and the second one the I filter (F606W).

Este documento incorpora firma electrónica, y es copia auténtica de un documento electrónico archivado por la ULL según la Ley 39/2015.
Su autenticidad puede ser contrastada en la siguiente dirección <https://sede.ull.es/validacion/>

Identificador del documento: 969870

Código de verificación: 8KFVZkZp

Firmado por: MARINA RAMÓN PÉREZ
UNIVERSIDAD DE LA LAGUNA

Fecha: 28/06/2017 21:15:24

ANGEL MANUEL BONGIOVANNI PEREZ
UNIVERSIDAD DE LA LAGUNA

29/06/2017 09:30:15

JORGE CEPA NOGUE
UNIVERSIDAD DE LA LAGUNA

29/06/2017 09:33:05

ANA MARIA PEREZ GARCIA
UNIVERSIDAD DE LA LAGUNA

29/06/2017 11:12:35

ERNESTO PEREDA DE PABLO
UNIVERSIDAD DE LA LAGUNA

04/07/2017 18:28:07

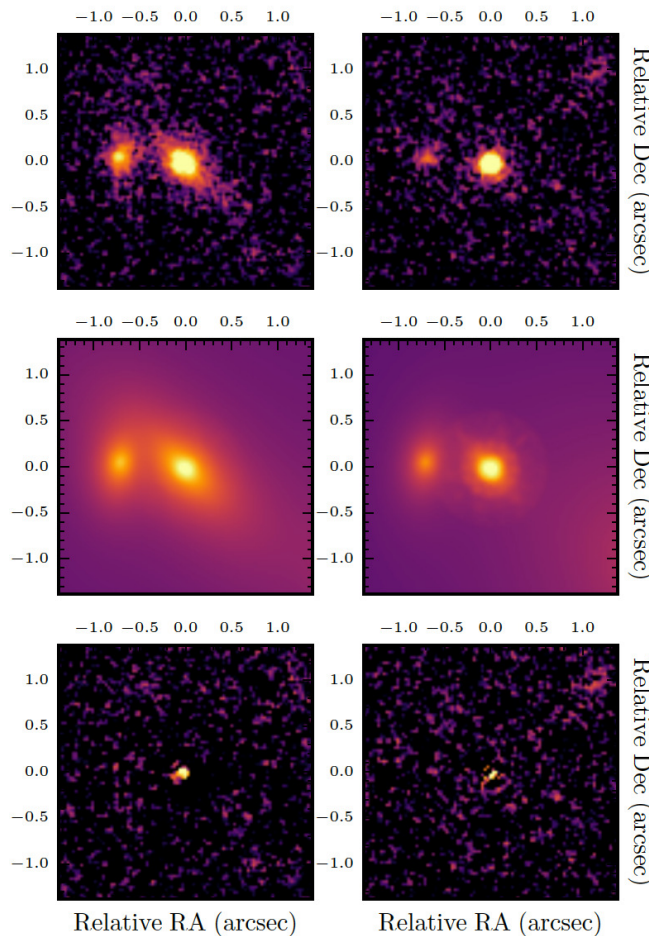


Figure A.9: Morphology of the object #5495. This object is an X-rays selected AGN. It seems to be an early-type galaxy (probably lenticular, S0) with a companion. First row: HST images of the object. Second row: GALFIT models. Third row: GALFIT residuals obtained by subtracting its model to the original image. The first column shows the V filter of HST (F814W) and the second one the I filter (F606W).

Este documento incorpora firma electrónica, y es copia auténtica de un documento electrónico archivado por la ULL según la Ley 39/2015.
Su autenticidad puede ser contrastada en la siguiente dirección <https://sede.ull.es/validacion/>

Identificador del documento: 969870

Código de verificación: 8KFVZkZp

Firmado por: MARINA RAMÓN PÉREZ
UNIVERSIDAD DE LA LAGUNA

Fecha: 28/06/2017 21:15:24

ANGEL MANUEL BONGIOVANNI PEREZ
UNIVERSIDAD DE LA LAGUNA

29/06/2017 09:30:15

JORGE CEPA NOGUE
UNIVERSIDAD DE LA LAGUNA

29/06/2017 09:33:05

ANA MARIA PEREZ GARCIA
UNIVERSIDAD DE LA LAGUNA

29/06/2017 11:12:35

ERNESTO PEREDA DE PABLO
UNIVERSIDAD DE LA LAGUNA

04/07/2017 18:28:07

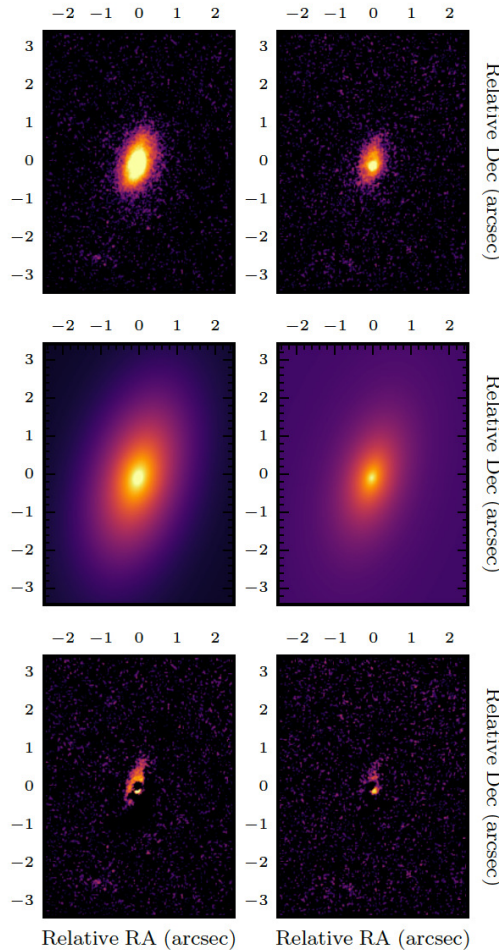


Figure A.10: Morphology of the object #8459. This object is an unobscured AGN (selected both in X-rays and infrared) with a morphological disk type (late-type). First row: HST images of the object. Second row: GALFIT models. Third row: GALFIT residuals obtained by subtracting its model to the original image. The first column shows the V filter of HST (F814W) and the second one the I filter (F606W).

Este documento incorpora firma electrónica, y es copia auténtica de un documento electrónico archivado por la ULL según la Ley 39/2015.
Su autenticidad puede ser contrastada en la siguiente dirección <https://sede.ull.es/validacion/>

Identificador del documento: 969870

Código de verificación: 8KFVZkZp

Firmado por: MARINA RAMÓN PÉREZ
 UNIVERSIDAD DE LA LAGUNA

Fecha: 28/06/2017 21:15:24

ANGEL MANUEL BONGIOVANNI PEREZ
 UNIVERSIDAD DE LA LAGUNA

29/06/2017 09:30:15

JORGE CEPA NOGUE
 UNIVERSIDAD DE LA LAGUNA

29/06/2017 09:33:05

ANA MARIA PEREZ GARCIA
 UNIVERSIDAD DE LA LAGUNA

29/06/2017 11:12:35

ERNESTO PEREDA DE PABLO
 UNIVERSIDAD DE LA LAGUNA

04/07/2017 18:28:07

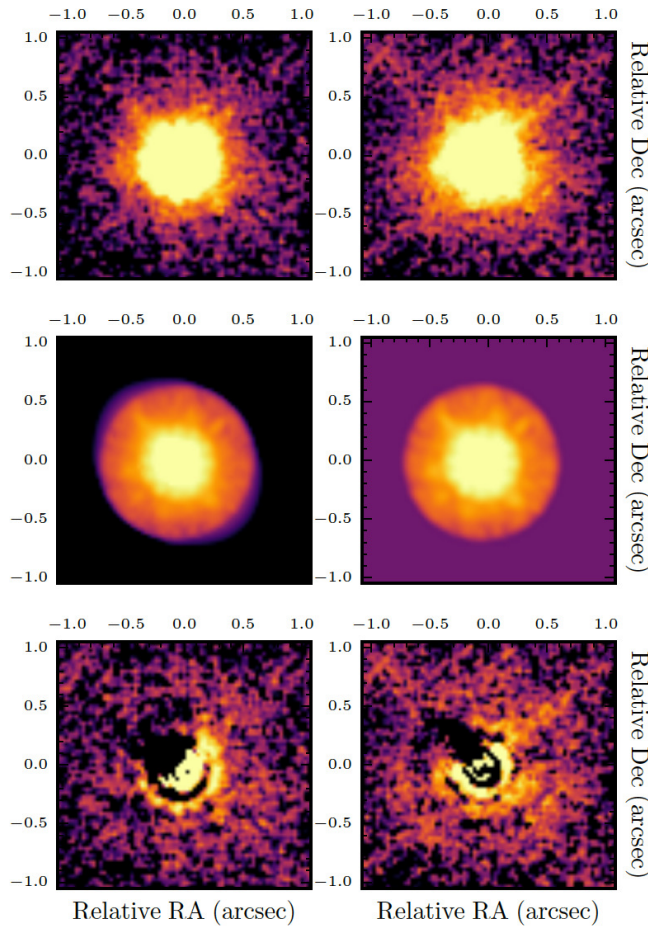


Figure A.11: Morphology of the object #8351. This object was selected as an AGN both in X-rays and MIR. It has a point-like appearance, and is probably a QSO, just like the object #6173, shown in Fig. A.8. First row: HST images of the object. Second row: GALFIT models. Third row: GALFIT residuals obtained by subtracting its model to the original image. The first column shows the V filter of HST (F814W) and the second one the I filter (F606W).

Este documento incorpora firma electrónica, y es copia auténtica de un documento electrónico archivado por la ULL según la Ley 39/2015.
Su autenticidad puede ser contrastada en la siguiente dirección <https://sede.ull.es/validacion/>

Identificador del documento: 969870

Código de verificación: 8KFVZkZp

Firmado por: MARINA RAMÓN PÉREZ
UNIVERSIDAD DE LA LAGUNA

Fecha: 28/06/2017 21:15:24

ANGEL MANUEL BONGIOVANNI PEREZ
UNIVERSIDAD DE LA LAGUNA

29/06/2017 09:30:15

JORGE CEPA NOGUE
UNIVERSIDAD DE LA LAGUNA

29/06/2017 09:33:05

ANA MARIA PEREZ GARCIA
UNIVERSIDAD DE LA LAGUNA

29/06/2017 11:12:35

ERNESTO PEREDA DE PABLO
UNIVERSIDAD DE LA LAGUNA

04/07/2017 18:28:07

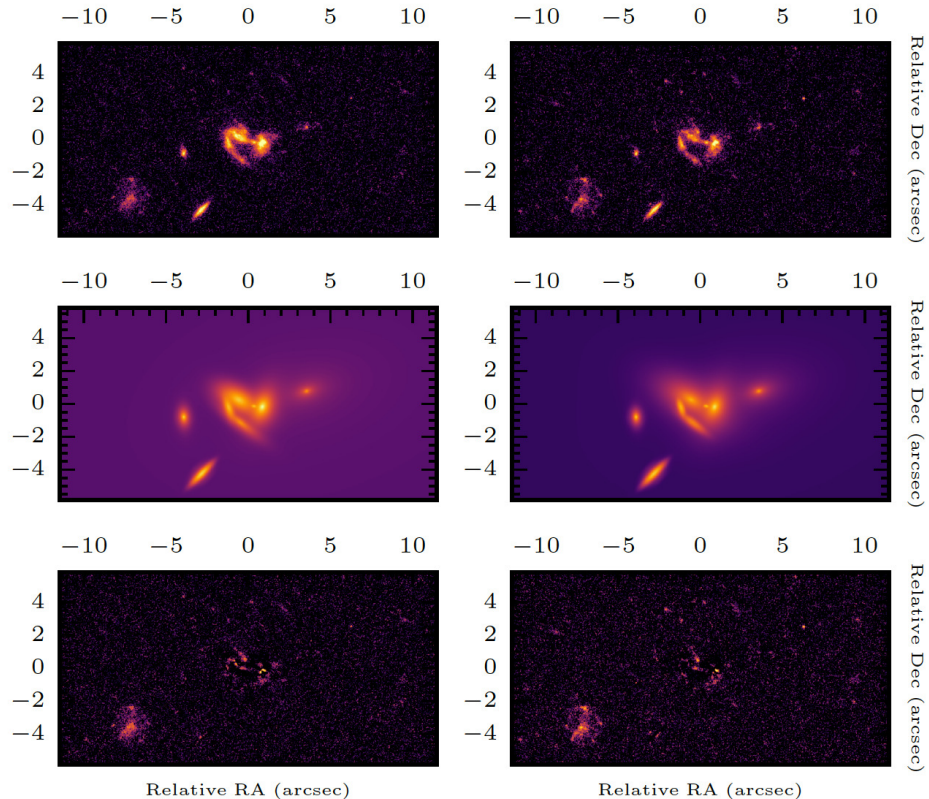


Figure A.12: Morphology of the object #11168. This system was selected by infrared methods as an AGN. Two interacting spiral galaxies are visible. First row: HST images of the object. Second row: GALFIT models. Third row: GALFIT residuals obtained by subtracting its model to the original image. The first column shows the V filter of HST (F814W) and the second one the I filter (F606W).

Este documento incorpora firma electrónica, y es copia auténtica de un documento electrónico archivado por la ULL según la Ley 39/2015.
Su autenticidad puede ser contrastada en la siguiente dirección <https://sede.ull.es/validacion/>

Identificador del documento: 969870

Código de verificación: 8KFVZkZp

Firmado por: MARINA RAMÓN PÉREZ
UNIVERSIDAD DE LA LAGUNA

Fecha: 28/06/2017 21:15:24

ANGEL MANUEL BONGIOVANNI PEREZ
UNIVERSIDAD DE LA LAGUNA

29/06/2017 09:30:15

JORGE CEPA NOGUE
UNIVERSIDAD DE LA LAGUNA

29/06/2017 09:33:05

ANA MARIA PEREZ GARCIA
UNIVERSIDAD DE LA LAGUNA

29/06/2017 11:12:35

ERNESTO PEREDA DE PABLO
UNIVERSIDAD DE LA LAGUNA

04/07/2017 18:28:07

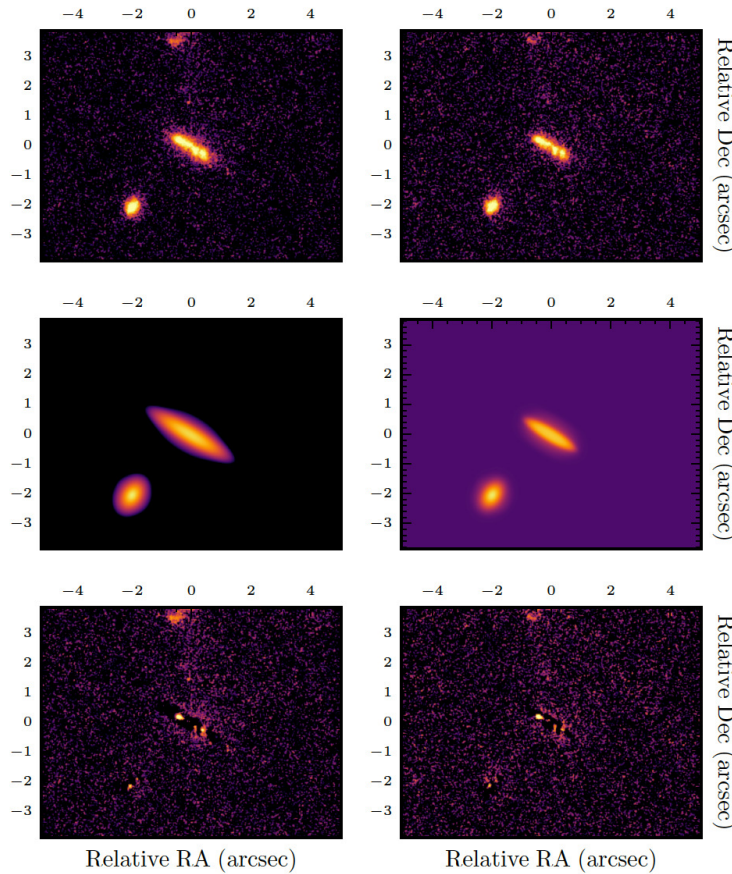


Figure A.13: Morphology of the object #7800. This object is an obscured AGN. It was selected with infrared methods and classified as an irregular object (late-type), seemingly a chain-galaxy. First row: HST images of the object. Second row: GALFIT models. Third row: GALFIT residuals obtained by subtracting its model to the original image. The first column shows the V filter of HST (F814W) and the second one the I filter (F606W).

Este documento incorpora firma electrónica, y es copia auténtica de un documento electrónico archivado por la ULL según la Ley 39/2015.
Su autenticidad puede ser contrastada en la siguiente dirección <https://sede.ull.es/validacion/>

Identificador del documento: 969870

Código de verificación: 8KFVZkZp

Fecha: 28/06/2017 21:15:24

Firmado por: MARINA RAMÓN PÉREZ
UNIVERSIDAD DE LA LAGUNA

ANGEL MANUEL BONGIOVANNI PEREZ
UNIVERSIDAD DE LA LAGUNA

JORGE CEPA NOGUE
UNIVERSIDAD DE LA LAGUNA

ANA MARIA PEREZ GARCIA
UNIVERSIDAD DE LA LAGUNA

ERNESTO PEREDA DE PABLO
UNIVERSIDAD DE LA LAGUNA

29/06/2017 09:30:15

29/06/2017 09:33:05

29/06/2017 11:12:35

04/07/2017 18:28:07

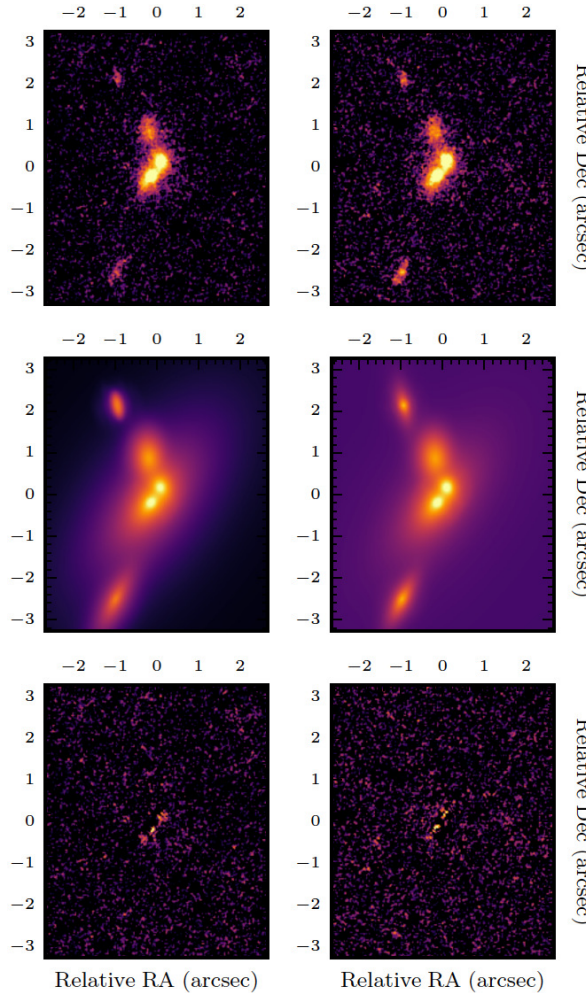


Figure A.14: Morphology of the object #10965. This object is an obscured AGN, selected only by infrared methods, which seems to be interacting. It was classified as a late-type galaxy. First row: HST images of the object. Second row: GALFIT models. Third row: GALFIT residuals obtained by subtracting its model to the original image. The first column shows the V filter of HST (F814W) and the second one the I filter (F606W).

Este documento incorpora firma electrónica, y es copia auténtica de un documento electrónico archivado por la ULL según la Ley 39/2015.
Su autenticidad puede ser contrastada en la siguiente dirección <https://sede.ull.es/validacion/>

Identificador del documento: 969870

Código de verificación: 8KFVZkZp

Firmado por: MARINA RAMÓN PÉREZ
UNIVERSIDAD DE LA LAGUNA

Fecha: 28/06/2017 21:15:24

ANGEL MANUEL BONGIOVANNI PEREZ
UNIVERSIDAD DE LA LAGUNA

29/06/2017 09:30:15

JORGE CEPA NOGUE
UNIVERSIDAD DE LA LAGUNA

29/06/2017 09:33:05

ANA MARIA PEREZ GARCIA
UNIVERSIDAD DE LA LAGUNA

29/06/2017 11:12:35

ERNESTO PEREDA DE PABLO
UNIVERSIDAD DE LA LAGUNA

04/07/2017 18:28:07

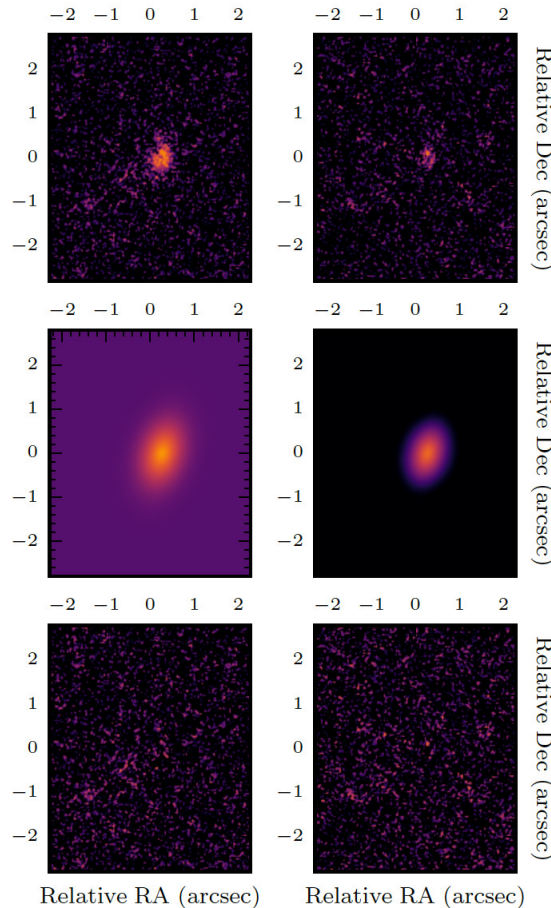


Figure A.15: Morphology of the object #7772. This object is a faint obscured AGN, classified as an irregular galaxy (late-type). First row: HST images of the object. Second row: GALFIT models. Third row: GALFIT residuals obtained by subtracting its model to the original image. The first column shows the V filter of HST (F814W) and the second one the I filter (F606W).

Este documento incorpora firma electrónica, y es copia auténtica de un documento electrónico archivado por la ULL según la Ley 39/2015.
Su autenticidad puede ser contrastada en la siguiente dirección <https://sede.ull.es/validacion/>

Identificador del documento: 969870

Código de verificación: 8KFVZkZp

Fecha: 28/06/2017 21:15:24

Firmado por: MARINA RAMÓN PÉREZ
UNIVERSIDAD DE LA LAGUNA

29/06/2017 09:30:15

ANGEL MANUEL BONGIOVANNI PEREZ
UNIVERSIDAD DE LA LAGUNA

29/06/2017 09:33:05

JORGE CEPA NOGUE
UNIVERSIDAD DE LA LAGUNA

29/06/2017 11:12:35

ANA MARIA PEREZ GARCIA
UNIVERSIDAD DE LA LAGUNA

04/07/2017 18:28:07

ERNESTO PEREDA DE PABLO
UNIVERSIDAD DE LA LAGUNA

BIBLIOGRAPHY

- Abdalla, F. B., Banerji, M., Lahav, O., & Rashkov, V. 2011, MNRAS, 417, 1891
- Abbott, B. P., Abbott, R., Abbott, T. D., et al. 2016, Physical Review Letters, 116, 061102
- Alexander, D. M., Brandt, W. N., Hornschemeier, A. E., et al. 2001, AJ, 122, 2156
- Alvarez, P., Rodríguez Espinosa, J. M., & Sánchez, F. 1998, New Astronomy Reviews, 42, 553
- Annunziatella, M., Mercurio, A., Brescia, M., Cavuoti, S., & Longo, G. 2013, PASP, 125, 68
- Antonucci, R. 1993, ARAA, 31, 473
- Arnouts, S., Cristiani, S., Moscardini, L., et al. 1999, MNRAS, 310, 540
- Arribas, S., Mediavilla, E., García-Lorenzo, B., & del Burgo, C. 1997, ApJ, 490, 227
- Atherton, P. D., & Reay, N. K. 1981, MNRAS, 197, 507
- Baldry, I. K., Robotham, A. S. G., Hill, D. T., et al. 2010, MNRAS, 404, 86
- Baldwin, J. A., Phillips, M. M., & Terlevich, R. 1981, PASP, 93, 5
- Barden, M., Häußler, B., Peng, C. Y., McIntosh, D. H., & Guo, Y. 2012, MNRAS, 422, 449
- Barmby, P., Huang, J.-S., Ashby, M. L. N., et al. 2008, ApJS, 177, 431
- Barro, G., Pérez-González, P. G., Gallego, J., et al. 2011, ApJS, 193, 13
- Beckmann, V., & Shrader, C. 2012, Proceedings of "An INTEGRAL view of the high-energy sky (the first 10 years)" - 9th INTEGRAL Workshop and celebration of the 10th anniversary of the launch (INTEGRAL 2012). 15-19 October 2012. Bibliothèque Nationale de France, Paris, France.
- Benítez, N., Ford, H., Bouwens, R., et al. 2004, ApJS, 150, 1
- Benitez, N., Dupke, R., Moles, M., et al. 2014, arXiv:1403.5237
- Bertin, E., & Arnouts, S. 1996, A&AS, 117, 393
- Bertin, E., Mellier, Y., Radovich, M., et al. 2002, Astronomical Data Analysis Software and Systems XI, 281, 228
- Bertin, E. 2009, MmSAI, 80, 422
- Bertin, E. 2011, Astronomical Data Analysis Software and Systems XX, 442, 435
- Bielby, R., Hudelot, P., McCracken, H. J., et al. 2012, A&A, 545, A23
- Blandford, R. D., Netzer, H., Woltjer, L., Courvoisier, T. J.-L., & Mayor, M. 1990, Active Galactic Nuclei, 97
- Bland-Hawthorn, J., & Jones, D. H. 1998, PASA, 15, 44
- Bohlin, R. C., Colina, L., & Finley, D. S. 1995, AJ, 110, 1316

Este documento incorpora firma electrónica, y es copia auténtica de un documento electrónico archivado por la ULL según la Ley 39/2015.
Su autenticidad puede ser contrastada en la siguiente dirección <https://sede.ull.es/validacion/>

Identificador del documento:	969870	Código de verificación:	8KFVZkZp
Firmado por:	MARINA RAMÓN PÉREZ UNIVERSIDAD DE LA LAGUNA	Fecha:	28/06/2017 21:15:24
	ANGEL MANUEL BONGIOVANNI PEREZ UNIVERSIDAD DE LA LAGUNA		29/06/2017 09:30:15
	JORGE CEPA NOGUE UNIVERSIDAD DE LA LAGUNA		29/06/2017 09:33:05
	ANA MARIA PEREZ GARCIA UNIVERSIDAD DE LA LAGUNA		29/06/2017 11:12:35
	ERNESTO PEREDA DE PABLO UNIVERSIDAD DE LA LAGUNA		04/07/2017 18:28:07

- Bongiovanni, A., Bruzual, G., Magris, G., et al. 2005, MNRAS, 359, 930
- Brandt, W. N., Alexander, D. M., Bauer, F. E., & Vignali, C. 2004, in Physics of Active Galactic Nuclei at All Scales, ed. D. Alloin, R. Johnson, & P. Lira (Berlin: Springer-Verlag) [arXiv:astro-ph/0403646]
- Bunker, A. J., Warren, S. J., Hewett, P. C., & Clements, D. L. 1995, MNRAS, 273, 513
- Cabrera-Lavers, A., Bongiovanni, A., Cepa, J., & Rutten, R. G. M. 2014, Canarian Observatories Updates (CUPs), 1
- Caccianiga, A., Severgnini, P., Braito, V., et al. 2004, A&A, 416, 901
- Calzetti, D., Armus, L., Bohlin, R. C., et al. 2000, ApJ, 533, 682
- Calzetti, D. 2011, EAS Publications Series, 46, 133
- Cepa, J., Aguiar, M., Bland-Hawthorn, J., et al. 2003, Revista Mexicana de Astronomia y Astrofisica Conference Series, 16, 13
- Cepa, J., Alfaro, E. J., Bland-Hawthorn, J., et al. 2003, Revista Mexicana de Astronomia y Astrofisica Conference Series, 16, 64
- Cepa, J. 2009, The Emission-Line Universe, XVIII Canary Islands Winter School of Astrophysics, Cambridge University Press
- Chang, C., Busha, M. T., Wechsler, R. H., et al. 2015, ApJ, 801, 73
- Chary, R., & Elbaz, D. 2001, ApJ, 556, 562
- Cid Fernandes, R., Stasińska, G., Schlickmann, M. S., et al. 2010, MNRAS, 403, 1036
- Ciliegi, P., Zamorani, G., Hasinger, G., et al. 2003, A&A, 398, 901
- Coe, D., Benítez, N., Sánchez, S. F., et al. 2006, The Astrophysical Journal, 132, 926
- Coil, A. L., Newman, J. A., Kaiser, N., et al. 2004, ApJ, 617, 765
- Coleman, G. D., Wu, C.-C., & Weedman, D. W. 1980, ApJS, 43, 393
- Cooper, M. C., Newman, J. A., Madgwick, D. S., et al. 2005, ApJ, 634, 833
- Coupon, J., Ilbert, O., Kilbinger, M., et al. 2009, A&A, 500, 981
- Cowley, M. J., Spitler, L. R., Tran, K.-V. H., et al. 2016, MNRAS, 457, 629
- Dahlen, T., Mobasher, B., Faber, S. M., et al. 2013, ApJ, 775, 93
- Davis, M., Guhathakurta, P., Konidaris, N. P., et al. 2007, ApJL, 660, L1
- Decarli, R., Walter, F., Aravena, M., et al. 2016, ApJ, 833, 69
- Della Ceca, R., Maccacaro, T., Caccianiga, A., et al. 2004, A&A, 428, 383
- de Ruiter, H. R., Willis, A. G., & Arp, H. C. 1977, A&AS, 28, 211
- di Césare, M. A., Hammersley, P. L., & Rodríguez-Espinosa, J. M. 2007, The Future of Photometric, Spectrophotometric and Polarimetric Standardization, 364, 289
- Djorgovski, S. G., Mahabal, A., Drake, A., Graham, M., & Donalek, C. 2013, Planets, Stars and Stellar Systems. Volume 2: Astronomical Techniques, Software and Data, 223
- Donley, J. L., Koekemoer, A. M., Brusa, M., et al. 2012, ApJ, 748, 142
- Drake, A. B., Simpson, C., Collins, C. A., et al. 2013, MNRAS, 433, 796
- Eales, S. A., Raymond, G., Roseboom, I. G., et al. 2010, A&A, 518, L23

Este documento incorpora firma electrónica, y es copia auténtica de un documento electrónico archivado por la ULL según la Ley 39/2015.
Su autenticidad puede ser contrastada en la siguiente dirección <https://sede.ull.es/validacion/>

Identificador del documento:	Código de verificación:
969870	8KFVZkZp
Firmado por: MARINA RAMÓN PÉREZ UNIVERSIDAD DE LA LAGUNA	Fecha: 28/06/2017 21:15:24
ANGEL MANUEL BONGIOVANNI PÉREZ UNIVERSIDAD DE LA LAGUNA	29/06/2017 09:30:15
JORGE CEPA NOGUE UNIVERSIDAD DE LA LAGUNA	29/06/2017 09:33:05
ANA MARIA PÉREZ GARCIA UNIVERSIDAD DE LA LAGUNA	29/06/2017 11:12:35
ERNESTO PEREDA DE PABLO UNIVERSIDAD DE LA LAGUNA	04/07/2017 18:28:07

- Elbaz, D., Dickinson, M., Hwang, H. S., et al. 2011, A&A, 533, A119
- Fabry, C., & Perot, A. 1901, ApJ, 13, 265
- Fabry, C., & Buisson, H. 1911, ApJ, 33, 406
- Fan, L., Fang, G., Chen, Y., et al. 2014, ApJL, 784, L9
- Fath, E. A. 1909, Lick Observatory Bulletin, 5, 71
- Fazio, G. G., Hora, J. L., Allen, L. E., et al. 2004, ApJS, 154, 10
- Gabor, J. M., Impey, C. D., Jahnke, K., et al. 2009, ApJ, 691, 705
- Galametz, A., Grazian, A., Fontana, A., et al. 2013, ApJS, 206, 10
- Gallego, J., Zamorano, J., Rego, M., & Vitores, A. G. 1997, ApJ, 475, 502
- Gavazzi, G., Boselli, A., Cortese, L., et al. 2006, A&A, 446, 839
- Geach, J. E., Smail, I., Best, P. N., et al. 2008, MNRAS, 388, 1473
- Gil de Paz, A., Madore, B. F., & Pevunova, O. 2003, ApJS, 147, 29
- Glazebrook, K., & Bland-Hawthorn, J. 2001, PASP, 113, 197
- Gómez-Guijarro, C., Gallego, J., Villar, V., et al. 2016, A&A, 591, A151
- González-Serrano, J. I., Cepa, J., Gallego, J., et al. 2005, Revista Mexicana de Astronomia y Astrofisica Conference Series, 24, 245
- González-Serrano, J. I., Cepa, J., Pérez-García, A. M., et al. 2005, Revista Mexicana de Astronomia y Astrofisica Conference Series, 24, 247
- González, J. J., Cepa, J., González-Serrano, J. I., & Sánchez-Portal, M. 2014, MNRAS, 443, 3289
- Griffin, M., Swinyard, B., Vigroux, L., et al. 2008, SPIE, 7010, 701006
- Griffith, R. L., & Stern, D. 2010, The Astrophysical Journal, 140, 533
- Gruen, D., Seitz, S., & Bernstein, G. M. 2014, PASP, 126, 158
- Hayashi, M., Tanaka, M., Shimakawa, R., et al. 2017, arXiv:1704.05978
- Hickox, R. C., Jones, C., Forman, W. R., et al. 2009, ApJ, 696, 891
- Ho, L. C., Filippenko, A. V., & Sargent, W. L. W. 1997, ApJS, 112, 315
- Hönig, S. F., & Kishimoto, M. 2010, A&A, 523, A27
- Homrighausen, D., Genovese, C. R., Connolly, A. J., Becker, A. C., & Owen, R. 2011, PASP, 123, 1117
- Hopkins, P. F., Hernquist, L., Cox, T. J., & Kereš, D. 2008, ApJS, 175, 356-389
- Ilbert, O., Arnouts, S., McCracken, H. J., et al. 2006, A&A, 457, 841
- Johnston, R. 2011, A&A Revs, 19, 41
- Jones, D. H. 2001, PASP, 113, 255
- Jones, H., Renzini, A., Rosati, P., & Seifert, W. 2001, The Messenger, 103, 10
- Jones, D. H., & Bland-Hawthorn, J. 2001, ApJ, 550, 593
- Jones, D. H., Shopbell, P. L., & Bland-Hawthorn, J. 2002, MNRAS, 329, 759
- Kaspi, S., Maoz, D., Netzer, H., et al. 1996, ApJ, 470, 336

Este documento incorpora firma electrónica, y es copia auténtica de un documento electrónico archivado por la ULL según la Ley 39/2015.
Su autenticidad puede ser contrastada en la siguiente dirección <https://sede.ull.es/validacion/>

Identificador del documento: 969870

Código de verificación: 8KFVZkZp

Fecha: 28/06/2017 21:15:24

Firmado por: MARINA RAMÓN PÉREZ
UNIVERSIDAD DE LA LAGUNA

29/06/2017 09:30:15

ANGEL MANUEL BONGIOVANNI PEREZ
UNIVERSIDAD DE LA LAGUNA

29/06/2017 09:33:05

JORGE CEPA NOGUE
UNIVERSIDAD DE LA LAGUNA

29/06/2017 11:12:35

ANA MARIA PEREZ GARCIA
UNIVERSIDAD DE LA LAGUNA

04/07/2017 18:28:07

ERNESTO PEREDA DE PABLO
UNIVERSIDAD DE LA LAGUNA

- Kennicutt, R. C., Jr. 1998, ARAA, 36, 189
- Kerscher, M., Pons-Bordería, M. J., Schmalzing, J., et al. 1999, ApJ, 513, 543
- Kewley, L. J., Dopita, M. A., Sutherland, R. S., Heisler, C. A., & Trevena, J. 2001, ApJ, 556, 121
- Kewley, L. J., Groves, B., Kauffmann, G., & Heckman, T. 2006, MNRAS, 372, 961
- Kinney, A. L., Calzetti, D., Bohlin, R. C., et al. 1996, ApJ, 467, 38
- Koratkar, A., & Blaes, O. 1999, PASP, 111, 1
- Kovač, K., Lilly, S. J., Cucciati, O., et al. 2010, ApJ, 708, 505
- Lacy, M., Storrie-Lombardi, L. J., Sajina, A., et al. 2004, ApJS, 154, 166
- Lacy, M., Petric, A. O., Sajina, A., et al. 2007, AJ, 133, 186
- Laird, E. S., Nandra, K., Georgakakis, A., et al. 2009, ApJS, 180, 102
- Lara-López, M. A., Cepa, J., Castañeda, H., et al. 2011, PASP, 123, 252
- Lee, N., Le Floc'h, E., Sanders, D. B., et al. 2010, ApJ, 717, 175
- Lilly, S. J., Le Fèvre, O., Renzini, A., et al. 2007, ApJS, 172, 70
- Lin, M.-Y., Hashimoto, Y., & Foucaud, S. 2016, MNRAS, 456, 2735
- Lonsdale, C. J., Farrah, D., & Smith, H. E. 2006, Astrophysics Update 2, 285
- López-Sanjuan, C., Tempel, E., Benítez, N., et al. 2017, A&A, 599, A62
- Luo, B., Brandt, W. N., Xue, Y. Q., et al. 2010, ApJS, 187, 560
- Lutz, D., Poglitsch, A., Altieri, B., et al. 2011, A&A, 532, A90
- Ly, C., Malkan, M. A., Kashikawa, N., et al. 2007, ApJ, 657, 738
- Ly, C., Malkan, M. A., Kashikawa, N., et al. 2012, ApJL, 747, L16
- Maccacaro, T., Gioia, I. M., Wolter, A., Zamorani, G., & Stocke, J. T. 1988, ApJ, 326, 680
- Magnelli, B., Popesso, P., Berta, S., et al. 2013, A&A, 553, A132
- Małek, K., Bankowicz, M., Pollo, A., et al. 2017, A&A, 598, A1
- Mancone, C. L., Gonzalez, A. H., Moustakas, L. A., & Price, A. 2013, PASP, 125, 1514
- Manti, S., Gallerani, S., Ferrara, A., Greig, B., & Feruglio, C. 2017, MNRAS, 466, 1160
- Manzer, L. H., & De Robertis, M. M. 2014, ApJ, 788, 140
- Marchesi, S., Lanzuisi, G., Civano, F., et al. 2016, ApJ, 830, 100
- Marscher, A. P. 2006, Relativistic Jets: The Common Physics of AGN, Microquasars, and Gamma-Ray Bursts, 856, 1
- Martin, D. C., Fanson, J., Schiminovich, D., et al. 2005, ApJL, 619, L1
- Martínez, V. J., & Saar, E. 2002, Statistics of the Galaxy Distribution, Published by Chapman & Hall/CRC, Boca Raton, ISBN: 1584880848
- Lieshout, M. N. M., & Baddeley, A.J. 1996, Statistica Neerlandica, 50,3, 344-361
- Masias, M., Freixenet, J., Lladó, X., & Peracaula, M. 2012, MNRAS, 422, 1674
- Mateos, S., Alonso-Herrero, A., Carrera, F. J., et al. 2012, MNRAS, 426, 3271

Este documento incorpora firma electrónica, y es copia auténtica de un documento electrónico archivado por la ULL según la Ley 39/2015.
Su autenticidad puede ser contrastada en la siguiente dirección <https://sede.ull.es/validacion/>

Identificador del documento:	Código de verificación:
969870	8KFVZkZp
Firmado por: MARINA RAMÓN PÉREZ UNIVERSIDAD DE LA LAGUNA	Fecha: 28/06/2017 21:15:24
ANGEL MANUEL BONGIOVANNI PEREZ UNIVERSIDAD DE LA LAGUNA	29/06/2017 09:30:15
JORGE CEPA NOGUE UNIVERSIDAD DE LA LAGUNA	29/06/2017 09:33:05
ANA MARIA PEREZ GARCIA UNIVERSIDAD DE LA LAGUNA	29/06/2017 11:12:35
ERNESTO PEREDA DE PABLO UNIVERSIDAD DE LA LAGUNA	04/07/2017 18:28:07

- Matthee, J., Sobral, D., Best, P., et al. 2017, arXiv:1702.04721
- Merlin, E., Bourne, N., Castellano, M., et al. 2016, A&A, 595, A97
- Messias, H., Afonso, J., Salvato, M., Mobasher, B., & Hopkins, A. M. 2012, ApJ, 754, 120
- Micic, M. 2013, Serbian Astronomical Journal, 186, 1
- Miller, C. J., Nichol, R. C., Gómez, P. L., Hopkins, A. M., & Bernardi, M. 2003, ApJ, 597, 142
- Moles, M., Benítez, N., Aguerri, J. A. L., et al. 2008, The Astrophysical Journal, 136, 1325
- Morrissey, P., Conrow, T., Barlow, T. A., et al. 2007, ApJS, 173, 682
- Mushotzky, R. 2004, Supermassive Black Holes in the Distant Universe, 308, 53
- Netzer, H. 2013, The Physics and Evolution of Active Galactic Nuclei, by Hagai Netzer, Cambridge, UK: Cambridge University Press, 2013,
- Netzer, H. 2015, ARAA, 53, 365
- Newman, J. A., Cooper, M. C., Davis, M., et al. 2013, ApJS, 208, 5
- Oliver, S. J., Bock, J., Altieri, B., et al. 2012, MNRAS, 424, 1614
- Osterbrock, D. E., & Ferland, G. J. 2006, Astrophysics of gaseous nebulae and active galactic nuclei, 2nd. ed. by D.E. Osterbrock and G.J. Ferland. Sausalito, CA: University Science Books, 2006,
- Peng, C. Y., Ho, L. C., Impey, C. D., & Rix, H.-W. 2002, The Astrophysical Journal, 124, 266
- Pérez-González, P. G., & Cava, A. 2013, Revista Mexicana de Astronomía y Astrofísica Conference Series, 42, 55
- Pérez-Martínez, R.M., 2016, *From Xrays to far infrared: galaxy cluster ZwCL0024+1652 under the multiwavelength limelight*
- Perot, A., & Fabry, C. 1899, ApJ, 9, 87
- Phillips, A. C., Faber, S., Kibrick, R., Wallace, V., & DEIMOS Team 2002, Bulletin of the American Astronomical Society, 34, 137.02
- Pickles, A. J. 1998, PASP, 110, 863
- Pilbratt, G. L., Riedinger, J. R., Passvogel, T., et al. 2010, A&A, 518, L1
- Pineau, F.-X., Motch, C., Carrera, F., et al. 2011, A&A, 527, A126
- Pintos-Castro, I. 2014, *Multi-wavelength study of the population of galaxies in intermediate-redshift clusters: the case of RXJ1257.2+4738 at z~0.9*
- Poglitsch, A., Waelkens, C., Geis, N., et al. 2010, A&A, 518, L2
- Polletta, M., Tajer, M., Maraschi, L., et al. 2007, ApJ, 663, 81
- Pović, M., Sánchez-Portal, M., Pérez García, A. M., et al. 2009, ApJ, 706, 810
- Pracy, M. B., Ching, J. H. Y., Sadler, E. M., et al. 2016, MNRAS, 460, 2
- Ramos Almeida, C., Sánchez-Portal, M., Pérez García, A. M., et al. 2011, MNRAS, 417, L46
- Rieke, G. H., Young, E. T., Engelbracht, C. W., et al. 2004, ApJS, 154, 25
- Roseboom, I. G., Oliver, S. J., Kunz, M., et al. 2010, MNRAS, 409, 48
- Sánchez-Portal, M., Pérez-García, A. M., Cepa, J., et al. 2005, Revista Mexicana de Astronomía y Astrofísica Conference Series, 24, 271

Este documento incorpora firma electrónica, y es copia auténtica de un documento electrónico archivado por la ULL según la Ley 39/2015.
Su autenticidad puede ser contrastada en la siguiente dirección <https://sede.ull.es/validacion/>

Identificador del documento:	Código de verificación:
969870	8KFVZkZp
Firmado por: MARINA RAMÓN PÉREZ UNIVERSIDAD DE LA LAGUNA	Fecha: 28/06/2017 21:15:24
ANGEL MANUEL BONGIOVANNI PEREZ UNIVERSIDAD DE LA LAGUNA	29/06/2017 09:30:15
JORGE CEPA NOGUE UNIVERSIDAD DE LA LAGUNA	29/06/2017 09:33:05
ANA MARIA PEREZ GARCIA UNIVERSIDAD DE LA LAGUNA	29/06/2017 11:12:35
ERNESTO PEREDA DE PABLO UNIVERSIDAD DE LA LAGUNA	04/07/2017 18:28:07

- Sánchez-Portal, M., Pintos-Castro, I., Pérez-Martínez, R., et al. 2015, A&A, 578, A30
- Sanders, D. B., & Mirabel, I. F. 1996, ARAA, 34, 749
- Schechter, P. 1976, ApJ, 203, 297
- Schmidt, M. 1968, ApJ, 151, 393
- Sérsic, J. L. 1963, Boletin de la Asociacion Argentina de Astronomia La Plata Argentina, 6, 41
- Seyfert, C. K. 1943, ApJ, 97, 28
- Shields, G. A. 1999, PASP, 111, 661
- Shioya, Y., Taniguchi, Y., Sasaki, S. S., et al. 2008, ApJS, 175, 128-137
- Singal, J., George, J., & Gerber, A. 2016, ApJ, 831, 60
- Skrutskie, M. F., Beichman, C., Capps, R., et al. 1995, Bulletin of the American Astronomical Society, 27, 75.07
- Sobral, D., Smail, I., Best, P. N., et al. 2013, MNRAS, 428, 1128
- Sobral, D., Kohn, S. A., Best, P. N., et al. 2016, MNRAS, 457, 1739
- Sobral, D., Matthee, J., Best, P., et al. 2017, MNRAS, 466, 1242
- Stasińska, G., Cid Fernandes, R., Mateus, A., Sodré, L., & Asari, N. V. 2006, MNRAS, 371, 972
- Stern, D., Eisenhardt, P., Gorjian, V., et al. 2005, ApJ, 631, 163
- Stern, J., & Laor, A. 2012, MNRAS, 423, 600
- Stocke, J. T., Morris, S. L., Gioia, I. M., et al. 1991, ApJS, 76, 813
- Sutherland, W., & Saunders, W. 1992, MNRAS, 259, 413
- Szokoly, G. P., Bergeron, J., Hasinger, G., et al. 2004, ApJS, 155, 271
- Taylor, M. B. 2005, Astronomical Data Analysis Software and Systems XIV, 347, 29
- Tilvi, V., Rhoads, J. E., Hibon, P., et al. 2010, ApJ, 721, 1853
- van Dokkum, P. G. 2001, PASP, 113, 1420
- Veilleux, S., & Osterbrock, D. E. 1987, ApJS, 63, 295
- Veilleux, S., Sanders, D. B., & Kim, D.-C. 1997, ApJ, 484, 92
- Veilleux, S., Weiner, B. J., Rupke, D. S. N., et al. 2010, The Astronomical Journal, 139, 145
- Virani, S. N., De Robertis, M. M., & VanDalfsen, M. L. 2000, The Astrophysical Journal, 120, 1739
- Waskett, T. J., Eales, S. A., Gear, W. K., et al. 2005, MNRAS, 363, 801
- Weinzirl, T., Aragón-Salamanca, A., Bamford, S. P., et al. 2015, MNRAS, 454, 1387
- Werner, M. W., Roellig, T. L., Low, F. J., et al. 2004, ApJS, 154, 1
- Wuyts, S., Förster Schreiber, N. M., Lutz, D., et al. 2011, ApJ, 738, 106

Este documento incorpora firma electrónica, y es copia auténtica de un documento electrónico archivado por la ULL según la Ley 39/2015.
Su autenticidad puede ser contrastada en la siguiente dirección <https://sede.ull.es/validacion/>

Identificador del documento:	Código de verificación:
969870	8KFVZkZp
Firmado por: MARINA RAMÓN PÉREZ UNIVERSIDAD DE LA LAGUNA	Fecha: 28/06/2017 21:15:24
ANGEL MANUEL BONGIOVANNI PEREZ UNIVERSIDAD DE LA LAGUNA	29/06/2017 09:30:15
JORGE CEPA NOGUE UNIVERSIDAD DE LA LAGUNA	29/06/2017 09:33:05
ANA MARIA PEREZ GARCIA UNIVERSIDAD DE LA LAGUNA	29/06/2017 11:12:35
ERNESTO PEREDA DE PABLO UNIVERSIDAD DE LA LAGUNA	04/07/2017 18:28:07